Robotic models for the honeybee visual odometer

Lucia Bergantin

Aix*Marseille université
Socialement engagée

NNT/NL : 2020AIXM0001/001ED000

THÈSE DE DOCTORAT

Soutenue à Aix-Marseille Université
le 22 mars 2023 par

Lucia BERGANTIN

Robotic models for the honeybee visual odometer

Discipline
Sciences du Mouvement Humain

École doctorale
ED 463 SCIENCES DU MOUVEMENT HUMAIN

Laboratoire/Partenaires de recherche
Institut des Sciences du Mouvement Etienne Jules Marey, BIOROB

Composition du jury

Prof. Luc JAULIN Université de Bretagne Occidentale - ENSTA	Président du jury
Prof. Barbara WEBB University of Edinburgh	Rapporteure
Prof. Luc JAULIN Université de Bretagne Occidentale - ENSTA	Rapporteur
Prof. Guido DE CROON Delft University of Technology	Examinateur
Prof. Antoine WYSTRACH CNRS, Université Paul Sabatier	Examinateur
Dr. Franck RUFFIER CNRS, Aix-Marseille Université	Directeur de thèse
Prof. Thibaut RAHARIJAONA Université de Lorraine	Co-directeur de thèse

DGA

INSTITUT DES SCIENCES DU MOUVEMENT ETIENNE JULES MAREY

cnrs

Affidavit

I, undersigned, Lucia Bergantin, hereby declare that the work presented in this manuscript is my own work, carried out under the scientific direction of Dr. Franck Ruffier et Prof. Thibaut Raharijaona, in accordance with the principles of honesty, integrity and responsibility inherent to the research mission. The research work and the writing of this manuscript have been carried out in compliance with both the french national charter for Research Integrity and the Aix-Marseille University charter on the fight against plagiarism.

This work has not been submitted previously either in this country or in another country in the same or in a similar version to any other examination body.

Marseille 04/01/2023

List of publications and conference participation

List of journal publications:

1. **L. Bergantin**, N. Harbaoui, T. Raharijaona and F. Ruffier, “Oscillations make a self-scaled model for honeybees’ visual odometer reliable regardless of flight trajectory,” *Journal of the Royal Society Interface*, 18.182 (2021): 20210567., doi: 10.1098/rsif.2021.0567
2. **L. Bergantin**, C. Coquet, J. Dumon, A. Negre, T. Raharijaona, N. Marchand, and F. Ruffier, “Indoor and outdoor in-flight odometry based solely on optic flows with oscillatory trajectories,” *International Journal of Micro Air Vehicles*, 2023;15, p. 17568293221148380, 2023, doi: 10.1177/17568293221148380

List of conference proceedings:

1. **L. Bergantin**, T. Raharijaona and F. Ruffier, “Estimation of the distance from a surface based on local optic flow divergence,” *2021 International Conference on Unmanned Aircraft Systems (ICUAS). IEEE.*, p. 1291–1298., 2021, doi: 10.1109/ICUAS51884.2021.9476751.
2. **L. Bergantin**, C. Coquet, A. Negre, T. Raharijaona, N. Marchand, and F. Ruffier, “Using trajectory oscillation timing improves in-flight odometry based solely on optic flows,” *13th International Micro Air Vehicle conference (IMAV), Delft, the Netherlands*, p. 66–74, 2022
3. J. J. Castillo-Zamora, **L. Bergantin**, and F. Ruffier. “Corridor 3D Navigation of a Fully-Actuated Multirotor by Means of Bee-Inspired Optic Flow Regulation." *2022 26th International Conference on System Theory, Control and Computing (ICSTCC). IEEE*, p. 318-324, 2022, doi: 10.1109/ICSTCC55426.2022.9931809
4. **L. Bergantin**, C. Coquet, A. Negre, T. Raharijaona, N. Marchand, and F. Ruffier, “Minimalistic in-flight odometry based on two optic flow sensors along a bouncing trajectory,” *2022 International Conference on Control, Automation and Systems (ICCAS). IEEE.*, p. 1321-1326, 2022, doi: 10.23919/ICCAS55662.2022.10003956

List of patents:

1. **L. Bergantin**, T. Raharijaona and F. Ruffier, "Dispositif d'estimation de distance et de longueur parcourue basé sur l'actionnement en va-et-vient de capteurs de flux optique," *France n° FR3118803*

Participation in conferences and summer schools during the thesis period:

1. Oral presentation of L. Bergantin et. al, "Estimation of the distance from a surface based on local optic flow divergence" at *2021 International Conference on Unmanned Aircraft Systems (ICUAS). IEEE.*, Athens, Greece, 15-18 June 2021
2. Oral presentation of L. Bergantin et. al, "Estimation of the distance from a surface based on local optic flow divergence" at *Journée GT UAV (Véhicules aériens)*, Paris, France, 6 July 2021
3. Oral presentation of L. Bergantin et. al, "Oscillations make a self scaled model for honeybees' visual odometer reliable regardless of flight trajectory" at *Robex Day*, ENSTA Bretagne, Brest, France, 24 Nov. 2021
4. Oral presentation of L. Bergantin et. al, "Oscillations make a self scaled model for honeybees' visual odometer reliable regardless of flight trajectory" at *Webinar Biorobotique*, Marseille, France, 25 Nov. 2021
5. Poster presentation of L. Bergantin et al., "Ups and downs to visually gauge the flight distance", at *17th Journée de l'Ecole Doctorale (JED) 2022*, Nice, France, 3 June 2022
6. Poster presentation of L. Bergantin et al., "Ups and downs to visually gauge the flight distance", at *International Congress of Neuroethology 2022*, Lisbon, Portugal, 24-29 July 2022
7. Oral presentation of L. Bergantin et al., "Using trajectory oscillation timing improves in-flight odometry based solely on optic flows" at *13th International Micro Air Vehicle conference (IMAV)*, Delft, the Netherlands, 12-16 Sep. 2022
8. Oral presentation of L. Bergantin et al., 'Minimalistic in-flight odometry based on two optic flow sensors along a bouncing trajectory" at *2022 International Conference on Control, Automation and Systems (ICCAS). IEEE.*, Busan, South Korea, 27 Nov. - 1 Dec. 2022

Awards:

1. Best Paper Award for L. Bergantin et al., "Using trajectory oscillation timing improves in-flight odometry based solely on optic flows" at *13th International Micro Air Vehicle conference (IMAV)*, Delft, the Netherlands, 12-16 Sep. 2022

Résumé

Dans la ruche, les abeilles butineuses informent leurs congénères de l'"emplacement" d'une source de nourriture en effectuant une danse en huit, qui indique la direction et la "distance" à parcourir. Des études précédentes ont suggéré que l'odomètre (servant de compteur de distance) de l'abeille évalue cette distance en intégrant mathématiquement la vitesse angulaire brute de l'image balayant vers l'arrière à travers leur champ de vision ventral, ce qui est connu comme le flux optique de translation. Dans les applications robotiques aériennes, la mise en œuvre d'une odométrie visuelle à bord de micro- et nano-drones est une tâche particulièrement difficile en raison des faibles ressources de calcul et des faibles moyens de perception disponibles. Plusieurs insectes ailés, tels que les abeilles et les papillons, oscillent de haut en bas tout en volant vers l'avant, ajoutant une composante d'expansion et de contraction à leur champ de vecteurs de flux optique ventral : il s'agit de la divergence du flux optique. La question se pose de comprendre comment l'intégration brute du flux optique (exprimée en rad/s) pourrait coder de manière suffisamment fiable une distance, puisque le flux optique dépend à la fois de la vitesse sol et de la hauteur sol. Dans cette thèse, un modèle de l'odomètre visuel de l'abeille, appelé SOFIa, est présenté. La hauteur courante par rapport au sol est estimée par un filtre de Kalman étendu et la divergence du flux optique générée par la trajectoire oscillante. L'estimation de la hauteur par rapport au sol permet la mise à l'échelle du flux optique de translation, qui est ensuite intégré mathématiquement pour obtenir la distance parcourue. En mesurant les indices de flux optique de translation et de divergence avec des capteurs de flux optique, l'odomètre visuel SOFIa a pu être testé sur un hexarotor à la fois en intérieur et en extérieur. Un second modèle d'odomètre visuel (appelé SuRf) a également été développé et testé en simulation. L'odomètre visuel SuRf est également basé sur la mise à l'échelle du flux optique de translation, mais dans ce cas, le flux optique pris en compte est toujours perçu perpendiculairement à la surface survolée. Pour cela, un processus de réorientation active a été ajouté afin de toujours garder le plan visuel parallèle au terrain en dessous. Le modèle SuRf a permis d'améliorer les performances odométriques obtenues sur terrain irrégulier par rapport à celles du modèle SOFIa brut. Modéliser l'odomètre visuel de l'abeille en se basant sur une vision biologiquement plausible est donc d'un grand intérêt pour deux raisons principales : (i) jeter une lumière nouvelle sur les processus neuro-éthologiques à l'œuvre chez les insectes ailés, et (ii) ouvrir la voie à la mise en œuvre sur des micro-robots volants de capacités odométriques visuelles minimalistes.

Mots clés: odométrie visuelle, abeilles, flux optique, facteur d'échelle, oscillations, robotique aérienne

Abstract

In the hive, foraging honeybees inform their nestmates about the "location" of a food source by performing a waggle dance, which carries knowledge about the direction and "distance" to travel. Previous studies have suggested that the odometer (serving as a distance-meter) of flying honeybees assesses distance by mathematically integrating the raw angular velocity of the image sweeping backwards across their ventral viewfield, which is known as the translational optic flow. In aerial robotic applications, performing visual odometry onboard micro- and nano-drones is a particularly challenging task due to the low computational and perception resources available. Several winged insects, such as bees and butterflies, oscillate up and down while flying forward, adding an expansion and contraction component to their ventral optic flow vector field: this is the optic flow divergence. The question arises as to how raw integration of the optic flow (expressed in rad/s) could reliably encode a distance, since optic flow depends on the ground speed and the ground height. In this thesis, a model for the honeybee visual odometer, called SOFIa, is presented. The current ground height is estimated solely by means of an Extended Kalman Filter (EKF) and the optic flow divergence generated by the oscillating trajectory. The ground height estimate scales the translational optic flow, which is then mathematically integrated to obtain the distance travelled. By measuring the translational and divergence optic flow cues with optic flow sensors, the SOFIa visual odometer could be tested onboard a hexarotor both indoors and outdoors. A second model for the visual odometer (called SuRf) was also developed and tested in simulation. The SuRf visual odometer is also based on the scaling of the translational optic flow, but in this case, the optic flow taken into account is always perceived perpendicularly to the surface below. For this purpose, an active reorientation process was added so as to always keep the visual plane parallel to the ground below. The SuRf model improved the odometric performances obtained over uneven terrain in comparison with those of the raw SOFIa model. Modelling of the honeybee visual odometer using biologically plausible vision is therefore of great interest for two main reasons: (i) shed new light on the neuro-ethological processes at work in winged insects, and (ii) open the way to providing micro flying robots with minimalistic visual odometric equipment and abilities.

Keywords: visual odometry, honeybees, optic flow, scaling factor, oscillations, aerial robotics

Acknowledgements

A PhD is a long journey with many ups and downs. On my own I could not have made it through. I would like to thank all the people who made this incredible journey possible with their love and support.
First of all, I would like to thank Dr. Franck Ruffier for being the best PhD supervisor I could have asked for. Over the past 3.5 years, you have always been there to help and support me. I will always be grateful to you for the opportunity to work on this amazing topic.
I would like to thank Prof. Thibaut Raharijaona for the support and suggestions. To Charles, Jean-Marc and the Gipsa-lab team, thank you for your great help in showing that what I was doing made sense. To Dr. Jessica Blanc, thank you for your corrections and your extraordinary patience.
I would like to thank all my colleagues (current and former) in the Biorobotique team for their support and the great energy they bring to work every day. You are the reason why our team has felt like a home away from home for the past 3.5 years. To my fellow PhD students, thank you for sharing this incredible journey with me.
I would like to thank my friends and family for their love and daily support. To the Quackers, thank you for being there despite the distance and lack of time. To my friends in Italy, thank you for always being there when I come back.
To Mom and Dad, none of this would have been possible without you. As long as you believe in me, I can do anything.
To Christophe, thank you for being there through thick and thin throughout this journey. Thank you for not letting me run far away... at least not without you.
To everyone reading this who is going through an incredible (and maybe sometimes a bit bumpy) journey, thank you and good luck!

Contents

List of Figures

List of Tables

1 Thesis contributions and outline

Foraging honeybees inform their nestmates about the direction and distance of a food source from the hive by performing a waggle dance. Previous studies have suggested that the odometer (serving as distance-meter) of the foragers' path integrator assesses distance by mathematically integrating the raw angular velocity of the image sweeping backwards across their ventral viewfield, which is known as translational optic flow. The question arises as to how integration of optic flow (expressed in rad/s) can reliably encode a distance, since optic flow depends on the ground speed and the ground height. Several winged insects, such as bees and butterflies, oscillate up and down at a frequency between $1Hz$ and $5Hz$ while flying forward. Thus, flying insects enrich their ventral optic flow vector field by adding an expansion and contraction component: this is the optic flow divergence. In aerial robotic applications, visual odometry performed with cameras has limitations due to environmental conditions and the high computational power required. This task is particularly challenging in the case of micro- and nano-drones, on which onboard computational and perception resources available tend to be low. The aim of this thesis project is to develop a model for the honeybee visual odometer in order to: (i) shed new light on the neuro-ethological processes at work in winged insects, and (ii) open the way to providing micro flying robots with minimalistic visual odometric equipment and abilities.

Contributions

The first contribution of this thesis is the presentation of a model for the honeybee visual odometer, called SOFIa (Self-scaled Optic Flow time-based Integration), to estimate the distance traveled solely on the basis of the translational and divergence optic flow cues perceived during forward flights with up-and-down self-oscillations. In the SOFIa visual odometer, the optic flow divergence cue is used to visually estimate the current ground height, which then scales the translational optic flow cue before its integration over time. The SOFIa visual odometer was tested on honeybees' trajectories in open-field simulations under a wide range of wind and terrain conditions.
In order to test the SOFIa visual odometer onboard a small flying robot, it was demonstrated that the optic flow divergence cue can be measured as the difference of two optic flow magnitudes perceived by two optic flow sensors placed at angles ϕ and $-\phi$ with respect to the normal to a surface. To experimentally test this strategy, a test bench was built consisting of two optic flow sensors set at fixed angles on a chariot placed on a slider in front of a panorama. The optic flow sensors were made to oscil-

late back and forth in front of the panorama (either static or moving) to mimic the up-and-down self-oscillations performed by honeybees while flying forward. The distance of the optic flow sensors from the panorama was estimated by means of an Extended Kalman Filter (EKF) receiving as measurement the measured optic flow divergence cue. Similarly, it was demonstrated that the translational optic flow cue can be measured as the sum of two optic flow magnitudes perceived by two optic flow sensors placed at angles ϕ and $-\phi$ with respect to the normal to a surface.
By measuring both translational and divergence optic flow cues with two optic flow sensors, the SOFIa visual odometer was tested onboard a hexarotor equipped with optic flow sensors placed downwards at fixed angles. To further improve the odometric performance of the SOFIa method, the idea of using prior knowledge of the oscillations imposed on the hexarotor to more accurately measure translational and divergence optic flow cues was also investigated. Two different sensor fusion strategies, respectively based on precise and rough prior knowledge of optic flow variations, were tested onboard the hexarotor both indoors and outdoors.
To improve the measurement of the optic flow cues, the idea of reorienting the simulated honeybee compound eye in order to keep the head pitch on a level with the surface below was investigated. This second model for the honeybee visual odometer, called SuRf (Surface Reference based), is also based on the scaling of the translational optic flow, but in this case, the optic flow taken into account is always perceived perpendicularly to the surface below. The SuRf visual odometer was tested on honeybees' trajectories in open-field simulations under a wide range of wind and terrain conditions.

Outline

In Chapter 2, observations on the ability of honeybees to assess the distance to a food source from the hive are discussed. The concept of the honeybee odometer based on visual cues is introduced. A review of odometric approaches in robotics is provided, with a focus on visual odometry performed with cameras.
In Chapter 3, the concept of optic flow is introduced. Observations on the use of optic flow by flying insects to navigate their environment are discussed. The measurement of optic flow with cameras is presented. Optic flow sensors are then described. Finally, insect-inspired robotic approaches based on the use of optic flow cues are presented.
In Chapter 4, the model for the honeybee visual odometer based on the mathematical integration of the raw angular velocity of the image sweeping backwards across the ventral viewfield is discussed. The self-oscillations observed in flying honeybees are introduced.
In Chapter 5, the SOFIa model for the honeybee visual odometer is presented. The SOFIa visual odometer is tested on honeybees' trajectories in open-field simulations and its odometric performance is compared with that of the model based on the mathematical integration of the raw angular velocity of the image sweeping backwards

across the ventral viewfield.
In Chapter 6, a strategy to measure the optic flow divergence cue with two optic flow sensors is discussed. This strategy is tested on a test bench consisting of two optic flow sensors oscillating back and forth in front of a moving panorama.
In Chapter 7, the SOFIa visual odometer is experimentally tested onboard a hexarotor equipped with optic flow sensors. Two sensor fusion strategies, based respectively on a precise and rough prior knowledge of optic flow variations, are tested in order to further improve the odometric performance of the SOFIa method.
In Chapter 8, the SuRf model for the honeybee visual odometer is presented. The SuRf visual odometer is tested on honeybees' trajectories in open-field simulations and its odometric performance is compared with that of the SOFIa visual odometer.
In Chapter 9, conclusions and future perspectives are discussed.

2 Introduction

Honeybees and flying robots may seem to have little in common. However, they both have the same problem to solve: navigating their environment to perform tasks and return to a starting point. Once they have reached a patch of flowers and collected pollen, foraging honeybees return to the hive and communicate the location of the food source to their nestmates so that they too can forage. These tasks are so important for the survival of the hive that honeybees have developed their own form of communication to convey information about the distance and direction of a food source from the hive: the waggle dance. Decades of research have made it possible to partially decode the dance language of honeybees. Many questions still remain unanswered, such as how honeybees estimate the distance to a food source from the hive.

This thesis focuses on the problem of estimating the distance travelled and how a better understanding of the innate abilities of honeybees in navigating their environment can help to develop solutions for flying robots. In this chapter, the dance language of honeybees is discussed and a review of solutions developed for robotic applications to estimate the distance travelled is given.

Table of contents

2.1 The visual system of flying insects and the compound eye

The world of insects is shaped by a variety of cues and landmarks: the position of the sun by day and the moon and stars by night, polarised light, the presence of trees and bushes, the perceived movement of their surroundings, etc... (see Figure 2.1) [80, 261]. Flying insects (such as honeybees, flies and dragonflies) perceive the surrounding visual scene thanks to the two compound eyes set on either side of their heads (see Figure 2.2.a). The visual system of honeybees also includes three small simple eyes, called ocelli, located dorsally on the top of their head.
The compound eye is composed of units called ommatidia [104]. An ommatidium perceives only a small portion of the visual scene and can be considered as a bundle of photoreceptors providing a brightness estimate [107]. Each ommatidium consists of a hexagonal lens (also called cornea or facet), a transparent crystalline cone and light-sensitive visual cells (called rhabdom) [74]. Ommatidia are separated from their neighbors by the inter-ommatidial angle $\Delta\phi$, which varies from region to region of the compound eye (see Figure 2.2.b). The size of each region is set by its optical radius, which is defined as the radius measured from the point where the optical axis of the ommatidia intersect. Measurements taken on the compound eyes of different species of insects indicated that the optical radius is greater at the front of the eye, suggesting that the visual scene perceived in the frontal region might be sampled more densely then elsewhere [104]. This frontal region is called fovea and is characterised by ommatidia with larger lenses. Some insects (such as dragonflies) have additional foveas that look upward or laterally [104].
The ommatidia of a compound eye are all connected to three ganglia: the lamina, the medulla and the lobula plate (see Figure 2.3). The neurons in the lamina act

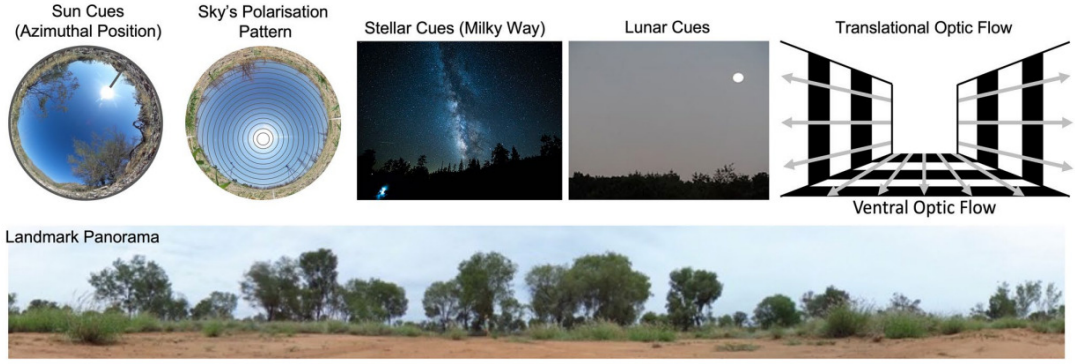

Figure 2.1: Examples of visual cues insects can rely on to orient themselves in their environment include the position of the sun, the position of the moon and stars, polarised light, the perceived movement of their surroundings (or optic flow) and the presence of landmarks (from C.A. Freas and M.L. Spetch, 2022 [80]).

a) b)

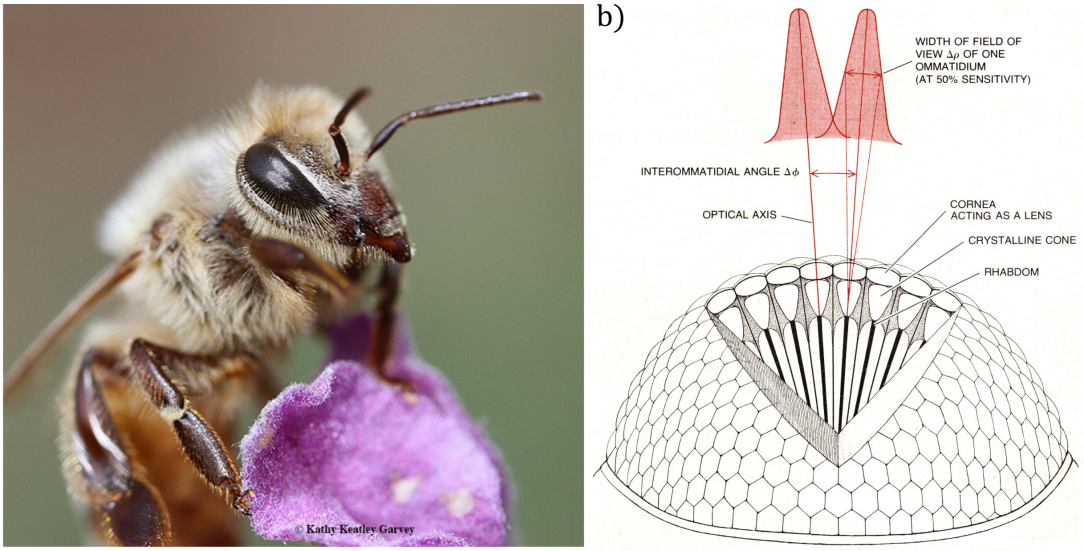

Figure 2.2: a) Close up of a honeybee and its compound eye (by K.K. Garvey, 2018 [84]). b) Scheme of the compound eye (from G.A. Horridge, 1977 [104]). The compound eye is composed of units called ommatidia, each consisting of a hexagonal lens (also called cornea or facet), a transparent crystalline cone and a rhabdom. Neighboring ommatidia are separated by the inter-ommatidial angle $\Delta\phi$, which varies from region to region of the compound eye.

as high-pass filters by amplifying temporal changes and auto-adjust to background illuminance. Relevant findings suggest that the local motion detection between neighboring ommatidia might take place in the medulla [52]. Thus, the medulla could be responsible for the detection of contrast in the visual scene. In the lobula plate, large-field collator neurons called lobula plate tangential cells (or LPTCs-neuron) respond to motion patterns and transmit the signal via the neck of the insect to the thoracic interneurons [95, 129, 232, 28, 55, 231, 239]. LPTCs-neuron also respond to local visual motion and their sensitivity seems to be based on constrast detection [77, 56]. In honeybees, the Velocity-Tuned neurons (or VT-neuron) respond monotonically with the visual angular speed [111].

2.2 To a food source and back again: a honeybee's journey

In 1973 K. von Frisch, N. Tinbergen and K. Lorenz shared the Nobel Prize in Physiology or Medicine for their behavioural studies on insects. This achievement crowned their work in developing the field of modern ethology, which had spread from the end of the 19th century to both continental Europe and North America. The work of K. von Frisch focused on honeybees and their sensory perception. In particular, K. von Frisch was

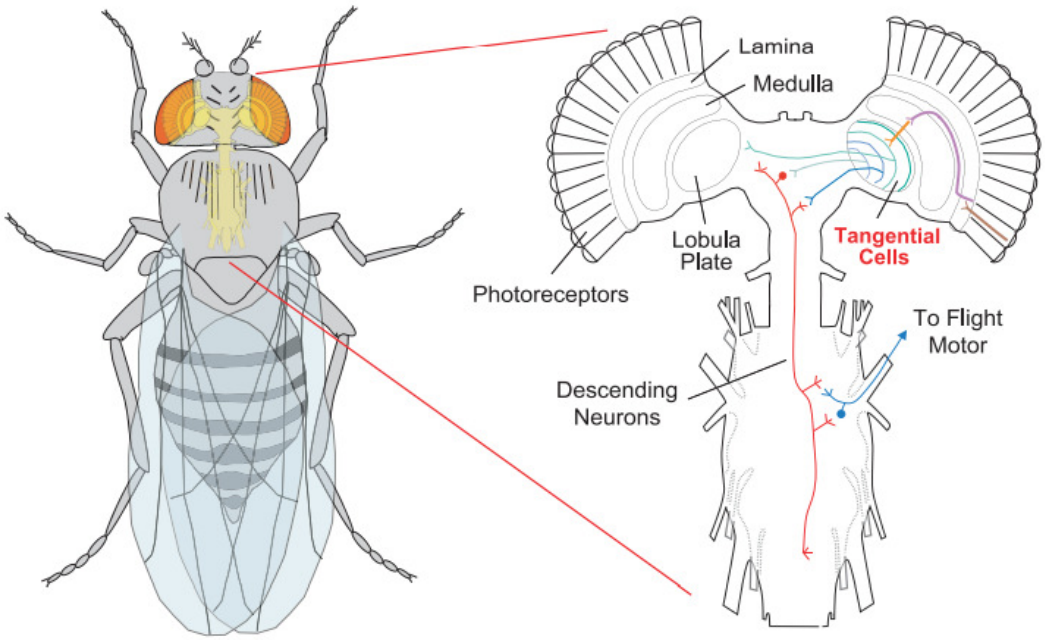

Figure 2.3: Scheme of the visual and central nervous system of flies (from J.S. Humbert, 2005 [107]). The ommatidia of each compound eye are connected to the corresponding lamina, medulla and lobula plate ganglia. The tangential cells of the lobular plate (or LPTCs-neuron) send the signal to the thoracic interneurons through the neck of the insect.

one of the first scientists to interpret the foragers' dance as a means of communicating to their nestmates the location of a food source by conveying information about its distance and direction from the hive.

2.2.1 The waggle dance

In 1967 K. von Frisch described in his book "The Dance Language and Orientation of Bees" the so called tail-wagging (or waggle) dance performed by foraging honeybees in the hive. During the waggle dance, foragers convey relevant information about the distance of a food source from the hive and the direction of the corresponding flight trajectory to their nestmates [247]. Foragers can be observed running a short stretch (called waggle run) while laterally waggling their abdomen before returning to the starting point in a semicircle alternately to the right and to the left (see Figure 2.4.a). This waggling motion is repeated several times per second during the waggle run, while foragers make buzzing noises.

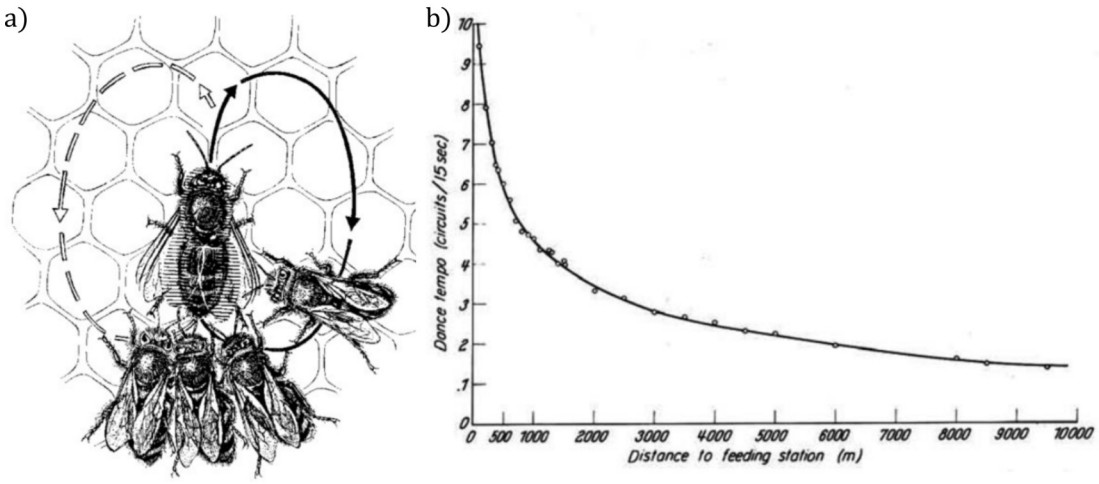

Figure 2.4: a) During the waggle dance, the forager runs a stretch (called waggle run) while laterally waggling her abdomen. The forager then returns to her starting point in a semicircle, alternately to the right and to the left. The nestmates attend the waggle dance to extract the relevant information about the distance of a food source from the hive and the direction of the corresponding flight trajectory in order to find the indicated food source themselves. b) Relationship between the distances of a feeding station from the hive and the tempo of the corresponding 6267 waggle dances observed, for experiments carried out over $10km$ (adapted from "The Dance Language and Orientation of Bees", K. von Frisch, 1967 [247]).

How do honeybees assess direction? Foraging honeybees assess the direction of a food source from the hive by means of the sun compass. This ability was tested in 1959 by P. Renner with experiments in which honeybees trained to feed between 1 and 2 p.m. in Saint James (in Long Island, near New York City) were taken overnight to Davis (in California, near San Francisco). As the time difference between the two locations is $3.25h$, P. Renner observed that honeybees shifted their search for food to suit the original position of the sun as perceived in Saint James during training [183]. Similar observations were made by M. Lindauer in 1957 when taking honeybees trained in Ceylon to Munich, Germany. According to reports, the change in the course of the sun strongly disoriented the honeybees for over a month and a half [139].
K. von Frisch observed that on horizontal surfaces foragers execute the waggle run at the same angle with respect to the sun that they held while reaching the food source during their outward flight. On vertical surfaces, the solar angle is transposed to the gravitational angle (see Figure 2.5). When the sun can be seen only intermittently or not at all, foragers orient relatively to the polarised light. This ability is confirmed by the fact that foragers continue to execute waggle dances that indicate the correct direction even when the sky is very cloudy and therefore the sun is not visible. When the hive was laid horizontally with an unobstructed view of the sky (in both clear and cloudy weather), the presence of filters that retained ultraviolet light disoriented

the foragers' dances. Under similar experimental conditions, filters that altered the polarisation of light caused the foragers to reorient themselves according to the new perceived angle [247].

How do honeybees assess distance? The innate ability of honeybees to assess the distance of a food source from the hive is referred to as the honeybee "odometer". K. von Frisch reported a monotonic relationship between the distance of a feeding station from the hive and the tempo of the corresponding waggle dance. The tempo of a waggle dance is defined as the number of circuits (with a circuit being a waggle run + a semicircle) performed over a span of 15s. The tempo of the waggle dances performed by foragers for a feeding station set at 100m, 500m and 1500m were reported. Over a span of 15s foragers executed 9-10 circuits in the case of the feeding station at 100m, 6 in the case of the feeding station at 500m and only 4 in the case of the feeding station at 1500m. This inversely proportional relationship was further confirmed by subsequent experiments conducted by K. von Frisch and his collaborators over several kilometres (see Figure 2.4.b) and later by other authors [60, 223]. However, the neuro-ethological mechanisms behind the honeybee odometer are not yet fully understood.

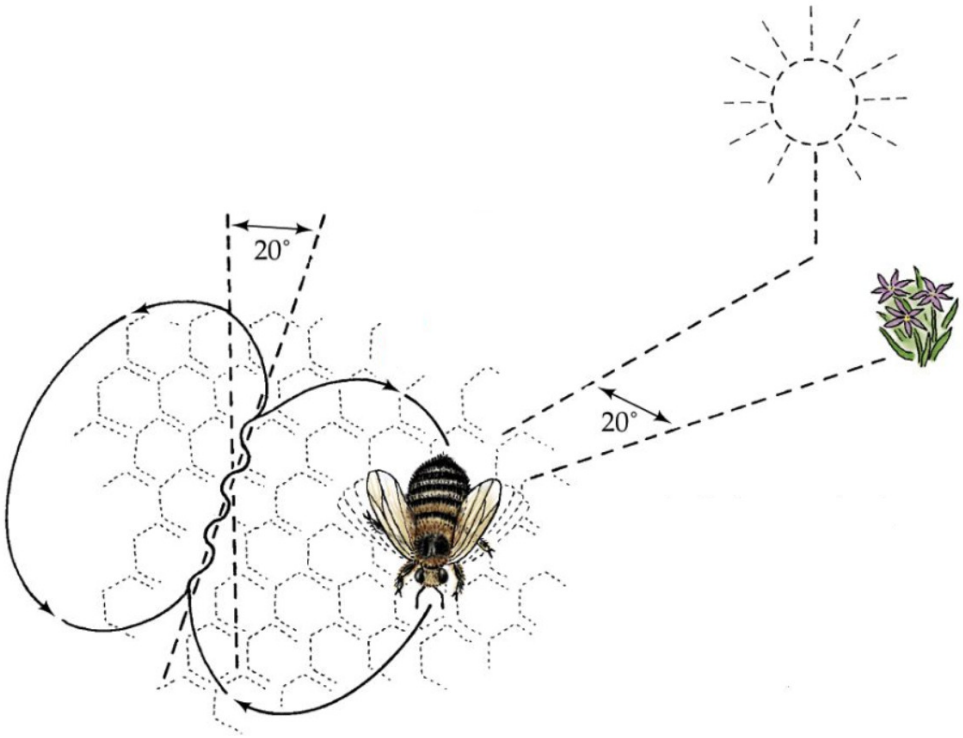

Figure 2.5: While executing a waggle dance on a vertical surface, the forager orients her waggle run by transposing the solar angle perceived while flying toward the food source (here 20 deg) with respect to gravity (adapted from A. Toth, 2007 [241]) .

In addition, it is still open to debate whether honeybees assess the distance travelled or the distance measured in a straight line.

2.2.2 Honeybees exploit visual cues to assess the distance travelled

K. von Frisch hypothesised that foragers assess the distance of a food source from the hive by means of the amount of energy spent in reaching their destination [247]. Later findings seemed to corroborate his "energy hypothesis" [167]. More recent studies have suggested that the "energy hypothesis" does not account for the honeybee odometer over distances up to few hundred meters [59]. In a behavioural study, it was reported that waggle dances executed by foragers trained to fly for $65m$ and then walk for $3m$ in a Teflon tube to reach a feeding station indicated the same distance information as those performed by foragers that did not walk the additional $3m$. The energy required to walk the additional $3m$ was measured through the consumption of O_2 and was estimated to be equivalent to the energy needed to fly over $128m$ (see Figure 2.6).

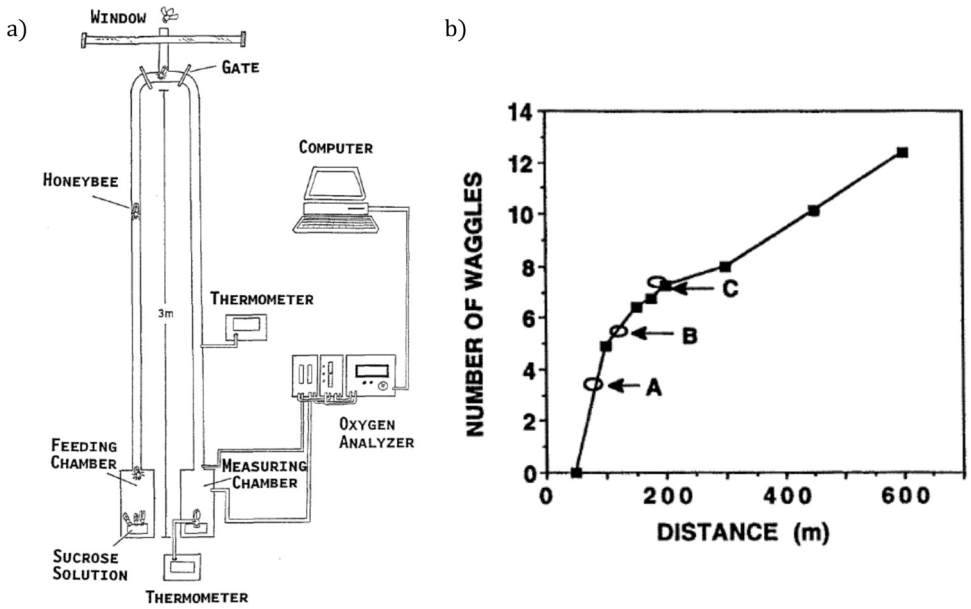

Figure 2.6: a) Representation of the experimental equipment and setup for measuring O_2 consumption. b) Relationship between the distance of the feeding station from the hive and the number of waggling motions per waggle run counted during waggle dances. (A) shows the experimental results obtained with 11 foragers who flew $65m$ and walked an additional $3m$, (B) shows the expected results according to the "energy hypothesis" and (C) shows the expected results according to the consumption of 0_2 (adapted from H. Esch and J.E. Burns, 1995 [60]).

In a subsequent experiment, foragers were trained to visit a feeding station attached to a weather balloon at a distance of 70m from the hive [60]. The weather balloon was held first at ground level and then at 30m, 60m and 90m from the ground. Contrary to what was expected according to the “energy hypothesis", the distance information indicated by the foragers during the recorded waggle dances decreased the higher the balloon was held. These findings led to the conclusion that foragers use the retinal image flow of the ground motion to assess the information conveyed on the distance. Several studies have further supported the hypothesis that the honeybee odometer relies on visual cues [60, 58, 225, 224, 223], and more specifically on optic flow [61] (see also [40] for a review). Examples of tests carried out in tunnels to investigate the capability of honeybees to assess the information conveyed on the distance by manipulating a variety of potential odometric cues (such as flight duration, energy consumption, image motion, airspeed, inertial navigation and landmarks) are shown in Figures 2.7 and 2.8. A more recent study has also proposed a circuit for path integration and steering in bees by anatomically identifying the neurons involved in processing light polarisation and optic flow cues [230].

2.3 Small as an insect, smart as an insect: insect-sized robots

Insects are able to carry out complex tasks such as navigation in a cluttered environment, take-off and landing, selection of food sources, etc... All these tasks are achieved despite the fact that insects can only rely on very simple nervous systems [221] and a considerably small size [146, 49]. These characteristics have led scientists from different fields to study insects in order to find computationally low-cost solutions applicable to robots. Previous studies have presented a honeybee-inspired mobile robot that can measure the distance to an object in terms of image velocity [252], a fly-sized flapping-wing robot capable of tethered but unconstrained stable hovering and basic maneuvers [146], a fly-sized flying robot capable of stabilising its flight by means of an accelerometer [82] (see Figure 2.9) and a honeybee-inspired strategy based on visual familiarity to perform homing flights onboard a quadrotor [228], for example. However, the majority of these solutions still have an important limitation: the lack of a closed-loop onboard perception and thus the need for external infrastructure, such as a motion capture system or an umbilical.

2.4 The problem of estimating distance in Robotics

As with honeybees, estimating distances in order to navigate the environment to perform tasks and return to a starting point is a problem that often arises in robotic

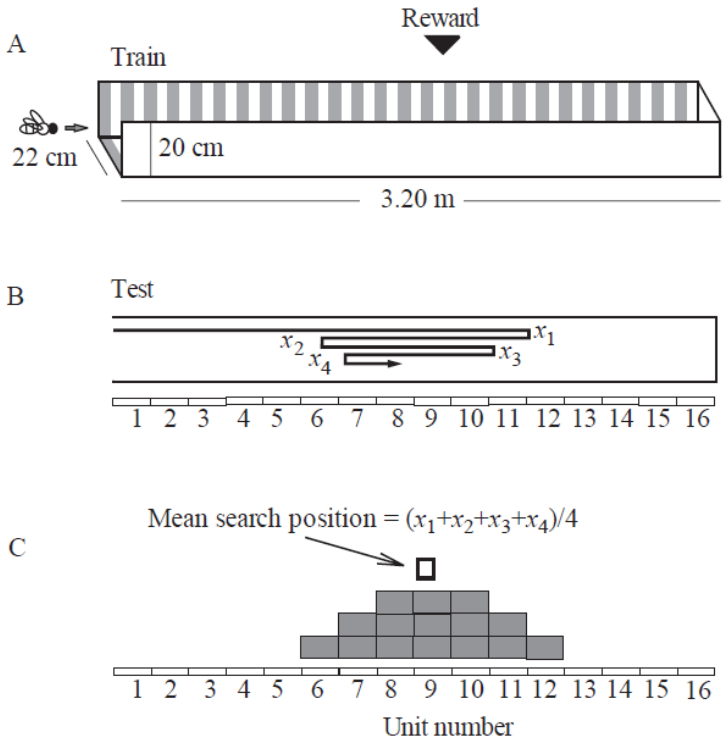

Figure 2.7: Example of test carried out with honeybees flying in a tunnel to investigate their capability to assess the information conveyed on the distance during short flights under controlled laboratory conditions (from M.V. Srinivasan et al., 1997 [224]). Honeybees were trained to find a reward in unit 9 of the tunnel (A). Searching trajectories (B) and spatial distribution (C) reported for trained honeybees during tests without a reward.

applications. In Robotics, the term “odometry" often refers to the use of sensors to estimate the position/location (x, y) or (x, y, z) of an agent (such as a robot, a camera, a vehicle, etc...) with respect to a known starting point.

2.4.1 Odometric strategies in Robotics

Various solutions based on the use of different technologies and sensors have been proposed to perform odometry in robotic applications [4] (see Figure 2.10 and 2.11). Examples of odometric strategies are based on the use of wheels, Inertial Navigation Systems and the mathematical integrations of speed and/or acceleration.

Wheel odometry In mobile Robotics, the position of a wheeled robot with respect to a starting point can be estimated by counting the number of revolutions of the wheels in contact with the ground [27]. This odometric strategy relies on the use

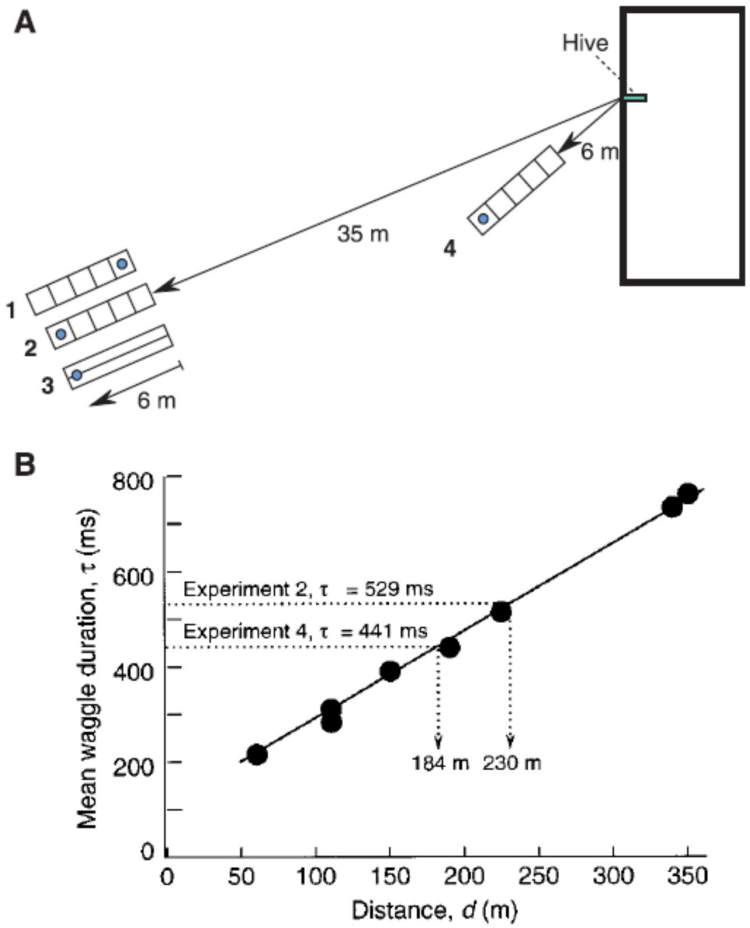

Figure 2.8: Example of test carried out with honeybees flying in a short narrow tunnel to collect a food reward. A) Experimental layout, with 4 tunnels equipped with feeders. B) Mean waggle duration reported for experiments 2 and 4 and their equivalent flight distances as from the regression line (adapted from M.V. Srinivasan et al., 2000 [223]).

of low-cost sensors, such as optical encoders (see Figure 2.11.a). Although wheel odometry is a straightforward and low-cost technique, the use of wheels limits its implementation to wheeled robots operating over regular terrain. Moreover, wheel odometry is subject to wheel slippage [70, 172].

Inertial Navigation Systems In Inertial Navigation Systems (INS), the position of an agent is estimated with respect to a known starting point, orientation and velocity. This is achieved by means of motion sensors (such as accelerometers) and rotation sensors (such as gyroscopes) [4] (see Figure 2.11.b). INS are self-contained and applicable to aerial robots. However, the mathematical integration of the sensors' outputs makes these odometric strategies highly prone to drift [187, 249, 258]. The

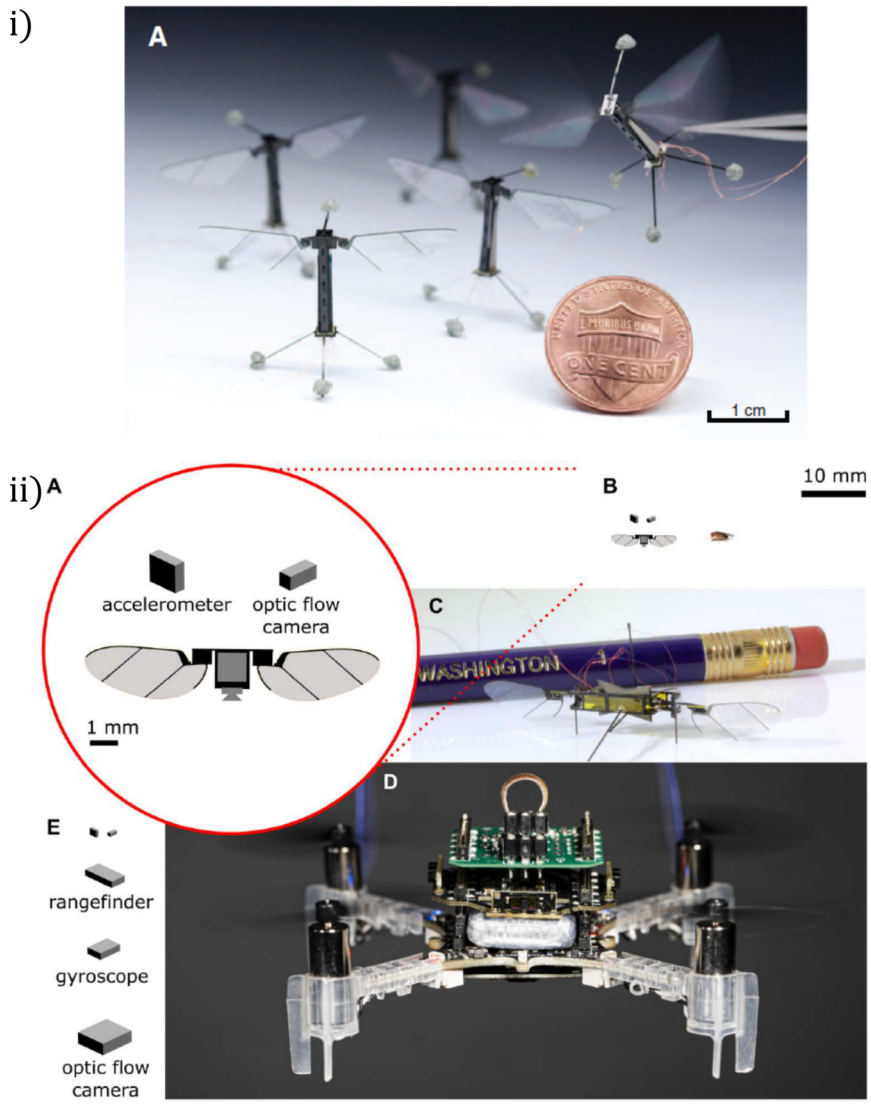

Figure 2.9: A.i) Five identical fly-inspired winged robots designed with a pair of independently actuated wings (adapted from K. Y. Ma et al., 2022 [146]). A.ii) Scheme of the $10mg$ fly-sized NAT flying robot equipped with off-the-shelf sensors. B.ii) The NAT robot compared to a $1mg$ fruit fly. C.ii) A $143mg$ fly-inspired winged robot [51, 39]. D.ii) A palm-sized $30g$ quad-rotor [3]. E.ii) The sensors used to perform stable hovering onboard the NAT robot (from S. Fuller et al., 2022 [82]).

accuracy of INS is highly dependent on the performance, size and cost of the sensors used. In micro- and nano-drones, the specifics of the equipped sensors most often limit INS accuracy. INS can also be used as a temporary solution when other odometric approaches fail due to environmental conditions or sensor constraints [213].

Dead reckoning in Robotics Dead reckoning in Robotics can be defined as the process of assessing the current position of an agent by updating a previously known position with estimates of speed and direction over a given time interval. Historically, dead reckoning approaches have been used in marine, air and automotive navigation. Dead reckoning is highly prone to cumulative errors and its accuracy largely depends on the specifics of the sensors used (such as accelerometers and magnetometers). However, dead reckoning can be combined with other strategies and technologies to achieve better accuracy. For example, a dead reckoning approach combined with INS was implemented on a quadrotor following a periodic trajectory [213].

Sensor/technology	Advantages	Disadvantages
Wheel odometry	Simple to determine position/orientation Short term accuracy, and allows high sampling rates Low cost solution	Position drift due to wheel slippage Error accumulation over time Velocity estimation requires numerical differentiation that produces additional noise
INS	Provides both position and orientation using 3-axis accelerometer and gyroscope Not subject to interference outages	Position drift (position estimation requires second-order integral) Have long-term drift errors
GPS/GNSS	Provides absolute position with known value of error No error accumulation over time	Unavailable in indoor, underwater, and closed areas Affected by RF interference
Ultrasonic sensor	Provides a scalar distance measurement from sensor to object Inexpensive solution	Reflection of signal wave is dependent on material or orientation of obstacle surface Suffer from interference if multiple sensors are used Low angular resolution and scan rate
Laser sensor	Similar to sonar sensors but has higher accuracy and scan rate Return the distance to a single point (rangefinder) or an array of distances (scanner)	Reflection of signal wave is dependent on material or orientation of obstacle surface Expensive solution
Optical camera	Images store a huge meaningful information Provide high localization accuracy Inexpensive solution	Requires image-processing and data-extraction techniques High computational-cost to process images

Figure 2.10: Comparison of advantages and disadvantages of different technologies used to perform odometry and localisation in robotic applications (from M.O.A. Aquel et al., 2016 [4]). Examples of odometric strategies and other localisation methods are based on the use of wheels, Inertial Navigation Systems (INS), Global Positioning System (GPS) and Global Navigation Satellite System (GNSS), ultrasonic sensors, laser sensors and cameras.

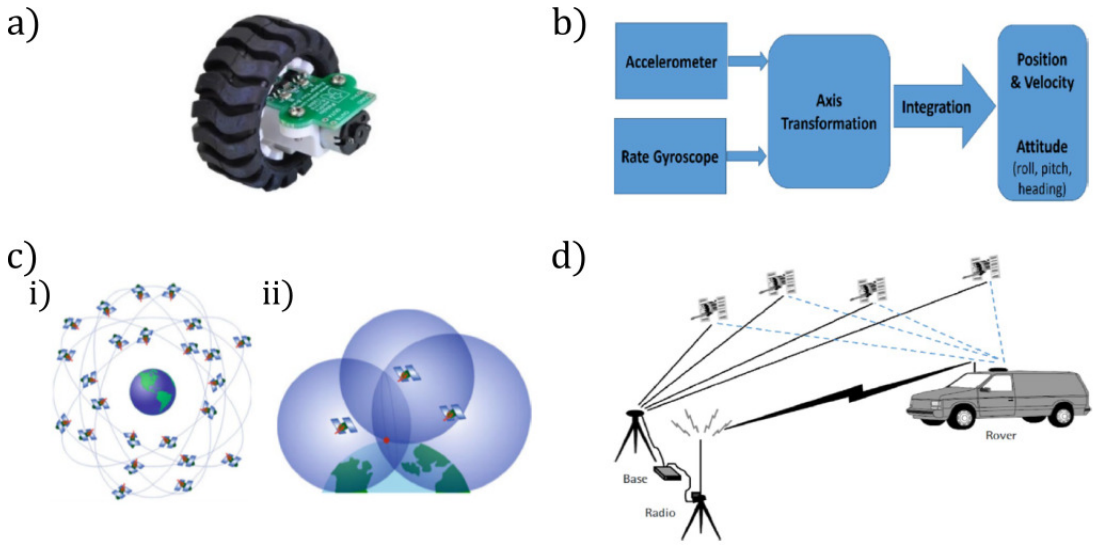

Figure 2.11: a) Example of optical encoder for wheel odometry (from Pololu Corporation, 2016). b) Example of Inertial Navigation System (INS) (adapted from M.O.A. Aquel et al., 2016 [4]). c) Scheme of the Global Positioning System (GPS) (i) and trilateration by means of 3 satellites (ii) (adapted from A. Noureldin et al., 2013 [173]). d) Scheme of real-time Differential GPS (DGPS) (adapted from M.O.A. Aquel et al., 2016 [4]).

2.4.2 Other localisation strategies

Examples of other localisation strategies used in Robotics include satellite-based systems, ultrasonic and laser sensors (see Figure 2.10 and 2.11).

Satellite-based strategies The Global Navigation Satellite System (GNSS) and the Global Positioning System (GPS) are satellite-based systems that provide position, navigation and timing information of an agent (almost) anywhere on Earth [181, 43] (see Figure 2.11.c). GPS consists of 24 operational satellites orbiting the Earth and transmitting radio frequency signals, arranged to provide worldwide coverage [181, 173]. GPS is not subject to error accumulation and is very effective outdoors, where it provides an accuracy within $10m$ [4]. Differential GPS (DGPS) and Real-Time Kinematic GPS (RTK-GPS) were developed to further improve GPS performance outdoors, lowering the accuracy in open-field conditions to the range of centimeters (see Figure 2.11.d). GPS has limitations indoors, in tunnels, in confined places and in urbanised areas [86, 148, 249, 43]. This is due to the presence of obstacles that interfere with radio signals, satellite signal blockage, high noise content and low bandwidth.

Sonar-based strategies Sonar (or ultrasonic) sensors rely on sound propagation to detect objects and assess distances in the environment. Ultrasonic sensors send an ultrasonic pulse into the environment and then receive the reflected signal from

nearby objects. By measuring the time-of-flight of the signal, the distance to the target can be assessed. In this way, the position of an agent equipped with the ultrasonic sensor can be estimated by triangulation with two sonar measurements acquired in two different poses. The incremental update of the assessed position can be used to perform odometry. However, this strategy is very sensitive to target material and orientation as well as environmental noise [187, 130, 199].

Laser-based strategies Similar to sonar sensors, laser (or lidar) sensors rely on light propagation to detect objects and assess distances in the environment. Distances are assessed based on the time-of-flight of the light waves sent by the laser sensor into the environment and reflected by objects. By means of two laser measurements taken in two different poses, the position of an agent equipped with the laser sensor can be estimated by triangulation. The incremental update of the assessed position can be used to perform odometry. Laser sensors require high computational costs due to iterative calculations to match two laser scans. In addition, the scan may fail depending on the material of the object reflecting the signal [236, 103, 141].

2.4.3 Visual odometry in Robotics

In Robotics, the term “visual odometry" was first proposed in 2004 [170] and often refers to the estimation of the position/location (x, y) or (x, y, z) of an agent equipped with one or more cameras by means of the stream of images captured [203, 169, 161]. The estimates of the position are incrementally updated, as this odometric strategy is based on the changes induced by the movement of the agent on the onboard cameras [203, 34, 86, 164]. In Robotics, visual odometry is a no-contact method and thus can be applied to aerial robots [164]. Its main advantages are the reduced cost [171, 86, 172] and the high accuracy [105]. Overall, in Robotics visual odometry has a good trade-off among cost, reliability and implementation complexity [170]. Also, as visual odometry is a self-contained technique, there is no risk that loss of information will cause significant errors, as in the case of GPS [236].

2.4.3.1 Optical cameras

Cameras (or optical cameras) are low-cost no-contact sensors providing a stream of images, which conveys a large amount of information. Since cameras are passive sensors, they are not subject to interference as ultrasonic or laser sensors [81, 187]. In Robotics, different types of cameras have been used to perform visual odometry, such as stereo (or binocular), monocular, omnidirectional and RGB-D cameras (see Figure 2.12).

Stereo cameras: Stereo cameras have two lenses, each of them equipped with an image sensor consisting of a pixel array (see Figure 2.12.b). The depth information can

Figure 2.12: Examples of monocular camera (a), stereo camera (b) and RGB-D camera (c) (adapted from Y. Lu et al., 2018 [144]).

be extracted by a single frame, as the stereo baseline is known. Thus, triangulation can be easily performed. However, synchronization of the two images is key to correctly retrieve depth information. Stereo cameras tend to be expensive and need extensive calibration [125].

Monocular cameras: Monocular cameras have one lens and are equipped with only one image sensor (see Figure 2.12.a). They are cheaper and easier to calibrate than stereo cameras. However, monocular cameras are subject to scale uncertainty [172, 86]. Several solutions have been proposed to solve this problem, such as the use of point cloud combined with bundle adjustment [125] or minimization of image projection error [262], for example.

Omnidirectional cameras: Omnidirectional cameras are stereo or monocular cameras characterised by a very wide field-of-view, up to 360 deg.

RGB-D cameras: RGB-D (RGB stands for Red, Green and Blue, while D stands for Depth) cameras are stereo or monocular cameras providing depth information and color data of the perceived visual scene (see Figure 2.12.c). The depth information is retrieved by means of a depth sensor, such as a time-of-flight sensor, for example.

The stream of images captured by a camera can be processed for a wide range of tasks, such as feature tracking and contrast detection. However, image analysis is typically computationally expensive. In visual odometry, image analysis may involve several steps such as extracting features (such as edges, angles, etc...), matching frames or calculating pixel displacement between frames. In addition, vision algorithms are sensitive to environmental conditions and may fail in a wide range of circumstances [173].

2.4.3.2 Visual odometry with cameras

In Robotics, visual odometric strategies can be classified based on the type of cameras used [243]. Most approaches are based on the use of either stereo or monocular

cameras. These two categories can be referred to as Stereo Visual Odometric Systems (SVOS) and Monocular Visual Odometric Systems (MVOS), respectively.

Stereo Visual Odometric Systems: SVOS rely on stereo cameras. The first example of SVOS was presented in 1980 by H. Moravec, with the aim of estimating the position of a rover on Mars [158]. The odometric strategy proposed was based on the use of a single camera that captured images at equidistant intervals while performing a translational motion as the rover moved in a stop-and-go fashion. This SVOS approach is referred to as a “stereo slider". In [158], the estimation of the distance travelled was performed by triangulating the position of the rover's corner detected in two consecutive positions. Later studies have proposed similar techniques based on feature tracking [152, 96], feature matching [105, 6, 118, 83] and template tracking [214]. SVOS have been implemented also with multispectral cameras [160] and laser-rangefinders [154] and combined with map-matching algorithms [1].

Monocular Visual Odometric Systems: MVOS rely on monocular cameras. Due to the unsolvable scale uncertainty, MVOS require ground height information providing the image scale. This scaling factor can be retrieved separately by using a static pressure sensor [119], an Inertial Measurement Unit (IMU) and range sensors [203, 94], stereo vision [234, 50], a telecentric camera [164] or it can be integrated when using the hybrid approach [246], for example. Image scale can also be retrieved by means of independent information on the observed scene, such as the size of a known object [48]. Other solutions proposed to recover the position/location of the agent include template matching [86, 260], maximizing conditional probability of intensity differences between two consecutive images [151], robust feature tracking combined with motion constraints [92] and the use of a probabilistic appearance-based ground classifier [133]. MVOS have been implemented for a wide range of applications, such as off-road navigation with a mobile robot [87], rear view parking in an urban area [142] and navigation of a micro-flyer in a GPS-denied environment [73].

Visual odometry with omnidirectional and RGB-D cameras: Several robotics studies have proposed different visual odometric approaches that rely on omnidirectional cameras and the use of feature matching [205, 204], optic flow integration [45] or stereo algorithms applied to panoramic image data [32], for example. Various studies have also proposed odometric approaches that rely on RGB-D cameras [69] and the use of a statistical confidence interval [67], a closed-form bound on the propagated error[66], linearization of the energy function [229] or minimization of the photometrical error [121], for example.

In Robotics, another possible classification of visual odometric strategies is based on mapping [144]. Some visual odometric strategies can be classified as Simultaneous Localisation and Mapping (SLAM) (see Figure 2.13). SLAM is an approach that allows

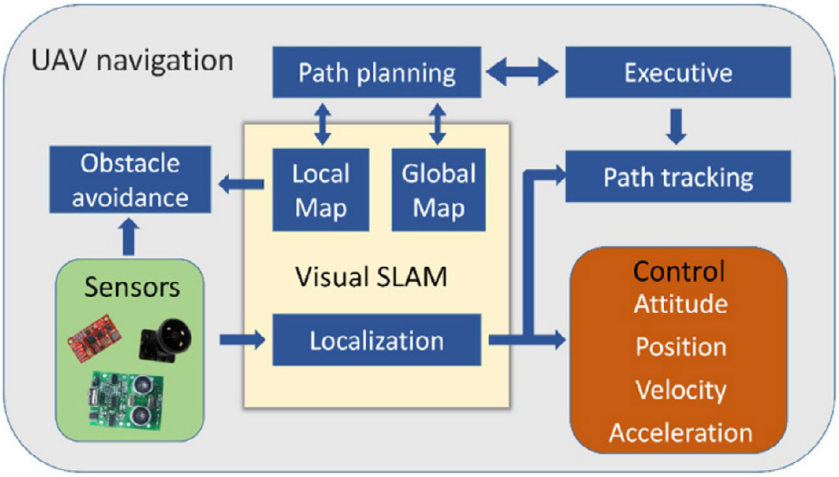

Figure 2.13: Example of Unmanned Aerial Vehicle (UAV) navigation strategy based on Simultaneous Localisation and Mapping (SLAM) (from Y. Lu et al., 2018 [144]).

to perform onboard visual odometry and mapping simultaneously [216, 68, 135, 156]. In SLAM, the robot locates itself in the environment while incrementally building a map to estimate its new position with respect to it. SLAM relies on monocular cameras to acquire data in order to build the map [248, 57, 162, 38]. SLAM requires the use of computationally intensive algorithms (e.g. feature detection) and constant feedback from the environment, resulting in high computational requirements. SLAM has also been implemented with omnidirectional [237] and RGB-D cameras [106, 53, 255].

2.4.3.3 The limitations of visual odometric strategies based on cameras

The main drawbacks of visual odometric strategies based on cameras are the dependence on environmental conditions and the high computational power required for image analysis [87, 164, 172, 260]. In indoor settings, environmental conditions can be controlled to reduce direct sunlight, image blur, shadows, etc.... However, this is not possible outdoors. Additionally, for aerial robotic applications, the use of computationally intensive algorithms is most often incompatible with onboard computers. This is particularly challenging in the case of micro- and nano-drones, where Speed, Size, Weight and Power (SSWaP) constraints play a key role. From these constraints stems the importance of using minimalistic equipment and low-cost processing solutions. Several studies have proposed minimalistic approaches for tasks such as landing [99] or hovering [82], for example.

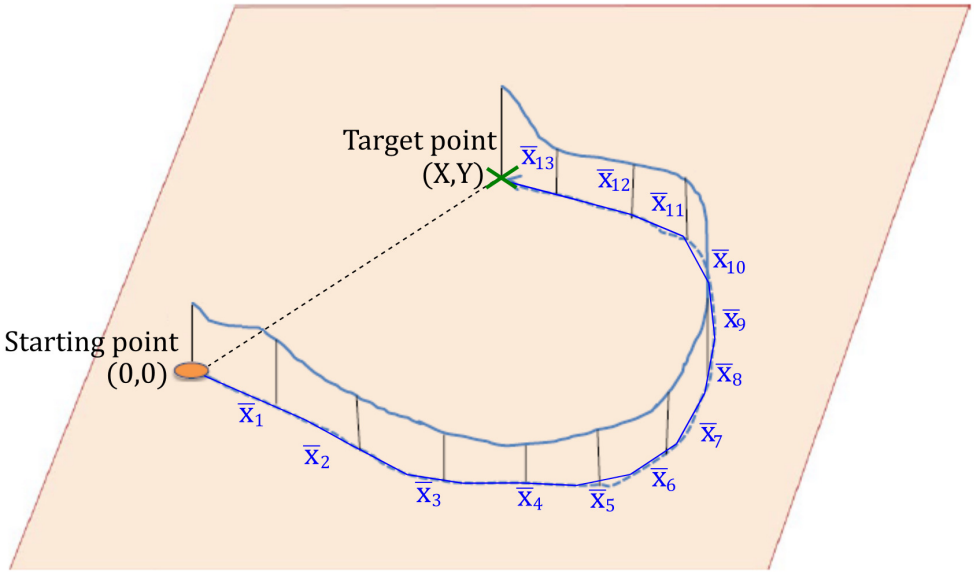

Figure 2.14: Representation of an outward trajectory of a desert ant. The insect odometer assesses the distance travelled along the trajectory $\overline{X} = \overline{x}_1 + \overline{x}_2 + ... + \overline{x}_{13}$ by integrating the velocity norm from a starting point (the nest) to a target point (a food source). Path integration assesses the position (X, Y) of the target point with respect to the known starting point $(0, 0)$ by integrating the velocity vector (adapted from M.V. Srinivasan, 2015 [220]).

2.5 Difference between odometry and path integration

Inspired by behavioural studies, in this chapter we define (see Figure 2.14):

- odometry as the mathematical integration of the velocity norm to assess the distance travelled along a trajectory $\overline{X} = \overline{x}_1 + \overline{x}_2 + ... + \overline{x}_n$ from a known starting point
- path integration as the mathematical integration of the velocity vector (thus including its direction component) to assess a position (X, Y) relative to a known starting point

Conclusion

The need to navigate the environment and return to a starting point is a common problem for flying insects and robots. The waggle dance performed by foraging honeybees provides an insight into the perception of distance in flying insects, which (at least in the case of honeybees) relies on visual cues, and more specifically on optic

flow. The perceptual capabilities observed in flying insects have inspired various computationally low-cost solutions applicable to small robots. The problem of estimating the position/location in Robotics has been addressed in different ways. In aerial robotic applications, odometry is most often performed with cameras, although these solutions have limitations due to environmental conditions and SSWaP constraints. As with honeybees, optic flow could be a possible answer to this problem.

3 Honeybees' solutions for visual guidance: the use of optic flow

Honeybees perceive the surrounding visual scene thanks to the two compound eyes set on either side of their heads. Several studies have suggested that the honeybee odometer relies on visual cues, and more specifically on optic flow. However, how honeybees are able to exploit optic flow to assess the distance of a food source from the hive is still an open question.
In robotics, various odometric approaches have been developed based on the use of different technologies and sensors. In aerial robotic applications, visual cues can be detected by processing the stream of images captured by a camera with algorithms generally requiring high computational costs. Nevertheless, the low computational and perception resources available make cameras relatively unsuitable for performing visual odometry onboard micro- and nano-drones. A possible solution is the use of optic flow, which can be measured either with cameras or with computationally low-cost optic flow sensors.
In this chapter, optic flow is defined and its exploitation by flying insects to navigate their environment is discussed. The measurement of optic flow with cameras is presented and alternative low-cost solutions are introduced. Finally, insect-inspired robotic solutions based on optic flow are presented.

Table of contents

3.1 The definition of optic flow

Optic flow can be defined as the pattern of apparent motion of objects and surfaces in the environment caused by the relative motion between the observer and the visual scene [33]. The concept of optic flow was introduced by the American psychologist J.J. Gibson in 1950 in his book "The perception of the visual word", where it was defined as the visual stimulus provided to animals moving through the world [85].
To define optic flow, let us consider the vantage point O of an observer (such as the nodal point of an eye, a camera, etc...). A fiducial point F can be defined as a landmark or feature that serves as marker in the environment for a short span of time. The position of F is considered fixed and unconstrained, except that it cannot coincide with O. O moves along a given path in space and this motion can be specified by a finite number of vectors, which unambiguously represent a translation $\vec{T}$ or a rotation about an axis $\vec{R}$.
Let us consider a system of spherical coordinates centered on O (see Figure 3.1). F is set at a distance $\vec{D}_i(\Phi,\Theta)$ (with Φ azimuthal angle and Θ elevation angle) in the direction $\vec{d}_i(\Phi,\Theta)$) with respect to O, which corresponds to a nearness $\sigma_i(\Phi,\Theta) = \frac{1}{D_i(\Phi,\Theta))}$. The displacement of F with respect to O for an (infinitesimal) incremental time Δt can be expressed as:

$$\Delta\vec{D}_i = -(\vec{T} + \vec{R} \times \vec{D}_i)\Delta t \tag{3.1}$$

The change in the direction of F can be expressed as:

$$\Delta\vec{d}_i = -\sigma_i(\vec{T} - (\vec{T}\vec{d}_i)\vec{d}_i + \vec{R} \times \vec{D}_i)\Delta t \tag{3.2}$$

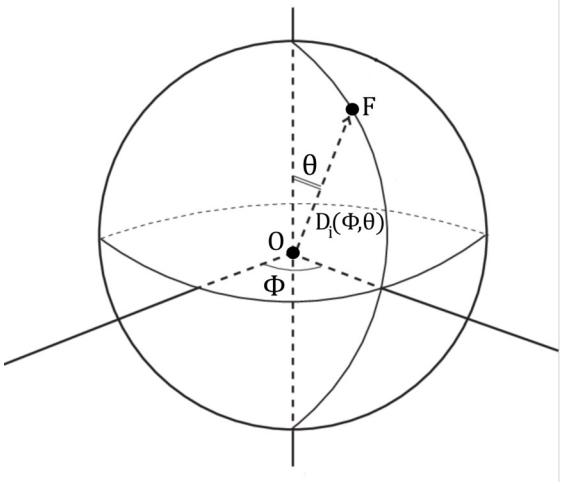

Figure 3.1: System of spherical coordinates centered on the vantage point of the observer O. The fiducial point F is set at a distance $D_i(\Phi,\Theta))$ with respect to O, with Φ azimuthal angle and Θ elevation angle.

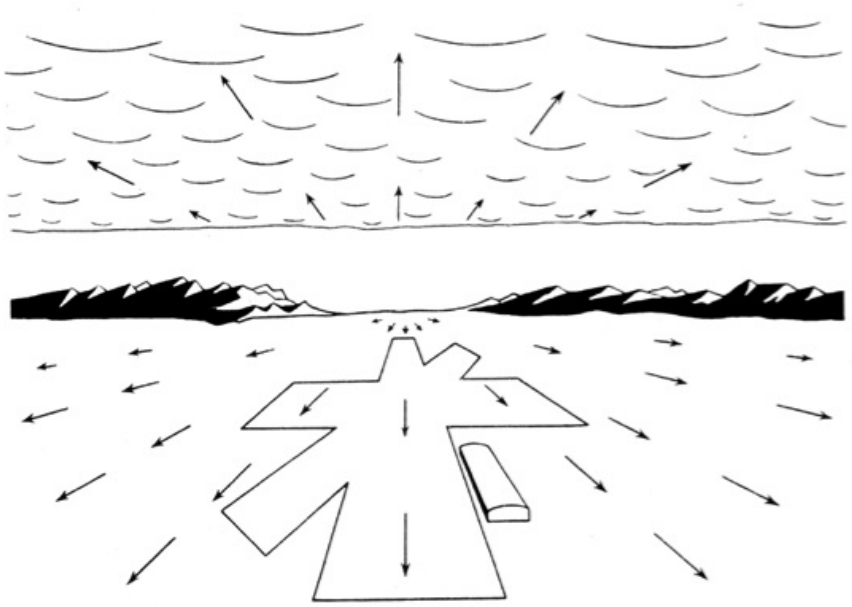

Figure 3.2: Representation as a vector field of the optic flow perceived by an aircraft pilot when landing at an airport (from "The perception of the visual world", J.J. Gibson, 1950 [85]).

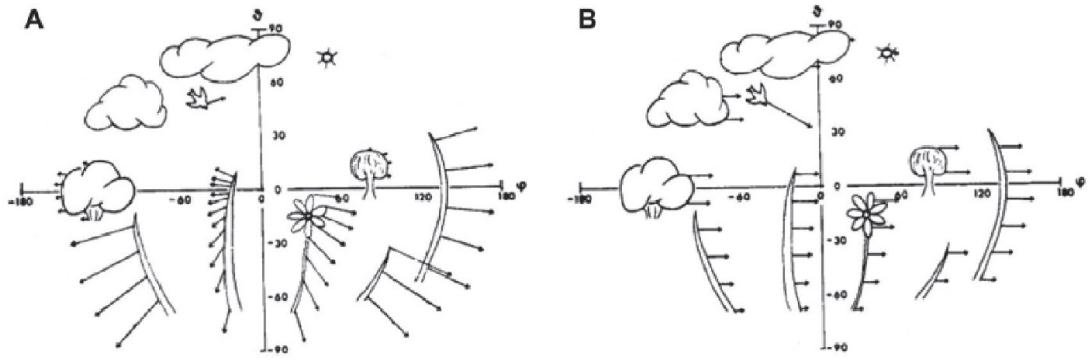

Figure 3.3: Representation of the optic flow vector field generated by a translational (A) and a rotational (B) motion of the observer with respect to the visual scene (from "Photoreception and vision in invertebrates", E. Buchner, 1984 [31]).

Thus, the optic flow due to the apparent motion of F with respect to O in the visual scene $p(\Phi,\Theta)$ (referred to also as motion field or parallax) is given by the time derivative of equation (3.2) [126]:

$$p(\Phi,\Theta) = \frac{\partial \vec{d}_i}{\partial t} = -\sigma_i(\vec{T} - (\vec{T}\vec{d}_i)\vec{d}_i) - \vec{R}\times\vec{d}_i \tag{3.3}$$

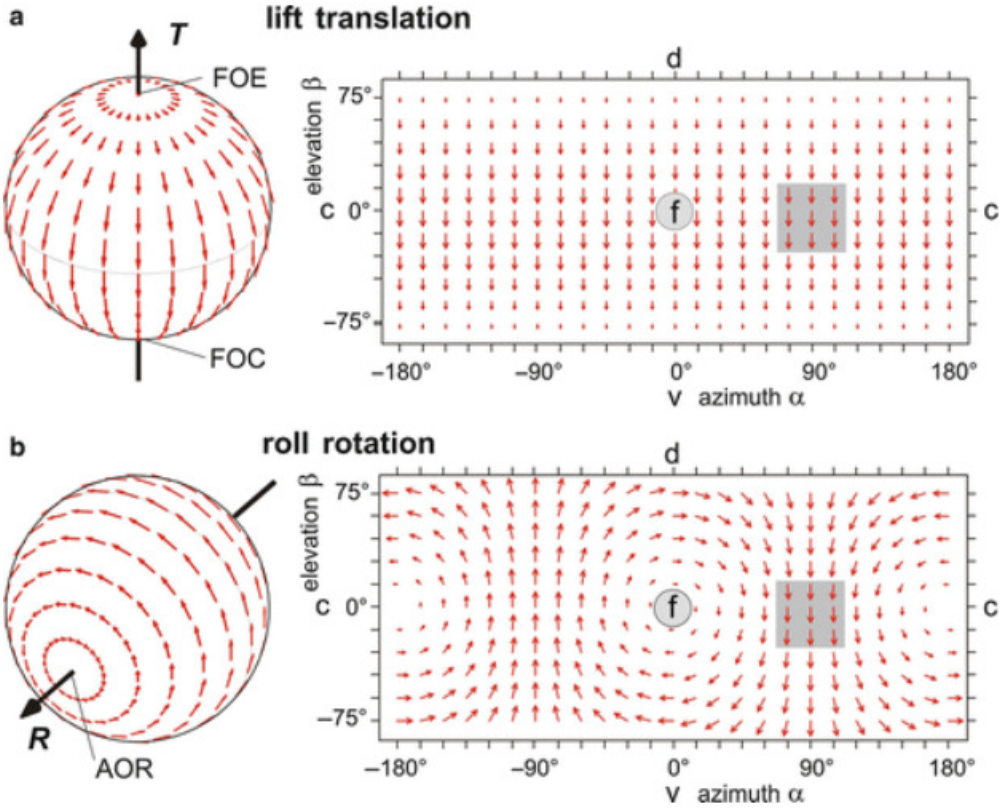

Figure 3.4: Representation of the optic flow vector field generated by a lift traslation along the vertical body axis (a) and a roll rotation around the longitudinal body axis (b) of an observer, respectively (from "Optic flow processing", H.G. Krapp, 2014 [128]).

The motion parallax $p(\Phi,\Theta)$ is always orthogonal to the direction $d_i(\Phi,\Theta)$. Only the translational component of the motion parallax is linked to the nearness and thus can be used to assess the distance of F with respect to O if the rotational component of the motion is null.
By means of equation (3.3), optic flow can be represented as a vector field [256, 165, 129], as shown in Figure 3.2. Figures 3.3 and 3.4 show the optic flow generated by a translational and a rotational motion of the observer, respectively [31, 128]. These motions generate two different optic flow cues: the translational optic flow and the rotational optic flow, respectively. Approaching and receding with respect to a surface causes respectively an expansion and contraction on the optic flow vector field: this is known as the optic flow divergence [99].

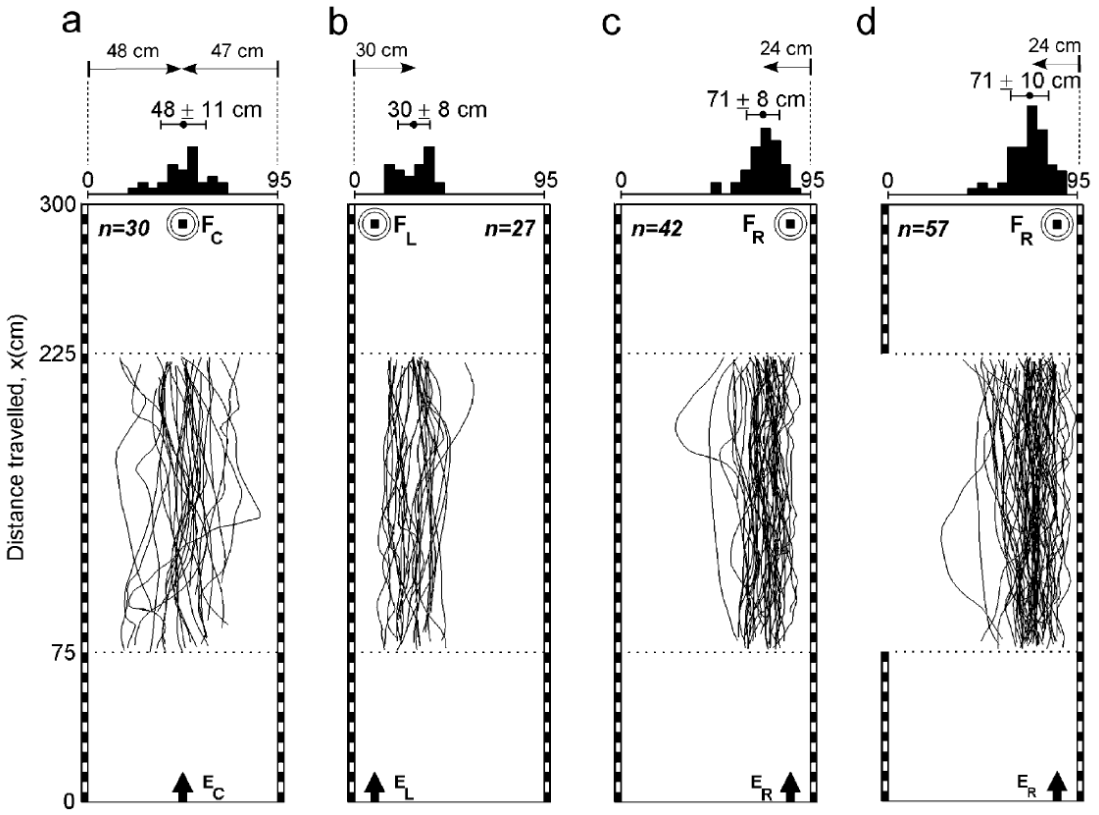

Figure 3.5: Trajectories of *n* honeybees tested in a tunnel under the following conditions: (a) the entrance and the feeding station were both in middle of the tunnel, (b) the entrance and the feeding station were both on the left side of the tunnel, (c) the entrance and the feeding station were both on the right side of the tunnel, (d) the entrance and the feeding station were both on the right side of the tunnel and part of the left wall was removed. On top, distributions of the means ordinate of each trajectory (from J. Serres et al., 2008 [211]).

3.2 Navigating by means of optic flow: a lesson from flying insects

Several studies have suggested that flying insects, such as honeybees and flies, navigate their environment relying on optic flow cues. Examples of the use of optic flow by flying insects include (and are not limited to) flight speed control, heading control, frontal obstacle avoidance, landing and odometry [209].

Flight speed control Experimental results have suggested that honeybees rely on optic flow to control their forward flight speed in tunnels [225, 178, 10, 10]. When the tunnel cross-section narrows, honeybees decrease their flight speed to keep the

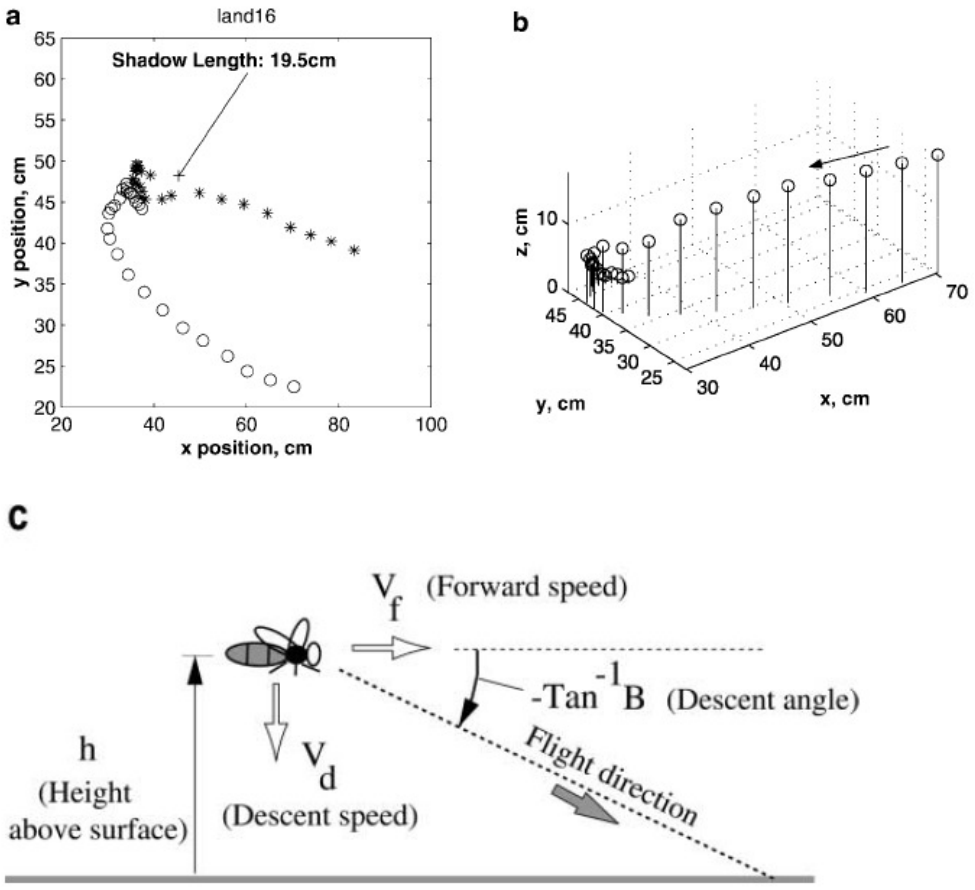

Figure 3.6: a) Landing trajectory of a honeybee on a flat surface, showing its position (circles) and shadow (stars) at $40ms$ intervals. b) 3D view of the landing trajectory. c) Representation of the honeybee landing, showing that the descent angle is kept constant (from M.V. Srinivasan et al., 2000 [226]).

sum of the two laterally perceived optic flows within a range of $460-640 rad/s$ [225, 10]. These observations led to the conclusion that honeybees might use an optic flow regulator to adjust their flight speed [210, 207, 9, 138].

Heading control While flying through a narrow gap or a straight tunnel with vertical stripes on both walls, honeybees were observed balancing distances on both the left and the right side [124]. These observations have been explained with the "centering response", according to which honeybees control their heading by minimizing the error between the two laterally perceived optic flows [222, 124, 211]. A different behaviour was displayed when one of the walls of the tunnel was moving, as honeybees showed a tendency to fly closer to the stationary wall [222]. Similar observations were reported for honeybees trained to reach a feeding station placed close to a wall, suggesting a "wall-following" behaviour [211] (see Figure 3.5). Thus, in tunnels

honeybees may follow either a “centering" or “wall-following" behaviour depending on the position of the entrance and of the feeding station during training [222, 211]. Subsequent experiments have suggested that honeybees adjust their forward speed to maintain the optic flow perceived on the wall constant [195].

Frontal obstacle avoidance In order to avoid frontal obstacles (such as sudden turns) while flying in a tunnel, winged insects are thought to recur to optic flow to estimate time-to-contact [134, 54, 168, 176]. Time-to-contact τ can be expressed as the inverse of the optic flow divergence ω_{div} [209]:

$$\tau = \frac{1}{\omega_{div}} \tag{3.4}$$

The expansion of the perceived optic flow in the frontal region of the compound eye allows flying insects to assess the distance to the surface of the obstacle and avoid it.

Landing Honeybees have been observed landing on a flat surface keeping the descent angle constant [226, 225] (see Figure 3.6). To explain this behaviour, it has been suggested that honeybees control their forward speed by keeping the optic flow perceived by the ventral region of their compound eye constant and that they keep descent speed proportional to forward speed [226]. When landing on vertical platforms, bumblebees alternately decelerate to maintain a constant optic flow expansion rate and accelerate to reach higher optic flow expansion rates in order to land quickly and robustly [89]. Honeybees have also been observed landing on a horizontally moving target [263].

The honeybee visual odometer relies on optic flow Nowadays, researchers consider the waggle duration as the metric used by foraging honeybees to communicate the distance of a food source from the hive to their nestmates during the waggle dance. The waggle duration is measured by [238]:

- averaging durations of the waggle runs executed by a forager during a single waggle dance,
- computing the mean of the waggle run durations for all waggle dances executed by a single forager for a given feeder position,
- computing the mean of the values obtained for all the foragers.

According to [223], the use of the waggle duration as the clue of the distance perception makes it possible to define an “absolute" calibration for the honeybee visual odometer, independent of the characteristics of the environment and equivalent to 17.7 deg of image motion per millisecond of waggle.
Experiments carried out with honeybees flying in narrow highly textured tunnels [223, 61] and over a lake [238] have suggested that the slope of the relationship between the

indicated distance of a food source from the hive and the waggle duration depends on the properties of the optic flow perceived. Two of the optic flow properties that seem to influence this relationship are its density (which depends on the visual contrast of the ground texture) and magnitude (an angular speed, which depends on both the ground speed and the ground height). Previous studies have suggested that this relationship depends on the accumulated ventral optic flow perceived by foraging honeybees during the outward flight [60, 58, 61, 238].

3.3 Measuring optic flow cues

Various techniques have been developed to measure optic flow cues with pixel-level accuracy by processing the stream of images captured by a camera [11] (see Figure 3.7). However, cameras are not the only sensors able to perceive optic flow. Other common sensors used to measure optic flow include optical mouse chips, optical motion tracking sensors and CCD/CMOS sensors [36].

3.3.1 Measuring optic flow cues with cameras

Optic flow can be measured as the difference in position of a point in two successive images captured by a camera. Thus, on the image plane optic flow can be expressed as follows:

$$[\dot{\mu}, \dot{\nu}]^T = f(\mu, \nu) \tag{3.5}$$

with (μ, ν) coordinates of a point in $pixel/s$ or $pixel/frame$ and f function used to measure the optic flow, dependent on the method applied [36] (see Figure 3.8).
Most camera-based optic flow measurement algorithms rely on the following assumptions [26, 188]:

- principle of brightness or feature consistency: only the movement of an object with respect to the camera can locally change image or feature intensity,
- principle of spatial smoothness: the motion is uniform for neighbouring pixels,
- principle of small motion: the sampling frequency of the stream of images is fast enough to accurately represent the motion over time.

The most common approaches to measure optic flow by processing the stream of images captured by a camera in aerial robotic applications are:

- differential methods, that measure optic flow by means of spatio-temporal derivatives of image intensity [14, 242], as the Lucas-Kanade method [145] and the Horn-Schunck method [102],
- image interpolation methods, that do not use feature tracking nor image velocity calculations [215],
- block matching algorithms, that minimize the sum of squared differences and/or

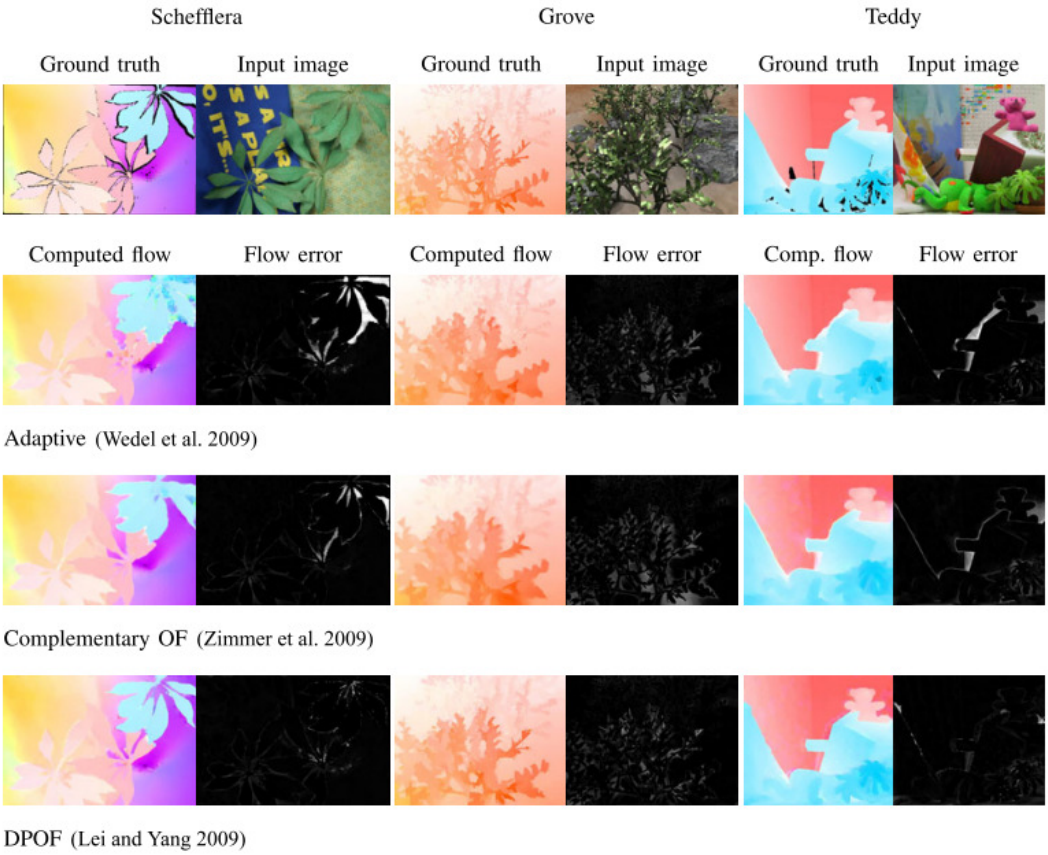

Figure 3.7: Comparison of Optic Flow (OF) measurement with three different methods using the stream of images captured by a camera: adaptive method [253], complementary OF method [264] and DPOF method [137] (from S. Baker et al., 2011 [11]).

of absolute differences [119],

- feature-based methods, that are based on the correlation of detected features into pixel movements [143].

Other methods include region-based matching methods [2], phase-based methods [71], fusion-based methods [235] and fractional-order-operator-based method [37]. Direct sunlight, image blur, shadows and increased speed are examples of factors that may impact negatively the measurement of optic flow. Nevertheless, optic flow cues can in principle be measured by processing the stream of images captured by a camera also under challenging environmental conditions. For example, optic flow divergence has been successfully exploited for underwater navigation [46] (see Figure 3.9).

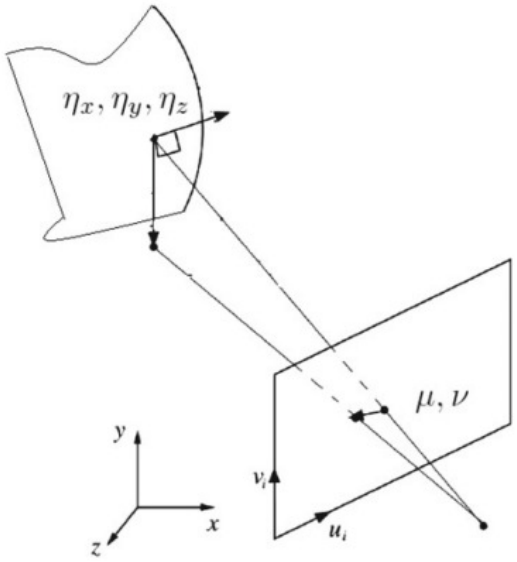

Figure 3.8: Projection of a 3D point of coordinates (η_x , η_y , η_z) on the image plane (from H. Chao et al., 2014 [36]).

3.3.2 Alternatives to cameras

The number of pixels of the image sensor greatly influences the computational power required to process the stream of images captured by a camera [35]. In aerial robotic applications, the low onboard computational and perception resources available lead to the use of minimalistic equipment, such as optic flow sensors and vision chips.

Optic flow sensors A minimalistic solution for measuring optic flow cues is the use of optical motion tracking (or optic flow) sensors. The technology on which optic flow sensors are based derives directly from the sensors first incorporated in optical mice in the 1980s. Optic flow sensors rely on small arrays of monochromatic pixels, ranging in size from about 2×2 [65] to 35×35. On the contrary, high-resolution cameras have big color-sensitive pixel arrays (e.g. FullHD cameras have 1920×1080 pixel arrays). Thus, optic flow sensors can be considered as small low-resolution cameras, with image sampling up to $1000 frames/s$ and higher [91, 123]. The measurement of the optic flow is based on digital image correlation: images are captured in continuous succession and compared with each other to determine how much the sensor has moved. Examples of optic flow sensors are the PAW3903 and PMW3901 models by PixArt Imaging Inc. [117] (see Figure 3.10.a).
Optic flow sensors have been used to develop a self-contained, light-weight navigation system tested on a robotic arm constrained to a horizontal plane [123]. The optic flow measurements obtained by means of two optical mouse chips were used to filter Interial Measurement Unit (IMU) outputs in order to estimate the full 6 degrees-of-freedom platform state by means of an Extended Kalman Filter (EKF). Optic flow

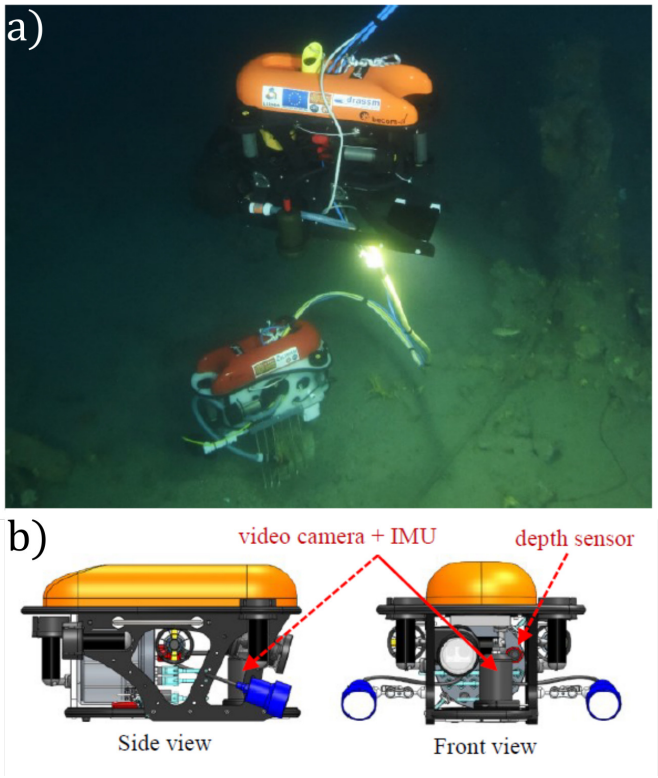

Figure 3.9: a) The Leonard ROV (Remotely Operated underwater Vehicle) (up) and the Speedy ROV (down) during coordinated archaeological operations on the Lune shipwreck (at a depth of 90m, in Toulon, France). b) Setup on the Leonard ROV (adapted from V. Creuze, 2017 [46]).

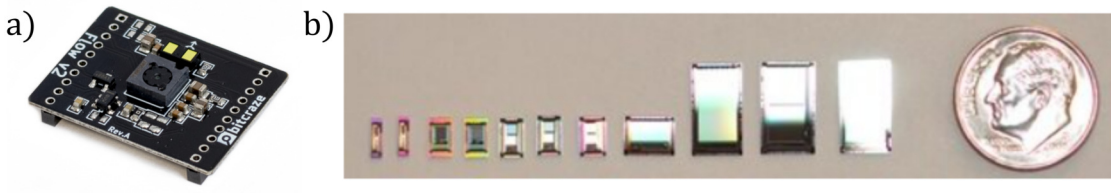

Figure 3.10: Examples of (a) optic flow sensor (PMW3901 model by PixArt Imaging Inc., [117]) and (b) vision chips (by CentEye Inc. [116]).

sensors coupled with inertial information were also used to perform stabilization and collision avoidance on a fly-inspired micro-flyer [266]. Visual odometric approaches implemented with optic flow sensors were tested on a mobile robot [136]. Forward speed control was performed by means of an onboard light-weight optic flow sensor on a flying robot over a steep relief [193].

Vision chips Technology similar to the one used in optic flow sensors has been applied by CentEye Inc. to develop vision chips to support embedded applications

with asynchronous interface, shutterless pixel circuits and flexible pixel window downsampling. The CentEye chips have small pixel arrays of about the same size of an optic flow sensor [116] (see Figure 3.10.b). CentEye vision chips have been employed to perform obstacle avoidance and hovering onboard a small aerial robot.

3.4 Insect-inspired robotic approaches based on optic flow

Although the mechanisms underlying its perception in insects is not yet fully understood [251], optic flow has been widely used in robotics as a low-cost alternative visual cue [209]. Taking inspiration from insects, it is possible to develop minimalistic approaches requiring fewer resources in terms of sensors and computational power for tasks involving navigation [131, 101, 93] or vision [76, 75], for example. Robotic approaches can also help explaining the innate abilities and performance of insects in navigating their cluttered environment [79, 218, 132, 115]. Insect-inspired robotic strategies based on optic flow have been developed to perform speed control, navigation in a tunnel, obstacle avoidance, take-off and landing, ground avoidance, ground following, etc... (see Figure 3.11).

Forward speed control A honeybee-inspired forward speed control system based on optic flow was first implemented in 1992 on the Bee-Bot mobile robot, keeping the bilateral optic flow within a measurable range [44]. The concept of bilateral optic flow, defined as the sum of the optic flows measured by two cameras placed on the left and right side respectively, was introduced and tested in a tapered tunnel on the Robee mobile robot [200] (see Figure 3.12). As observed in honeybees, the higher the desired bilateral optic flow, the faster the robot advanced close to the walls. Similar strategies have been proposed in later studies [221, 5, 108, 109].
Forward flight speed control has been achieved by means of a vertical optic flow regulator called OCTAVE (Optic flow based ConTrol system for Aerial VEhicles) on a rotorcraft [196, 193] (see Figure 3.13). The OCTAVE autopilot ensures that the flight height of the rotorcraft is proportional to its forward flight speed.

Navigation in a tunnel Taking inspirations from honeybees, a dual optic flow regulator called LORA (Lateral Optic Regulator Autopilot) has been developed for avoiding collisions in a tapered tunnel [192, 78]. The dual optic flow regulator consists of:

- a unilateral controller to regulate lateral movement in order to maintain the highest perceived lateral optic flow around a given set-point,
- a bilateral controller to adjust the forward movement in order to keep the sum of the two perceived lateral optic flows around a second given set-point.

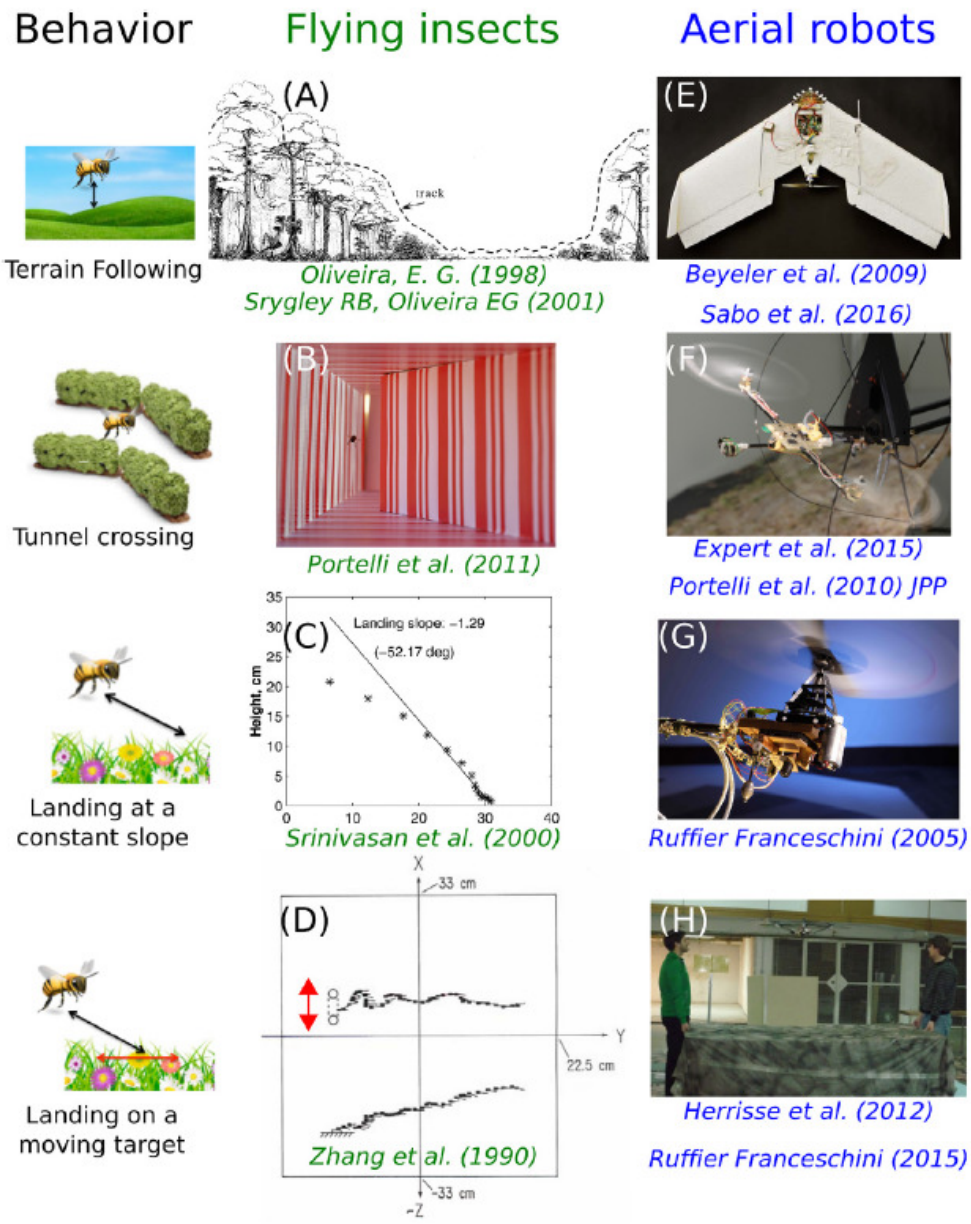

Figure 3.11: Examples of behaviours observed in flying insects and their robotic counterparts developed. (A) Terrain-following behaviour [174, 227] that inspired (E) the development of a free-flying aerial robot following the ground [24, 198]. (B) Navigation in a tapered tunnel [178] that inspired (F) ground-following and speed adjustment in complex tunnels with micro-flyers [64, 177]. (C) Landing at a constant slope [226] that inspired (G) a ventral optic flow regulator [192]. (D) Landing on a moving target [263] that inspired (H) landing on a moving platform with a micro-flyer [98, 194] (from J. Serres and F. Ruffier, 2017 [209]).

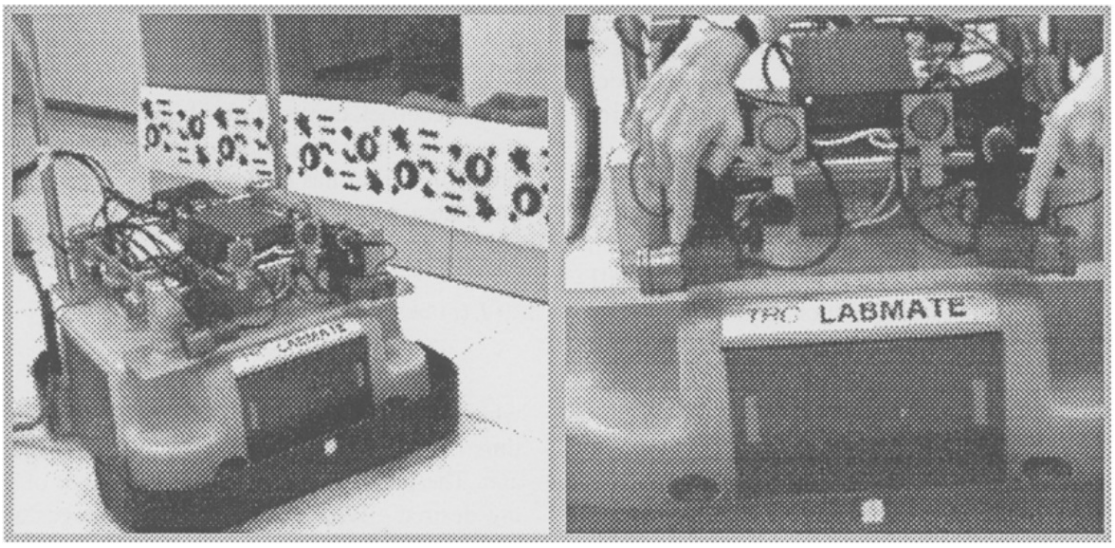

Figure 3.12: The mobile robot Robee equipped with a divergent stereo (from J. Santos-Victor et al., 1995 [200]).

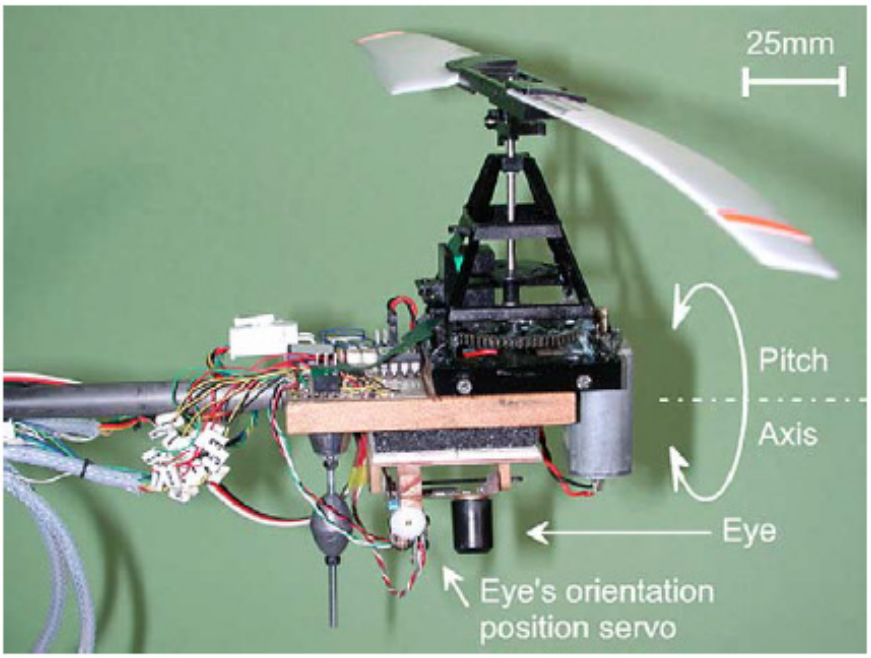

Figure 3.13: The 100g rotorcraft developed to test the OCTAVE (Optic flow based CnTrol system fro Aerial VEhicles) autopilot (from F. Ruffier and N. Franceschini, 2005 [192]).

The unilateral controller maintains the distance to the nearest wall proportional to the forward speed, while the bilateral controller scales the forward speed according to the width of the tunnel [210, 207]. If the unilateral set-point is reduced while keeping the

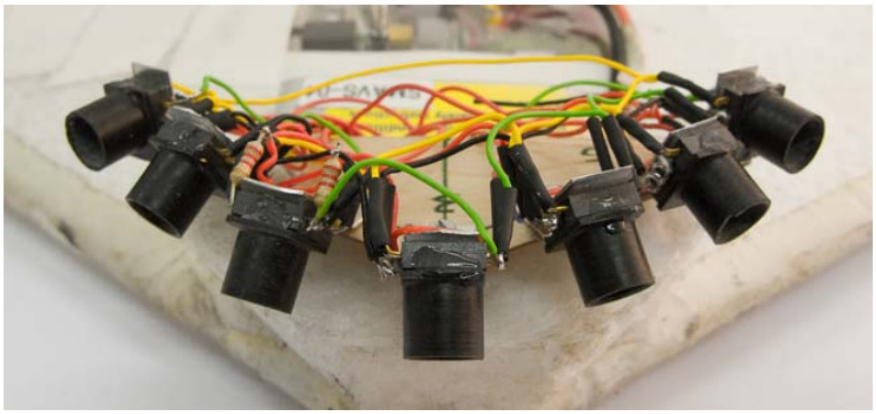

Figure 3.14: Close-up view of the vision system consisting of 7 optic flow sensors onboard a small aircraft to perform fly-inspired collision avoidance (from A. Beyeler et al., 2009 [24]).

bilateral set-point constant, wall-following behaviour is observed. Centring behaviour occurs when the unilateral set-point is less than half of the bilateral set-point.

Frontal obstacle avoidance The expansion of the optic flow vector field has been exploited to estimate the time-to-contact with respect to a frontal obstacle by triggering a given angle of rotation around the axis of a robot [168, 176]. This strategy was tested in simulation on a flying robot [163] and experimentally onboard a wheeled robot [54, 13, 252]. Optic flow divergence combined with inertial sensing has been successfully exploited to detect obstacles onboard a 158g quadrotor both indoors and outdoors [259]. Another strategy inspired by flies [122] and based on open-loop commands (or saccades) has been proposed, either using constant given values [186, 265, 21] determined by means of a Gaussian distribution [182] or by means of optic flow [23, 24, 198, 140, 184] (see Figure 3.14). The saccade-based strategy was tested on a fully actuated hovercraft using the LORA autopilot, allowing the robot to navigate a complex tunnel presenting S-shaped turns [191, 190] (see Figures 3.15 and 3.16).

Take-off, ground following and landing A honeybee-inspired strategy for landing was implemented onboard a small fixed-wing aircraft [35]. However, the altitude of the aircraft decreased linearly with time and not exponentially as expected. Optic flow has also been used to perform ground avoidance with a small glider [15] and with a fixed-wing aircraft [90]. The OCTAVE autopilot was used to perform take-off, ground following and landing [196, 192, 78, 194]. With this strategy, landing can also be performed on a moving target. Optic flow divergence has been exploited to estimate the distance with respect to a surface in order to achieve stable hover and landing onboard a small flying robot [47, 99].

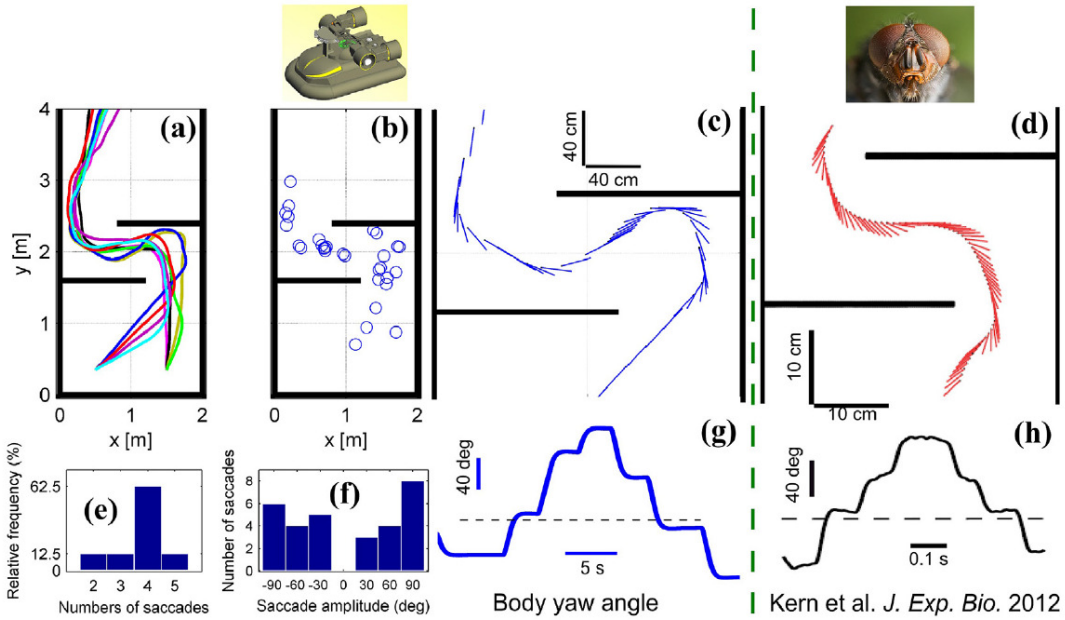

Figure 3.15: Comparison of the behaviour of the simulated LORA (Lateral Optic Regulator Autopilot) rotorcraft and the behaviour displayed by the blowfly in a tunnel with S-shaped turns. a) 8 trajectories executed by the rotorcraft in the tunnel. b) Points in the tunnel where the saccades occur. c) Typical trajectory of the rotorcraft in the tunnel, plotted every 400ms. d) Typical trajectory of the blowfly in the tunnel (from Kerne et al., 2012 [122]; image from J. J. Harrison, Wikimedia commons). e) Relative frequency of saccades per trajectory. f) Number of saccades in the range [−90 deg; 90 deg], with a step of 30 deg. g) Yaw angle of the rotorcraft body during the typical trajectory shown in (c). f) Yaw angle of the blowfly during the typical trajectory shown in (d) (from J. Serres et al., 2015 [212]).

ALIS: an optic flow based autopilot that mimics the 3D behaviour of honeybees A 3D optic flow based autopilot called ALIS (AutopiLot using an Insect-based vision System) has been developed by combining the OCTAVE and LORA autopilots [177] (see Figure 3.17). The ALIS autopilot consists of:

- a forward speed control loop based on feedback from the maximum value of the two optic flows perceived along the vertical axis,
- a positioning control loop based on feedback from the maximum value of perceived lateral, vertical and dorsal optic flows.

The ALIS autopilot was tested in simulation in straight and tapered tunnels in the presence disturbances, such as temporary lack of texture or changes in the tunnel section. With this strategy, the simulated flying robot considers the minimum cross-section of the tunnel to adjust its forward speed and the nearest surface to adjust its distance from the walls.

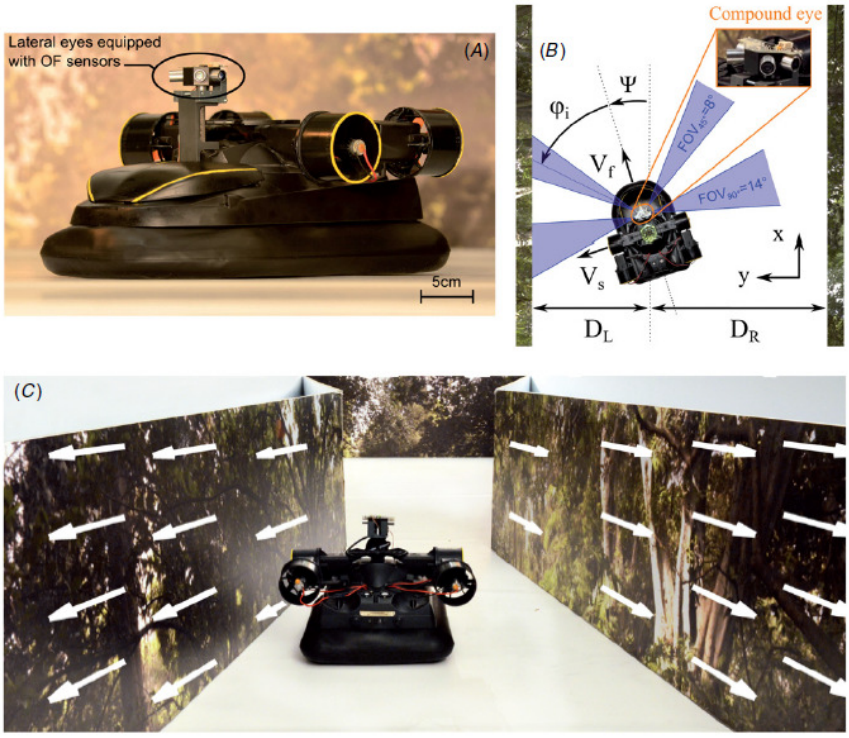

Figure 3.16: A) The LORA (Lateral Optic Regulator Autopilot) fully autonomous hovercraft equipped with an artificial compound eye of 8 pixels. B) Small fully actuated hovercraft equipped with four fly-inspired Local Motion Sensors (LMSs) of 2 pixels, navigating along an unknown textured tunnel. C) The LORA hovercraft moves along a tapered tunnel solely on the basis of translational optic flow (in white on the walls) (from F.L. Roubieu et al., 2014 [190]).

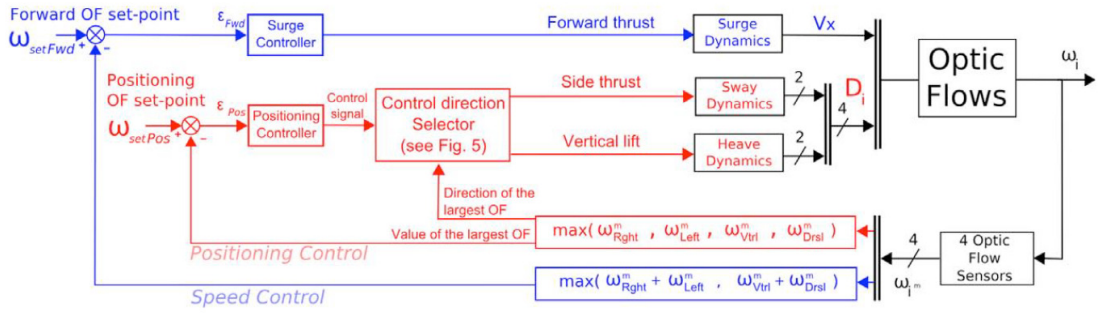

Figure 3.17: Scheme of the ALIS (AutopiLot using an Insect-based vision System) autopilot, resulting from the combination of the dual optic flow regulator LORA (Lateral Optic Regulator Autopilot) and the vertical optic flow regulator OCTAVE (Optic flow based ConTrol system fro Aerial VEhicles) (from G. Portelli et al., 2010 [177]).

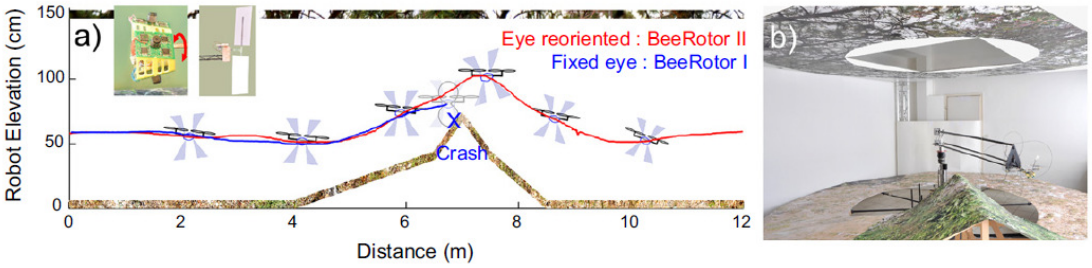

Figure 3.18: a) Trajectory of the BeeRotor robot following the ground while keeping the artificial compound eye CurvACE (in the picture) fixed (BeeRotor I, in blue) and while reorienting the artificial compound eye to keep its equator parallel to the ground (BeeRotor II, in red). b) Experimental setput (from F. Expert and F. Ruffier, 2015 [64]).

The ALIS autopilot was tested onboard a rotocraft called BeeRotor [64] (see Figure 3.18). A third feedback loop was added to reorient an artificial compound eye called CurvACE equipped on the rotorcraft in order to keep its equator always parallel to the nearest surface.

Conclusion

Flying insects rely on optic flow to perform tasks fundamental to their survival, such as flight control, obstacle avoidance, landing, etc... Optic flow is also the visual cue on which the honeybee odometer seems to rely. Thus, optic flow represents a possible solution to the problem of visual odometry onboard micro- and nano-drones, since it can be measured both by processing the stream of images captured by a camera and with computationally low-cost sensors such as optic flow sensors and vision chips. Several insect-inspired solutions based on the use of optic flow have been developed for forward speed control, tunnel navigation, obstacle avoidance, etc...

4 New considerations on the role of optic flow in the honeybee visual odometer

Several studies have suggested that the honeybee visual odometer assesses the distance of a food source from the hive by mathematically integrating the raw angular velocity of the image sweeping backwards across the ventral viewfield, which is known as the translational optic flow. However, the question arises as to how the integration of the optic flow (expressed in rad/s) can reliably encode a distance, as it depends on the ground speed and the ground height. Furthermore, honeybees have been observed to oscillate while flying forward both in tunnels and in open field. These self-oscillations add an additional cue to their optic flow vector field: this is the optic flow divergence.
In this chapter, the role of optic flow cues in the honeybee visual odometer is discussed. The self-oscillations observed in flying honeybees are introduced and the optic flow cues generated by following such self-oscillatory trajectories are identified.

Table of contents

4.1 Oscillating while flying forward

Experiments carried out in horizontal [124] and vertical [178] tunnels have shown that honeybees oscillate while flying forward (see Figure 4.1). The oscillation frequencies reported range around $2Hz$, while the oscillation amplitude is approximately $3cm$ in width (in narrow $12cm$-wide tunnels) [124] and $10cm$ in height (in $40cm$-high tunnels) [178]. According to a recent study, honeybees flying in narrow tunnels might control their ground height by means of lateral self-oscillations with a mean frequency of $4.7 \pm 1.6Hz$ [8].
Similar self-oscillations have also been observed in lepidopterans [257, 201]. As with honeybees, oscillation frequencies of about $2Hz$ were reported in moths [12]. The flight direction of migratory moths crossing the landing strip at La Sirena (Parque Nacionai Corcovado, Costa Rica) were sampled with the aid of a sighting compass [174, 227]. Up-and-down oscillations at an average ground height of about $1m$ can be observed in Figure 4.2, in which the flight track used by the migratory moths is shown. Figure 4.3 shows the chronophotography of the flight of a butterfly in the Luminy Campus (Marseille, France), in which up-and-down self-oscillations can be observed. In tunnels, the direction of the self-oscillations (either on the vertical or horizontal plane) seems to depend strongly on the geometric configuration of the tunnel itself and on the entrance point of the insect. Therefore, the impact of tunnel geometry is stronger for smaller tunnels. Experimental results obtained with lepidopterans and qualitative observations on both lepidopterans and hymenopterans have indicated that flying insects oscillate up and down in open field conditions.

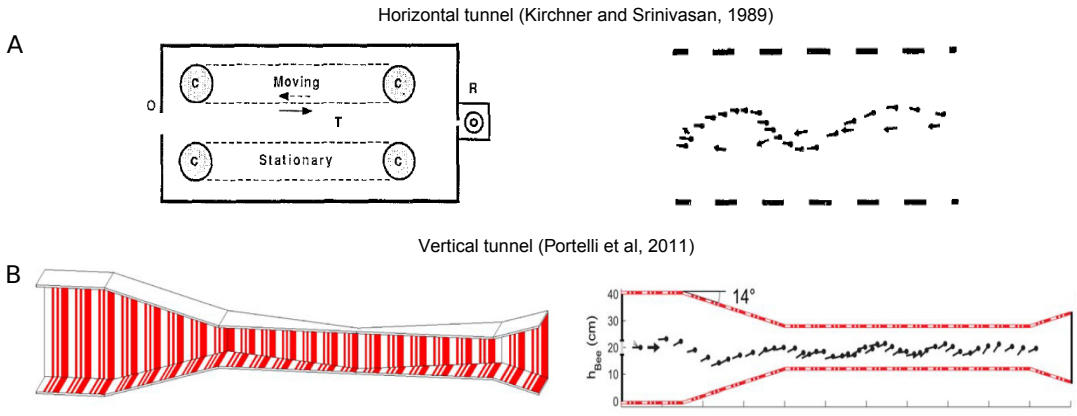

Figure 4.1: A) Top view of the trajectory of a flying honeybee presenting side-to-side oscillations (on the right) in a horizontal tunnel (on the left) (adapted from W.H. Kirchener and M. V. Srinivasan, 1989 [124]) B.i) Side view of the trajectory of a flying honeybee presenting up-and-down oscillations (on the right) in a vertical doubly-tapered tunnel (on the left) (adapted from G. Portelli et al., 2011 [178]).

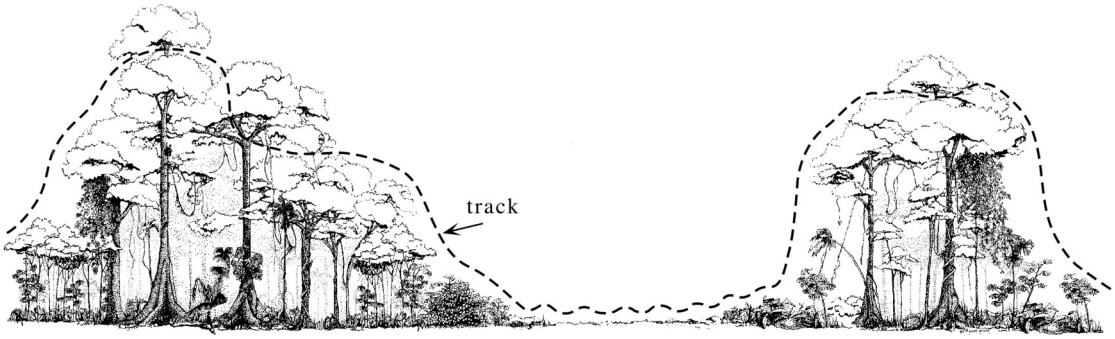

Figure 4.2: Flight track used by migratory moths (Urania fulgens) while approaching, crossing and leaving the landing strip at La Sirena in the Parque Nacionai Corcovado, Costa Rica (from E.G. Oliveira, 1998 [174]). The up-and-down self-oscillations can be observed as the moth crosses the landing strip.

Figure 4.3: Chronophotography of a butterfly flying in open field over an irregular pattern of grass (recorded on the Luminy Campus in Marseille, France). Up-and-down self-oscillations are observable.

4.1.1 Optic flow cues perceived by the ventral region of the honeybee compound eye

The optic flow vector field perceived by the ventral region of the honeybee compound eye during self-oscillatory forward flights in open field is shown in Figure 4.4. Three optic flow cues can be identified: the translational, divergence and rotational optic flow cues.
The translational optic flow cue is the pattern due to the translational motion of the honeybee flying forward above the ground [85]. Assuming a linear flight on a vertical plane (x, z) with a null rotational component of motion, the local translational optic flow ω_T can be expressed downward as the ratio between the horizontal component V_x of the velocity V and the ground height h of the honeybee [256] (shown in red in Figure 4.4):

$$\omega_T = \frac{V_x}{h} \tag{4.1}$$

The up-and-down self-oscillatory motion generates a series of contractions and expansions in the ventral optic flow vector field, which can be quantified as the optic

flow divergence cue. The optic flow divergence is superimposed in the optic flow vector field on the translational optic flow component.
Let us consider a point of coordinates (x_i, y_i) perceived on the ground below. The optic flow divergence can be expressed as the partial derivatives of its velocities (u, v) with respect to its image position (x_i, y_i) [153, 100]:

$$\omega_{div}(x_i, y_i) = \frac{\partial u(x_i, y_i)}{\partial x_i} + \frac{\partial v(x_i, y_i)}{\partial y_i} \tag{4.2}$$

Assuming a linear flight on a vertical plane (x, z) with a null rotational component of motion, the local optic flow divergence ω_{div} can be expressed downward as the ratio between the vertical component V_h of the velocity V and h (shown in blue in Figure 4.4):

$$\omega_{div} = \frac{V_h}{h} \tag{4.3}$$

Honeybees also perform turns and saccades as they fly forward while oscillating. These rotational motions generate distortions in the ventral optic flow vector field, which can be quantified as the rotational optic flow cue. The rotational optic flow depends on the rotational speed of the honeybee and is superimposed in the optic flow vector field on the translational and divergence optic flow components. Assuming a linear flight on a vertical plane (x, z) with a null translational component of motion, the local rotational optic flow ω_R due to a rotation about the y axis can be expressed as the derivative over time of the honeybee pitch θ:

$$\omega_R = \frac{d(\theta)}{dt} \tag{4.4}$$

4.2 Estimating the distance of a food source from the hive: the honeybee visual odometer

Several studies have proposed a model for the honeybee visual odometer based on the mathematical integration of the accumulated raw translational optic flow measured in the ventral viewfield (here called OFacc model for Optic Flow accumulation model) [58, 225, 224, 61, 238]. The OFacc model can be expressed as follows:

$$\hat{X}_{acc} = \int \omega_T dt \tag{4.5}$$

The estimates of the distance travelled $\hat{X}_{acc}$ obtained with the OFacc model are given in $radians$. Figure 4.5 shows the distribution of the final distance estimates obtained in simulation of honeybees' trajectories over a $100m$-long open field with 3 small hills separated by flat areas in the presence of wind (see Chapter 5 for more details). The OFacc model was tested in simulation under a total number of 630 parametric

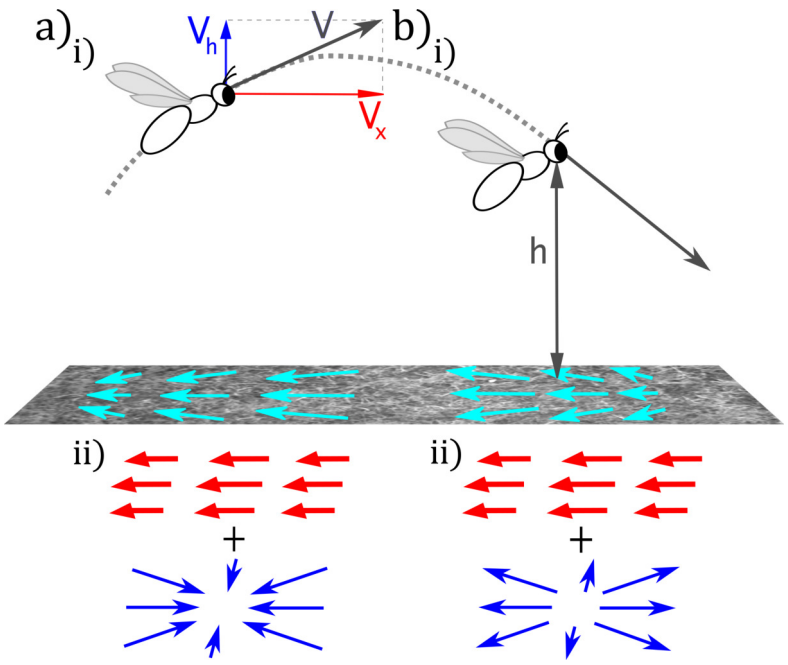

Figure 4.4: Honeybees oscillate up (a.i) and down (b.i) while flying forward over the ground, generating a series of contractions (a.ii) and expansions (b.ii) in the ventral optic flow vector field quantified as the optic flow divergence cue (in blue). The optic flow divergence is superimposed in the optic flow vector field on the translational optic flow (in red).

conditions. The final distance estimates were calibrated to show the results in $meters$. The calibration factor (called $k_{comparisons}$) was computed in order to set at $100m$ the median value of the distribution:

$$k_{comparisons} = \frac{100}{median} = 1.161 \quad [m/rad] \tag{4.6}$$

The Median Absolute Deviation (MAD) of the final distance estimates amounted to $25.62rad$, equivalent to $29.74m$. Thus, the OFacc model does not seem to account well for the accuracy observed in foraging honeybees returning to a previously visited food source.

Conclusion

Several studies have proposed a model for the honeybee visual odometer that mathematically integrates the raw translational optic flow perceived across the ventral viewfield during outward flights. When tested in simulation, this model for the honeybee visual odometer proved to be not very accurate. Honeybees and butterflies have been observed oscillating up and down while flying forward in open field. This oscilla-

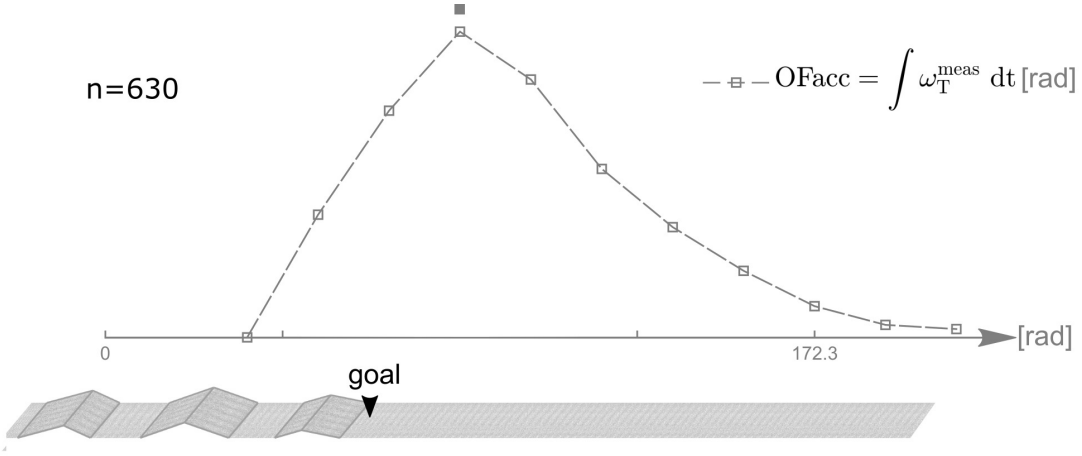

Figure 4.5: The curve gives the distribution of the final distance estimates obtained with the Optic Flow accumulation (OFacc) model for the honeybee visual odometer. The OFacc model was tested on honeybees' trajectories in open field simulations in the presence of wind and ground irregularities, under a total number of 630 parametric conditions. The set of simulated conditions was generated by modulating i) the peak height of the ground relief ii) the wind speed iii) the translational optic flow setpoint and iv) the ground speed of the simulated honeybee. The median value of the final distance estimates obtained with the OFacc model was aligned with the 100m tick on the meter abscissa (here called goal).

tory motion generates an additional optic flow cue: this is the optic flow divergence. The optic flow divergence cue could play a key role in the innate ability of honeybees to assess the distance travelled.

5 The SOFIa model for the honeybee visual odometer

Foraging honeybees inform their nestmates about the distance of a food source from the hive by performing a waggle dance. Several studies have suggested that the honeybee odometer relies on visual cues, and more specifically on optic flow. A model for the honeybee visual odometer based only on the mathematical integration of the raw translational optic flow perceived across the ventral viewfield (here called OFacc for Optic Flow accumulation) has been proposed. However, the accuracy of the OFacc model does not seem to account for observations on honeybees.
Honeybees have been observed performing self-oscillations while flying forward in horizontal and vertical tunnels. These oscillatory movements enrich the ventral optic flow vector field of honeybees with a sequence of contractions and expansions, which can be quantified as the optic flow divergence cue. Changes in ground height and ground speed due to the self-oscillations make these two variables observable and thus they can both be estimated by means of the optic flow divergence cue.
In this chapter, we present a model for the honeybee visual odometer, called SOFIa (Self-scaled Optic Flow time-based Integration model), to estimate the distance travelled exclusively on the basis of translational and divergence optic flow cues. The optic flow divergence cue is given as measurement to an Extended Kalman Filter to visually estimate the ground height, which scales the translational optic flow cue before its integration over time. The SOFIa visual odometer was tested on honeybees' trajectories in simulation over a $100m$-long open field with 3 small hills, under a wide range of wind and terrain conditions.
The SOFIa visual odometer proved to be approximately 10 times more accurate than the OFacc model tested under the same conditions. Additionally, the output of the SOFIa model is expressed in $metres$, whereas that of the OFacc model is expressed in $radians$. Therefore, the SOFIa visual odometer is doubly interesting, as it is both bio-plausible and opens up the possibility of performing minimalistic visual odometry onboard small flying robots.

Table of contents

5.1 Oscillations make a self-scaled model for honeybees' visual odometer reliable regardless of flight trajectory

Published as:
L. Bergantin, N. Harbaoui, T. Raharijaona and F. Ruffier, "Oscillations make a self-scaled model for honeybees' visual odometer reliable regardless of flight trajectory," *Journal of the Royal Society Interface*, 18.182 (2021), p. 20210567., 2021

5.1.1 Abstract

Honeybees foraging and recruiting nestmates by performing the waggle dance need to be able to gauge the flight distance to the food source regardless of the wind and terrain conditions. Previous authors have hypothesized that the foragers' visual odometer mathematically integrates the angular velocity of the ground image sweeping backward across their ventral viewfield, known as translational optic flow. The question arises as to how mathematical integration of optic flow (usually expressed in $radians/sec$) can reliably encode distances, regardless of the height and speed of flight. The vertical self-oscillatory movements observed in honeybees trigger expansions and contractions of the optic flow vector field, yielding an additional visual cue called optic flow divergence. We have developed a self-scaled model for the visual odometer in which the translational optic flow is scaled by the estimated current clearance from the ground. In simulation, this model, which we have called *SOFIa*, was found to be reliable in a large range of flight trajectories, terrains and wind conditions. It reduced the statistical dispersion of the estimated flight distances approximately 10-fold in comparison with the mathematically integrated raw optic flow model. The *SOFIa* model can be directly implemented in robotic applications based on minimalistic visual equipment.

5.1.2 Introduction

It was reported in 1967 by von Frisch [247] that honeybees perform the waggle dance to convey relevant information about the distance from the hive to a food source and the direction of the corresponding flight trajectory. The nestmates extract the relevant distance and direction information from the waggle dance and use it to find the food source themselves. However, it has not yet been established exactly how foragers assess the flight distance. It has been previously concluded that honeybees estimate this flight distance by gauging the amount of energy spent in reaching their destination [247, 167]. However, recent findings have suggested that this "energy hypothesis" does not actually account for the honeybees' odometer, at least not in the case of medium distances of a few hundred meters [59]. Several authors have established that in this

case, the honeybees' odometer relies on visual cues [60, 58, 225, 224, 223] especially the optic flow [61] (see also [40] for a review).
The duration of the waggle run depends quite linearly on the flight distance from the hive to the food source, especially in the case of open field flights [60, 223]. The slope of this linear relationship depends on some properties of the optic flow, such as those perceived when flying through a narrow highly textured tunnel [223, 61] or over low-contrast lake water ripples [238]. The ventral optic flow has several properties of this kind: (i) the optic flow density, which depends on the visual contrast of the ground texture and (ii) the magnitude of the optic flow, which depends on both the ground speed and the ground height. Some authors have concluded that the duration of the waggle run observed in the hive depends on the accumulated ventral optic flow perceived during the forager's flight to the food source [60, 58, 61, 238]. Lastly, it has been suggested that honeybees may gauge the flight distance by accumulating the raw translational optic flow measured in their ventral viewfield [58, 225, 224, 61, 238], as described in the previous model for the visual odometer which we have referred to here as the *OFacc* model.
The question arises as to how mathematical integration of the raw translational optic flow (usually expressed in $radians/sec$) can reliably encode a distance. It has not yet been established how a visual flight odometer fed solely with translational optic flow can be reliable, since this cue depends on both the insects' velocity and their height of flight with respect to the ground. A pioneering biorobotic study has shown that raw mathematical integration of the optic flow does not suffice to obtain a reliable visual odometer [114]. Several visual odometric approaches involving the use of either optic flow [234] or the sparse-snapshot method [50] have been successfully tested on flying robots. All these approaches require ground height information providing the factor scaling the visual information. This scaling factor is often determined separately, using a static pressure sensor [119] or stereovision [234, 50], for example. A neuroanatomical constraint model for the bee brain's path integration process based on raw accumulated optic flow was recently tested on a mobile robot [230]: this terrestrial robot was endowed with an optic flow camera moving at an intrinsically constant height from the ground.
Horizontal and vertical oscillations have been observed during forward flight in Hymenopterans in horizontal [124] and vertical tunnels [178] (see *Suppl. Information* Figure S1). These movements generate a sequence of contractions and expansions in the optic flow vector field, which has been quantified and termed the optic flow divergence. During oscillatory forward flight, the sequence of contractions and expansions is superimposed on the translational optic flow. Various optic flow cues such as translational optic flow [78] and optic flow divergence [7, 244] have been used to explain insects' visually controlled landing performances. Moreover, translational optic flow [192] and optic flow divergence [98, 30, 99] have been used to control robots' manoeuvres. The present study was based on the previously developed visuo-motor model for honeybee flight [78, 180], which includes the honeybee's dynamics and the optic flow regulation process [192], which keeps the translational ventral optic flow constant (as observed in honeybees [226, 177]).

In this section, we present a new honeybee-inspired model for the visual odometer assessing the flight distance on the sole basis of optic flow cues. In this new model, self-induced oscillations generating optic flow divergence are used to gauge the depth, which we have also called the ground height or the clearance from the ground. This information serves to scale the time-based integration of the concomitant translational optic flow. The present model has been called the ***SOFIa*** model, which stands for **S**elf-scaled **O**ptic **F**low time-based **I**integr**a**tion model. The output resulting from the scaling by the current clearance from the ground is given here in $meters$, whereas that of the model based solely on the raw mathematical integration of the optic flow is given in $radians$. The *SOFIa* model was tested in simulation under a large range of flight trajectories and wind conditions, as well as over flat and irregular surfaces representing the ground.

5.1.3 A model for bees' visual odometer based solely on optic flow cues

The *SOFIa* model assesses the flight distance by integrating over time the translational optic flow scaled by the current estimated height of flight $\hat{h}$. The self-oscillations

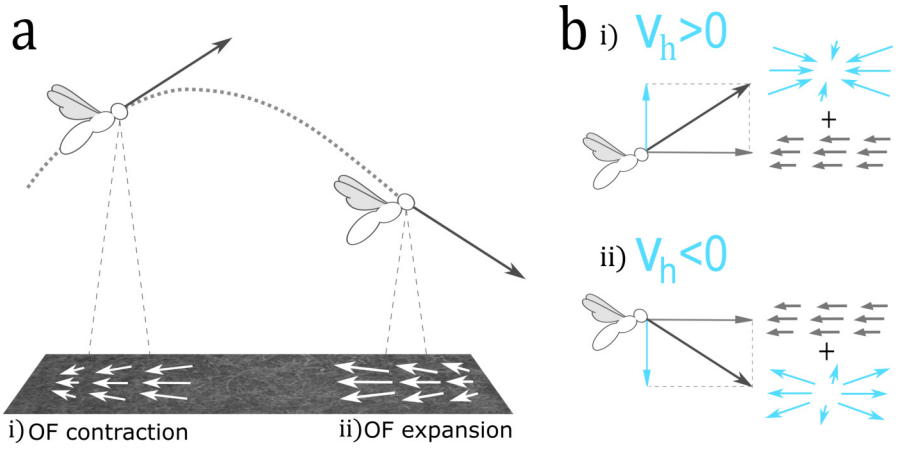

Figure 5.1: a) Honeybees perform up-and-down oscillatory movements while flying forward over the ground. This process of self-oscillation generates alternating contractions and expansions of the ventral optic flow vector field, which can be quantified using the optic flow divergence cues. The optic flow divergence depends downward on the ratio $\omega_{div} = \frac{V_h}{h}$. b) If the vertical velocity with respect to the ground V_h is positive, the optic flow divergence component will be a contraction (i); if it is negative, the optic flow divergence component will be an expansion (ii). The contraction or expansion of the optic flow is superimposed in the optic flow vector field on the translational optic flow, whose magnitude depends downward on the ratio $\omega_T = \frac{V_x}{h}$.

performed by the simulated honeybee flying over a surface result in the superimposition of two vector field components of the optic flow (see Figure 5.1), from which the simulated honeybee can extract:

- the translational optic flow, whose magnitude depends downward on the ratio between the forward ground speed V_x and the height of flight h:

$$\omega_T = \frac{V_x}{h} \quad [rad/s] \tag{5.1}$$

and

- the optic flow divergence, which depends downward on the ratio between the vertical speed V_h and the height of flight h:

$$\omega_{div} = \frac{V_h}{h} \quad [rad/s] \tag{5.2}$$

The optic flow divergence makes the clearance from the ground $\hat{h}$ observable via an Extended Kalman Filter (EKF) (see *Materials and Methods* for the state space representation of the EKF as well as for the observability analysis; see also the EKF equations A.1-A.7 in section A.2 of appendix 5.1.6). The estimated flight distances $\hat{X}_{SOFIa}$ were determined by integrating over time an estimated linear speed, defined as the translational optic flow ω_T^{meas} scaled by the estimated height of flight $\hat{h}$, as follows:

$$\hat{X}_{SOFIa} = \int \omega_T^{meas} \cdot \hat{h}\, dt \tag{5.3}$$

The honeybees' trajectories were simulated using the results of previous modelling studies on honeybees, focusing in particular on the ventral optic flow regulator [78] and the simplified honeybees' flight dynamics [180] (see Honeybees' vertical dynamics section *a* of *Material and Methods* and the video at this and the video at this link [1]). To test the *SOFIa* model for the visual odometer, we simulated a honeybee performing self-controlled oscillatory movements regulating its downward translational optic flow in the presence of disturbances (see Figure 5.2). The self-scaled model for the visual odometer was first tested in simulation over flat ground in the presence of tail and head wind, and then with additional ground irregularities with various heights and slopes.

The honeybee-inspired autopilot scheme includes an optic flow feedback loop controlling the simulated honeybee's vertical dynamics [78, 180], as shown in Figure 5.2. The vertical controller adjusts the wing stroke amplitude $u_{\Delta\Phi}$, which drives the vertical dynamics and hence the clearance from the ground (or height of flight) h in order to keep the ventral optic flow constant. The wing stroke amplitude $u_{\Delta\Phi}$ is the sum of the vertical controller's output and the self-oscillatory control input (see Simulated honeybee flight parameters section *b* of *Material and Methods*). The height of flight is disturbed by the presence of irregularities on the ground. In parallel, the forward

[1] https://www.youtube.com/watch?v=SRAafqcSeAo

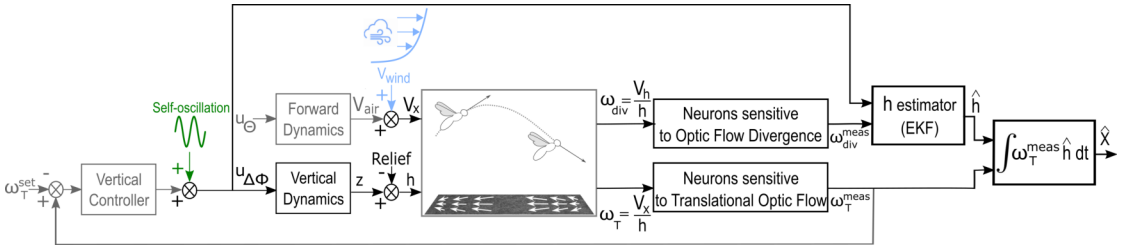

Figure 5.2: The control scheme implemented in the honeybee-inspired autopilot includes a feedback loop for vertical control, which keeps the translational optic flow constant, feeding the vertical controller with the difference between the translational optic flow perceived ω_T^{meas} and its setpoint ω_T^{set}. The forward dynamics are modelled by a transfer function between the simulated bee's pitch u_Θ and the air speed V_{air}. The velocity of the wind is added to V_{air}, giving the forward velocity V_x. A height estimator (an EKF) receives i) the wing stroke amplitude $u_{\Delta\Phi}$ as an the control input (or efference copy) and ii) the optic flow divergence ω_{div}^{meas} measurements. The estimated flight distances are assessed by mathematically integrating over time the translational optic flow ω_T^{meas} scaled by the estimated height of flight $\hat{h}$. Neurons sensitive to optic flow divergence and translational optic flow have been identified in honeybees (see Discussion section).

dynamics fed by the honeybee's pitch u_Θ give the honeybee's forward velocity, which can be is affected by the wind velocity (see Wind modelling section *e* of *Material and Methods*).
The translational optic flow cannot give either the ground speed or the ground height directly, but only the ratio between these two variables. This means that the use of an optic flow regulator controlling the wing stroke amplitude involves an inverse nonlinearity ($\frac{1}{x}$): the feedback loop does not linearly act on the optic flow, but rather provides the means of adjusting the denominator on which the optic flow depends, i.e., the height of flight h (see Figure 5.2).

5.1.4 Results

5.1.4.1 Self-oscillations make the height of flight h assessable whatever the wind conditions

Simulations of a vertically oscillating honeybee flying forward over a $8m$-long flat ground were performed. These self-oscillations generated an undulating pattern of optic flow divergence, as shown in Figure 5.3.e. The simulations included automatic take-off, cruise flight and landing based on the ventral optic flow regulator (see Simulated honeybee flight parameters section *b* of *Material and Methods*). Two different wind conditions (tail and head wind) were studied (see Figure 5.3.b).
As shown in Figure 5.3.a, the simulated honeybee's height of flight depended on the

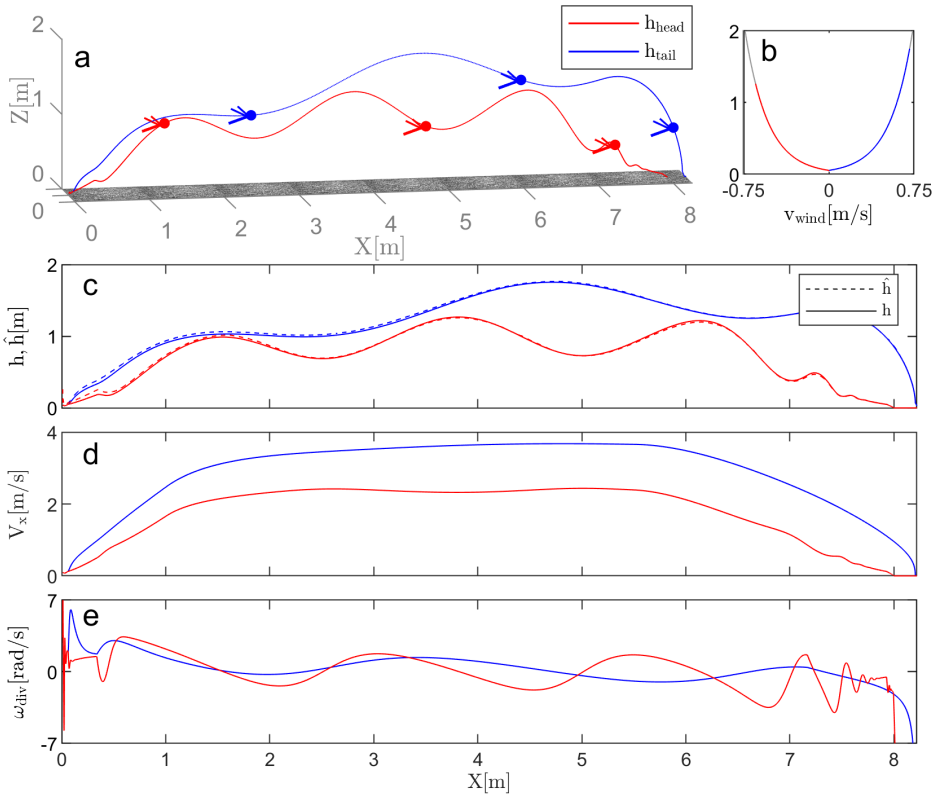

Figure 5.3: Oscillating forward flights of honeybees were simulated over a 8m-long flat ground (see Simulated honeybee flight parameters section *b* of *Material and Methods*). a) The trajectory including take-off, cruise flight and landing was simulated under tail (blue) and head (red) wind conditions. The honeybee's pitch determined the speed and hence the height of flight h, in line with the optic flow regulation scheme. The change in the pitch u_Θ was responsible for take-off and landing. b) The wind was modelled as in equation 8.18 (see Wind modelling section *e* of *Material and Methods*). Its sign depended on its direction: it was positive in the case of tail wind (blue) and negative in that of head wind (red). c) The estimated height of flight $\hat{h}$ (in dashed lines) converged quickly to h under various initial EKF conditions. d) The velocity V_x increased during take-off, ranged around a constant value during cruise flight, and decreased during landing. Its value during cruise flight depended on the wind conditions: it was higher in the case of tail wind (blue) and lower in that of head wind (red). e) The undulating patterns of optic flow divergence were due to the vertical self-oscillatory movements. At a given optic flow setpoint, the amplitude of the optic flow divergence was greater in the case of head wind due to the honeybee being closer to the ground (see appendix 5.1.6 Figure A.4).

wind conditions. Under tail wind conditions, the simulated honeybee flew higher with respect to the ground in order to keep the perceived translational optic flow near the optic flow regulator's setpoint. It has been previously reported that a stronger tail wind results in a higher ground speed in honeybees [254], and that flying insects (such as locusts and honeybees) ascend by tail wind and descend by head wind ([120] and [29], respectively). For the same reason, a head wind results in a lower value of V_x and hence in a lower height of flight.
Even in the presence of wind, it was possible to estimate the simulated honeybee's clearance from the ground accurately using an EKF. As shown in Figure 5.3.c, the height of flight estimates $\hat{h}$ converged quickly with the ground-truth h and followed h accurately throughout the entire trajectory. The final estimation error amounted to 3.67% in the case of head wind and 5.18% in that of tail wind. $\hat{h}$ can therefore be used as a scaling factor by the SOFIa visual odometer model in order to determine the estimated flight distances accurately.

5.1.4.2 *SOFIa* odometer assesses flight distances under various conditions

To test the robustness of the *SOFIa* model even in the presence of ground disturbances, simulations were performed over a $100m$-long ground surface including irregularities with various heights and slopes in the presence of wind (see Figure 5.4). As shown in Figure 5.4, even in the presence of multiple disturbances, including here the presence of a relief, the clearance from the ground $\hat{h}$ was still accurately estimated using the EKF thanks to the self-controlled oscillations. Again, $\hat{h}$ can be used as a scaling factor the SOFIa visual odometer model to estimate the distance flown. Figure 5.4.e gives examples of the results obtained in the estimation of $\hat{X}_{SOFIa}$: the final estimation error here was 1.1% in the absence of wind, 0.69% under tail wind and 1.8% under head wind.

5.1.4.3 The *SOFIa* odometer is more precise than the *OFacc* model

The two models for the honeybee's visual odometer (the *OFacc* model based solely on the raw mathematical integration of optic flow and the *SOFIa* model) were both tested in simulation under the same set of 630 parametric conditions in order to analyse and compare fairly the statistical distributions of the estimated flight distances. The set of simulated conditions was generated by varying: i) the peak height of the ground relief, taking 3 different values of h_{peak} (no relief, 1m and 2m), ii) the wind speed, taking 7 different k_{wind} values ranging from -1.5 to 1.5 with a 0.5 interval, giving a full set of wind conditions ranging from head to tail wind, iii) the translational optic flow setpoint, taking 4 different values of ω_T^{set} ranging from 2 to 3.5 rad/sec with a 0.3 rad/sec interval and iv) the honeybee's flight speed, taking 5 different time-profiles of the pitch u_Θ, the cruising values of which ranged between 30 deg and 50 deg with an interval of 5 deg.

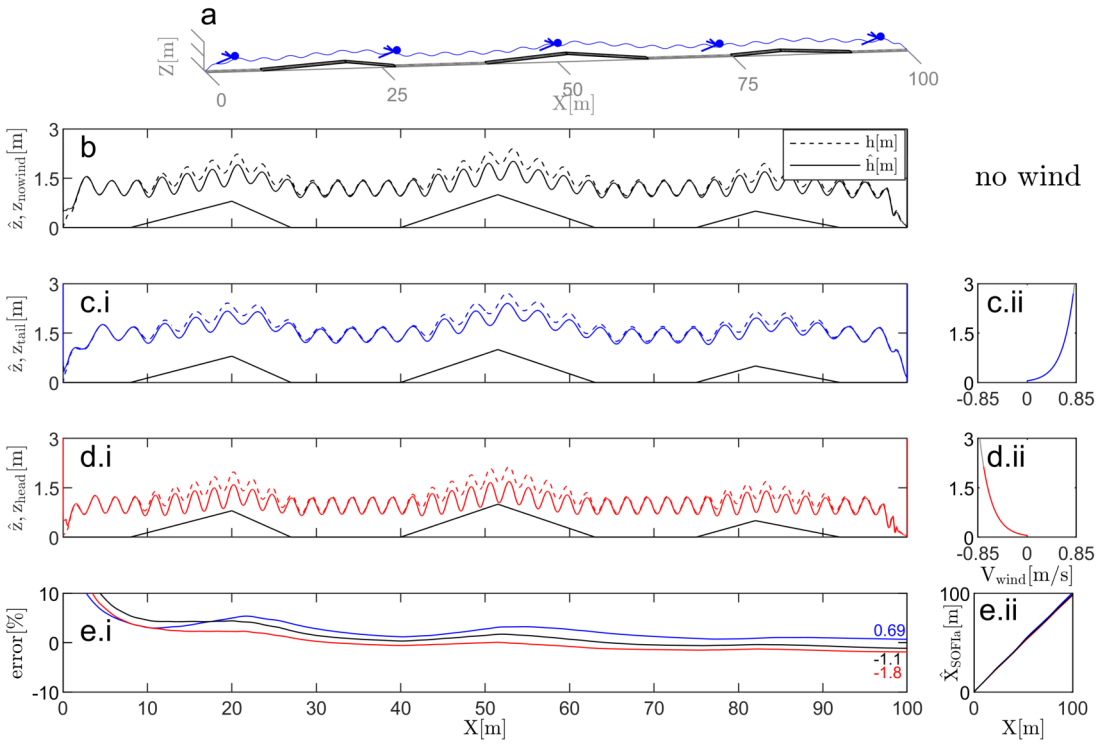

Figure 5.4: Oscillating forward honeybee flights were simulated over a 100m-long ground including irregularities with various heights and slopes (see Simulated honeybee flight parameters section *b* of *Material and Methods*). a-d) The simulated trajectory included take-off, cruise flight and landing under three different wind conditions: no wind (b) in black, tail wind (c) in blue, and head wind (d) in red. When wind was present, its sign depended on its direction: it was positive in the case of tail wind, c.ii, and negative in that of head wind, d.ii. The estimated height of flight $\hat{h}$ (in dashed lines) converged quickly with h under various initial EKF conditions. e.i) The error in the estimated flight distances with respect to the ground truth was normalized and expressed in %. In the absence of wind, its final value was −1.1%, under tail wind, it was 0.69%, and under head wind, it was −1.8%. e.ii) The $\hat{X}_{SOFIa}$ estimated flight distance values were compared with the ground truth X throughout the entire trajectory: the estimates were found to be accurate although they were based on optic flow cues alone.

The *SOFIa* model's outputs were quite accurate, giving a median distance of 104.8m when simulated over a 100m-long irregular surface under various wind conditions (ranging between 1.38m/s and −1.25m/s) and relief heights (up to 2m). The two models for the visual odometer were also simulated in a large range of heights of flight h and ground speeds V_x, from 0 to 4.35m and from 0 to 4.95m/s, respectively.
The distribution of the *OFacc* visual odometer's outputs was multiplied by $k_{comparisons}$ after the simulation runs just to be compared statistically with that of the *SOFIa* model,

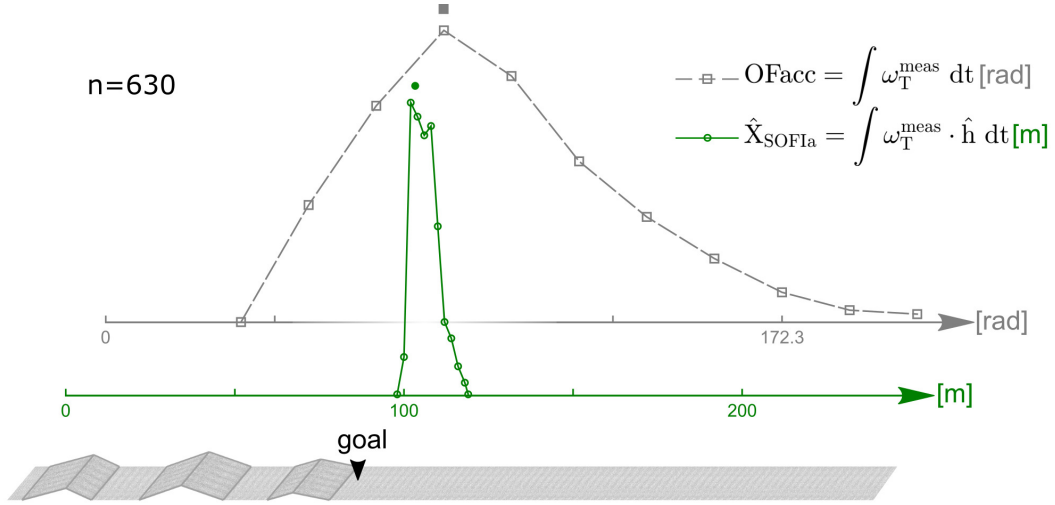

Figure 5.5: The curves give the distributions of the two models for the visual odometer simulated during a 100m-long flight above 3 small hills with gentle slopes separated by flat areas, under a total number of 630 parametric conditions. The set of simulated conditions was generated by modulating i) the peak height of the ground relief ii) the wind speed iii) the translational optic flow setpoint and iv) the honeybee's flight speed. For the sake of visual comparisons, the median value in $radians$ of the *OFacc* model was aligned with the 100m tick on the meter abscissa using the factor $k_{comparisons}$ (see section f of *Material and Methods*). The line carrying the ∘ markers denotes the relative frequency distribution given by the *SOFIa* model, and the line with the □ markers denotes the relative frequency distribution given by the *OFacc* model based on the raw accumulated optic flow. The symbol • placed above the curves at 104.8m gives the median value of the estimated flight distances based on the *SOFIa* model in comparison with the goal (the virtual food source) located 100m away. The spread of the two models' outputs differed significantly (Brown-Forsythe-test, df = 502, F: 383.66, p-value << 0.001). The statistical dispersion of the distribution obtained with the *SOFIa* model was found to be considerably smaller than that obtained with the *OFacc* model: the Median Absolute Deviation (MAD) of the *SOFIa* model was 3.09m, while that of the *OFacc* model amounted to 25.62rad, i.e. 29.74m after multiplication by $k_{comparisons}$.

since its output is given in $radians$ and not in $meters$ (see section f of *Materials and Methods*). As shown in Figure 5.5, the statistical dispersion of the estimated flight distances with respect to the wind obtained with the *SOFIa* model differed considerably from those obtained with the *OFacc* model (Brown-Forsythe-test, df = 502, F: 383.66, p-value << 0.001). The Median Absolute Deviation (MAD) of the results obtained with the *SOFIa* model amounted to 3.09m, whereas that obtained with the previous model amounted to 29.74m after multiplication by $k_{comparisons}$. Figure 5.6 shows the statistical distributions of the outputs of the *SOFIa* model and those of the

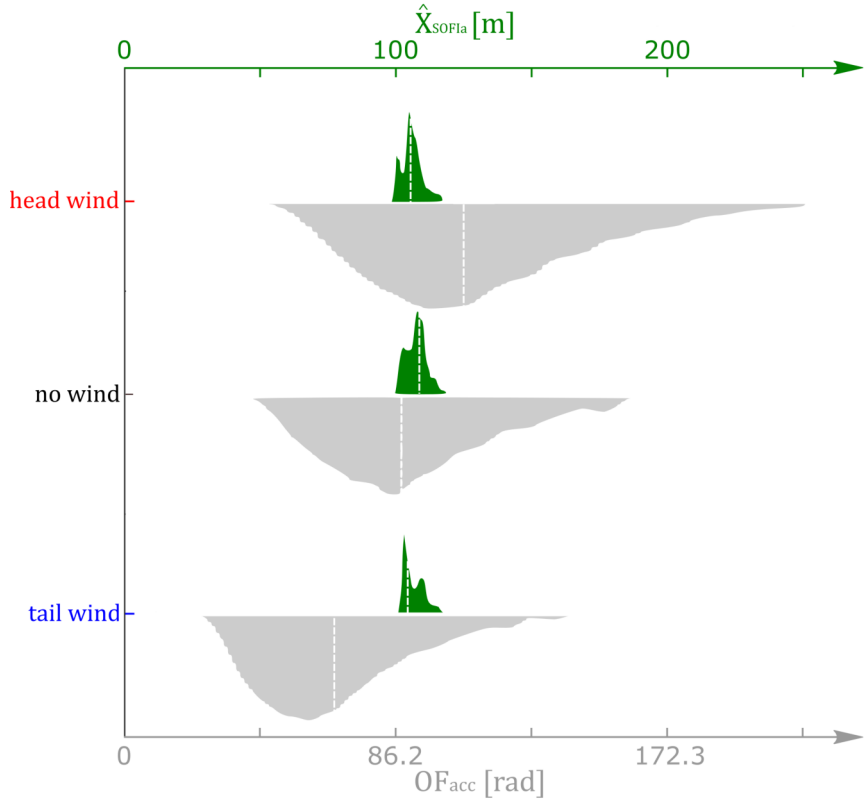

Figure 5.6: The plots give the statistical distributions obtained under the same 630 parametric conditions with the *SOFIa* model (in green) and the *OFacc* model based solely on the raw mathematical integration of the optic flow (in grey) under tail wind, no wind and head wind conditions. Under tail wind conditions, the median values of the statistical distribution obtained were 77.7m with the *OFacc* model (after multiplication by $k_{comparisons}$) and 103.72m with the *SOFIa* model. In the absence of wind, the median values were 100.67m with the *OFacc* model (after multiplication by $k_{comparisons}$) and 106.67m with the *SOFIa* model. Under head wind conditions, the median values obtained were 122.96m with the *OFacc* model (after multiplication by $k_{comparisons}$) and 104.78m with the *SOFIa* model. The median values of the *OFacc* model outputs differed significantly among the three wind conditions (Kruskal-Wallis test, p-value < 10^{-49} with the *OFacc* model). Under the various wind conditions considered, the median values of the two visual odometer models' outputs differed significantly (Wilcoxon test, p-value < 0.001, Z=20.13 ; 11.64 ; 20.13, under tail wind, no wind and head wind conditions, respectively). Overall, the *SOFIa* model's odometric performances were consistently more reliable regardless of the wind conditions.

OFacc model under tail wind, no wind and head wind conditions. The median values given by the *SOFIa* model ranged between 103.72m and 106.67m, whereas those given by the *OFacc* model ranged between 77.7m and 122.96m after multiplication by $k_{comparisons}$. The MAD of the *SOFIa* model was consistently lower than 3.16m, while the MAD of the *OFacc* model ranged between 19.72m and 28.71m after multiplication by $k_{comparisons}$. Our findings show that the statistical dispersion of the estimated flight distances obtained with the *SOFIa* model was about 10 times smaller than that of the estimates obtained with the *OFacc* model. Similar results were obtained upon comparing the odometric performances of the two models in terms of the honeybee's body pitch u_Θ, which drives its forward speed, as well as in terms of the height of the simulated relief h_{peak} (see Figure A.5.a and b in section A.6 in appendix 5.1.6).
At a given optic flow setpoint, the honeybee flies at a slower ground speed under head wind or low body pitch conditions and therefore takes longer to reach the food source (see Figure 5.6 and Figure A.5.a in appendix 5.1.6, respectively). As a result, the *OFacc* model integrates this regulated ventral optic flow mathematically during a longer time and hence overestimates the flight distance. Conversely, in the case of tail wind or high body pitch, the honeybee flies at a faster ground speed and takes less time to reach the food source, and therefore the *OFacc* model integrates this optic flow during a shorter time, and hence underestimates the flight distance. In short, in the case of head or tail wind and low or high speed, the output of the *OFacc* model deviates increasingly with time from the actual distance flown by the simulated honeybee. By contrast, the output of the *SOFIa* model varies very little, especially depending on the forward flight speed or the wind direction or speed.

5.1.5 Discussion

The new model for the honeybee's visual odometer called *SOFIa* presented in this section was based on biologically plausible optic flow cues. This reliable bio-plausible visual odometer can be used to assess the flight distance based on two different characteristics of the ventral vector field of the optic flow, while at the same time accounting for honeybees' visual odometric performances.

5.1.5.1 *Open-field* simulation and height of flight

Here we have presented the results obtained on simulated honeybees flying over a *virtual* open field, possibly in the presence of landforms. Under these conditions, the simulated honeybee's ventral optic flow regulator is free to adjust its altitude without being constrained by the height of a tunnel. In tunnels, the honeybees' height and lateral position depend on the tunnel's geometrical configuration and on the position of the initial entrance point, while the flight speed depends on the smallest tunnel cross-section [177, 178, 179]. The impact of the tunnel's geometrical configuration on the height of flight and thus on the performances of the ventral visual odometer is therefore more pronounced in narrow low-roofed tunnels. For example, the accuracy

of the behaviour observed in honeybees while searching in narrow tunnels [224] and in the open field [185] differs considerably under tail wind conditions, when the mean errors recorded were −14,4% and 3%, respectively (see Table A.1 in section A.4 in appendix 5.1.6).

5.1.5.2 Reliability of the honeybee's visual odometer documented in the literature

To reach a food source in the close vicinity, honeybees are thought to rely on several mechanisms, such as those based on visual snapshots and smell. This makes it difficult to assess the accuracy of the honeybees' visual odometer alone, since it has not yet been established when and where on their trajectory honeybees conclude that they have reached their target. Many observations [247] have shown that honeybees are able to assess distances accurately when searching for a target containing a food source. Heran [97] has reported that honeybees signal the position of a food source in the same way whether it is placed downhill or uphill, and Bräuninger [29] has observed that honeybees can retrieve food from a source whatever the wind direction. It has also been reported that bees can sometimes fail their first attempt to find a food source immediately after attending a waggle dance [206]. Some intra- and inter-individual variability is known to exist in Hymenopterans, and this has been observed in honeybees' trajectories while they are landing on a food source [226], as well as during altitude control in a vertical tunnel [179]. To our knowledge, only two quantitative studies have been published so far on honeybees' visual odometric estimation of the flight distance to a food source. These two behavioural studies were conducted under very different conditions, the one in narrow tunnels [224] and the other in the open field [185]. In addition, the honeybees' trajectories were analysed using two very different methods: based on honeybees' successive U-turns in the proximity of a target in [224], and on the truncation of the tracks when they deviated by more than 90deg in [185]. These two behavioural studies have yielded substantially different results in terms of the accuracy and the statistical dispersion (see Table A.1 in section A.4 in appendix 5.1.6 for a quantitative comparison expressed in % error and relative dispersion). It is therefore difficult to make comparisons between these two behavioural studies and either the *SOFIa* model or the *OFacc* model. These comparisons might be possible only in a single case: under tail wind conditions, the accuracy of the results of the *SOFIa* model obtained in the *virtual* open field (0.69%) matches the accuracy observed in [185] (3%) better than that of the *OFacc* model (-26% after multiplication by $k_{comparisons}$). Generally speaking, the distribution spread and the accuracy of the results obtained with the *SOFIa* model correspond to the fact that visual cues, especially optic flow cues, can reliably feed the honeybee's visual odometer over distances of the order of a few hundred meters regardless of the trajectory taken [58, 225, 223, 61, 40].

5.1.5.3 Oscillations help bees to gauge their clearance from the ground

Self-controlled oscillations generate a sequence of contractions and expansions in the optic flow vector field. These contractions and expansions, which in each case can be quantified by the optic flow divergence, are superimposed on the translational optic flow component. These self-oscillatory movements make the state vector $[h; v_h]$ locally observable, and therefore the height of flight h can be estimated using an EKF (see sections *c* and *d* of *Materials and Methods*). In fact, an EKF is a nonlinear filter that estimates the h, which is also called the clearance from the ground or the depth, using the optic flow divergence and the wing stroke amplitude control signals. On this basis, the self-controlled oscillations make it possible for the ventral translational optic flow to be scaled by the clearance from the ground.
Previous experiments with honeybees flying both freely and in tunnels have shown the presence of these self-oscillatory movements. Honeybees' self-oscillations have also been described quantitatively in narrow horizontal and vertical tunnels: the oscillation frequency ranges around $2Hz$, and the amplitude of the oscillations is approximately $3cm$ in width (in narrow $12cm$-wide tunnels) [124] and $10cm$ in height (in $40cm$-high tunnels) [178] (see appendix 5.1.6 Figure A.1). Baird et al. [8] have recently investigated the hypothesis that honeybees flying in narrow tunnels might control their height of flight by means of sideways self-oscillations with a mean frequency of $4.7 \pm 1.6Hz$. Besides Hymenopterans, vertical oscillations are also known to occur in Lepidopterans: one can easily observe the erratic bouncing and fluttering flight patterns of butterflies inhabiting various continents [257, 201] as well as series of up-and down vertical curves described by moths at a frequency of about $2Hz$ [12].
The $SOFIa$ model was tested in simulation under conditions resembling those pertaining in an open field or a wide tunnel, where honeybees seem to oscillate at lower frequencies. In all the figures presented here in the main text, the simulated honeybees oscillated with a frequency of $1Hz$ and an amplitude of 35 to $55cm$, depending on the height of flight, the air speed, and the optic flow setpoint. Further experiments performed with a simulated honeybee oscillating at $2Hz$, $3Hz$ and $4Hz$ showed there were no significant differences in the spread of the flight distance estimates $\hat{X}_{SOFIa}$ assessed by the *SOFIa* model (Brown-Forsythe-test, df ={3, 2516}, p-value = 0.899) (see section A.3 in appendix 5.1.6 Figure A.2 and Figure A.3).

5.1.5.4 Biological plausibility of the *SOFIa* model

In honeybees, various motion-sensitive neurons respond to specific motion patterns: i) the Velocity-Tuned neurons (VTs) and some Descending Neurons (DNs) respond to translational optic flow [110, 111] and ii) other DN neurons respond to the expansion and contraction of the optic flow [25, 113]. DN motion-sensitive neurons cover the ventral field of view [88] and respond to downward visual motion [112]. Honeybees are therefore sensitive to the ventral optic flow of translation, of expansion and of contraction generated by their oscillatory forward flights. The use of stereo visual

cues is not biologically plausible here because flying insects lack both a binocular ventral visual field aimed toward the ground and a sufficiently large spatial resolution in their ventral visual region to be able to estimate their height of flight. Nor did stereo visual signals play a role in the case of gulls' offshore take-off [208]. In particular, birds' binocular visual field is rather used to guide their beaks for manipulation purposes, for example [149, 150]. The optic flow-based estimator of the scale factor is a nonlinear filter (EKF) based here on i) a nonlinear model, ii) a control input (or called the efference copy in biological systems) and iii) a biologically plausible sensory output (the optic flow divergence). The *SOFIa* model can therefore be said to be biologically plausible even if it is not entirely anatomically constrained. Nevertheless, it opens up some interesting functional perspectives for mesoscale modelling [250].
The *SOFIa* model would be reliable regardless of the base unit and the coding in which the information flow is processed, including those possibly used by honeybees to evaluate the scaling factor based on the flow divergence to detect the translational optic flow, to process the efference copy (or control input), to weigh and accumulate input signals, and thus to assess the flight distance.

5.1.5.5 Conclusion

In conclusion, the Self-scaled time-based Optic Flow Integration model called *SOFIa* involves the use of a scaling factor extracted from the optic flow vector field. This scaling factor is the clearance from the ground estimated by means on an EKF based on the optic flow divergence generated by the bees' self-oscillatory movements. Since the time-based integration of the ventral optic flow is scaled, the *SOFIa* model is less sensitive to changes occurring in the environment such as changes in the direction of the wind or in the trajectory taken. As shown here in the simulations and the standard deviation analysis, the estimated flight distances obtained were particularly reliable and accurate with a large range of ground surfaces and wind conditions. The *SOFIa* model for the visual odometer was found to be reliable even in the presence of multiple disturbances as well as changes in the simulated honeybees' internal parameters, such as the optic flow setpoint and the flight speed. This model reduces the statistical dispersion of the estimated flight distance 10-fold in comparison with the previous model for the visual odometer based on the raw mathematical integration of the translational optic flow. Therefore, the SOFIa visual odometer model shows that their bouncing trajectory may help honeybees (i) to retrieve a food source, (ii) to return to the close vicinity of the hive and (iii) to communicate to their nest-mates a reliable flight distance between the hive and the food source.
Since the scaling was performed using a optic flow-based estimation of the clearance from the ground, the output of the *SOFIa* model is given in $meters$. In fact, the precision of the *SOFIa* model, combined with the dimension of its output, opens up the possibility of implementing the model directly in the field of flying robotic applications. One particularly promising future application of the *SOFIa* model might be in GPS-denied environments, where it would enable flying robots to assess the

flight distance accurately using only minimalistic visual equipment.

Materials and Methods

Honeybees' vertical dynamics A simplified dynamic honeybee model was previously developed, based on behavioural studies [180]. The honeybees' vertical dynamics were expressed in that study as follows:

$$G_{Vz}(s) = \frac{V_z(s)}{u_{\Delta\Phi}(s)} = \frac{K_z}{1+\tau_z s} \tag{5.4}$$

where $u_{\Delta\Phi}$ [deg] is the difference in the wing stroke amplitude in comparison with hovering, V_z $[m/sec]$ is the vertical speed, $\tau_z = 0.22[sec]$ and $K_z = 0.11$. The honeybees' forward dynamics were expressed here as follows:

$$G_{V_{air}}(s) = \frac{V_{air}(s)}{u_\theta(s)} = \frac{K_{surge}}{1+\tau_{surge} s} \tag{5.5}$$

where u_θ [deg] is the honeybee's pitch during hovering, V_{air} $[m/sec]$ air speed, $\tau_{surge} = 0.22[sec]$ and $K_{surge} = 0.10$.

Simulated honeybee flight parameters The controller of the ventral optic flow regulator was a PD controller with a proportional coefficient $k_P = 15$ and a derivative coefficient $k_D = 0.3$. When $h \geq 5cm$, the self-oscillation command $A_{osc}\, sin(2\pi f_{osc})$ was added to the PD vertical controller output to form the wing stroke amplitude $u_{\Delta\Phi}$ control signal feeding the vertical dynamics. The $5cm$ height condition made the honeybee's take-off and landing manoeuvres suitably smooth [62]. Take-off was determined by imposing an ascending ramp on the pitch u_Θ between $0m$ and $1m$. Landing was determined by imposing a descending ramp on u_Θ starting at $5.5m$ in the case of simulations over an $8m$-long flat ground and at $95.5m$ in that of simulations over a $100m$-long irregular ground. In Figures 5.3 and 5.4, the self-oscillatory movements were simulated by a sine wave with a frequency of $f_{osc} = 1Hz$ and an amplitude of $A_{osc} = 18$ deg. In Figures 5.3, 5.4 and A.3 in appendix 5.1.6, the translational optic flow setpoint was set at $2.5 rad/sec$.

State space representation of the EKF used to visually gauge $\hat{h}$ To estimate the current height of flight h, the EKF used i) the downward perceived optic flow divergence as its measurement input, ii) the model for the vertical dynamics of the simulated honeybee and iii) the control input signal (the wing stroke amplitude $\Delta\Phi$) regulating the vertical dynamics (see EKF equations A.1-A.7 in appendix 5.1.6). The

continuous state space model was therefore written as follows:

$$\begin{aligned} \dot{x}(t) &= f(x(t), \Delta\Phi(t)) = A.x(t) + B.\Delta\Phi(t) \\ &= \begin{bmatrix} 0 & 1 \\ 0 & \frac{-1}{\tau_z} \end{bmatrix} \begin{bmatrix} h \\ v_h \end{bmatrix} + \begin{bmatrix} 0 \\ \frac{K_z}{\tau_z} \end{bmatrix} \Delta\Phi \end{aligned} \tag{5.6}$$

$$y(t) = g(x(t)) = [x_2(t)/x_1(t)] = v_h/h = \omega_{div} \tag{5.7}$$

where $x = \begin{bmatrix} h \\ v_h \end{bmatrix}$ is the state vector, $\Delta\Phi$ is the control input and ω_{div} is the optic flow divergence. All the results presented here were obtained with the following initial EKF conditions: $h_{EKF_i} = 0.5m$, $V_{EKF_i} = 1m/s$.
It is worth noting that the model's dynamics given in equation 5.6 are linear, whereas the EKF's observation equation in 5.7 is nonlinear. We slightly adapted one EKF equation by taking the absolute value of the height of flight given in the previous state estimates in order to take into account the fact that the ground height can only be positive (see appendix 5.1.6 eq. A.1). In practice, this helped to achieve a much faster and more reliable convergence of the EKF estimates.

Self-oscillations make the scaling factor observable The optic flow divergence and the self-controlled oscillatory movements make the system observable, i.e., the observation process based on the measurement input during a finite period of time (t_0, t_1) makes it possible to determine the state vector at the instant t_1. To check the observability of the system, the observability rank condition was analysed. First the observability matrix was calculated using the EKF observation equation 5.7 with respect to the model dynamics given in equation 5.6 [99]. The successive Lie derivatives of $g(.)$ were then calculated. A system is observable if and only if the Jacobian function of the observability matrix is full rank. In the present case, the observability matrix was expressed as follows:

$$O = \begin{bmatrix} L_f^0(g(x(t))) \\ L_f^1(g(x(t))) \end{bmatrix} = \begin{bmatrix} g(x(t)) \\ \frac{g(x(t)}{\partial x(t)} * f(x(t), u(t)) \end{bmatrix} = \begin{bmatrix} \frac{V_h(t)}{h(t)} \\ \frac{-V_h(t)^2}{h(t)^2} + \frac{u}{h} \end{bmatrix} \tag{5.8}$$

$$rank(O) = n \tag{5.9}$$

Next, an analysis of O was performed in order to check whether its Jacobian was full-rank. The first function of the observability matrix was $y(t) = V_h/h = \omega_{div}$, and its second function was the first Lie derivative with respect to the dynamics $-V_h(t)^2/h(t)^2 + u/h$. This result showed that the system is (locally) observable if and only if the input disturbance $u \neq 0$, and $h \neq 0$ and $V_h \neq 0$. The continuous variation of the control signal u due to the self-induced input disturbances ensured that the values of the states h and V_h and the control signal were rarely zeroed. Therefore, the

oscillatory movements made the clearance from the ground observable via the optic flow divergence.

Wind modelling A logarithmic law was used to model the wind profile along the altitude [240] as follows:

$$v_{wind} = k_{wind} \cdot v_0 \ln \frac{h}{h_0} \tag{5.10}$$

with the reciprocal of the Von Kármán constant $v_0 = 0.2 m/s$, the current height h and the roughness height $h_0 = 0.05 m$. In Figures 5.3 and 5.4 the range of values spanned by the wind in each case is given in the coloured portion of the wind curves.

OFacc model and $k_{comparisons}$ computation The model for the visual odometer based on the accumulated (time-based integrated) raw translational ventral optic flow (named in this paper $OFacc$) gives as its output an angle expressed here in $radians$ (and not in $meters$) as follows:

$$OFacc = \int \omega_T^{meas} \, dt \quad [rad] \tag{5.11}$$

The distribution of the *OFacc* model's output was calibrated after the simulation runs to be expressed in $meters$ only to be compared statistically with the distribution of the *SOFIa* model's output. The calibration factor was called $k_{comparisons}$ and was computed in order to set at $100 m$ the median value of the distribution of the *OFacc* model's output obtained after a 100m-simulated flight under the 630 parametric conditions:

$$k_{comparisons} = \frac{100}{median\{OFacc\}} = 1.161 \quad [m/rad] \tag{5.12}$$

Final flight distance estimates and flight distance error estimate The distributions plotted in Figure 5.5 and 5.6 were final flight distance estimates across combinations of simulation parameters. The final flight distance estimate was obtained at $X = 100 m$. The error (expressed as a %) was computed as follows:

$$err_{\%} = \frac{\hat{X}_{SOFIa} - X}{X} \times 100 \tag{5.13}$$

where $\hat{X}_{SOFIa}$ is the estimated flight distance and X is the ground truth.

Computation of the relative dispersion The relative dispersion, which is also known as the Coefficient of Variation (CV), is a standardised measure of the dispersion of a probability distribution. It was expressed here as a percentage in Table A.1 in appendix 5.1.6. The relative Standard Deviation (rSD) was defined as the ratio between the Standard Deviation (SD) and the mean in the case of the parametric data, i.e.,

those based on [185]. The relative Median Absolute Deviation (rMAD) is the ratio of the MAD to the median in the case of the non-parametric data, i.e., the present set of final odometric errors obtained with both simulated models.

Computer simulations The two visual odometers were both simulated using Matlab/Simulink 2020 software. Raw data will be available online, which includes all detailed simulation results of the trajectories for oscillation frequencies of $1Hz$, $2Hz$, $3Hz$ and $4Hz$.

5.1.6 Supplemental Information

5.1.6.1 Honeybees' self-oscillation

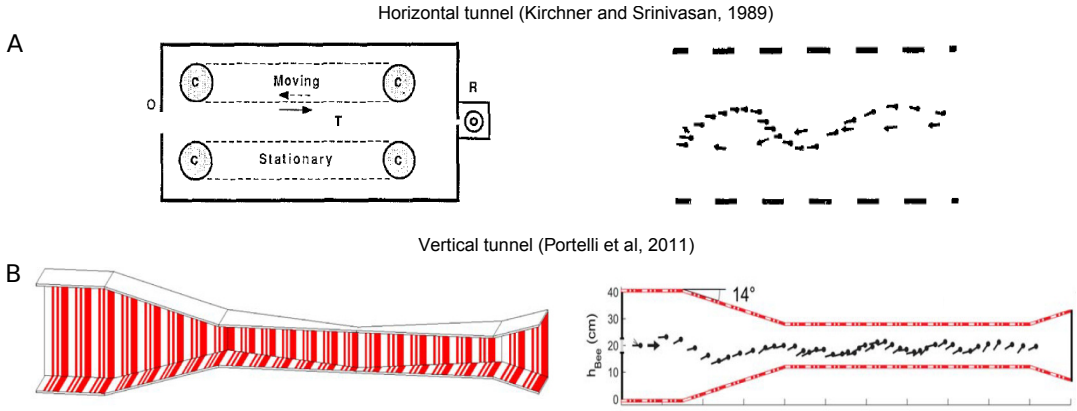

Figure 5.7: A.i) Honeybees were trained to enter a horizontal tunnel via the opening O and fly along it to the box R containing a sugar water reward. A.ii) The oscillatory trajectory of one honeybee flying along the horizontal tunnel (adapted from [124]). B.i) Perspective view of the whole doubly-tapered tunnel in which the experiments were carried out. B.ii) Side view of a honeybee's oscillatory trajectory (adapted from [178]).

5.1.6.2 Extended Kalman Filter equations

The following processing steps were performed by the Extended Kalman Filter (EKF) to estimate the simulated bees' height of flight h, based on the downward-perceived optic flow divergence as the measurements and the stroke amplitude as the inputs feeding the vertical dynamics. In order to apply the EKF, the system was discretised and linearised around an estimated nominal trajectory in order to obtain a linear model for the error. One EKF equation was slightly adapted by adding an absolute function to the first state (the ground height) in the previous state estimate, in order to account for the fact that the ground height can only be positive (see expression of X_{k-1} in eq. 5.14). In practice, this helps to obtain a much faster and more reliable convergence of the EKF estimates. The covariance of the measurement noise R was $3 \cdot 10^{-6}$, and that of the process noise Q was $1 \cdot 10^{-3}$.

Prediction step

(a) One-step-ahead predictions

$$X_{k|k-1} = f(X_{k-1}, u_{k-1}) \tag{5.14}$$

with $X_{k-1} = \begin{bmatrix} |h| \\ v_h \end{bmatrix}$ (because the height is always positive)

(b) Covariance matrix of the state prediction error vector

$$P_{k|k-1} = F_{k-1} P_{k-1|k-1} F_{k-1}^T + Q_{k-1} \tag{5.15}$$

where F_k is the Jacobian matrix of $f(.)$

$$F_{k-1} = \frac{\partial f}{\partial X}|_{X=X_{k-1|k-1}} \tag{5.16}$$

Correction step

(c) Measurement update

$$X_{k|k} = X_{k|k-1} + W_k(Z_k - g(X_{k|k-1})) \tag{5.17}$$

(d) Covariance matrix of the state estimation error vector

$$P_{k|k} = P_{k|k-1} + W_k[H_k P_{k|k-1} H_k^T + R_k] W_k^T \tag{5.18}$$

$$W_k = P_{k|k-1} H_k^T [H_k P_{k|k-1} H_k^T + R_k]^{-1} \tag{5.19}$$

where H_k is the Jacobian matrix of the nonlinear function defined as follows:

$$H_k = \frac{\partial g}{\partial X}|_{X=X_{k|k-1}} \tag{5.20}$$

where:
W_k is the Kalman gain.
$Z_k - g(X_{k|k-1})$ is called the innovation of EKF.
$H_k P_{k|k-1} H_k^T + R_k$ is the covariance of the innovation.

5.1.6.3 Robustness of the *SOFIa* visual odometer at the various self-oscillation frequencies applied

To further determine its robustness at various self-oscillation frequencies, the *SOFIa* visual odometer was tested in simulation under the 630 parametric conditions with the following four sets of self-oscillation parameters: $f_{osc} = 1Hz$ and $A_{osc} = 18$ deg; $f_{osc} = 2Hz$ and $A_{osc} = 40$ deg; $f_{osc} = 3Hz$ and $A_{osc} = 60$ deg; $f_{osc} = 4Hz$ and $A_{osc} = 80$ deg. Figure 5.8 shows the distributions of the *SOFIa* model outputs with the four self-oscillation frequencies studied. Their spreads were not found to differ significantly from each other, and therefore they did not depend on the self-oscillation frequency (Brown-Forsythe-test, df ={3, 2516}, p-value = 0.899).
Figure A.3 shows examples of simulations performed over a $100m$-long ground surface including 3 small hills with gentle slopes separated by flat areas under no wind, tail wind and head wind conditions at 4 different self-oscillation frequencies, f_{osc}: $1Hz$, $2Hz$, $3Hz$ and $4Hz$. The simulations were performed with a peak height h_{peak} of $1m$, a wind speed gain k_{wind} of $-1m/s$, $0m/s$ and $1m/s$, a translational optic flow setpoint ω_T^{set} of $2.5 radians/sec$ and a pitch u_Θ of 30 deg. Figure A.3 shows that in each of the four self-oscillation frequencies under consideration, the error with respect to the goal located at a distance of $100m$ ranged between 0.1% and 2.2%.

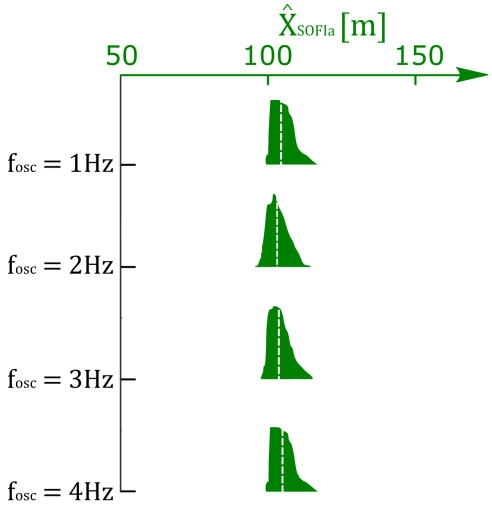

Figure 5.8: The plots show the statistical dispersions of the outputs of the *SOFIa* model tested in simulation under the 630 parametric conditions with f_{osc} of $1Hz$, $2hz$, $3Hz$ and $4Hz$. The median values of the distributions ranged between $102.79m$ and $104.8m$, while their MAD ranged between $3.03m$ and $3.09m$. The spreads of the four distributions did not depend on the self-oscillation frequency because they were not found to differ significantly from each other (Brown-Forsythe-test, df ={3, 2516}, p-value = 0.899).

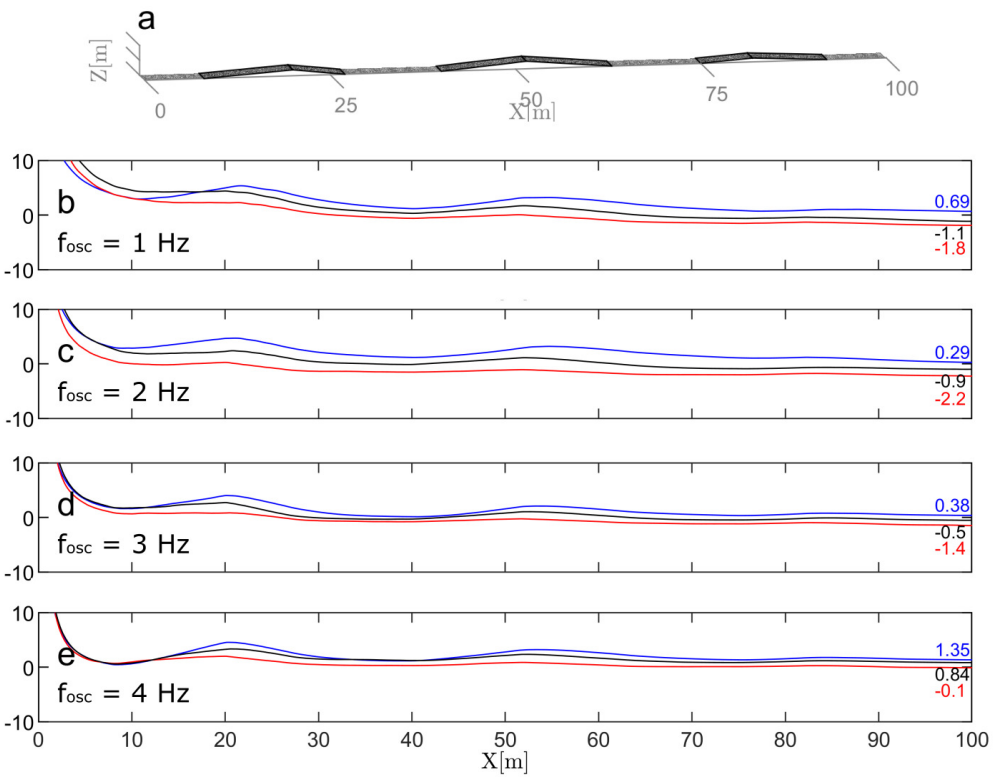

Figure 5.9: (a) Examples of simulated oscillatory flights over a 100m-long ground surface including 3 small hills with gentle slopes separated by flat areas under no wind (in black), tail wind (in blue) and head wind (in red) conditions were plotted. The self-oscillatory movements were simulated by a sine wave with (b) $f_{osc} = 1Hz$ and $A_{osc} = 18$ deg, (c) $f_{osc} = 2Hz$ and $A_{osc} = 40$ deg, (d) $f_{osc} = 3Hz$ and $A_{osc} = 60$ deg and (e) $f_{osc} = 4Hz$ and $A_{osc} = 80$ deg. At each oscillation frequency under consideration, the error in the estimated flight distances with respect to the ground truth was normalised and expressed in %. The error ranged between 0.1% and 2.2%.

5.1.6.4 Final % errors in the flight distances estimated under three different wind conditions

	head wind	no wind	tail wind
$\hat{X}_{SOFIa}$ ($f_{osc} = 1Hz$) *(% error ± % rMAD)*	-1.8 ± 2.69	-1.1 ± 2.75	0.69 ± 3.16
$k_{comparisons} \cdot OFacc$ ($f_{osc} = 1Hz$) *(% error ± % rMAD)*	20.6 ± 28.7	-3.3 ± 22.45	-26 ± 19.72
Open field, data from [185] *(% error ± % rSD)*			3 ± 25.7 [2]
Narrow tunnel, data from [224] *(% error)*	6.66 [3]	-3.33 [4]	-14.4 [5]

Table 5.1: Table of the final % errors in the flight distances assessed by the *SOFIa* model, the *OFacc* model calibrated with $k_{comparisons}$, based on data published by [185] and [224]. To obtain the datasets with the *SOFIa* and the *OFacc* models, honeybee flights were simulated over a 100m-long ground surface including 3 small hills with gentle slopes separated by flat areas under no wind, tail wind and head wind conditions. With both models, the relative Median Absolute Deviation (rMAD) was computed under the three wind conditions under consideration. In [185] data were collected in the open field under cross-tail wind conditions. The final % error was retrieved, and the relative Standard Deviation (rSD) was computed. In [224], the data were collected in a narrow tunnel 3.2m long, 22cm wide and 20cm high. The final % error was determined under no wind, tail wind and head wind conditions. It was difficult to make fair comparisons between the four datasets in question because the conditions under which the experiments in the studies by [185] and [224] were conducted and the methods used to analyse the data were very different.

[4] Data from [185] collected under a mean crosswind of 3.3m/s oriented at 38 deg with respect to the normal from the hive to the feeder, i.e. with a mean tail wind component of 2.6m/s.
[5] Data recomputed from Figure 3a in [224] collected under a head wind of 0.7m/s.
[6] Data recomputed from Figure 3a in [224] collected in still air.
[7] Data recomputed from Figure 3a in [224] collected under a tail wind of 0.65m/s.

5.1.6.5 Simulations under tail and head wind conditions with respect to time

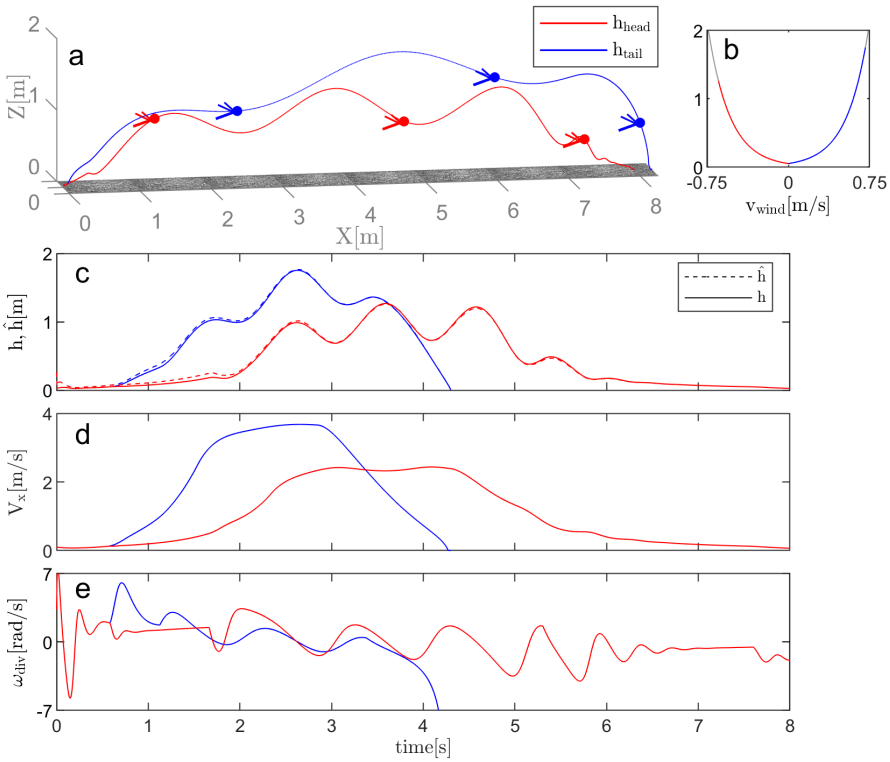

Figure 5.10: Oscillating forward flights of honeybees were simulated over a $8m$-long flat ground (see Simulated honeybee flight parameters section in *Material and Methods*). a) The trajectory including take-off, cruise flight and landing was simulated under tail (blue) and head (red) wind conditions. The results of the simulations were plotted here with respect to the distance flown. b) The wind was modelled as in equation 4.7. c) The results of the simulations were plotted here with respect to time. To reach the goal position at $8m$, the simulated honeybee took about $4s$ under tail wind and about $7.5s$ under head wind conditions. d) The ground speed, V_x, obtained during cruise flight depended on the wind conditions. The ground speed was higher in the case of tail wind (blue), which made the simulated honeybee fly at a higher altitude due to the optic flow regulation process; the ground speed was lower in the case of head wind (red), which made the honeybee fly at a lower altitude. e) The optic flow divergence patterns observed were due to the vertical self-oscillatory movements. At a given optic flow setpoint, the amplitude of the optic flow divergence was greater in the case of head wind due to the honeybee being closer to the ground.

5.1.6.6 Statistical dispersion: comparisons in terms of u_Θ and h_{peak}

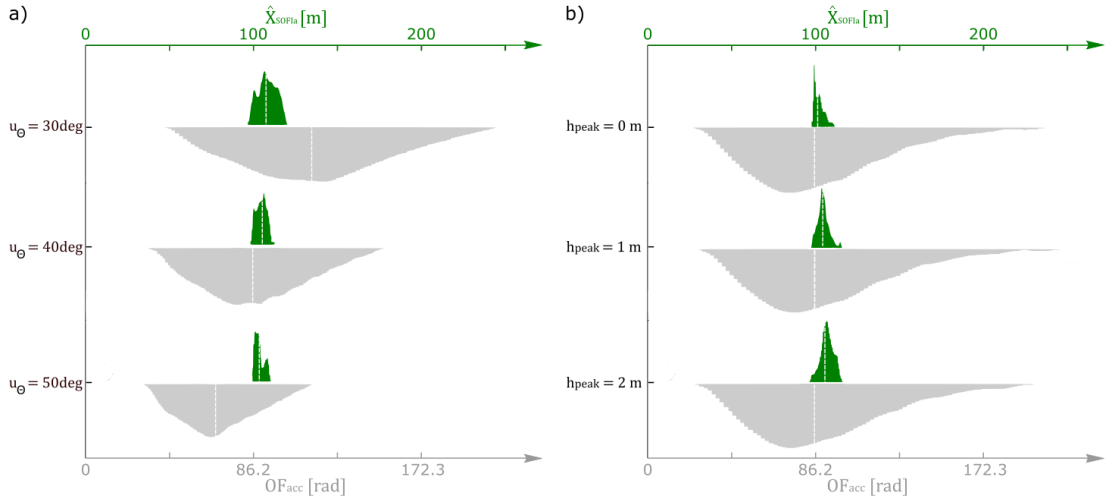

Figure 5.11: The plots give the statistical distributions of the results obtained with the *SOFIa* model (in green) and the *OFacc* model (in grey) with various values of u_Θ and h_{peak}. Both models were tested in simulation under a total number of 630 parametric conditions, as described in Section 3.c. The *OFacc* model was calibrated with $k_{comparisons}$ (see *Materials and Methods*) so as to be able to make direct comparisons with the *SOFIa* model. (a) The median values of the statistical dispersions of the data obtained with the *SOFIa* model with various values of the pitch u_Θ (which drives the forward speed) ranged between 103.6m and 107.78m, while those of the *OFacc* model ranged between 77.6m and 134.7m. The MAD of the *SOFIa* model ranged between 2.22m and 4.07m, whereas the MAD of the *OFacc* model ranged between 17.83m and 34.5m. At a given optic flow setpoint, in the case of low body pitch, the slower the honeybee flies, the longer the *OFacc* model accumulates the optic flow magnitude and hence, the more greatly the flight distance is overestimated. Conversely, in the case of high body pitch, the faster the honeybee flies, the quicker the honeybee reaches the food source, and the shorter the time during which the *OFacc* model integrates the magnitude of the optic flow mathematically and hence, the more greatly the flight distance is underestimated. Therefore, in the case of both low and high speeds, the output of the *OFacc* model deviates increasingly with time from the actual distance flown by the simulated honeybee. Overall, the pitch parameter significantly affected the median values of the *OFacc* model distributions (Friedman-test, df=2, p-value << 0.001), whereas the output of the *SOFIa* model varied very little depending on this parameter. Under each of the

Figure 5.11: u_Θ conditions considered, the median values of the two models' outputs differed significantly (Wilcoxon test, p-value << 0.001, Z=13.76 in the case of each pitch). (b) The median values of the statistical distributions of the data obtained with the *SOFIa* model with various values of h_{peak} ranged between $101.6m$ and $106.75m$, while those of the data obtained with the *OFacc* model ranged between $99.58m$ and $99.76m$. The MAD of the *SOFIa* model was consistently lower than $3.26m$, whereas the MAD of the *OFacc* model ranged between $29.99m$ and $31.01m$. Under each of the h_{peak} conditions tested in simulation, the spread of the two models' outputs differed significantly (Brown-Forsythe-test, df:278, p-value << 0.001, F=182.37;181.80;170.71, with $h_{peak} = 0m; 1m; 2m$, respectively).

6 Measurement of the local optic flow divergence cue with two optic flow sensors

Visual odometric approaches based on the use of cameras have limitations due to environmental conditions and the high computational power required. A minimalistic alternative to cameras is represented by optic flow sensors. The first step towards implementing the SOFIa visual odometer onboard a small flying robot was to find a way to measure the optic flow divergence cue by means of optic flow sensors.
In this chapter, it was mathematically and experimentally demonstrated that the local optic flow divergence cue can be measured as the difference of two optic flow magnitudes perceived by two optic flow sensors placed at angles ϕ and $-\phi$ with respect to the normal to a surface. To test this strategy, a test bench was built with two optic flow sensors, each weighing approximately $1.6g$. The optic flow sensors were placed at fixed angles ϕ and $-\phi$ (with $\phi = 15deg$) on a chariot set on a slider in front of a panorama. In order to mimic the up-and-down self-oscillations performed by honeybees, the two optic flow sensors were made to oscillate back and forth in front of the panorama (either static or moving) by means of a DC motor connected to the slider end opposite the panorama. The panorama could move along the axis perpendicular to the optic flow sensors at variable speed, mimicking the translational component of the honeybees' motion while flying forward. Due to the changes induced by the self-oscillations, the distance and speed of the optic flow sensors with respect to the panorama could be observed locally. Therefore, the distance was estimated by means of an Extended Kalman Filter receiving as measurement the measured local optic flow divergence.
Tests were performed under two different illuminance conditions of $120lux$ and $974lux$, with panorama velocities between $0.25m/s$ and $0.75m/s$ and oscillation frequencies between $0.25Hz$ and $1Hz$. The results of the distance estimation were accurate to the ground truth provided by a lidar sensor and were not affected by illuminance conditions.

Table of contents

6.1 Estimation of the distance from a surface based on local optic flow divergence

Published as:
L. Bergantin, T. Raharijaona and F. Ruffier, "Estimation of the distance from a surface based on local optic flow divergence," *2021 International Conference on Unmanned Aircraft Systems (ICUAS). IEEE.*, p. 1291–1298., 2021

6.1.1 Abstract

Estimating the distance from a surface is a well-known problem for all kinds of applications involving robots moving in an unknown environment. For flying robots this issue is often coupled with weight constraints, from which the importance of carrying out the estimation of distances with minimalistic equipment. In this section, we present a method to exploit the optic flow divergence cue in order to assess the distance from a surface by means of an Extended Kalman Filter. First, we demonstrated mathematically that the optic flow divergence can be assessed by computing the subtraction between two local optic flow magnitudes. Then, we tested this method on a test bench consisting of two on-the-shelf optic flow sensors performing a back-and-forth oscillatory movement in front of a static or moving panorama. Our findings showed that the optic flow divergence measured as a subtraction of two local optic flow magnitudes was in line with the optic flow divergence computed theoretically under two different lighting conditions. Thus, we were able to use the optic flow divergence measured to assess the distance from the static or moving panorama for low ($120 lux$) and bright ($974 lux$) illuminance respectively. Future work will focus on the implementation of this method on a micro-flier to estimate the distance from a surface, with little mass and computational power.

6.1.2 Introduction

The problem of distance estimation while navigating in an unknown environment is common to all types of robots. In flying robots, and more specifically in micro-fliers, this need is often coupled with weight constraints. From these considerations stems the importance of carrying out an accurate visual distance estimation by means of minimalistic equipment. Previous authors have suggested the use of stereo vision to avoid obstacles in vehicle environment perception [22, 166] and in flying robots [157], as well as the use of monocular vision for depth perception [202]. All these approaches rely on the use of cameras and often require the use of complex computer vision algorithms. Optic flow (OF) cues have been used on board flying robots to visually control landing with translational OF [192] and with OF divergence [98, 244, 47, 99], to follow uneven terrain [64] or to attempt visual odometry and localisation [114, 119] (see [209] for review). Moreover, instabilities have been used to determine the height

of flight of a micro-flier by exploiting the linear relation between the oscillation and the fixed control gain [47]. Local OF sensors have been extensively tested in a wide range of lighting conditions for OF based guidance. More generally, the criteria for evaluating the suitability of translational OF sensors for robotic applications include [245]:

- Robustness to light level variations, defined by the number of irradiance decades in which the visual sensor can operate,
- Range of OF angular speeds (or magnitudes) covered, defined by the minimum and maximum values measured,
- Accuracy and precision, defined by systematic errors and coefficients of variation,
- Output refresh rate, defined by the instantaneous output frequency.

To measure the translational OF, a OF sensor was based on the M^2APix (Michaelis-Menten Auto-adaptive Pixel) retina that can auto-adapt in a 7-decade lighting range [147]. Moreover, it has been demonstrated that a single Local Motion Sensor (LMS) fitted with two auto-adaptive pixels allows to measure an OF range of $[50°/s; 350°/s]$ despite variations in lighting conditions from $\sim 50 lux$ to $10,000 lux$ [65]. A similar OF range of $[50°/s; 250°/s]$ (i.e., 0.7-decade) was measured with a semi-panoramic artificial eye, called CurvACE [72]. The OF range can also be measured for outdoor flights, as in [197]. In [189], LMSs were used in front of a moving panorama to measure translational OF.
Small self-oscillatory movements have been observed in honeybees flying in horizontal [124] and vertical tunnels [178]. These self-induced oscillations are different from side-to-side parallax movements observed in insects (more specifically in locusts [41] and in praying mantis [127]). These oscillations generate a pattern of expansions and contractions in the OF vector field, known as OF divergence. The changes in the vertical speed and in the height of flight due to the oscillations make both variables locally observable [99]. Therefore, by having a device performing back-and-forth oscillatory movements in front of a surface, the local observability of its speed and distance from the surface is ensured.
Taking inspiration from honeybees, in this section we exploit the OF divergence cue to visually estimate the distance from a static or moving surface. In previous studies, authors have used cameras to assess the OF divergence and in some cases to estimate the distance from a surface using an Extended Kalman Filter (EKF) on board a flying robot [99]. In this section, we assessed the distance from a static or moving surface by measuring the OF divergence solely based on the subtraction of the magnitudes of two local OF sensors.
In section 6.1.3, we demonstrate mathematically that the OF divergence can be measured solely based on the subtraction of the magnitudes of two local OF sensors: this subtraction results in the OF divergence even in front of a static or a moving surface. In section 6.1.4.1, we present the test bench consisting of two OF sensors placed on a slider performing a back-and-forth oscillatory movement in front of a panorama. In

section 6.1.5, we show experimentally that the signal obtained was equivalent to the OF divergence computed theoretically. Then, the signal was conveyed to the EKF to assess the distance from the static or moving panorama under two different lighting conditions.
Due to their low weight, OF sensors are particularly interesting for flying robotic applications. Thus, we plan to test the method presented to estimate the distance of a flying robot at about one meter from a surface.

6.1.3 The optic flow divergence

6.1.3.1 Definition of the local optic flow divergence

Oscillatory movements generate a sequence of expansions and contractions in the OF vector field. This pattern is known as OF divergence and is superimposed on the translational OF component of the OF vector field. The OF divergence is defined as the ratio of the velocity in the direction normal to a surface v_h and the distance from the surface h:

$$\omega_{DIV}^{th} = \frac{v_h}{h} \tag{6.1}$$

These oscillations make the state vector of the oscillating system locally observable [99] and hence allow to assess the distance from the surface by means of an estimator, i.e. an EKF. The OF divergence can be used by flying robots as an additional visual cue for distance estimation purposes.

6.1.3.2 True local optic flow divergence measured by only two optic flow sensors

We mathematically demonstrate here that the local OF divergence ω_{div}^{meas} can be computed as the subtraction between the magnitudes of two OF sensors' outputs.

Proof. To compute the OF divergence, we consider the case of a device equipped with two OF sensors oriented forward at ϕ and $-\phi$ with respect to the horizontal axis z and placed in front of a surface. The device moves forward oscillating back-and-forth in front of the surface, that moves at a speed $-v_x$. The OF divergence can be measured as follows

$$\omega_{DIV}^{meas} = \omega(\phi) - \omega(-\phi) \tag{6.2}$$

with $\omega(\phi)$ and $\omega(-\phi)$ the OF magnitudes measured by the two OF sensors respectively. By definition, the OF due to the translation movement of the surface can be written as follows

$$\omega(\phi) = \frac{\left\| \vec{V} \right\|}{D} \sin\widehat{\left(\vec{D}, \vec{V}\right)} \tag{6.3}$$

with

$$\widehat{(\vec{D},\vec{V})} = \frac{\pi}{2} - \phi + \alpha \tag{6.4}$$

We can express the two components of the velocity vector $\overrightarrow{V}$ of the device in front of the surface as:

$$v_x = \left\| \overrightarrow{V} \right\| \cdot \cos\alpha$$
$$v_h = \left\| \overrightarrow{V} \right\| \cdot \sin\alpha$$

with

$$\left\| \overrightarrow{V} \right\| = \sqrt{v_x^2 + v_h^2}$$

from which we obtain:

$$\cos\alpha = \frac{v_x}{\sqrt{v_x^2 + v_h^2}}$$
$$\sin\alpha = \frac{v_h}{\sqrt{v_x^2 + v_h^2}}$$

Thus

$$\omega(\phi) = \frac{\left\| \overrightarrow{V} \right\|}{D} \sin\widehat{(\vec{D},\vec{V})} \tag{6.5}$$
$$= \frac{\sqrt{v_x^2 + v_h^2}}{D} . \sin\left(\frac{\pi}{2} - \phi + \alpha\right) \tag{6.6}$$
$$= \frac{\sqrt{v_x^2 + v_h^2}}{D} . \left(\sin\left(\frac{\pi}{2} - \phi\right)\cos\alpha + \cos\left(\frac{\pi}{2} - \phi\right)\sin\alpha\right) \tag{6.7}$$
$$= \frac{\sqrt{v_x^2 + v_h^2}}{D} . \left(\sin\left(\frac{\pi}{2} - \phi\right)\frac{v_x}{\sqrt{v_x^2 + v_h^2}} + \cos\left(\frac{\pi}{2} - \phi\right)\frac{v_h}{\sqrt{v_x^2 + v_h^2}}\right) \tag{6.8}$$
$$= \frac{v_x}{D}\sin\left(\frac{\pi}{2} - \phi\right) + \frac{v_h}{D}\cos\left(\frac{\pi}{2} - \phi\right) \tag{6.9}$$
$$= \frac{v_x}{D}\sin\left(\frac{\pi}{2} - \phi\right) + \frac{v_h}{D}\sin\phi \tag{6.10}$$
$$= \frac{\|\vec{v}_x\|}{D}\sin\widehat{(\vec{D},\vec{v}_x)} + \frac{\|\vec{v}_h\|}{D}\sin\widehat{(\vec{D},\vec{v}_h)} \tag{6.11}$$

We can then express $\omega(-\phi)$ and $\omega(\phi)$ as:

$$\omega(-\phi) = \frac{v_x}{D}\sin\left(\frac{\pi}{2} - \phi\right) - \frac{v_h}{D}\sin\phi \tag{6.12}$$

$$\omega(\phi) = \frac{v_x}{D}\sin\left(\frac{\pi}{2} - \phi\right) + \frac{v_h}{D}\sin\phi \tag{6.13}$$

Thus, the OF divergence can be computed as

$$\omega(\phi) - \omega(-\phi) = 2.\frac{v_h}{D} \cdot \sin(\phi) \tag{6.14}$$

where $h = D \cdot cos(\phi)$ is the distance from the surface.

$$\omega(\phi) - \omega(-\phi) = 2 \cdot \frac{v_h}{h}.\sin(\phi).\cos(\phi) \tag{6.15}$$

Since $\sin(\phi) \cdot \cos(\phi) = \frac{1}{2} \cdot \sin(2 \cdot \phi)$, we can express equation (6.14) as follows:

$$\omega_{DIV}^{meas} = \omega(\phi) - \omega(-\phi) = \frac{v_h}{h}.\sin(2.\phi) \tag{6.16}$$

where ω is the OF magnitude, ϕ is the visual direction of the OF sensor with respect to the axis z and h is the distance from the panorama. The maximum sensitivity of such a local OF divergence device corresponds to a OF sensor orientation of $\phi = 45°$. □

6.1.4 Materials and Methods

To show that it is possible for an oscillating system to retrieve its distance from a surface solely on the basis of OF cues, we built a test bench consisting of two OF sensors set at fixed angles ϕ and $-\phi$ which performed a back-and-forth oscillatory movement in front of a panorama. Since the system was locally observable due to the oscillations, it was possible to estimate the distance from the static or moving panorama by means of the EKF. The EKF received as measurement the OF divergence computed as in equation (6.2), with $\omega(\phi)$ and $\omega(-\phi)$ the OF magnitudes measured by the two OF sensors. To test the robustness of this method, we considered two lighting conditions: bright ($974lux$, $6.95 \cdot 10^{-5} W/cm^2$) and low ($120lux$, $5.42 \cdot 10^{-6} W/cm^2$) illuminance, respectively. In the test bench, $V_x = -V_{panorama}$ because the movement of the panorama mimicked the flight forward above a surface of the system to which the OF sensors were attached.

6.1.4.1 The test bench

The test bench built consisted of two OF sensors set on a chariot at ϕ and $-\phi$ (with $\phi = 15°$) with respect to the horizontal axis z and placed on a slider in front of a panorama, as shown in Figure 6.1. A DC motor was connected at the end of the slider opposite to the panorama and induced a back-and-forth movement on the chariot along the slider on the horizontal axis z. The panorama moved on the x axis at a varying velocity $V_{panorama}$. A lidar set on the chariot provided the ground

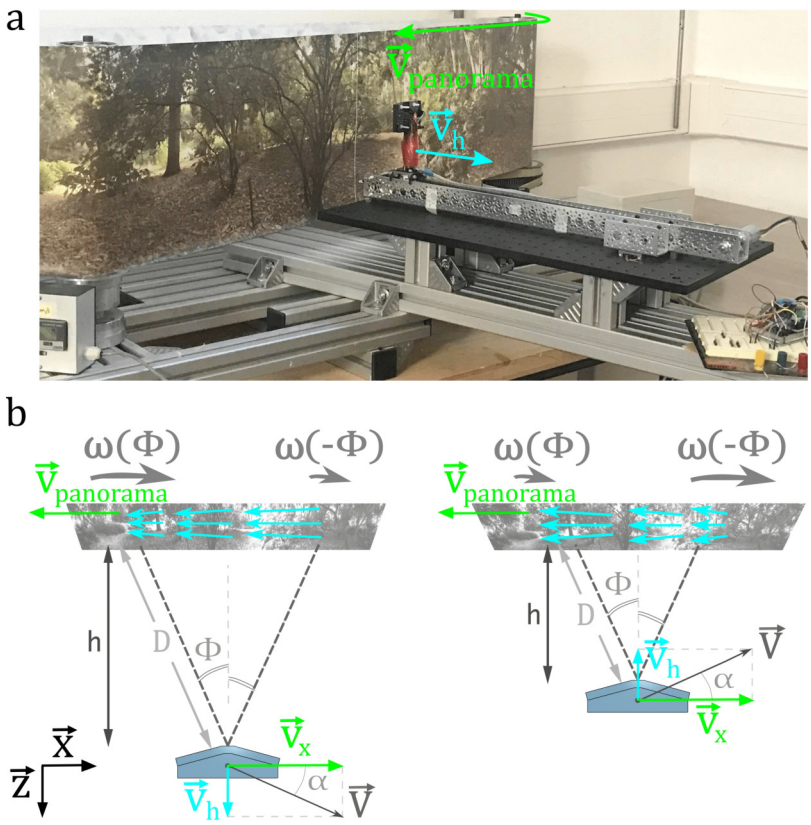

Figure 6.1: (a) The test bench consisted of two OF sensors set on a chariot at ϕ and $-\phi$ (with $\phi = 15°$) with respect to the horizontal axis z and placed on a slider in front of a panorama. The DC motor connected at the end of the slider opposite to the panorama induced a back-and-forth oscillatory movement on the chariot on the horizontal axis z. The direction of the chariot's movement was associated with the velocity v_h, represented in blue. The panorama moved on the x axis at a varying velocity $V_{panorama}$ (in green). A lidar placed on the chariot measured the distance $D \cdot \cos(\phi)$ to the panorama and hence provided the ground truth for the experiment. (b) The two OF sensors measured the OF magnitudes $\omega(\phi)$ and $\omega(-\phi)$, respectively. When the DC motor induced a velocity v_h in the direction of the z axis, the movement of the two OF sensors coupled with the movement of the panorama mimicked an ascending flight above a static surface. The resulting velocity V was oriented upward with an angle α and a contraction was perceived on the OF vector field. When the DC motor induced a velocity v_h in the opposite direction with respect to the z axis, the movement of the two OF sensors coupled with the movement of the panorama mimicked a descending flight above a static surface. In this case, V was oriented downward with an angle α and an expansion was perceived on the OF vector field.

truth measuring the distance $D \cdot \cos(\phi)$ from the panorama. The back-and-forth movement of the OF sensors reproduced the self-oscillations observed in honeybees, while the movement of the panorama mimicked the motion forward above a surface. Synchronization was guaranteed by the use of an interface that initialized the OF sensors, the lidar and the DC motor at the same time. More specifically, we used two Flow Deck V2 from https://www.bitcraze.io/. On each deck were set a PixArt PMW3901 OF sensor and a VL53L1x ToF lidar. The sensors were connected to an Arduino DUE board. To compute the ground truth, we relied on the output of the lidar on the left. The interface MyViz was used for synchronization purposes and to change the frequency of the chariot's oscillation when required.

6.1.4.2 Calibration of the optic flow sensors

To compute the OF divergence, we relied on the OF magnitudes $\omega(\phi)$ and $\omega(-\phi)$ measured by the two OF sensors set on the chariot. The OF sensors' raw outputs were given in [pixel/s] and thus needed to be calibrated to be expressed in [rad/s]. To find the calibration coefficients, a position on the slider was chosen ($0.14m$). One OF sensor was kept stationary with $\phi = 0°$ with respect to the axis z, while the panorama moved with nine values of velocity $V_{panorama}$ (from $0.2m/s$ up to $1m/s$ with a step of $0.1m/s$). For each $V_{panorama}$, were computed the theoretical translational OF w_T^{th} and the average of the measured translational OF $\overline{w}_T^{meas}$. Nine points of coordinates $(w_T^{th}, \overline{w}_T^{meas})$ were obtained and used to fit an affine line $\overline{w}_T^{meas} = m \cdot w_T^{th} + q$, where m and q were the calibration coefficients. This procedure was applied to the two OF sensors separately.

6.1.4.3 The model of the test bench

The system of the test bench can be represented as the block diagram in Figure 6.2. The system's input was the velocity setpoint of the DC motor Ω, while its output was the distance h of the two OF sensors from the panorama. The slider dynamics

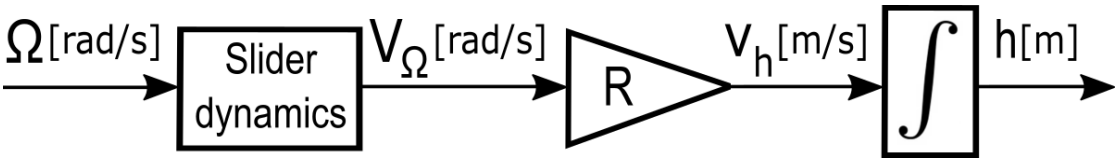

Figure 6.2: Block diagram of the test bench system. The system of the test bench received as input the velocity setpoint of the DC motor Ω [rad/s] and as output the distance h [m] of the two OF sensors from the panorama. More specifically, the slider dynamics received Ω as input and gave the velocity induced on the chariot by the DC motor V_Ω [rad/s] as output. V_Ω was scaled by the radius R of the pulley connecting the DC motor to the chariot in order to compute v_h [m/s]. v_h was then integrated in order to obtain h.

represents the motion control system, as to say a feedback loop over a PID and the motor dynamics. The slider dynamics received as input the DC motor's velocity setpoint Ω in [rad/s] and gave as output the velocity induced by the DC motor on the chariot V_Ω in [rad/s]. V_Ω was scaled by the radius R (with $R = 0.012m$) of the pulley connecting the DC motor to the chariot in order to compute v_h, which was then integrated to compute h. We identified the slider's system between the setpoint input Ω and the chariot's displacement h in [m] using a transfer function that can be expressed as

$$G(s)_{Slider} = \frac{Z(s)}{U(s)} = \frac{0.3498}{s(s+54.27)} \tag{6.17}$$

The system's state space representation can then be expressed as

$$\begin{cases} \dot{X} = A \cdot X + B \cdot u = \begin{bmatrix} 0 & 1 \\ 0 & -54.27 \end{bmatrix} X + \begin{bmatrix} 0 \\ 0.3498 \end{bmatrix} u \\ Y = C \cdot X + D \cdot u = \begin{bmatrix} 1 & 0 \\ 0 & 1 \end{bmatrix} X \end{cases} \tag{6.18}$$

where u is the velocity setpoint Ω and $X = [h; v_h]$ is the state vector. It is important to notice that the measurement equation of the model is nonlinear, since it can be expressed as

$$Y = \omega_{DIV} = \frac{v_h}{h} \tag{6.19}$$

This is the reason why the use of an EKF is necessary. Once defined the model of the test bench system in equation (6.18), we proceeded to its discretization (see Appendix 6.2.1 for the EKF calculations). The EKF received as input the velocity setpoint of the DC motor Ω and as measurement the OF divergence measured.

6.1.5 Results

To show experimentally that the measured OF divergence obtained as in equation (6.2) was equivalent to the theoretical OF divergence computed as in equation (7.3.3), several datasets were collected under different conditions. The two OF sensors performed a back-and-forth oscillatory movement in front of the panorama, which was moving with different values of velocity $V_{panorama}$ ($0m/s$, $0.25m/s$, $0.5m/s$ and $0.75m/s$). The panorama speed $V_{panorama}$ can not exceed $0.75m/s$ steadily because of mechanical constraints. For each $V_{panorama}$, four oscillation frequencies were considered: $0.25Hz$, $0.5Hz$, $0.75Hz$ and $1Hz$. The maximum peak-to-peak amplitude was reached for $0.25Hz$ (see details in caption of the Figure 6.3). For oscillation frequencies below $1Hz$, the oscillation amplitude was too small to allow an effective estimation of the distance from the panorama with the current setup. To test the robustness of the method, the datasets were taken under two different lighting conditions: bright ($974lux$, $6.95 \cdot 10^{-5} W/cm^2$) and low ($120lux$, $5.42 \cdot 10^{-6} W/cm^2$) illuminance, respectively. For each dataset we subtracted the OF magnitudes measured by the two OF

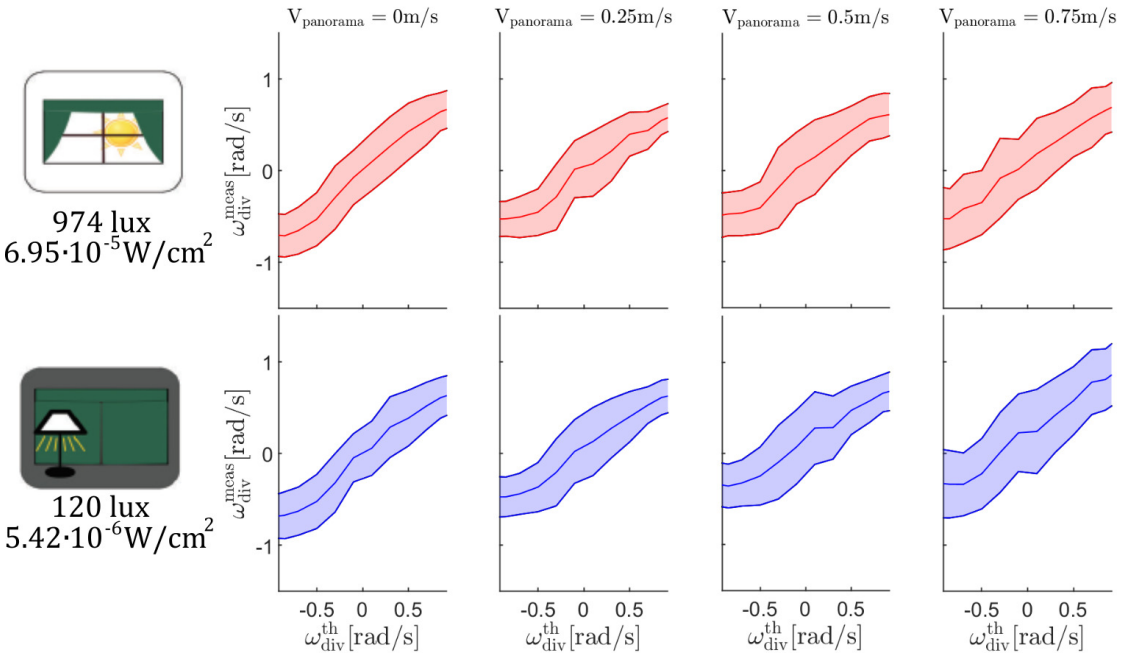

Figure 6.3: The plots show a linear relation between ω_{div}^{meas} and ω_{div}^{th} and are therefore an experimental counterpart of the mathematical proof shown in section 6.1.3.2. The Median Absolute Deviation (MAD) of each plot was low (see Table 6.1). The OF divergence ω_{div}^{meas} was measured in front of the static or moving panorama under two lighting conditions: bright ($974 lux$, $6.95 \cdot 10^{-5} W/cm^2$) and low ($120 lux$, $5.42 \cdot 10^{-6} W/cm^2$) illuminance, respectively. For each value of $V_{panorama}$ ($0 m/s$, $0.25 m/s$, $0.5 m/s$ and $0.75 m/s$) four values of oscillation frequency were considered ($0.25 Hz$, $0.5 Hz$, $0.75 Hz$ and $1 Hz$). For all datasets, the starting position of the chariot on the slider was $0.14 m$. The peak-to-peak amplitude covered by the chariot on the slider ranged from the starting position to about $0.3 m$ for a frequency of $0.25 Hz$, $0.25 m$ for $0.5 Hz$, $0.2 m$ for $0.75 Hz$ and $0.17 m$ for $1 Hz$. The theoretical OF divergence ω_{div}^{th} was computed for every dataset. The values of ω_{div}^{meas} measured for all the oscillation frequencies for a velocity $V_{panorama}$ under a given lighting condition were put together and plotted in comparison with the corresponding ω_{div}^{th}.In each plot, the median values of ω_{div}^{th} and the curves representing its MAD are shown to display the range of values measured. The subtraction between the OF magnitudes obtained by means of the two OF sensors can measure reliably a stimuli of OF divergence between $-0.93 rad/s$ and $1.3 rad/s$.

sensors as in equation (6.2), obtaining the corresponding OF divergence ω_{div}^{meas}. In parallel, we computed the theoretical OF divergence ω_{div}^{th} as in equation (7.3.3). To compare ω_{div}^{meas} and ω_{div}^{th}, all the values of ω_{div}^{meas} measured for all the oscillation frequencies for the panorama moving with a given $V_{panorama}$ under a set lighting

condition were put together and plotted in comparison with the corresponding ω_{div}^{th}. Figure 6.3 shows experimentally that the subtraction between the OF magnitudes obtained by means of the two OF sensors can measure the OF divergence as demonstrated mathematically in section 6.1.3.2. The plots show that ω_{div}^{meas} and ω_{div}^{th} were in the same range of values for every set of conditions. The Median Absolute Deviation (MAD) was low for every case considered, ranging between $0.25 rad/s$ and $0.38 rad/s$ (see Table 6.1). Thus, the OF divergence measured ω_{div}^{meas} can be considered in line with ω_{div}^{th} under every set of conditions analysed and hence can be given as measurement to an EKF to estimate the distance from a static or moving surface.

Average MAD of the OF divergence	low light	bright light
$V_{panorama} = 0 m/s$	$0.27 rad/s$	$0.27 rad/s$
$V_{panorama} = 0.25 m/s$	$0.26 rad/s$	$0.25 rad/s$
$V_{panorama} = 0.5 m/s$	$0.29 rad/s$	$0.30 rad/s$
$V_{panorama} = 0.75 m/s$	$0.38 rad/s$	$0.34 rad/s$

Table 6.1: Table of the average MAD obtained for the comparison of ω_{div}^{meas} and ω_{div}^{th} for four values of $V_{panorama}$ ($0 m/s$, $0.25 m/s$, $0.5 m/s$ and $0.75 m/s$) under bright ($974 lux$, $6.95 \cdot 10^{-5} W/cm^2$) and low ($120 lux$, $5.42 \cdot 10^{-6} W/cm^2$) illuminance, respectively. The values of the average MAD ranged between $0.25 rad/s$ and $0.38 rad/s$.

Since we showed that the OF divergence can be measured reliably as the subtraction of two OF magnitudes, we used it to estimate the distance from the static or moving panorama by means of the EKF. The OF sensors moved back and forth in front of the panorama for $10 s$ with a frequency of $0.5 Hz$. This was done for four values of $V_{panorama}$ ($0 m/s$, $0.25 m/s$, $0.5 m/s$ and $0.75 m/s$) under bright and low illuminance. Figure 6.4.a shows the results obtained under bright illuminance. The estimates of the distance from the panorama $\hat{h}$ converged quickly (about $2 s$) to the ground truth h for $V_{panorama}$ equal to $0 m/s$, $0.25 m/s$ and $0.5 m/s$. For $V_{panorama}$ equal to $0.75 m/s$ the converging time increased slightly (about $3 s$). In every case, the OF divergence was a sinusoidal signal due to the pattern of expansion and contraction in the OF vector field induced by the oscillatory movement. The OF divergence measured presented noise, due to the OF measurement noise, the limitations in the view-field of PixArt OF sensors and the mechanical noise caused by the movement of the chariot on the slider. In general, the noise increased with $V_{panorama}$. The presence of a higher noise magnitude explained the slightly higher convergence time for $V_{panorama} = 0.75 m/s$. Figure 6.4.b shows the results obtained under low illuminance. As in the case of bright illuminance, the estimates of the distance from the panorama $\hat{h}$ converged quickly (about $2 s$) to the ground truth h for $V_{panorama}$ equal to $0 m/s$ and $0.25 m/s$. For $V_{panorama}$ equal to $0.5 m/s$ and $0.75 m/s$ the converging time increased (about $3 s$) due to higher noise magnitudes. The noise was present in every case and increased with $V_{panorama}$.
To compare the estimation performances of the method under the two lighting con-

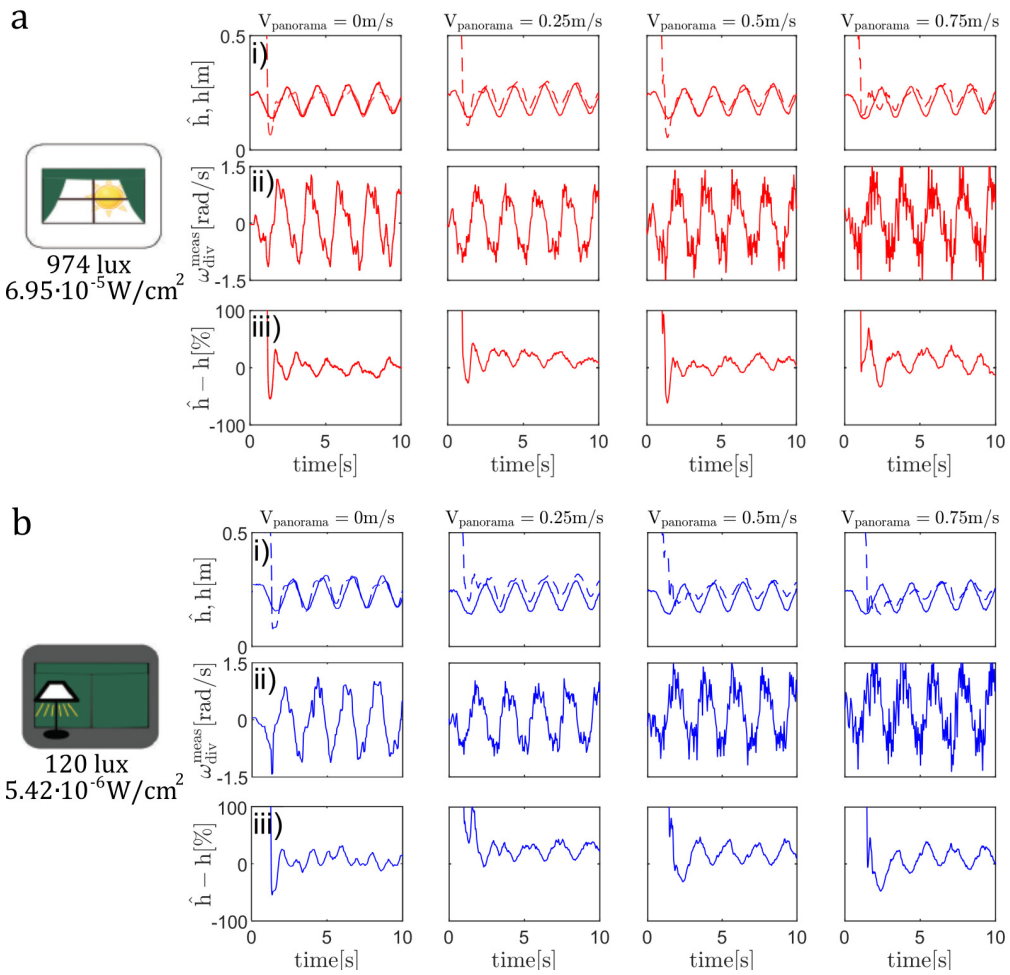

Figure 6.4: The OF divergence was measured with an oscillation frequency of $0.5Hz$ under (a) bright ($974lux$, $6.95 \cdot 10^{-5} W/cm^2$) and (b) low ($120lux$, $5.42 \cdot 10^{-6} W/cm^2$) illuminance in front of the panorama moving with four values of $V_{panorama}$ ($0m/s$, $0.25m/s$, $0.5m/s$ and $0.75m/s$). i) The estimates of the distance from the panorama $\hat{h}$ converged quickly (from about $2s$ to $3s$) to the ground truth h for every value of $V_{panorama}$. The distance h covered by the chariot on the slider ranged between $0.14m$ and $0.25m$. ii) In every case, the OF divergence measured ω_{div}^{meas} was a sinusoidal signal. The noise magnitude increased with $V_{panorama}$ and in general was slightly higher for datasets taken under low illuminance. The higher noise magnitude resulted in a slightly higher convergence time in the case of $V_{panorama}$ equal to $0.75m/s$ under bright illuminance and $0.5m/s$ and $0.75m/s$ under low illuminance. iii) In (a.iii), the average error values computed after convergence were 0.31%, 12.09%, 3.29% and 8.29%, respectively. In (b.iii), the average error values computed after convergence were 4.49%, 15.73%, 12.03% and 5.41%, respectively (see Table (6.2)).

ditions, an analysis of the average error of the estimates of the distance from the panorama $\hat{h}$ after the convergence to the ground truth h was performed. The results are shown in Table 6.2.

Estimation average errors	low light	bright light
$V_{panorama} = 0m/s$	4.49%	0.31%
$V_{panorama} = 0.25m/s$	15.73%	12.09%
$V_{panorama} = 0.5m/s$	12.03%	3.29%
$V_{panorama} = 0.75m/s$	5.41%	8.29%

Table 6.2: Table of the average errors of the estimates of the distance from the panorama $\hat{h}$ after the convergence to the ground truth h for four values of $V_{panorama}$ ($0m/s$, $0.25m/s$, $0.5m/s$ and $0.75m/s$) under bright and low illuminance ($974lux$ and $120lux$, respectively). We computed the average error between $3s$ and $10s$ to guarantee that all the datasets converged. The average errors ranged between 0.31% and 15.73%.

We considered as time of convergence $3s$ in order to include all the datasets analysed. The average errors computed ranged between 0.31% and 15.73%. The errors computed under low illuminance were slightly higher than those obtained under bright illuminance. The only exception was $V_{panorama} = 0.75m/s$, for which the average error under bright illuminance was about 3% higher than under low illuminance. The results obtained under bright and low illuminance can be considered similar. Thus, our findings show that ω_{div}^{meas} can be used to estimate reliably the distance from a surface under both lighting conditions.

6.1.6 Conclusion

The observation of self-induced oscillatory movements in honeybees [124, 178] has led to consider the use of an additional OF cue: the OF divergence. The presence of oscillations makes the oscillating system always locally observable and hence opens the possibility of using the OF divergence cue to assess the distance from a surface, regardless of the maneuver performed. OF divergence has already been used to visually control landing in a micro-flier [99].
In this section, we exploit the OF divergence cue in order to assess the distance from a surface without the need of previous knowledge of the environment or of emissive sensors. The OF divergence can be computed as the subtraction between the magnitudes measured by two OF sensors. To test this method a test bench was built, consisting of two OF sensors performing a back-and-forth oscillatory movement in front of a static or moving panorama. The OF sensors were set on a chariot at an angle of 15° and −15° respectively from the normal to the panorama. The chariot was placed on a slider and was actuated by a DC motor in order to move back and forth along the slider in front of the panorama. To test the robustness of this method, datasets were taken while the panorama was moving at different velocities under bright and

low lighting conditions.
Our findings show that it is possible to compute reliably the OF divergence between $-0.93 rad/s$ and $1.3 rad/s$ as the subtraction of OF magnitudes measured by two OF sensors. Hence, the OF divergence measured this way can be used to assess the distance from the panorama by means of an EKF. We successfully tested this method for distances ranging between $0.14m$ and $0.25m$. The estimates of the distance from the panorama were generally more accurate for lower velocities of the panorama, due to a lower noise magnitude. In every case considered, the estimates of the distance from the panorama converged within $3s$ to the ground truth. The ground truth was obtained by a separate mean: a lidar placed on the chariot. The lighting conditions tested did not influence the results obtained.
Given the low weight of the OF sensors and the low computational power required to compute the OF divergence, this method can be easily implemented on flying robots and more specifically on micro-fliers. In this section, we tested the method presented only for a small range of distances, all of them fairly short if considering the flight of a micro-flier. Our results were promising and showed that it is worthwhile to test the method further. Future work will include an analysis of the estimation of the distance from the panorama for a wider range of oscillation frequencies and of $V_{panorama}$ to prepare for the implementation of this method on a micro-flier. Moreover, we plan to use OF sensors with wider optical aperture lenses to expand the range of lighting conditions. Ultimately, we plan to test the presented method to estimate the distance of a flying robot at about one meter from a surface.

6.2 Appendices

6.2.1 Appendix A: The Extended Kalman Filter calculations for the estimation of distance from the panorama

The discretized model of the test bench can be expressed as

$$\begin{cases} X[k+1] = \Phi \cdot X[k] + \Gamma \cdot u[k] \\ y[k] = C_k \cdot X[k] + D_k \cdot u[k] \end{cases} \tag{6.20}$$

with

$$\Phi = e^{A \cdot dt} \tag{6.21}$$

$$\Gamma = (\int_0^{dt} e^{A \cdot \tau} d\tau) \cdot B = (A^T \cdot e^{A \cdot dt} - A^T) \cdot B \tag{6.22}$$

$$C_k = h(x_k) = \left[\frac{x_2[k]}{x_1[k]} \right] \tag{6.23}$$

$$D_k = 0 \tag{6.24}$$

where dt is the discretization time.
To estimate the distance h from the panorama, the EKF took the following iterative steps for each k^{th} time
Prediction step
(a) One-step ahead prediction

$$X_{k/k-1} = \Phi \cdot X_{k-1/k-1} + \Gamma \cdot u_{k-1/k-1} \tag{6.25}$$

(b) Covariance matrix of the state prediction error vector

$$P_{k/k-1} = \Phi \cdot P_{k-1/k-1} \cdot \Phi^T + Q \tag{6.26}$$

Correction step
(c) Measurement update

$$X_{k/k} = X_{k/k-1} + K_k \cdot (y_k - H_k \cdot X_{k/k-1}) \tag{6.27}$$

with K_k Kalman gain defined as

$$K_k = P_{k/k-1} \cdot H_k^T \cdot [H_k \cdot P_{k/k-1} \cdot H_k^T + R_k]^{-1} \tag{6.28}$$

and H_k Jacobian matrix for the non linear function defined as follows

$$H_k = \frac{\partial h}{\partial X}|_{X=X_{k/k-1}} = \begin{bmatrix} -\frac{\dot{x}}{x^2} & \frac{1}{x} \end{bmatrix} \tag{6.29}$$

(d) Covariance matrix of state estimation error vector

$$P_{k/k} = P_{k/k-1} + K_k \cdot [H_k \cdot P_{k/k-1} \cdot H_k^T + R_k] \cdot K_k^T \tag{6.30}$$

(e) Innovation

$$\tilde{y}_k = y_k - H_k \cdot x_{k/k} \tag{6.31}$$

7 Minimalistic in-flight odometry based on optic flows with oscillatory trajectories

Carrying out visual odometry is a challenging task especially in the case of micro- and nano-drones, on which onboard computational and perception resources available tend to be low. The use of optic flow sensors combined with computationally low-cost algorithms represents a minimalistic alternative to solve this problem.
In this chapter, it was mathematically and experimentally demonstrated that the local translational optic flow cue can be measured as the sum of two optic flow magnitudes perceived by two optic flow sensors placed at angles ϕ and $-\phi$ with respect to the normal to a surface. The SOFIa visual odometer was then tested on a hexarotor equipped with four optic flow sensors positioned downwards at fixed angles ϕ and $-\phi$ (with $\phi = 30deg$) on either side of the drone's vertical axis along the horizontal axis x and the lateral axis y, respectively.
The idea of using prior knowledge of the oscillations imposed on the hexarotor to further improve the Signal-to-noise Ratio (SnR) of both the measured local translational and divergence optic flow cues was also investigated. Two sensor fusion strategies were developed, based on precise and rough prior knowledge of optic flow variations, respectively.
Tests were performed in a flight arena, where the hexarotor executed approximately $50m$-long circular trajectories while oscillating up and down under different illuminance conditions. In all cases considered, the odometry results obtained were accurate to the ground truth provided by the flight arena motion-capture system and were not affected by illuminance conditions or trajectory variations. Subsequently, preliminary tests were performed outdoors on approximately $20m$-long longitudinal bouncing trajectories over a field irregularly covered with grass in the presence of wind. The sensor fusion strategies presented increased the SnR of both measured optic flow cues and thus decreased the error in the distance traveled estimates in all cases considered, improving odometric performance. This was the case even when only rough prior knowledge of optic flow variations was taken into account.

Table of contents

7.1 Indoor and outdoor in-flight odometry based solely on optic flows with oscillatory trajectories

Published as:
L. Bergantin, C. Coquet, J. Dumon, A. Negre, T. Raharijaona, N. Marchand, and F. Ruffier, "Indoor and outdoor in-flight odometry based solely on optic flows with oscillatory trajectories," *International Journal of Micro Air Vehicles*, 2023;15, p. 17568293221148380, 2023

7.1.1 Abstract

Estimating distance traveled is a frequently arising problem in robotic applications designed for use in environments where GPS is only intermittently or not at all available. In UAVs, the presence of weight and computational power constraints makes it necessary to develop odometric strategies based on minimilastic equipment. In this section, a hexarotor was made to perform up-and-down oscillatory movements while flying forward in order to test a self-scaled optic flow based odometer. The resulting self-oscillatory trajectory generated series of contractions and expansions in the optic flow vector field, from which the flight height of the hexarotor could be estimated using an Extended Kalman Filter. For the odometry, the downward translational optic flow was scaled by this current visually estimated flight height before being mathematically integrated to obtain the distance traveled. Here we present three strategies based on sensor fusion requiring no, precise or rough prior knowledge of the optic flow variations generated by the sinusoidal trajectory. The "rough prior knowledge" strategy is based on the shape and timing of the variations in the optic flow. Tests were performed first in a flight arena, where the hexarotor followed a circular trajectory while oscillating up and down over a distance of about $50m$ under illuminances of $117lux$ and $1518lux$. Preliminary field tests were then performed, in which the hexarotor followed a longitudinal bouncing $20m$-long trajectory over an irregular pattern of grass.

7.1.2 Introduction

Estimating distance traveled by an aerial robot is a problem which frequently arises when designing applications for use in situations where GPS is available only intermittently or not at all. In UAVs (Unmanned Aerial Vehicles), reducing the Size, Weight and Power (SWaP) of the perceptual equipment is often of great importance in order to ensure that the robot's task will be performed successfully.
Several visual odometric approaches involving the use of either optic flow [234, 159], events, images & IMU (Inertial Measurement Unit) combinations [246] or the sparse-

snapshot method [50] have been successfully tested on flying robots. All these approaches require ground height information providing the factor used to scale the visual information. This scaling factor can be determined separately using a static pressure sensor [119] or stereovision [234, 50], or it can be integrated when using the hybrid approach [246], for example. One of the approaches used to estimate the 2D position of a drone is a combination of onboard odometry and visual mapping, known as SLAM (Simultaneous Localisation and Mapping) [68, 135, 156].
Most of these approaches require the use of computationally intensive algorithms and feedback from the environment (such as the detection of a beacon or feedback from a map). A minimalistic alternative is IMU based dead reckoning - i.e. inertial integration [213]. A dead reckoning signal could be used by a UAV to return to the close proximity of its base station before reaching it a second time using other means of perception. In this case, the landing of the UAV on its base station can provide a new known starting point. Another minimalistic alternative consists in using optic flow cues, such as translational optic flow and optic flow divergence cues. Translational optic flow has been used on UAVs to control landing visually [192], to follow uneven terrain [64] and to attempt visual odometry and localisation [114, 119] (see [209] for a review).
Self-oscillations have been observed in honeybees flying forward in horizontal [124, 211], doubly tapered [178] and high-roofed [177, 179] tunnels. The self-oscillatory motion generates a series of expansions and contractions in the optic flow vector field, providing the optic flow divergence cue. Visually controlled landing has been achieved based on the optic flow divergence cue [98, 244, 47, 99]. The instabilities due to oscillatory movements have been used to determine the flight height of a micro-flyer based on the linear relationship between the oscillation and the fixed control gain [47]. The instabilities due to depth variations have been used to assess the optic flow scale factor of the scene observed to perform visual odometry onboard an underwater vehicle [46]. The local optic flow divergence was measured by means of two optic flow magnitudes perceived by two basic optic flow sensors placed on a chariot performing back-and-forth oscillatory movements in front of a moving panorama [20]. The local optic flow divergence was then used to estimate the local distance between the chariot and the moving panorama by means of an Extended Kalman Filter (EKF) [20].
A SOFIa (**S**elf-scaled **O**ptic **F**low time-based **I**ntegr**a**tion) model has been previously tested as a means of modeling the visual odometer of honeybees with simulations [19] as well as with preliminary indoor flights [17]. The SOFIa method to estimate the distance traveled is based on the integration of the local translational optic flow scaled by the drone's flight height, determined by means of an EKF taking the local optic flow divergence as measurement [19]. The SOFIa model was found to be about 10 times more accurate than the values obtained in simulations based on the raw mathematical integration of the optic flow [19]. Using an integration scheme of this kind can therefore be regarded as a minimalistic dead reckoning method based on the optic flow.
Here we investigated how to include some knowledge about the oscillations occurring during the trajectory in an odometric strategy based on optic flow cues alone. For

this purpose, the optic flow based odometric scheme called SOFIa was tested both indoors and outdoors on a hexarotor equipped with optic flow sensors (see Figure 7.1). First we applied the SOFIa method using only 2 optic flow measurements perceived along the longitudinal axis of the drone, with no prior knowledge of the optic flow variations. In order to improve the odometric accuracy, a sensor fusion strategy based on the parameters of the self-oscillation using 4 optic flow sensors embedded in the hexarotor was then tested. The idea was to use some prior knowledge about the oscillations imposed on the drone in order to measure the optic flow divergence and the translational optic flow cues more accurately. Two different sensor fusion strategies, based on precise and on rough prior knowledge of the optic flow variations, respectively, were tested. The sensor fusion strategy based on rough prior knowledge consisted solely in using the shape and timing of the variations in the optic flow. All three optic flow based odometric processing methods were tested first indoors on bouncing circular trajectories about $50m$-long under illuminances of $117lux$ and $1518lux$ and then outdoors on bouncing longitudinal trajectories about $20m$-long in

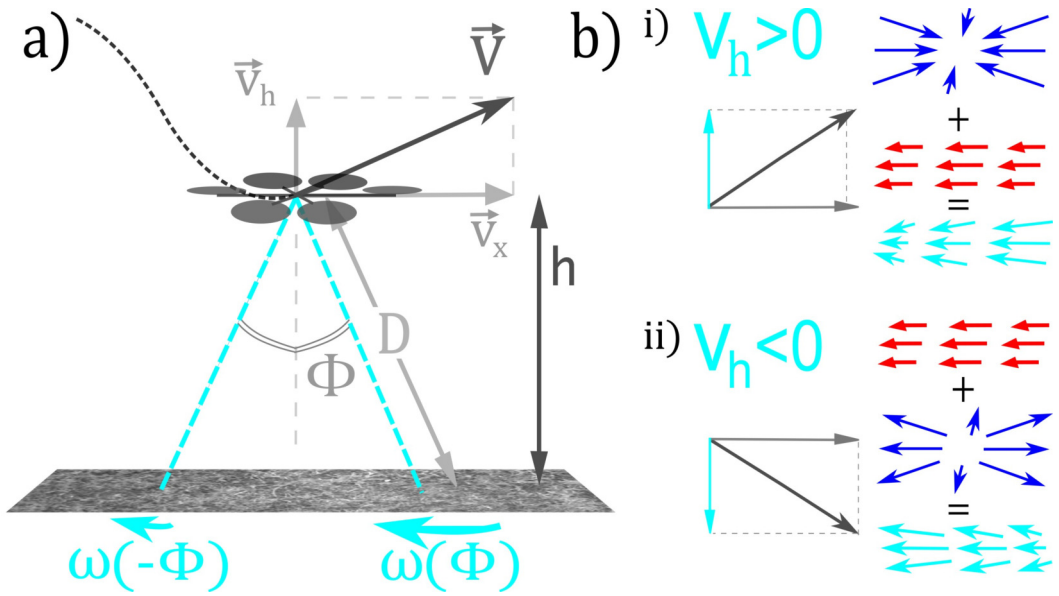

Figure 7.1: Hexarotor oscillating up and down while flying forward over the ground at the flight height h. a) The hexarotor's velocity V can be decomposed into the components V_x and V_h. Along the hexarotor's longitudinal axis x, the optic flow sensors are set at angles $\pm\phi$ with respect to the hexarotor's vertical axis, at the distance D with respect to the ground. They perceive the optic flow magnitudes $\omega(\phi)$ and $\omega(-\phi)$, respectively. This configuration is also present along the hexarotor's lateral axis y. b) If V_h is positive, the optic flow divergence component is a contraction (in blue) (i); if it is negative, the optic flow divergence component is an expansion (in blue) (ii). The contraction or expansion of the optic flow is superimposed in the ventral optic flow vector field on the translational optic flow (in red).

the presence of various wind and irregular grass conditions.
In section 7.1.3, the hexarotor used to perform both indoor and outdoor experiments is described. In section 7.1.4, the measurement of the local translational and divergence optic flow cues is discussed. In section 7.1.5, the minimalistic visual odometric method is discussed. In section 7.1.6, the odometric processing method based on raw measurements of 2 optic flow sensors without any prior knowledge of the optic flow variations is discussed. In section 7.1.7, the sensor fusion odometric processing method based on 4 optic flow sensors is discussed, both with precise and with rough prior knowledge of the optic flow variations. In section 7.1.8, the indoor experimental setup is first described, and experiments are then presented showing that the two sensor fusion strategies based on the knowledge of optic flow variations increased the measurement quality of the local optic flow cues. Lastly, the performances of the three minimalistic in-flight optic flow based odometric processing methods are compared. In section 7.1.9, we first discuss the outdoor experimental setup and then present experiments showing that the same considerations also apply to preliminary flight tests performed outdoors. In section 7.1.10, conclusions are drawn and projects for future studies are discussed.

7.1.3 The SOFIa hexarotor

The hexarotor was developed together with Hexadrone^{TM} and equipped with 4 Pixart PAW3903 optic flow sensors (see Figure 7.2 and Table 7.2). The Pixart PAW3903 optic flow sensors were embedded on printed circuits to be set on the drone. The hexarotor's onboard low-level flight controller was the PX4 autopilot system [155], using a trajectory tracking algorithm[1]. Based on the intrinsic attitude stability of the hexarotor, we can assume that no rotational component is measured by the optic flow sensors. In addition, the pitch and roll components were taken to be negligible. The downward translational optic flow can therefore be measured along the x axis of the optic flow sensors.

Specifics	Optic flow sensors
Sensor chip	Pixart PAW3903
Sensor PCB	4 × 2g
Hardware read-out of the 4 sensors	Arduino Nano

Table 7.1: Characteristics of the optic flow sensors equipped on the hexarotor.

7.1.4 Measurement of the local optic flow cues

The translational optic flow is the angular speed magnitude of the optic flow vector field generated by the translational motion of a drone flying above the ground [85].

[1] https://github.com/gipsa-lab-uav/trajectory_control

The theoretical local translational optic flow ω_T^{th} can be expressed as the ratio between the V_x component of the drone's velocity and its flight height h (see Figure 7.1):

$$\omega_T^{th} = \frac{V_x}{h} \tag{7.1}$$

The local translational optic flow can be measured on a hexarotor as the sum of two optic flow magnitudes $\omega(\phi)$ and $\omega(-\phi)$ perceived by two optic flow sensors oriented at angles $\pm\phi$ with respect to the hexarotor's vertical axis, divided by a known factor of

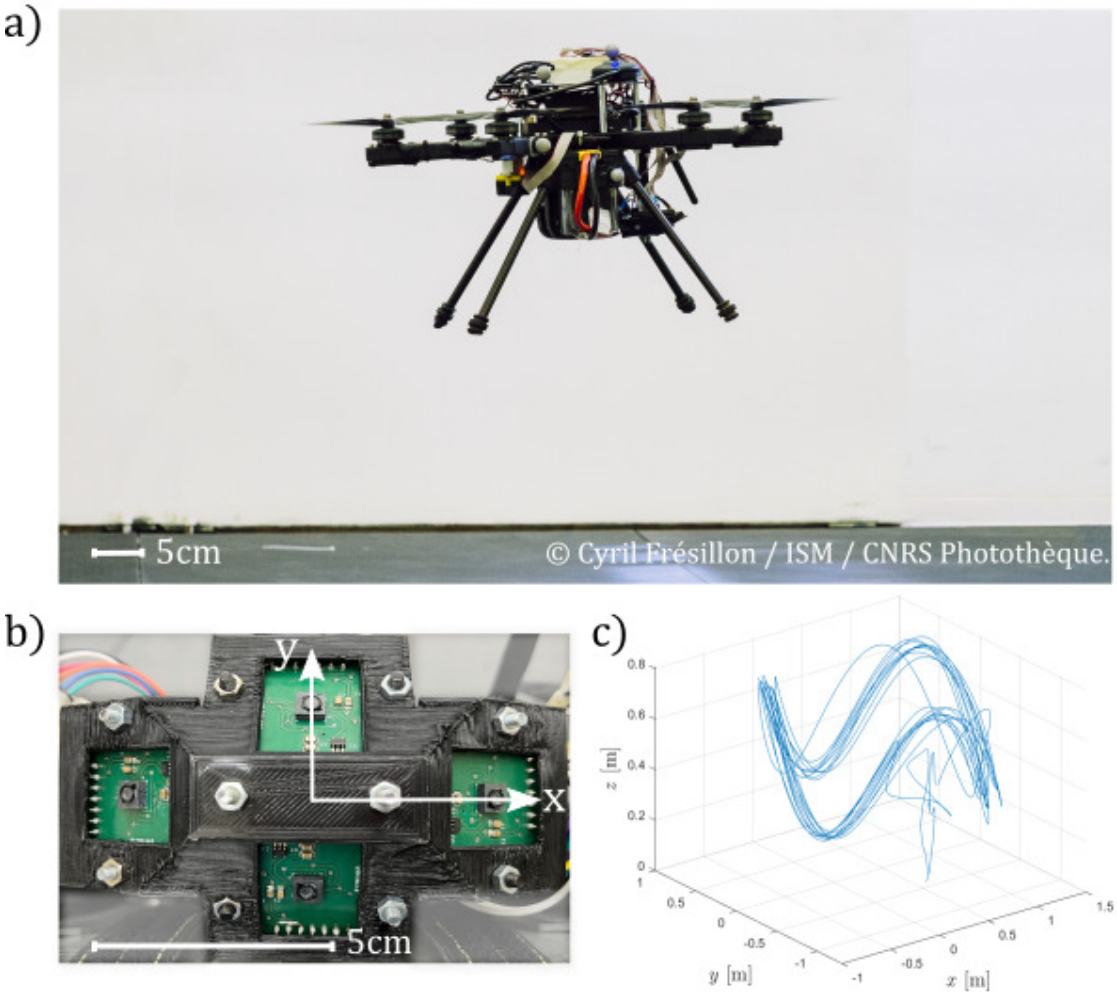

Figure 7.2: a) Hexarotor equipped with 4 optic flow sensors oriented towards the ground flying along a bouncing circular trajectory in the Mediterranean Flight Arena. b) 2 optic flow sensors were set along the longitudinal axis x at angles $\phi = \pm 30^o$ with respect to the hexarotor's vertical axis z, while the other 2 optic flow sensors were set along the lateral axis y at angles $\phi = \pm 30^o$ with respect to the axis z. c) Example of a flight test trajectory over a distance of $53m$ at an oscillation frequency of $0.28Hz$.

$2 \cdot \cos^2 \phi$ (see mathematical proof in Appendix 7.3.3):

$$\omega_T^{meas} = \frac{\omega(\phi) + \omega(-\phi)}{2 \cdot \cos^2 \phi} = \frac{V_x}{h} \tag{7.2}$$

In the case of a hexarotor equipped with 4 optic flow sensors as illustrated in Figure 7.2.b, three translational optic flow cues can be measured as follows:

- the sum of the two optic flow magnitudes perceived by the two optic flow sensors set along the longitudinal axis x, namely $\omega_{T_1}^{meas}$,
- the sum of the two optic flow magnitudes perceived on the x axis by the two optic flow sensors set along the lateral axis y, namely $\omega_{T_2}^{meas}$,
- the median value of the four optic flow magnitudes sensed along the hexarotor's longitudinal axis by the 4 optic flow sensors, scaled by a $1/\cos(\phi)$ factor, namely $\omega_{T_3}^{meas}$.

The series of contractions and expansions generated in the optic flow vector field by up-and-down oscillatory movements is known as the optic flow divergence. When a drone flies forward while oscillating up and down above the ground, the optic flow divergence is superimposed on the translational optic flow in the optic flow vector field. Due to the oscillatory movements, the state vector $X = [h, V_h]^T$ is locally observable [99]. The theoretical local optic flow divergence ω_{div}^{th} can be expressed as the ratio between the V_h component of the drone's velocity and h (see Figure 7.1):

$$\omega_{div}^{th} = \frac{V_h}{h} \tag{7.3}$$

We have previously proved mathematically that the local optic flow divergence can be measured on a micro-flyer as the difference between two optic flow magnitudes $\omega(\phi)$ and $\omega(-\phi)$ perceived by two optic flow sensors oriented at angles $\pm\phi$ with respect to the normal to a surface, divided by a known factor of $\sin 2\phi$ (see mathematical proof in Appendix 7.3.3) [20]:

$$\omega_{div}^{meas} = \frac{\omega(\phi) - \omega(-\phi)}{\sin 2\phi} = \frac{V_h}{h} \tag{7.4}$$

In the case of a hexarotor equipped with 4 optic flow sensors, two optic flow divergence cues can be measured as follows:

- the difference between the two optic flow magnitudes perceived by the two optic flow sensors set along the longitudinal axis x, namely $\omega_{div_x}^{meas}$,
- the difference between the two optic flow magnitudes perceived by the two optic flow sensors set along the lateral axis y, namely $\omega_{div_y}^{meas}$.

7.1.5 The SOFIa visual odometer method

A model for the honeybee's visual odometer called SOFIa (**S**elf-scaled **O**ptic **F**low time-based **I**integr**a**tion model) was tested in simulations [19]. The SOFIa model is based on the integration of the local translational optic flow ω_T scaled by the estimated distance with respect to the ground $\hat{h}$:

$$\hat{X}_{SOFIa} = \int \omega_T \cdot \hat{h} \, dt \tag{7.5}$$

$\hat{h}$ was estimated by means of an EKF. The use of an EKF was necessary due to the non-linearity of the local optic flow divergence, as the measurement depends on the ratio between the two states V_h and h (see equation (7.3)).

State space representation of the hexarotor along the vertical axis: The hexarotor's system was modeled in the form of a double integrator receiving as its input the acceleration a_z on the vertical axis z given by the drone's IMU. The hexarotor's state space representation can therefore be expressed as follows:

$$\begin{cases} \dot{X} = f(X, a_z) = A \cdot X + B \cdot a_z = \begin{bmatrix} 0 & 1 \\ 0 & 0 \end{bmatrix} \cdot X + \begin{bmatrix} 0 \\ 1 \end{bmatrix} \cdot a_z \\ Y = g(X) = [X(2)/X(1)] = V_h/h = \omega_{div} \end{cases} \tag{7.6}$$

where $X = \left[h, V_h\right]^T$ is the hexarotor's state vector.

7.1.6 Odometric method based on 2 optic flow sensors with No Prior Knowledge (NPK) of the optic flow variations

The local optic flow divergence ω_{div}^{2S} was measured by taking the difference between the two raw optic flow magnitudes perceived by the 2 optic flow sensors set along the x axis, while the local translational optic flow ω_T^{2S} was measured in the form of their sum. To estimate the flight height $\hat{h}$, the EKF received the following:

- input: the acceleration of the drone a_z,
- measurement: the local optic flow divergence ω_{div}^{2S}.

See Appendix 7.3.2 for the EKF calculations.
$\hat{h}$ was then used to scale the integration of the local translational optic flow ω_T^{2S} in order to perform the odometry. This odometric method based on 2 raw optic flow measurements does not require any prior knowledge about any parameters to assess the distance traveled.

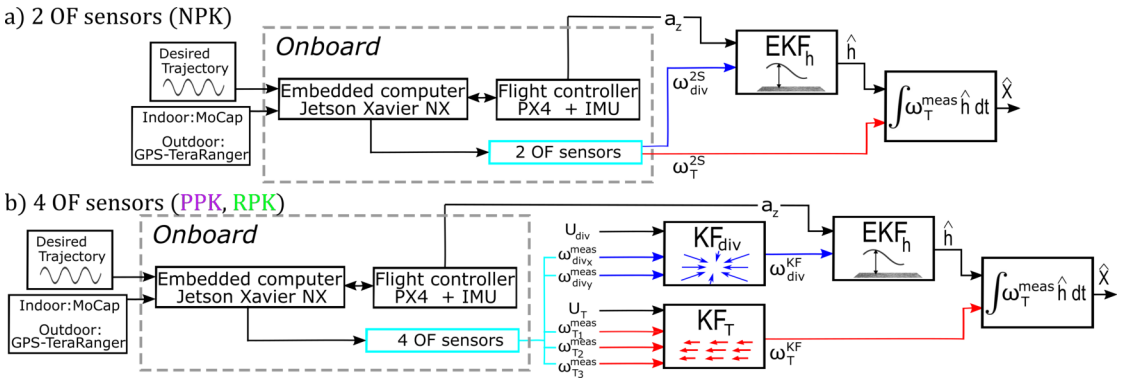

Figure 7.3: a) The sensor fusion based on 2 Optic Flow (OF) sensors is achieved using an Extended Kalman Filter (EKF). The embedded computer handles the outputs of the optic flow sensors set on the hexarotor, whose outputs are used to measure the local optic flow divergence ω_{div}^{2S} and the local translational optic flow ω_T^{2S}. The EKF receives as its input the hexarotor's acceleration a_z and as its measurement ω_{div}^{2S} to estimate the current flight height $\hat{h}$. The EKF output $\hat{h}$ scales ω_T^{2S}, which is then integrated in order to perform the odometry. b) The sensor fusion based on 4 optic flow sensors is achieved by inserting additional Kalman Filters (KF). $\omega_{div_x}^{meas}$ and $\omega_{div_y}^{meas}$ are taken as measurements by a KF (denoted KF_{div}) receiving as its input the current value U_{div} of the model for the optic flow divergence. The output of the KF is the local optic flow divergence ω_{div}^{KF}. $\omega_{T_1}^{meas}$, $\omega_{T_2}^{meas}$ and $\omega_{T_3}^{meas}$ are taken as measurements by a KF (denoted KF_T) receiving as its input the current value U_T of the model for the translational optic flow. The output of the KF is the local translational optic flow ω_T^{KF}. The EKF receives as its input the hexarotor's acceleration a_z and as its measurement ω_{div}^{KF} to estimate the current flight height $\hat{h}$. The EKF output $\hat{h}$ scales ω_T^{KF}, which is then integrated in order to perform the odometry.

7.1.7 Fusion strategies based on 4 optic flow sensors

7.1.7.1 Fusion strategy using Precise Prior Knowledge (PPK) of the optic flow variations

Here we investigated how to use prior knowledge about the self-oscillations to further improve the accuracy of the distance traveled estimates with 4 optic flow sensors. The optic flow divergence induced by the self-oscillation serving as an input to a Kalman Filter (KF) was expressed as follows (see Figure 7.4.a):

$$\omega_{div} = \frac{\dot{h}}{h} \longrightarrow U_{div}(k) = \frac{A_{osc} 2\pi f_{osc} \cos(2\pi f_{osc} k\delta t)}{h_0 + A_{osc} \sin(2\pi f_{osc} k\delta t)} \tag{7.7}$$

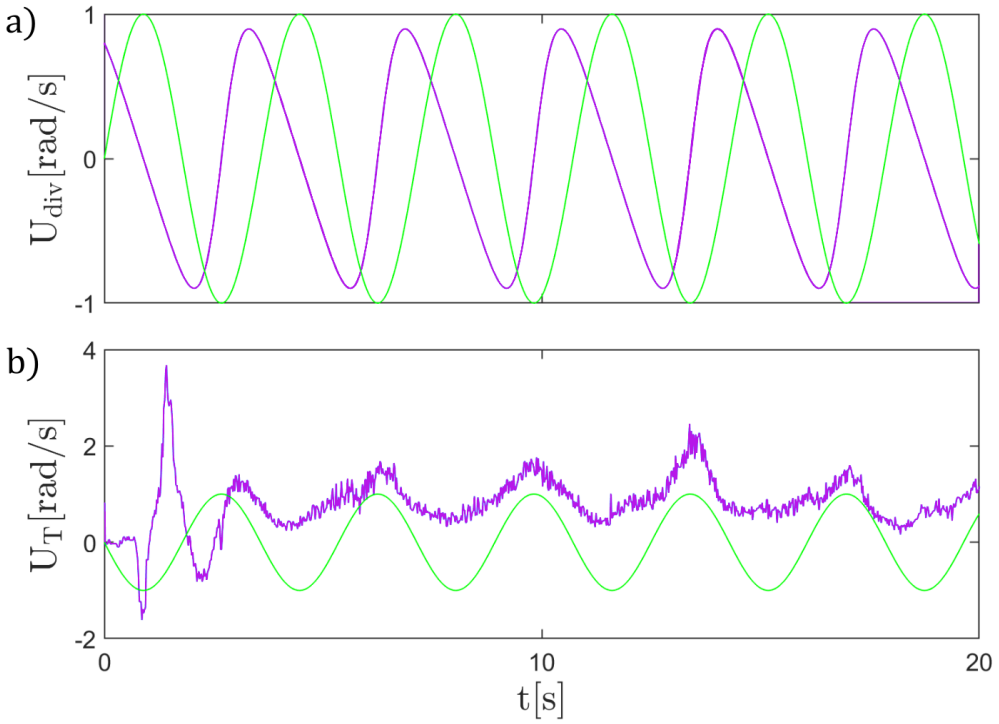

Figure 7.4: Inputs U_{div} (a) and U_T (b) to the Kalman Filters (KF) used to fuse optic flow divergence cues and translational optic flow cues with both the **P**recise **P**rior **K**nowledge (PPK) fusion strategy (in purple) and the **R**ough **P**rior **K**nowledge (RPK) fusion strategy (in green). In the RPK fusion strategy, a sinus helps the KFs to keep the timing of the oscillations and the shapes of the inputs in (a) and (b) are a rough approximation of the complex optic flow cues variations that are considered in the inputs of the PPK fusion strategy.

where f_{osc}, the oscillation frequency, was equal to $0.28Hz$, A_{osc}, the oscillation amplitude, was equal to $0.25m$, and h_0, the average flight height, was equal to $0.55m$. To fuse $\omega_{div_x}^{meas}$ and $\omega_{div_y}^{meas}$, a KF was used (see Figure 7.3). At each k^{th} step, the KF received as input the current value of the model in the equation (7.7) and as measurements $\omega_{div_x}^{meas}$ and $\omega_{div_y}^{meas}$. See Appendix 7.3.1 for the KF calculations.
The translational optic flow induced by the forward motion serving as the input to a KF was expressed as follows (see Figure 7.4.b):

$$\omega_T = \frac{V_x}{h} \longrightarrow U_T(k) = \frac{\omega_T^{KF}(k-1)\cdot\hat{h}(k-1)}{h_0 + A_{osc}\sin(2\pi f_{osc} k\delta t)} \tag{7.8}$$

$V_x(0) \approx \omega_T^{KF}(k=0)\cdot\hat{h}(k=0)$ was initialized at $0.45m/s$. To fuse the three translational optic flow cues $\omega_{T_1}^{meas}$, $\omega_{T_2}^{meas}$ and $\omega_{T_3}^{meas}$, a KF was used (see Figure 7.3). At each k^{th} step, the KF received as input the current value of the model in the equation (7.8) and

as measurements $\omega_{T_1}^{meas}$, $\omega_{T_2}^{meas}$ and $\omega_{T_3}^{meas}$. See Appendix 7.3.1 for the KF calculations.

7.1.7.2 Fusion strategy using Rough Prior Knowledge (RPK) of the optic flow variations

Here we investigated how to implement the sensor fusion strategy based on 4 optic flow sensors without any knowledge of the oscillation amplitude A_{osc} or the average flight height h_0, just using the information about the general shape and timing of the oscillations during the trajectory.
For this purpose, we approximated very roughly both the optic flow divergence and the translational optic flow cues in the form of a sinusoidal signal serving as the input to both KFs as follows (see Figure 7.4):

$$U_{div}(k) = -U_T(k) = \sin(2\pi f_{osc} k\delta t) \tag{7.9}$$

where the oscillation frequency f_{osc} was taken to be equal to $0.28Hz$. At each k^{th} step, the two KFs received as input the current value of the model in the equation (7.9) and as measurements the optic flow divergence measurements ($\omega_{div_x}^{meas}$ and $\omega_{div_y}^{meas}$) and the translational optic flow measurements ($\omega_{T_1}^{meas}$, $\omega_{T_2}^{meas}$ and $\omega_{T_3}^{meas}$), respectively. See Appendix 7.3.1 for the KF calculations.
By using as KF input $U_T(k) = -sin(2\pi f_{osc} k\delta t)$, the fusion strategy takes into account the fact that the variation of the translational optic flow is inversely proportional to the flight height h, since it depends only on the ratio V_x/h (see equation (7.1)). As shown in Figure 7.4, only a rough approximation of the actual shape and timing is taken into account.

7.1.7.3 Extended Kalman Filter in the fusion strategy with 4 optic flow sensors

To estimate the drone's flight height $\hat{h}$, the EKF used received the following:

- input: the acceleration of the drone a_z,
- measurement: the local optic flow divergence ω_{div}^{KF} filtered by the KF based on the optic flow divergence measurements.

See Appendix 7.3.2 for the EKF calculations.
$\hat{h}$ was used to scale the local translational optic flow ω_T^{KF} (filtered by the KF based on the translational optic flow measurements), which was then integrated to perform the odometry as follows:

$$\hat{X}_{SOFIa} = \int \omega_T^{KF} \cdot \hat{h}\, dt \tag{7.10}$$

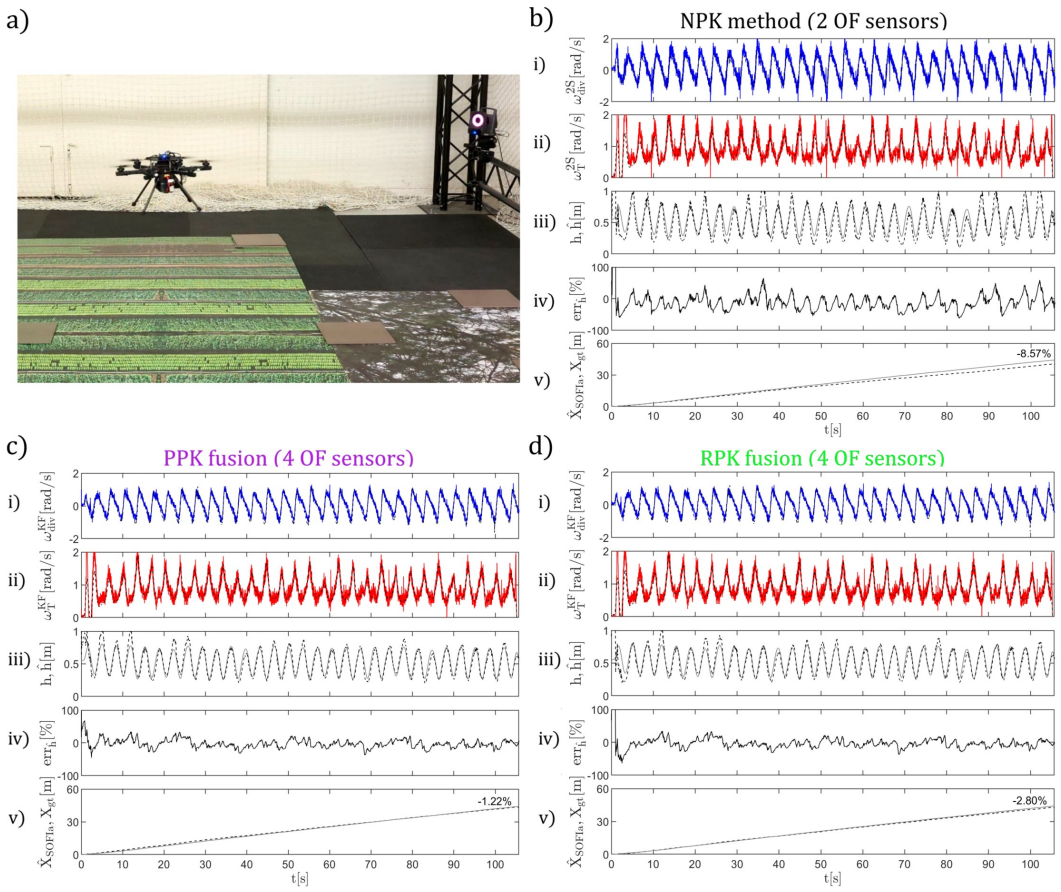

Figure 7.5: Hexarotor flying in the Mediterranean Flight Arena (a). The same dataset taken at $1518lux$ was processed with the **N**o **P**rior **K**nowledge (NPK) method (b), the **P**recise **P**rior **K**nowledge (PPK) strategy (c) and the **R**ough **P**rior **K**nowledge (RPK) strategy (d). The local Optic Flow (OF) divergence (in blue) measured with the NPK method had a Signal-to-noise Ratio (SnR) of $5.62dB$ (b.i), while with both the PPK and the RPK strategies the SnR was $6.72dB$ (c and d.i). The local translational optic flow (in red) measured with the NPK method had a SnR of $19.12dB$ (b.ii), $25.74dB$ with the PPK strategy (c.ii) and $25.9dB$ with the RPK strategy (d.ii). The flight height estimates $\hat{h}$ converged within $4s$ with the ground truth values h given by the MoCap system in all 3 cases (b, c and d.iii). The average percentage error of $\hat{h}$ with respect to h after convergence was -9.77% with the NPK method (range: $[-61.5\%, 65.34\%]$) (b.iv), -2.16% with the PPK strategy (range: $[-36.89\%, 34.13\%]$) (c.iv) and -2.55% with the RPK strategy (range: $[-36.88\%, 34.25\%]$) (d.iv). The final percentage error of the distance traveled estimates $\hat{X}_{SOFIa}$ with respect to the ground truth X_{gt} was -8.57% with the NPK method (b.v), -1.22% with the PPK strategy (c.v) and -2.80% with the RPK strategy (d.v).

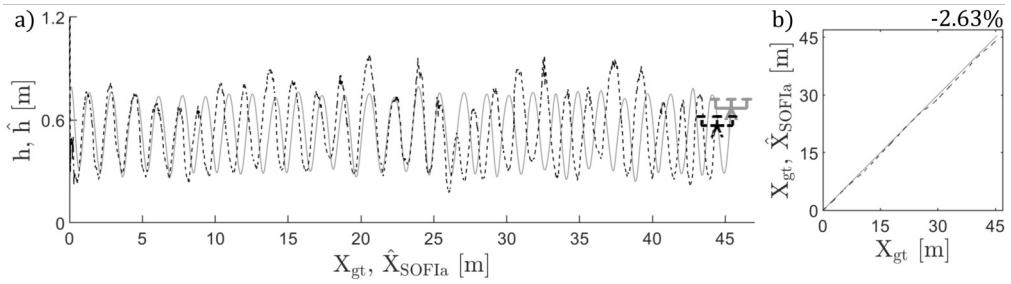

Figure 7.6: a) Comparison of the position of the hexarotor on the vertical plane (x,z) estimated with the **R**ough **P**rior **K**nowledge (RPK) fusion strategy (dashed line) with the ground truth given by the MoCap system (continuous line). The flight height estimates $\hat{h}$ were plotted on the distance traveled estimates $\hat{X}_{SOFIa}$, while the ground truth h was plotted on X_{gt}. This flight test was performed at an illuminance of $1518lux$. b) The final percentage error in the distance traveled estimates $\hat{X}_{SOFIa}$ with respect to the ground truth X_{gt} was -2.63%.

7.1.8 Indoor experimental flight tests

7.1.8.1 Indoor experimental setup

Indoor flight tests were performed in the Mediterranean Flight Arena (see Figure 7.5.a). The position and orientation used in the hexarotor's control system were taken from the motion-capture (MoCap) system installed in the flight arena, consisting of 17 motion-capture cameras covering a 6 × 8 × 4 m (lxLxH) volume using a VICON^{TM} system. Datasets including the optic flow measurements were recorded via the Robot Operating System (ROS) and processed with the Matlab/Simulink 2022 software.

7.1.8.2 Indoor experimental results

The sensor fusion strategies based on **P**recise **P**rior **K**nowledge (PPK) and **R**ough **P**rior **K**nowledge (RPK) of the optic flow variations (using 4 optic flow sensors) were compared with the strategy based on **N**o **P**rior **K**nowledge (NPK) of the optic flow variations (using 2 optic flow sensors). 7 bouncing circular flight tests over a distance of about $50m$ were performed with the hexarotor under an illuminance of $117lux$ ($5.36\cdot10^{-6}W/cm^2$) and an illuminance of $1518lux$ ($2.71\cdot10^{-4}W/cm^2$), amounting to a total number of 14 flight tests. First, the 14 datasets were processed with the NPK method (see Section (7.1.6)). The 14 datasets were then processed using the PPK strategy (see Section (7.1.7.1)) and the RPK strategy (see Section (7.1.7.2)). Supp. video n° 1[2] shows a synchronised video of the odometry results obtained with the RPK fusion strategy for the same flight test processed in Figure 7.5 and 7.6. The KF parameters discussed in Appendix 7.3.1 were defined experimentally as $\Phi = 10$, $\Gamma = 10$

[2]https://www.youtube.com/watch?v=qzCzenY5_xg

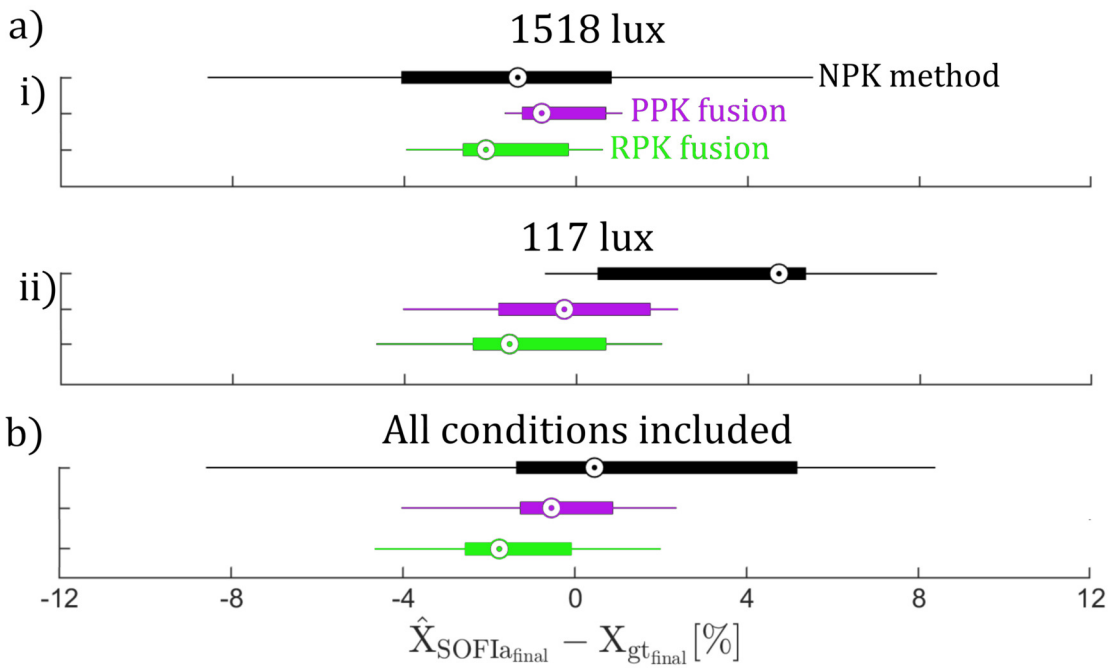

Figure 7.7: Distributions of the final percentage errors in the distance traveled estimates $\hat{X}_{SOFIa}$ with respect to the ground truth X_{gt} (traveled along the x axis) for 7 datasets recorded at $1518lux$ and 7 datasets recorded at $117lux$. a.i) At an illuminance of $1518lux$, the final percentage error ranged between -8.57% and 5.52% (with a median value of -1.14%) in the case of the **N**o **P**rior **K**nowledge (NPK) method (in black), between -1.65% and 1.08% (with a median value of -0.8%) in that of the **P**recise **P**rior **K**nowledge (PPK) strategy (in purple) and between -3.95% and 0.63% (with a median of -1.55%) in that of the **R**ough **P**rior **K**nowledge (RPK) strategy (in green). a.ii) At an illuminance of $117lux$, the final percentage error ranged between -0.72% and 8.4% (with a median value of 4.73%) with the NPK method, between -4.02% and 2.38% (with a median of -0.27%) with the PPK strategy and between $-4.65\%\%$ and 2% (with a median value of -1.14%) with the RPK strategy. b) Upon combining all 14 datasets recorded, the final percentage error ranged between -8.57% and 8.4% (median value: 0.47%) with the NPK method, between -4.02% and 2.38% (median value: -0.53%) with the PPK strategy and between -4.65% and 2% (median value: -1.34%) with the RPK strategy.

and $H_k = 10$, based on the first dataset recorded under an illuminance of $1518lux$ and used to process all 14 datasets for both PPK and RPK fusion strategies.
As shown in Figure 7.5, the optic flow measurements were processed with the three strategies (NPK, RPK and PPK), taking the same dataset recorded under an illuminance of $1518lux$. The increase in the Signal-to-noise Ratio (SnR, computed as the square ratio of the root mean square of the signal and the root mean square of its noise) for

the local optic flow divergence and the local translational optic flow in the case of the PPK and the RPK strategies in comparison with the NPK method affected the average percentage error of the flight height estimates after convergence (at $4s$). The average percentage error of the flight height estimates was -9.77% with the NPK method, -2.16% with the PPK strategy and -2.8% with the RPK strategy. Similar results were obtained with all 14 datasets. The SnR of the local translational optic flow measured with the NPK method ranged between $18.08dB$ and $24.79dB$, between $24.84dB$ and $29.93dB$ with the PPK strategy and between $24.84dB$ and $31.39dB$ with the RPK strategy. The SnR of the local optic flow divergence measured with the NPK method ranged between $5.41dB$ and $5.71dB$, and between $6.47dB$ and $7.11dB$ with both the PPK and RPK strategies.
The flight height estimates $\hat{h}$ and distance traveled estimates $\hat{X}_{SOFIa}$ were used to assess the position of the hexarotor on the vertical plane (x,z). An example is shown in Figure 7.6, where the flight height estimates $\hat{h}$ were plotted on the distance traveled estimates $\hat{X}_{SOFIa}$ (which are given directly in meters) and compared with the ground truth values given by the MoCap system. Since the 2D position estimates were based on the optic flow based odometry, they were subject to an accumulated error increasing with the distance covered.
Overall, the final percentage error in the distance traveled estimates $\hat{X}_{SOFIa}$ with respect to the ground truth X_{gt} (traveled along the x axis) ranged between -8.57% and 8.4% with the NPK method, between -4.02% and 2.38% with the PPK strategy and between -4.65% and 2% with the RPK strategy (see Figure 7.7.b). Similar results were obtained taking the two different illuminances separately (see Figure 7.7.a).

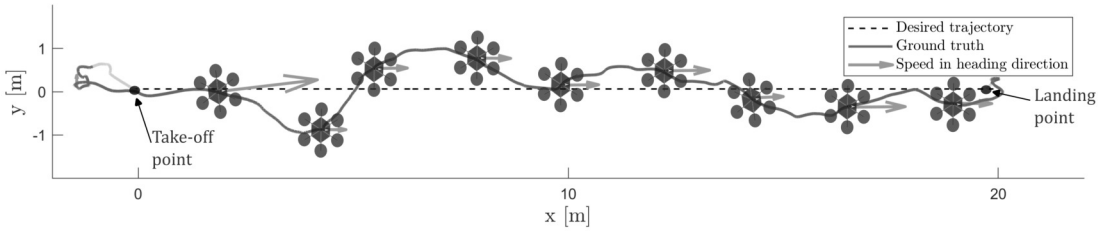

Figure 7.8: Top view of the drone's horizontal trajectory during an outdoor flight test (outdoor flight n°2). The drone was equipped with a TeraRanger Evo 3m distance sensor to measure the flight height and a Pixhawk GPS to measure its position on the horizontal plane (x, y). The take-off point of the flight was taken to be $[0,0]$. The optic flow based odometry is performed along the darker part of the trajectory.

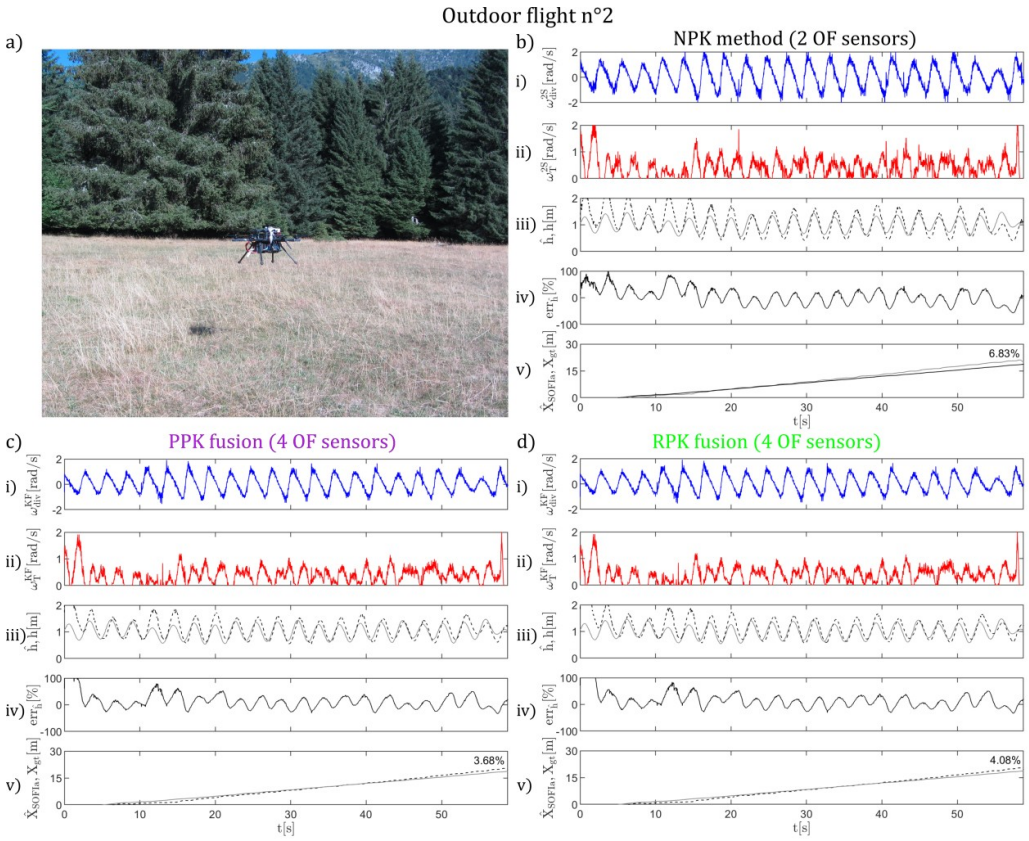

Figure 7.9: Hexarotor flying over a field irregularly covered with grass (outdoor flight n°2) (a). The same dataset recorded outdoors was processed with the **N**o **P**rior **K**nowledge (NPK) method (b), the **P**recise **P**rior **K**nowledge (PPK) strategy (c) and the **R**ough **P**rior **K**nowledge (RPK) strategy (d). The local Optic Flow (OF) divergence (in blue) measured had a Signal-to-noise Ratio (SnR) of $5.74dB$ with the NPK method (b.i), $6.15dB$ with the PPK strategy (c.i) and $6.14dB$ with the RPK strategy (d.i). The local translational optic flow (in red) measured had a SnR of $5.9dB$ with the NPK method (b.ii), $7.41dB$ with the PPK strategy (c.ii) and $7.4dB$ with the RPK strategy (d.ii). The flight height estimates $\hat{h}$ converged within $5s$ with the ground truth values h given by the distance sensor in all 3 cases (b, c and d.iii). The average percentage error of $\hat{h}$ with respect to h after convergence was 1.1% with the NPK method (range: $[-56.77\%, 85.65\%]$) (b.iv), 7.12% with the PPK strategy (range: $[-33.91\%, 79.94\%]$) (c.iv) and 7.19% with the RPK strategy (range: $[-33.91\%, 83.34\%]$) (d.iv). The distance traveled estimates $\hat{X}_{SOFIa}$ with respect to the ground truth X_{gt} were computed only after convergence. The final percentage error was 6.83% with the NPK method (b.v), 3.68% with the PPK strategy (c.v) and 4.08% with the RPK strategy (d.v).

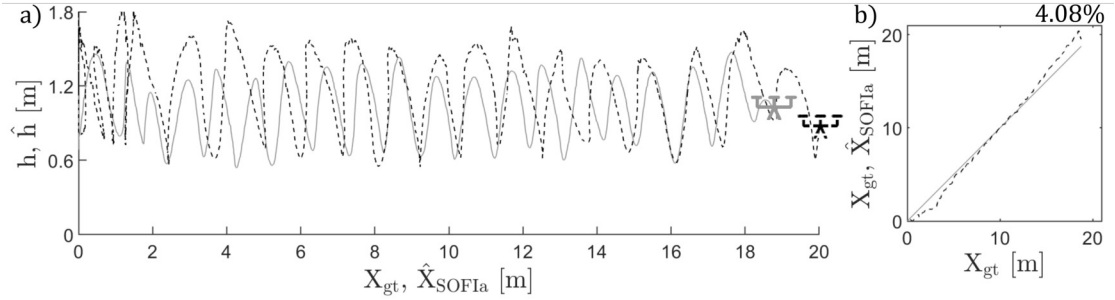

Figure 7.10: a) Comparison between the position of the hexarotor on the vertical plane (x,z) estimated with the **R**ough **P**rior **K**nowledge (RPK) fusion strategy (dashed line) and the ground truth values given by the distance sensor (continuous line) (outdoor flight n°2). The flight height estimates $\hat{h}$ were plotted on the distance traveled estimates $\hat{X}_{SOFIa}$, while h was plotted on X_{gt} (the ground truth values). b) The final percentage error in the distance traveled estimates $\hat{X}_{SOFIa}$ with respect to the ground truth values X_{gt} was 4.08%.

7.1.9 Preliminary outdoor experimental flight tests

7.1.9.1 Outdoor experimental setup

Outdoors, for trajectory tracking purposes, the hexarotor was equipped with a TeraRanger Evo 3m distance sensor in order to measure the flight height of the drone and with a Pixhawk GPS sensor (from Holybro) in order to measure the horizontal position. These 2 sensors were connected directly to the PX4 flight controller. In order to validate the precision of the TeraRanger Evo 3m distance sensor with the help of the MoCap system, a test was performed in the flight arena, in which we observed that TeraRanger Evo 3m was very reliable. This reliability was confirmed by the quality of the TeraRanger Evo 3m sensor's output, which was devoid of high frequency noise when measured on the field (see Section (2) of Supp. Information). According to the PX4 documentation, the standard deviation of the horizontal position error is 0.8 m using GPS outdoors. We observed that the hexarotor flying in the horizontal plane had a maximum deviation of about 1 m with respect to the desired trajectory (see Figure 7.8). Besides, the physical distance on the hexarotor of $5cm$ between the TeraRanger Evo 3m sensor and the optic flow sensors has been subtracted to the flight height estimates $\hat{h}$ to be compared to the ground truth h (measured by the TeraRanger Evo 3m sensor) in Figures 7.9, 7.10 and 7.11.
The outdoor experiments were performed using the same set of Pixart PAW3903 optic flow sensors, but adding a neutral density filter of 2 in front of the lenses to attenuate the solar luminosity. Without these filters, the optic flow sensors would have been saturated.

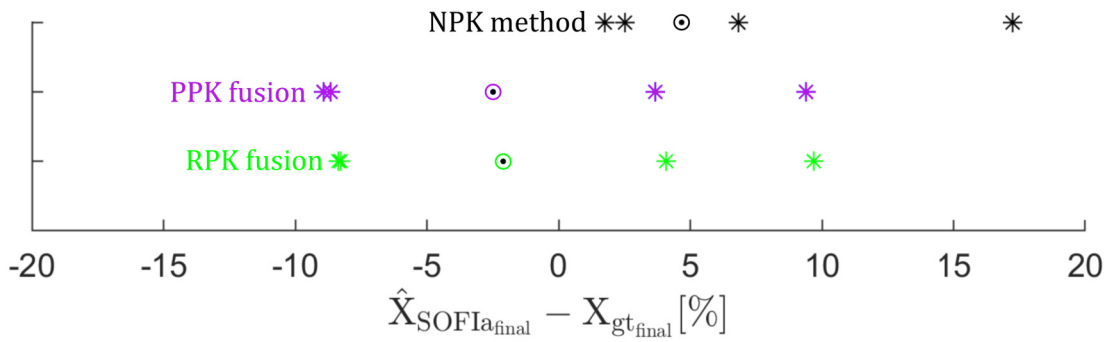

Figure 7.11: In the 4 datasets recorded outdoors, the final percentage error in the distance traveled estimates $\hat{X}_{SOFIa}$ with respect to the ground truth values X_{gt} ranged between 1.77% and 17.23% (median value: 4.67%) with the **No** **P**rior **K**nowledge (NPK) method (in black), between −8.92% and 9.4% (median value: −2.49%) with the **P**recise **P**rior **K**nowledge (PPK) strategy (in purple) and between −8.37% and 9.7% (median value: −2.1%) for **R**ough **P**rior **K**nowledge (RPK) (in green).

7.1.9.2 Results of preliminary outdoor experiments

4 bouncing longitudinal flight tests over a distance of about $20m$ were performed with the hexarotor outdoors over a field irregularly covered with grass (see Supp. video n° 2[3] and 3[4]). In Figure 7.9, the optic flow measurements of the outdoor flight number 2 were processed with the NPK method, the PPK strategy and the RPK strategy (see the odometry results obtained with the RPK fusion strategy in Supp. video n°2 for the outdoor flight number 2). The values of the KF parameters defined in Appendix 7.3.1 were those previously used in the indoor flight tests. As with the indoor flight tests, the SnRs of the local optic flow divergence and those of the local translational optic flow were greater with the PPK and RPK strategies than with the NPK method (see Section (1) of Supp. Information). Figure 7.10 gives the 2D position estimation on the vertical plane (x,z) for the outdoor flight number 2.
Due to the presence of wind disturbances and the greater convergence time required by the EKF in outdoor visual setting, the distance traveled $\hat{X}_{SOFIa}$ was estimated only after a convergence time of $5s$. Overall, the final percentage error in the distance traveled estimates $\hat{X}_{SOFIa}$ with respect to the ground truth values X_{gt} ranged between 1.77% and 17.23% with the NPK method, between −8.92% and 9.4% with the PPK strategy and between −8.37% and 9.7% with the RPK strategy (see Figure 7.11). As with the indoor flights (see Figure 7.7), Figure 7.11 shows comparable results between the PPK and the RPK fusion strategies. The RPK fusion strategy seems to be very interesting because it only uses knowledge of the timing and general shape of the translational and divergence optic flow cues. This knowledge can be considered reasonable since it is available onboard the UAV: it is in fact the drone itself that shapes

[3] https://www.youtube.com/watch?v=G9uT6Cj2Hs8
[4] https://www.youtube.com/watch?v=u88ZnfkUIVg

the optic flow cues by creating these oscillations.

7.1.10 Conclusion

In this section, we investigated how to use information about the oscillating trajectory to improve a minimalistic odometry based on optic flow cues. The experiments were performed onboard a hexarotor first indoors, following circular bouncing trajectories at a frequency of $0.28Hz$ over distances of about $50m$ under illuminances of $117lux$ and $1518lux$. The results were not affected by the illuminance conditions. A few tests were then performed outdoors, where the hexarotor followed bouncing longitudinal trajectories over a distance of about $20m$ over a field irregularly covered with grass in the presence of various wind conditions.
The findings obtained in this section show that the sensor fusion strategies based on the use of 4 optic flow sensors make it possible to measure the optic flow divergence and the translational optic flow cues more reliably thanks to the use of additional Kalman Filters. This was the case even when taking only rough prior knowledge about the optic flow variations into account, and more specifically, only the general shape and timing of the oscillations during the trajectory. This prior knowledge can be considered acceptable since the general shape and timing of the oscillations are imposed by the drone itself on its own forward trajectory. The sensor fusion strategies presented decreased the error in the flight height estimates, and thus decreased the percentage error in the distance traveled estimates in all the cases considered, improving the odometric performances. These considerations also applied in the case of the few outdoor flight tests performed in the presence of wind and an irregular pattern of grass.
With all three odometric processing methods, the final distance traveled estimates were admittedly subject to small errors as the odometric strategy is a dead reckoning method involving no feedback from the environment. Nevertheless, we show here that the SOFIa model can be accurate and precise enough to move in close proximity to a target without GPS, indoors and outdoors. Likewise, this highly minimalistic optic flow based odometric strategy could also be used to enable a future drone to assess whether it is returning near its base station without any need for a GPS. So far, the present findings can be said to constitute the first experimental proof-of-concept of the SOFIa model [19] before this optic flow based odometric strategy is implemented on a nanodrone requiring very little computational power [175]. We now intend to test the robustness of these strategies in a range of forward speeds, in cases where a large drone pitch occurs and in the presence of strong reliefs.
Future studies will also include the implementation of an optic flow regulator keeping the translational optic flow around a given setpoint.

7.1.11 Supplemental Information

7.1.11.1 Preliminary outdoor flight tests

Figure 7.12: Hexarotor flying over a field irregularly covered with grass.

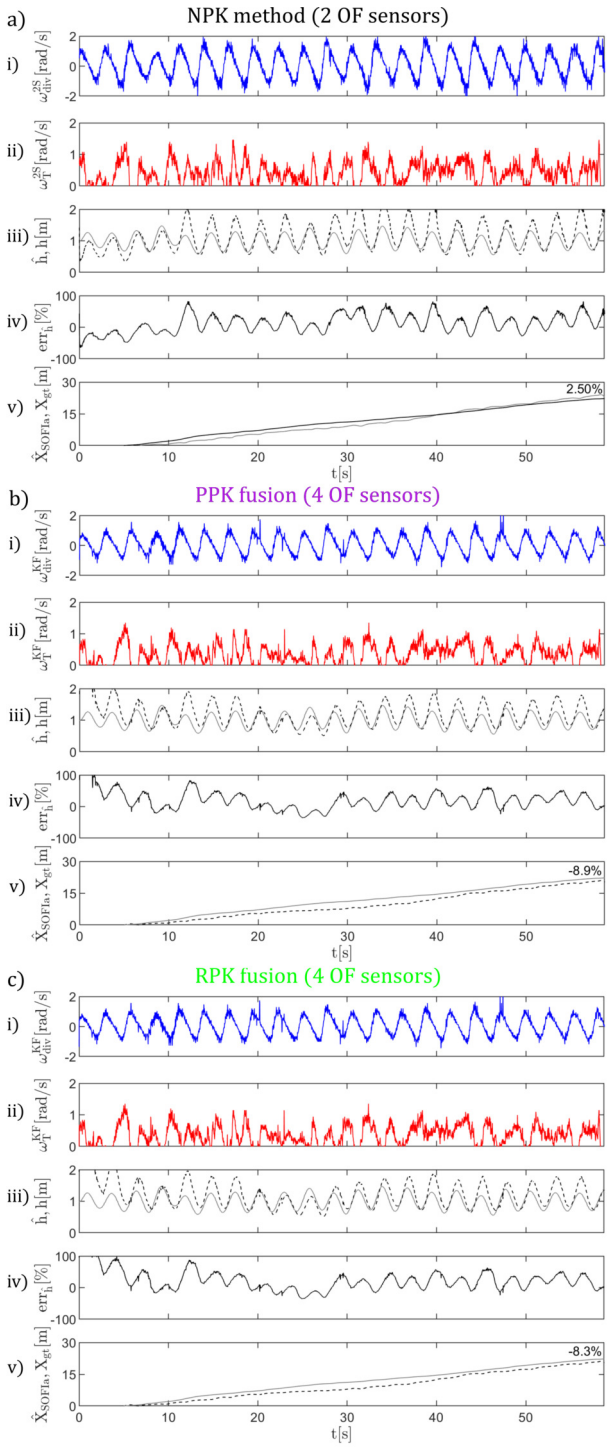

Figure 7.13: Outdoor flight test number 1 processed with the **N**o **P**rior **K**nowledge (NPK) method (a), the **P**recise **P**rior **K**nowledge (PPK) strategy (b) and the **R**ough **P**rior **K**nowledge (RPK) strategy (c).

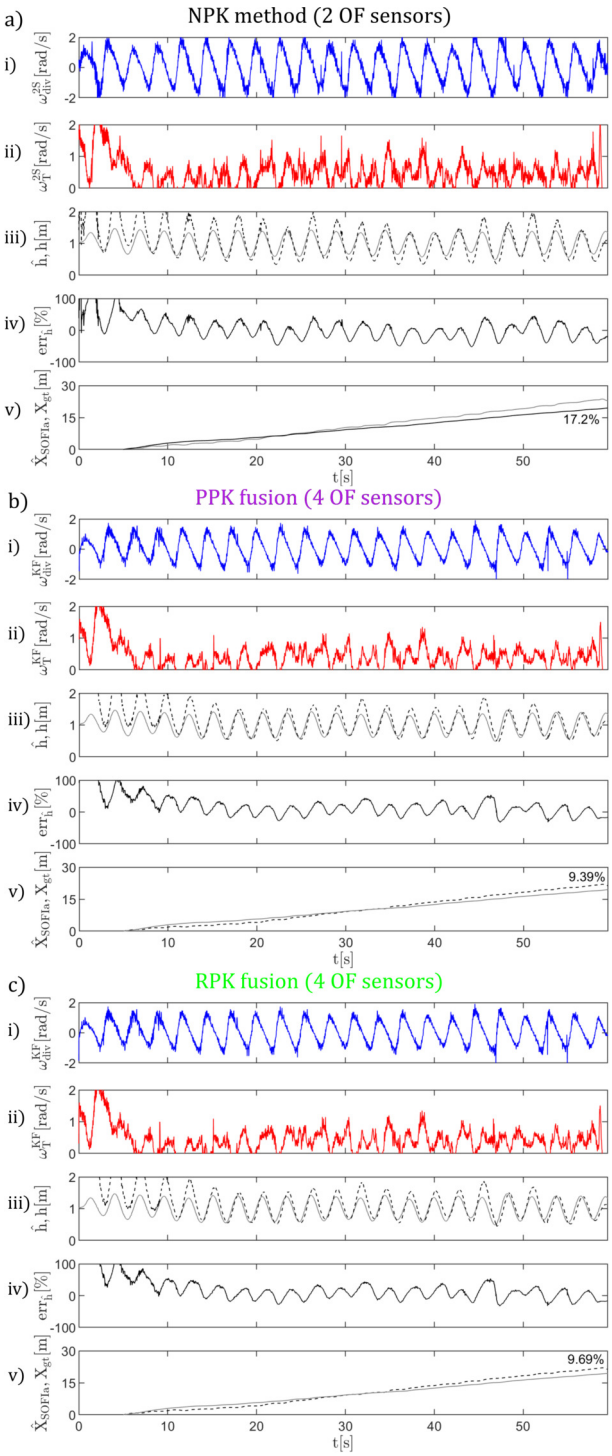

Figure 7.14: Outdoor flight test number 3 processed with the **N**o **P**rior **K**nowledge (NPK) method (a), the **P**recise **P**rior **K**nowledge (PPK) strategy (b) and the **R**ough **P**rior **K**nowledge (RPK) strategy (c).

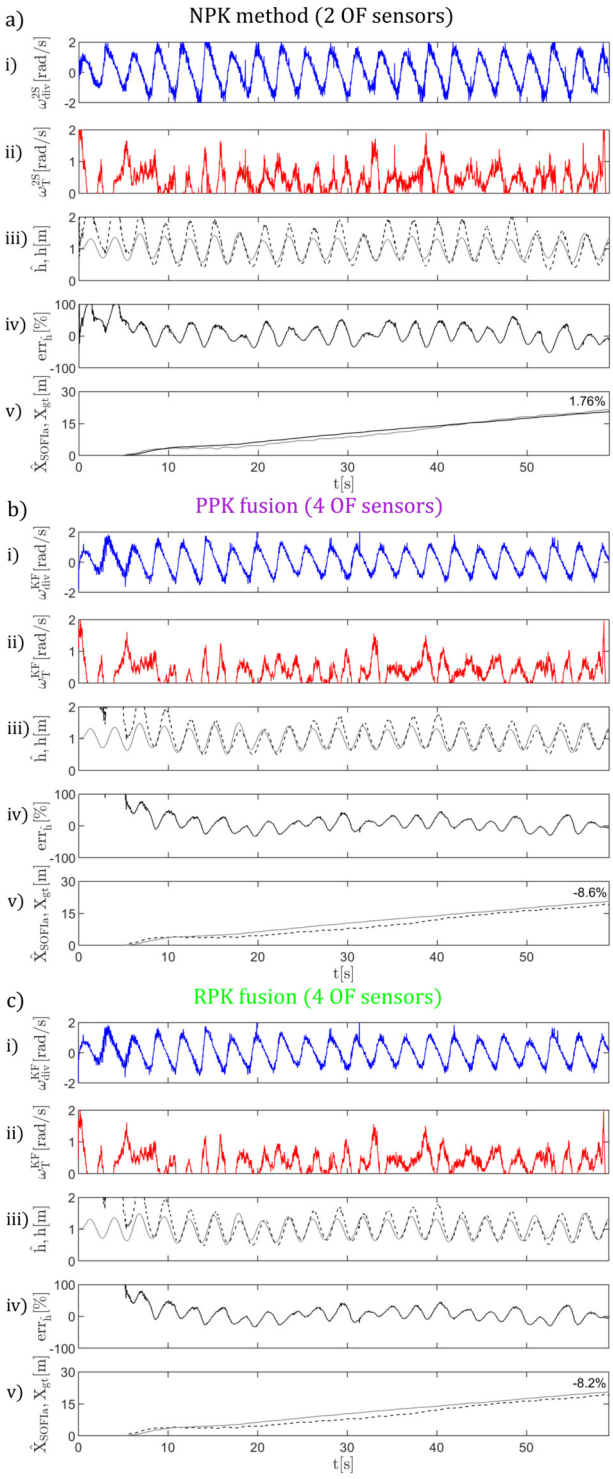

Figure 7.15: Outdoor flight test number 4 processed with the **N**o **P**rior **K**nowledge (NPK) method (a), the **P**recise **P**rior **K**nowledge (PPK) strategy (b) and the **R**ough **P**rior **K**nowledge (RPK) strategy (c).

Outdoor test n°1	SnR ω_T^{meas}	SnR ω_{div}^{meas}	% $\hat{h}-h$	% $\hat{X}_{SOFIa}-X_{gt}$
NPK	$6.04dB$	$5.84dB$	12.28%	2.5%
PPK	$7.13dB$	$5.83dB$	12.09%	−8.9%
RPK	$7.12dB$	$5.82dB$	11.9%	−8.3%
Outdoor test n°2				
NPK	$5.9dB$	$5.74dB$	1.1%	6.83%
PPK	$7.41dB$	$6.15dB$	7.12%	3.68%
RPK	$7.4dB$	$6.14dB$	7.19%	4.08%
Outdoor test n°3				
NPK	$7.67dB$	$5.77dB$	−0.06%	17.2%
PPK	$10.06dB$	$6.04dB$	9.18%	9.39%
RPK	$10.05dB$	$6.03dB$	8.76%	9.69%
Outdoor test n°4				
NPK	$5.42dB$	$5.81dB$	4.29%	1.76%
PPK	$6.72dB$	$6.1dB$	6.65%	−8.6%
RPK	$6.72dB$	$6.08dB$	6.34%	−8.2%

Table 7.2: Table showing the Signal-to-noise Ratio (SnR) of the local translational optic flow ω_T^{meas}, the SnR of the local optic flow divergence ω_{div}^{meas}, the average percentage error of the flight height estimates $\hat{h}$ with respect to the ground truth h and the final percentage error of the distance traveled estimates $\hat{X}_{SOFIa}$ with respect to the ground truth X_{gt} in the 4 flight tests performed outdoors.

7.1.11.2 Comparison between the flight height ground truth obtained using the MoCap Sytem and the TeraRanger Evo 3m distance sensor

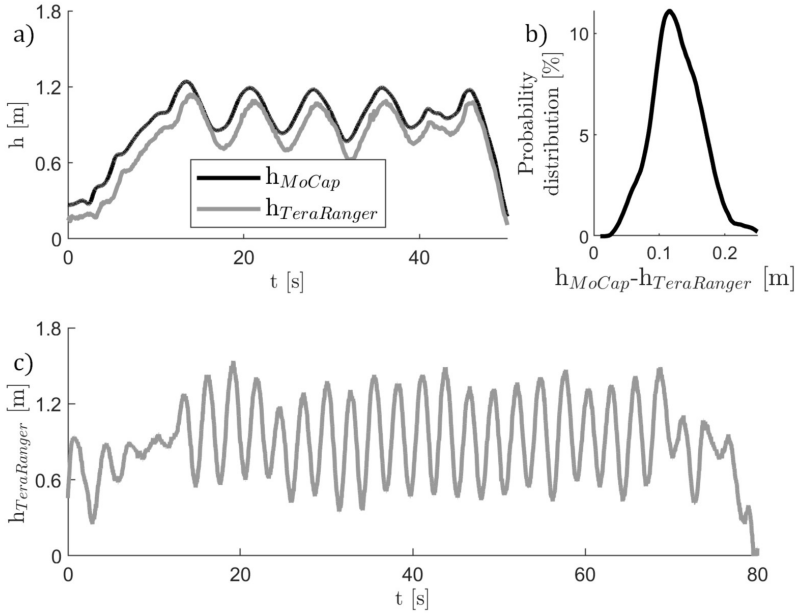

Figure 7.16: a) Comparison between the TeraRanger Evo 3m distance sensor's output and the MoCap system's output during the oscillatory trajectory. b) Distribution of the error between the flight height measured by the MoCap system and the distance sensor. A mean deviation of $11cm$ and a standard deviation of $3.7cm$ were observed. The offset of $11.1cm$ is due to the distance between the center of the "reflective markers set" used with the MoCap system and the position of the TeraRanger Evo 3m sensor. c) Flight height measured by the TeraRanger Evo 3m sensor during an oscillatory trajectory, while the hexarotor was flying over a field covered with an irregular pattern of grass. No pics can be observed on the raw TeraRanger Evo 3m sensor's output. Therefore, the TeraRanger Evo 3m sensor can be seen as precise and accurate and be considered as a reliable ground truth outdoors.

7.2 Supplemental indoor results

Published as part of:
L. Bergantin, C. Coquet, A. Negre, T. Raharijaona, N. Marchand, and F. Ruffier, "Minimalistic in-flight odometry based on two optic flow sensors along a bouncing trajectory," *2022 International Conference on Control, Automation and Systems (ICCAS). IEEE.*, p. 1321-1326, 2022

7.2.1 Computation of the optic flow cues by means of two optic flow magnitudes onboard a hexarotor

To show experimentally that the signals measured by means of equations (7.4) and (7.2) on the hexarotor were indeed respectively the divergence and the translational OF cues, 12 tests were performed at an oscillation frequency of $0.28Hz$ for each of the following illuminance conditions: $1518lux$ ($2.71\cdot10^{-4}W/cm^2$), $814lux$ ($2.15\cdot10^{-5}W/cm^2$) and $117lux$ ($5.36\cdot10^{-6}W/cm^2$). As shown in Figure 7.17.a, the values of the measured local OF divergence ω_{div}^{meas} of the 12 tests performed at $1518lux$ pooled together and of the corresponding theoretical local OF divergence ω_{div}^{th} (computed as in equation (7.3)) presented a linear relation, as did those of the measured local translational OF ω_T^{meas} and of the corresponding theoretical local translational OF ω_T^{th} (computed as in equation (7.1)). Similar results were obtained for the 12 tests performed at $117lux$ (see Figure 7.17.b). Thus, we can use equation (7.4) to measure the local OF divergence cue and equation (7.2) to measure the local translational OF cue reliably onboard the hexarotor.

7.2.2 Robustness of the visual odometry strategy based on two optic flow magnitudes to different trajectories

To analyse the robustness of the NPK visual odometry strategy presented to different trajectories, we performed 12 tests at an oscillation frequency of $0.25Hz$, 12 tests at an oscillation frequency of $0.28Hz$ and 12 tests at an oscillation frequency of $0.31Hz$ under an illuminance of $1518lux$ (see Figure 7.18). At an oscillation frequency of $0.25Hz$, the average percentage error of the estimates of $\hat{h}$ with respect to h ranged between -6.49% and 10.37%, with a median of -2.08%. Similarly, at an oscillation frequency of $0.31Hz$ the average percentage error ranged between -7.14% and 8.59%, with a median of 4.12%. At $0.25Hz$ the final percentage error of the odometry had a median of 0.96% (corresponding to about $0.48m$), while at $0.31Hz$ it had a median of 3.37% (corresponding to about $1.69m$). The performance of the method presented was similarly accurate for all three oscillation frequencies considered.

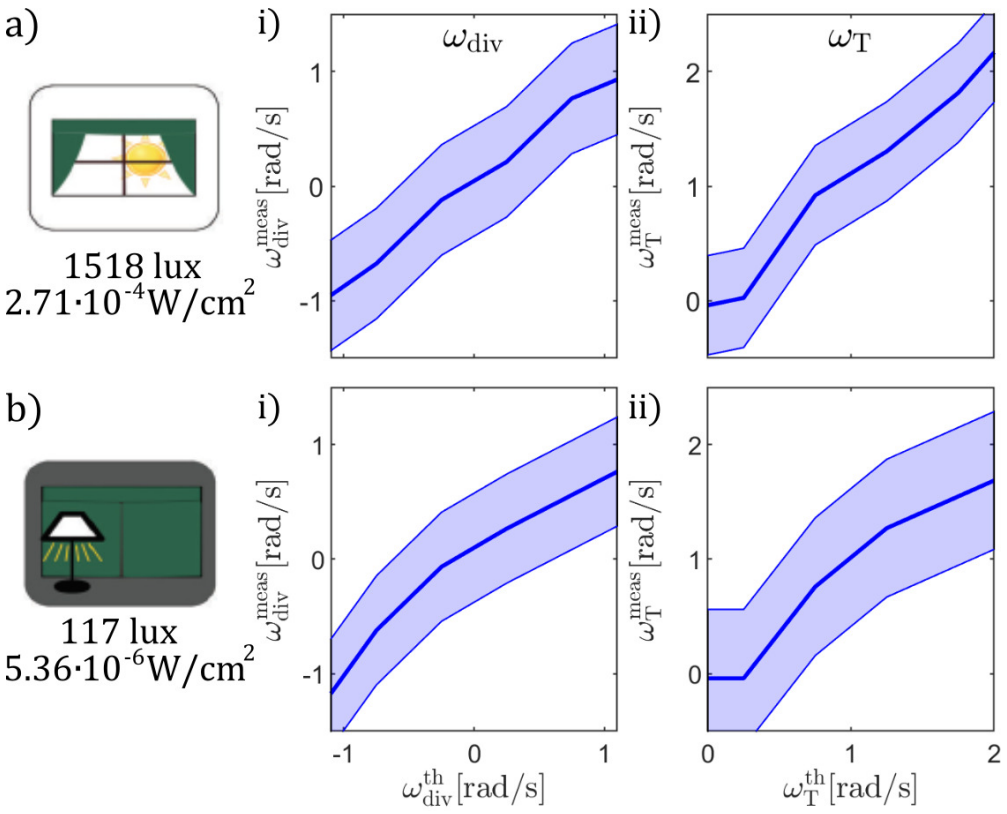

Figure 7.17: The plots show the characteristics of the measured Optic Flow (OF) cues with respect to their theoretical counterparts as perceived onboard the hexarotor oscillating vertically at $0.28Hz$. The median values and the curves representing the Median Average Deviation (MAD) of the OF cues are shown to display the range of values measured. At $1518lux$, the local OF divergence presented a MAD of $0.48rad/s$ (a.i), while the local translational OF presented a MAD of $0.43rad/s$ (a.ii). At $117lux$, the local OF divergence presented a MAD of $0.47rad/s$ (b.i), while the local translational OF presented a MAD of $0.6rad/s$ (b.ii). All plots show linear relations between the measured OF cues and the theoretical OF cues computed under the same illuminance conditions. Therefore, they can be considered as experimental counterparts of the mathematical proofs of equations (7.4) and (7.2) respectively.

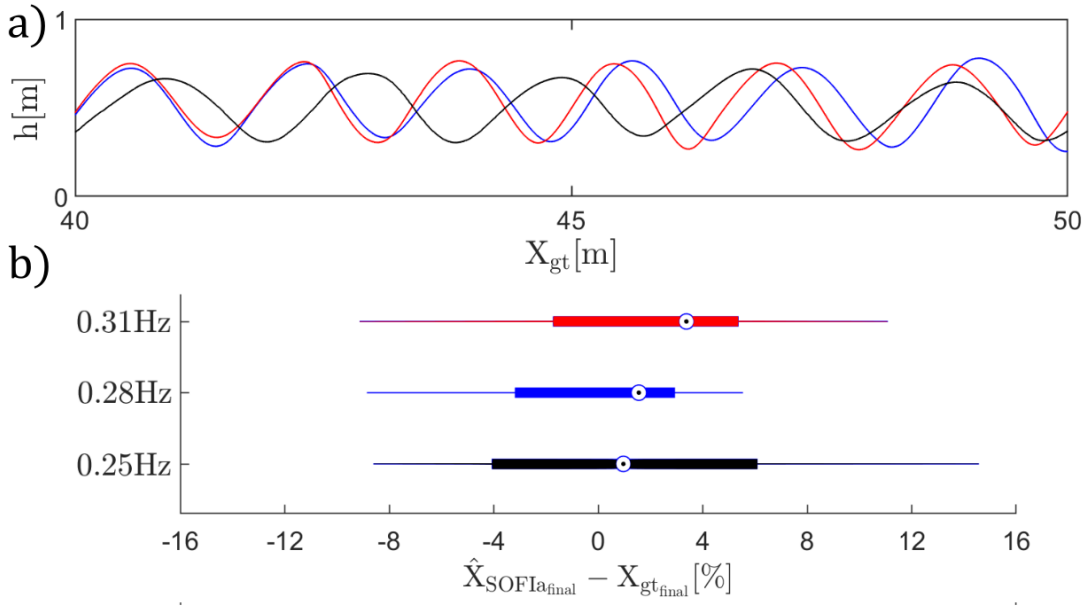

Figure 7.18: (a) Examples of test trajectories performed with oscillation frequencies of $0.25Hz$ (in black), $0.28Hz$ (in blue) and $0.31Hz$ (in red) at $1518lux$. (b) The error in the estimates of the distance traveled $\hat{X}_{SOFIa}$ with respect to the ground truth X_{gt} was expressed in %. For the 12 tests performed at $0.25Hz$ the final percentage error ranged between -8.61% and 14.58%, with a median of 0.96%. For the 12 tests performed at $0.28Hz$ the final percentage error ranged between -8.86% and 5.54%, with a median of 1.55%. For the 12 tests performed at $0.31Hz$ the final percentage error ranged between -9.13% and 11.09%, with a median of 3.37%.

7.3 Appendices

7.3.1 Appendix A: Kalman Filter calculations

In the PPK strategy, the optic flow divergence and the translational optic flow cues were expressed as in the equations (7.7) and (7.8), respectively. In the RPK strategy, the optic flow divergence and the translational optic flow cues were both expressed as in the equation (7.9). With each optic flow cue, at each k^{th} step, the current value of the corresponding model was computed and given to the corresponding KF as input (see Figure 7.3). In the following paragraph, the notation $A > 0$ indicates a strictly positive definite matrix. The KF took the following iterative steps at each k^{th} time:

Prediction step

(a) One-step ahead prediction

$$X_{k/k-1} = \Phi \cdot X_{k-1/k-1} + \Gamma \cdot U_{k-1/k-1} \tag{7.11}$$

with $\Phi > 0, \Gamma > 0$.

(b) Covariance matrix of the state prediction error vector

$$P_{k/k-1} = \Phi \cdot P_{k-1/k-1} \cdot \Phi^T + Q \tag{7.12}$$

Correction step

(c) Measurement update

$$X_{k/k} = X_{k/k-1} + K_k \cdot (Y_k^i - H_k \cdot X_{k/k-1}) \tag{7.13}$$

with Y_k^i current value of the i^{th} measurement, $H_k > 0$ and K_k Kalman gain defined as:

$$K_k = P_{k/k-1} \cdot H_k^T \cdot [H_k \cdot P_{k/k-1} \cdot H_k^T + R_k]^{-1} \tag{7.14}$$

The measurement update step was repeated for each i^{th} measurement (2 times for the optic flow divergence and 3 times for the translational optic flow).

(d) Covariance matrix of state estimation error vector

$$P_{k/k} = P_{k/k-1} + K_k \cdot [H_k \cdot P_{k/k-1} \cdot H_k^T + R_k] \cdot K_k^T \tag{7.15}$$

(e) Innovation

$$\tilde{Y}_k = Y_k - H_k \cdot X_{k/k} \tag{7.16}$$

7.3.2 Appendix B: Extended Kalman Filter calculations

The discretized model for the hexarotor along the vertical axis (see equation (7.6)) can be expressed as follows:

$$\begin{cases} X[k+1] = \Phi \cdot X[k] + \Gamma \cdot U[k] \\ Y[k] = C_k \cdot X[k] + D_k \cdot U[k] \end{cases} \tag{7.17}$$

with

$$\Phi = e^{A \cdot dt} \tag{7.18}$$

$$\Gamma = (\int_0^{dt} e^{A \cdot \tau} d\tau) \cdot B = (A^T \cdot e^{A \cdot dt} - A^T) \cdot B \tag{7.19}$$

$$C_k = g(X_k) = \left[\frac{X_2[k]}{X_1[k]} \right] = \left[\frac{V_h[k]}{h[k]} \right] \tag{7.20}$$

$$D_k = 0 \tag{7.21}$$

where dt is the discretization time. To estimate the flight height h, the EKF took the following iterative steps at each k^{th} time:

Prediction step

(a) One-step ahead prediction

$$X_{k/k-1} = \Phi \cdot X_{k-1/k-1} + \Gamma \cdot U_{k-1/k-1} \tag{7.22}$$

(b) Covariance matrix of the state prediction error vector

$$P_{k/k-1} = \Phi \cdot P_{k-1/k-1} \cdot \Phi^T + Q \tag{7.23}$$

Correction step

(c) Measurement update

$$X_{k/k} = X_{k/k-1} + K_k \cdot (Y_k - H_k \cdot X_{k/k-1}) \tag{7.24}$$

with K_k Kalman gain defined as:

$$K_k = P_{k/k-1} \cdot H_k^T \cdot [H_k \cdot P_{k/k-1} \cdot H_k^T + R_k]^{-1} \tag{7.25}$$

and H_k Jacobian matrix for the non linear function defined as follows:

$$H_k = \frac{\partial g}{\partial X}|_{X=X_{k/k-1}} = \begin{bmatrix} -\frac{V_h}{h^2} & \frac{1}{h} \end{bmatrix} \tag{7.26}$$

(d) Covariance matrix of state estimation error vector

$$P_{k/k} = P_{k/k-1} + K_k \cdot [H_k \cdot P_{k/k-1} \cdot H_k^T + R_k] \cdot K_k^T \tag{7.27}$$

(e) Innovation

$$\tilde{Y}_k = Y_k - H_k \cdot X_{k/k} \tag{7.28}$$

7.3.3 Appendix C: Computation of the local divergence and translational optic flow cues

The local optic flow divergence can be measured as the difference between two optic flow magnitudes $\omega(\phi)$ and $\omega(-\phi)$ perceived by two optic flow sensors oriented at angles $\pm\phi$ with respect to the normal to a surface, divided by a known factor of $\sin 2\phi$:

$$\omega_{div}^{meas} = \frac{\omega(\phi) - \omega(-\phi)}{\sin 2\phi} = \frac{V_h}{h} \tag{7.29}$$

The local translational optic flow can be measured as the sum of $\omega(\phi)$ and $\omega(-\phi)$, divided by a known factor of $2 \cdot \cos^2 \phi$:

$$\omega_{T}^{meas} = \frac{\omega(\phi) + \omega(-\phi)}{2 \cdot \cos^2 \phi} = \frac{V_x}{h} \tag{7.30}$$

Proof. We take a drone equipped with two optic flow sensors oriented toward the ground at angles ϕ and $-\phi$ with respect to its vertical axis. The optic flow magnitudes perceived by each optic flow sensor can be expressed as follows:

$$\omega(\phi) = \frac{\left\| \overrightarrow{V} \right\|}{D} \cdot \sin\widehat{\left(\vec{D}, \vec{V}\right)} = \frac{\left\| \overrightarrow{V} \right\|}{D} \cdot \sin(\frac{\pi}{2} - \phi + \alpha)$$

The two components of the velocity vector $\overrightarrow{V}$ of the drone flying above the ground can be expressed as follows:

$$V_x = \left\| \overrightarrow{V} \right\| \cdot \cos\alpha$$
$$V_h = \left\| \overrightarrow{V} \right\| \cdot \sin\alpha$$

with

$$\left\| \overrightarrow{V} \right\| = \sqrt{V_x^2 + V_h^2}$$

From which we obtain:

$$\cos\alpha = \frac{V_x}{\sqrt{V_x^2 + V_h^2}}$$
$$\sin\alpha = \frac{V_h}{\sqrt{V_x^2 + V_h^2}}$$

Thus

$$\begin{aligned}
\omega(\phi) &= \frac{\left\|\vec{V}\right\|}{D} \cdot \sin\widehat{\left(\vec{D},\vec{V}\right)} \\
&= \frac{\sqrt{V_x^2+V_h^2}}{D} \cdot \sin\left(\frac{\pi}{2}-\phi+\alpha\right) \\
&= \frac{\sqrt{V_x^2+V_h^2}}{D} \cdot \left(\sin\left(\frac{\pi}{2}-\phi\right)\cdot\cos\alpha+\cos\left(\frac{\pi}{2}-\phi\right)\cdot\sin\alpha\right) \\
&= \frac{V_x}{D}\cdot\sin\left(\frac{\pi}{2}-\phi\right)+\frac{V_h}{D}\cdot\cos\left(\frac{\pi}{2}-\phi\right) \\
&= \frac{V_x}{D}\cdot\sin\left(\frac{\pi}{2}-\phi\right)+\frac{V_h}{D}\cdot\sin\phi \\
&= \frac{\left\|\vec{V}_x\right\|}{D}\cdot\sin\widehat{\left(\vec{D},\vec{V}_x\right)}+\frac{\left\|\vec{V}_h\right\|}{D}\cdot\sin\widehat{\left(\vec{D},\vec{V}_h\right)}
\end{aligned}$$

We can then express the optic flow magnitudes $\omega\phi$ and $\omega(-\phi)$ perceived by the two optic flow sensors as follows:

$$\omega(\phi) = \frac{V_x}{D}\cdot\sin\left(\frac{\pi}{2}-\phi\right)+\frac{V_h}{D}\cdot\sin\phi \tag{7.31}$$

$$\omega(-\phi) = \frac{V_x}{D}\cdot\sin\left(\frac{\pi}{2}-\phi\right)-\frac{V_h}{D}\cdot\sin\phi \tag{7.32}$$

Subtracting equations (7.31) and (7.32), we obtain:

$$\omega(\phi)-\omega(-\phi) = 2\cdot\frac{V_h}{D}\cdot\sin\phi \tag{7.33}$$

Since $h = D\cdot cos\phi$ is the distance of the drone from the ground, equation (7.33) can be written as follows:

$$\omega(\phi)-\omega(-\phi) = 2\cdot\frac{V_h}{h}\cdot\sin\phi\cdot\cos\phi \tag{7.34}$$

Using the trigonometric formula $\sin\phi\cdot\cos\phi = \frac{1}{2}\cdot\sin(2\phi)$, we can rewrite equation (7.34) as follows:

$$\omega_{div}^{meas} = \frac{\omega(\phi)-\omega(-\phi)}{\sin(2\phi)} = \frac{V_h}{h}$$

Summing equations (7.31) and (7.32), we obtain:

$$\omega(\phi)+\omega(-\phi) = 2\cdot\frac{V_x}{h}\cdot\sin(\frac{\pi}{2}-\phi)\cdot\cos\phi \tag{7.35}$$

Using the trigonometric formula $\sin(\frac{\pi}{2}-\phi) = \cos\phi$, we can rewrite equation (7.35) as follows:

$$\omega_T^{meas} = \frac{\omega(\phi)+\omega(-\phi)}{2\cdot\cos^2\phi} = \frac{V_x}{h}$$

□

8 The SuRf model for the honeybee visual odometer

In previous chapters, the SOFIa visual odometer was tested on honeybees' trajectories in open field simulations and experimentally onboard a hexarotor equipped with optic flow sensors. Two sensor fusion strategies were developed with the aim of measuring local translation and divergence optic flow cues more accurately, in order to improve the odometric performance of the SOFIa method.
In this chapter, another solution is investigated to improve odometric performance in order to better rely on the surface below. The idea of reorienting the honeybees' compound eye so that the head pitch is on a level with the surface below was tested in open field simulations. This model for the honeybee visual odometer, called SuRf (Surface Reference based), is also based on the scaling of the translational optic flow, but in this case, the optic flow taken into account is always perceived perpendicularly to the surface below.
To test the SuRf visual odometer, the ventral region of the honeybees' compound eye was simulated by means of 9 downward-facing optic flow sensors at orientation angles between $20deg$ and $-20deg$. The head reorientation is based on the maximum optic flow perceived along this field-of-view. To ensure that the optic flow cues were measured perpendicularly to the surface below regardless of the presence of abrupt changes in the terrain slope, the pitch of the compound eye was adjusted to keep the head pitch on a level with the surface below. The SuRf visual odometer was tested on honeybees' trajectories in simulation over a $70m$-long open field with terrain slope irregularities, under a wide range of wind and terrain conditions.
The SuRf visual odometer proved to be more accurate than the SOFIa visual odometer tested under the same conditions. This tendency was particularly pronounced when considering flights in the absence of wind and under head wind conditions. In general, the lack of head reorientation led to an underestimation of the distance travelled in all cases considered. Therefore, the SuRf visual odometer is interesting for two main reasons, as it (i) takes into account the accuracy and the tendency to follow an optic flow pattern on a surface observed in honeybees and (ii) provides a more precise odometric approach for aerial robotic applications.

Table of contents

8.1 Head reorientation increases the reliability of a model for the honeybee odometer over uneven terrain

Article in preparation as:
L. Bergantin, X. Daïni, T. Raharijaona and F. Ruffier, "Head reorientation increases the reliability of a model for the honeybee odometer over uneven terrain"

8.2 Abstract

Foraging honeybees communicate to their nestmates information about the direction and distance to a food source from the hive during the waggle dance. Previous studies have suggested that the honeybees' odometer relies on the mathematical integration of the raw angular velocity of the image sweeping backwards across their ventral viewfield, which is known as the translational optic flow cue. Winged insects, such as honeybees and butterflies, oscillate up and down while flying forward. These self-oscillations enrich the ventral optic flow vector field by adding an expansion and contraction component: this is the optic flow divergence cue. To assess the distance to a food source from the hive, the current flight height might be estimated by means of the optic flow divergence cue to scale the translational optic flow before its integration over time. Honeybees have been observed adjusting altitude in vertical tunnels to follow the floor or roof depending on the release point of their training flights. In this study, we present a model for the honeybee visual odometer, called SuRf, which relies on head reorientation to improve optic flow based terrain-following behaviour and then optic flow based odometry. In this model, the honeybee head pitch is adjusted so that it is always oriented parallel to the surface below. Thus, the translational and divergence optic flow cues are perceived perpendicularly to the surface below. The SuRf model was tested in open field simulations in the presence of terrain slope irregularities, under a wide range of flight trajectories and wind conditions. The SuRf model has proved to be more reliable than the model without head pitch adjustment tested in simulation under the same conditions. The reliability of the SuRf model opens up possibilities for minimalistic aerial robotic applications taking place over irregular terrain.

8.3 Introduction

Flying insects (such as honeybees, flies and dragonflies) perceive the surrounding visual scene also thanks to the two compound eyes set on either side of their heads. Each compound eye is composed of units called ommatidia, that can be considered as bundles of photoreceptors providing a brightness estimate of a patch of the vi-

sual scene [104, 107]. During the waggle dance, foraging honeybees communicate information about the direction and distance to a food source from the hive to their nestmates [247]. Previous studies have suggested that to assess the distance travelled to a food source from the hive the honeybee odometer relies on visual cues [60, 58, 225, 224, 223], and more specifically on optic flow [61] (see also [40] for a review). The portion of the waggle dance dedicated to the communication of the distance travelled is called waggle run and consists of a straight stretch run by the forager while performing waggling body motions and buzzing noises [247]. The duration of the waggle run depends quite linearly on the distance travelled [60, 223] and in particular on the properties of the optic flow perceived during the flight to reach the food source (or outward flight) [223, 61, 238]. Optic flow has several properties, such as density (which depends on the visual contrast of the scene texture) and magnitude (which depends on both flight speed and height).

Previous studies have suggested that the honeybee visual odometer assess the distance travelled as the mathematical integration over time of the raw translational optic flow perceived across the ventral viewfield during the outward flight [58, 225, 224, 61, 238]. However, when tested in open field simulations in the presence of wind and ground irregularities, this raw integration of optic flow for the honeybee visual odometer does not account well for the accuracy observed in honeybees flying back to a food source [19]. In aerial robotic applications, translational optic flow has been used to visually control landing [192], follow uneven terrain [64] and attempt visual odometry and localisation [114, 119] (see [209] for review). The local translational optic flow was measured as the sum of two optic flow magnitudes perceived by two optic flow sensors onboard a small flying robot [16].

Honeybees have been observed oscillating while flying forward both in horizontal and vertical tunnels ([124] and [178], respectively). Up-and-down self-oscillations have also been reported for lepidopterans [257, 201, 174]. The up-and-down self-oscillatory movement generates a series of expansions and contractions in the ventral optic flow vector field, which is known as the optic flow divergence cue. The changes in vertical speed and flight height due to the self-oscillations make the two variables observable [99]. Instabilities due to oscillatory movements have been used to determine the flight height of a landing micro-flyer by exploiting the linear relationship between the oscillations and a fixed control gain [47]. Similarly, instabilities due to depth variation have been exploited to asses the scale factor of the observed scene to perform visual odometry onboard an underwater vehicle [46]. The local optic flow divergence was measured as the difference of two optic flow magnitudes perceived by two optic flow sensors oscillating back-and-forth in front of a moving panorama [20]. The measured local optic flow divergence was then used to estimate the distance of the optic flow sensors from the panorama by means of an Extended Kalman Filter (EKF). The optic flow divergence cue has been exploited to achieve visually controlled landing in small flying robots [98, 244, 47, 99].

A model for the honeybee visual odometer, called **SOFIa** (**S**elf-scaled **O**ptic **F**low time-based **I**ntegr**a**tion model), has been assessed in bio-plausible open field simulations [19]. The SOFIa model is based on the integration over time of the translational optic

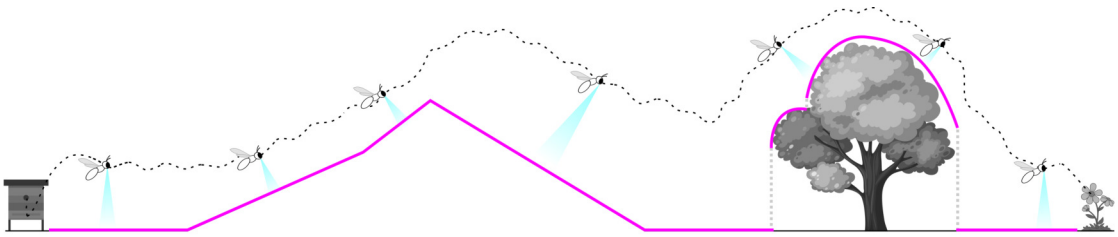

Figure 8.1: Example of outward flight to reach a food source from the hive in the presence of wind and terrain slope irregularities. In open field, honeybees oscillate up and down while flying forward. The head pitch is adjusted in order to keep its orientation parallel to the surface below (in purple).

flow scaled by the current flight height estimated by means of the optic flow divergence cue. When tested in simulation over uneven terrain in the presence of wind, the SOFIa model was 10 times more accurate than the raw integration over time of optic flow. The SOFIa visual odometer was tested onboard a hexarotor equipped with optic flow sensors performing 50m-long circular bouncing flights indoors [18] and 20m-long longitudinal bouncing flights outdoors [16].
Honeybees have been observed adjusting their altitude to follow the floor or the roof of a vertical tunnel according to the release point of their training flights [179]. These findings have led to the hypothesis that honeybees might follow an optic flow pattern previously memorized over a surface. It has been mathematically and experimentally demonstrated that adjusting the pitch of an artificial compound eye onboard a micro-flyer to keep the head pitch on a level with the surface below improves terrain following capabilities [64]. The Beerotor aerial robot successfully performed complex nap-of-the-earth maneuvers by adjusting its flight height in order to maintain the magnitude of the optic flow perceived by the ventral region of its reoriented compound eye constant [64].
In this study, we present a model for the honeybee visual odometer, called **SuRf** (**Su**rface **Ref**erence based model), that relies on optic flow cues perceived perpendicularly to the surface below. A honeybee-inspired controller is used to simulate honeybees' trajectories in open field in the presence of wind and terrain slope irregularities [177]. The ventral region of the honeybee compound eye is simulated by means of 9 optic flow sensors facing downward at orientation angles between $-20°$ and $20°$. To ensure that the optic flow cues are measured perpendicularly to the surface below regardless of the presence of terrain slope irregularities, the pitch of the simulated honeybee compound eye is adjusted in order to keep the head pitch on a level with the surface below (see Figure 8.1 and the video at this link [1]). To analyse the impact of such a reorientation strategy, the odometric performance of the SuRf model is then compared to that of the raw SOFIa model without head pitch adjustment in the presence of highly steep terrain.

[1] https://www.youtube.com/watch?v=AMb0IN36-G0

8.4 The optic flow cues

The translational optic flow cue is the pattern perceived by the honeybee compound eye on the ventral optic flow vector field due to the translational motion of the honeybee flying forward above a surface [85]. The theoretical local translational optic flow ω_T^{th} can be expressed downward as the ratio of the horizontal component V_x of the velocity of the simulated honeybee V and the flight height h:

$$\omega_T^{th} = \frac{V_x}{h} \tag{8.1}$$

Up-and-down self-oscillations generate a series of contractions and expansions on the ventral optic flow vector field, which can be quantified as the optic flow divergence cue. On the ventral optic flow vector field, the optic flow divergence is superimposed on the translational optic flow. Due to the oscillatory motion, both the vertical component V_h of the velocity of the simulated honeybee V and the flight height h are locally observable [99]. The theoretical local optic flow divergence ω_{div}^{th} can be expressed downward as the ratio of V_h and h:

$$\omega_{div}^{th} = \frac{V_h}{h} \tag{8.2}$$

Honeybees perform turns and saccades while flying forward. These rotational motions generate distortions on the ventral optic flow vector field, which can be quantified as the rotational optic flow cue. The rotational optic flow depends on the rotational speed of the compound eye and is superimposed on the ventral optic flow vector field on the translational and divergence optic flow. The theoretical local rotational optic flow ω_R^{th} can be expressed as the derivative over time of the pitch of the simulated honeybee compound eye θ_{eye}:

$$\omega_R^{th} = \frac{d(\theta_{eye})}{dt} \tag{8.3}$$

The rotational optic flow cue is positive when the velocity of the simulated honeybee V is negative, while it is negative when V is positive.

8.5 The Surface Reference based (SuRf) model

8.5.1 Simulation of the ventral region of the honeybee compound eye

The ventral region of the honeybee compound eye is simulated by means of 9 optic flow sensors facing downward at angles $\phi = [-20°; 20°]$ with respect to the normal of the compound eye, with a step of 5°. Each $i-th$ optic flow sensor is set at an

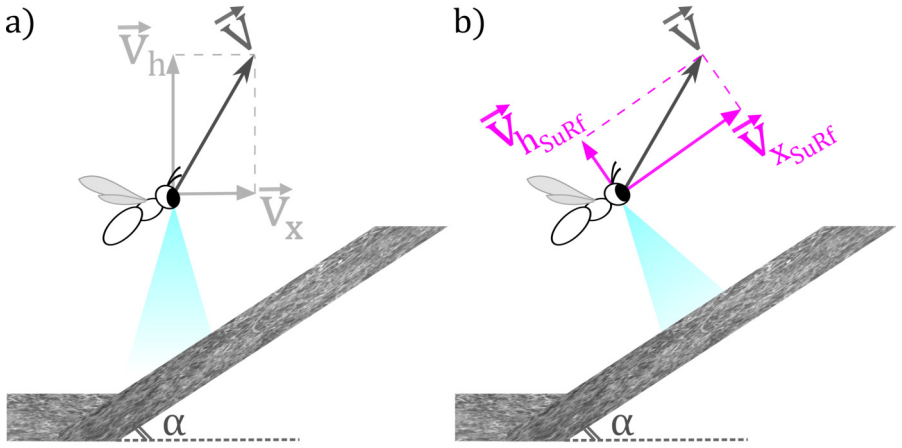

Figure 8.2: a) Inertial Reference (IR) frame with axis (x, z), in which the velocity of the simulated honeybee V can be decomposed as (V_x, V_h). b) Compound Eye Reference (CER) frame with axis (x_{SuRf}, z_{SuRf}), in which V can be decomposed as $(V_{x_{SuRf}}, V_{h_{SuRf}})$. The pitch of the simulated honeybee compound eye is adjusted in order to keep the head pitch on a level with the surface below while flying over a terrain irregularity of slope α. The CER frame is rotated of an angle $\theta_{eye/I}$ with respect to the IR frame.

orientation angle ϕ_i at a distance D_i from the surface below and thus measures an optic flow magnitude $\omega(\phi_i)^{meas}$:

$$\omega(\phi_i)^{meas} = \frac{\left\|\vec{V}\right\|}{D_i} \sin\left(\widehat{\vec{D}_i, \vec{V}}\right) \tag{8.4}$$

The optic flow sensors have a sampling frequency of $20Hz$ and are subject to a white noise of magnitude $1e^{-6} rad/s$.
We define two reference frames:

- an Inertial Reference (IR) frame with axis (x, z) (see Figure 8.2.a),
- a reference frame with origin in the centre of the compound eye with axis (x_{SuRf}, z_{SuRf}), referred to as Compound Eye Reference (CER) frame (see Figure 8.2.b).

V can be decomposed in the IR frame as (V_x, V_h) and in the CER frame as $(V_{x_{SuRf}}, V_{h_{SuRf}})$. When the simulated honeybee flies above a flat surface, the two reference frames coincide. When the simulated honeybee flies over a terrain irregularity of slope α, the pitch of the compound eye in the IR frame $\theta_{eye/I}$ is adjusted in order to keep the head pitch on a level with the surface below. Therefore, the CER frame is rotated of an angle $\theta_{eye/I}$ with respect to the IR frame. When the equator of the compound eye is parallel to the surface, $\theta_{eye/I} = \alpha$.

8.5.2 Measurement of the local optic flow cues

The local translational optic flow ω_T^{meas} is measured as the sum of the two optic flow magnitudes perceived by the two optic flow sensors set at $\phi = \pm 20°$, divided by a given factor $2 \cdot \cos^2 \phi$ [18]:

$$\omega_T^{meas} = \frac{\omega(\phi) + \omega(-\phi)}{2 \cdot \cos^2 \phi} \tag{8.5}$$

Similarly, the local optic flow divergence ω_{div}^{meas} is measured as the difference of the two optic flow magnitudes perceived by the two optic flow sensors set at $\phi = \pm 20°$, divided by a given factor $\sin 2\phi$ [20]:

$$\omega_{div}^{meas} = \frac{\omega(\phi) - \omega(-\phi)}{\sin 2\phi} \tag{8.6}$$

To measure the local rotational optic flow cue ω_R^{meas}, the pitch of the compound eye in the IR frame $\theta_{eye/I}$ is derived over time:

$$\omega_R^{meas} = \frac{d(\theta_{eye/I})}{dt} \tag{8.7}$$

If the rotational speed of the simulated honeybee $\frac{d(D_{0°})}{dt}$ (with $D_{0°}$ distance to the surface below of the optic flow sensor set at $\phi = 0°$) is negative, ω_R^{meas} is added to the optic flow magnitudes $\omega(\phi_i)^{meas}$ measured by the simulated honeybee compound eye. If the rotational speed is positive, ω_R^{meas} is subtracted.

8.5.3 Adjustment of the head pitch

If the equator of an artificial compound eye onboard a micro-flyer is kept parallel to a surface, the relationship between the orientation angles of the optic flow sensors mimicking the ommatidia and the perceived relative optic flows is a cosine-square function [64]. Thus, a least-squares regression method can be used to retrieve the angle between the slope of the surface below and the equator of the compound eye through the maximal value of the perceived relative optic flows .
To adjust the pitch of the simulated honeybee compound eye in the IR frame $\theta_{eye/I}$, we consider that the cosine square function can be approximated by a polynomial second order function using a Taylor expansion around zero. The optic flow magnitudes measured by the simulated honeybee compound eye are approximated as follows:

$$\omega(\phi_i)^{meas} \approx a \cdot (\phi)'^2 + b \cdot \phi' + c \tag{8.8}$$

We define $\Phi = [(\phi)'^2, \phi', 1]$ and Γ the vector of the optic flow magnitudes $\omega(\phi_i)^{meas}$ measured at a given time t_i. We can then compute the coefficients $[a, b, c]$ using the

least-squares regression method:

$$[a,b,c] = inv(\Phi \cdot \Phi') \cdot \Phi \cdot \Gamma' \tag{8.9}$$

The angular shift between the equator of the compound eye and the slope of the surface below can be estimated as:

$$\hat{\theta}_{eye/slope} = -\frac{b}{2 \cdot a} \tag{8.10}$$

To reduce noisy behaviour,, a confidence index I_{conf} is computed as:

$$I_{conf} = \frac{\sum |\Phi' \cdot [a,b,c] - \omega(\phi_i)^{meas}|}{median(\omega(\phi_i)^{meas})} \tag{8.11}$$

If at a given time t_i I_{conf} is higher than a given threshold, the estimate of $\hat{\theta}_{eye/slope}$ is discarded and its estimate at t_{i-1} is used instead.

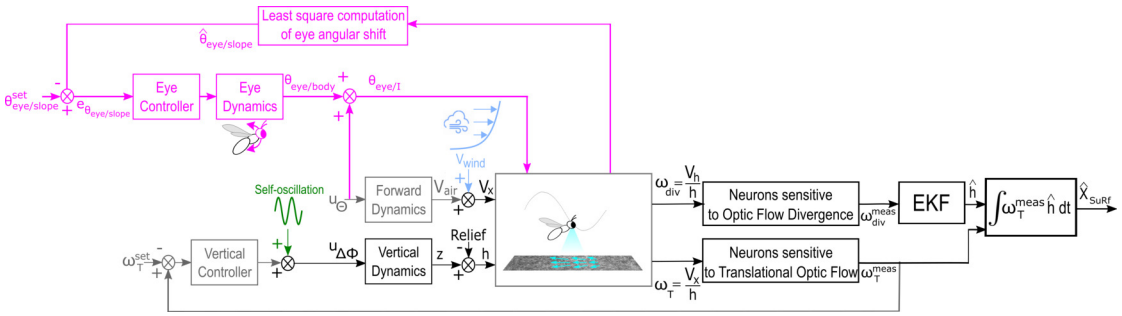

Figure 8.3: A vertical control feedback loop keeps the measured local translational optic flow ω_T^{meas} constant around a given setpoint ω_T^{set}. The self-oscillations (in blue) are added to the vertical controller output to compute the wing stroke amplitude $u_\Delta\Phi$, which feeds the vertical dynamics to obtain the flight height h. The forward dynamics are modelled by a transfer function between the body pitch of the simulated honeybee u_θ and the air speed V_{air}. The velocity of the wind V_{wind} (in orange) is added to the air speed V_{air}, obtaining the forward velocity V_x. The head pitch adjustment feedback loop (in purple) adjusted the pitch of the compound eye in the Inertial Reference (IR) frame $\theta_{eye/I}$ to keep the head pitch on a level with the surface below. The estimates of the angular shift $\hat{\theta}_{eye/slope}$ feed the compound eye dynamics to compute the pitch of the compound eye in the Compound Eye Reference (CER) frame $\theta_{eye/slope}$, to which the body pitch of the honeybee u_θ is added obtaining $\theta_{eye/I}$.

8.5.4 The honeybee-inspired autopilot

Honeybees' trajectories are simulated by means of a minimalistic honeybee-inspired autopilot [78]. The vertical and forward dynamics are modelled on simplified honeybees' flight dynamics [180] (see Section 8.7.1).
The autopilot includes a feedback loop for vertical control, where the measured local translational optic flow ω_T^{meas} is kept constant around a given setpoint ω_T^{set} (see Figure 8.3). The output of the vertical controller is perturbed by the self-oscillations simulated by a sinusoidal signal with a frequency of $2Hz$ and an amplitude of $40rad$. The vertical dynamics take the wing stroke amplitude of the simulated honeybee $u_{\Delta\Phi}$ as input to compute the flight height z, to which the surface relief is added to obtain the flight height h. The forward dynamics are modelled by a transfer function between the pitch of the simulated honeybee u_θ and the air speed V_{air}, to which the velocity of the wind V_{wind} is added to obtain the forward velocity V_x.
A head pitch adjustment feedback loop keeps the head pitch on a level with the surface below (in purple in Figure 8.3). The pitch of the compound eye in the IR frame $\theta_{eye/I}$ is derived over time to measure the local rotational optic flow ω_R^{meas}, which is either added or subtracted to the measurements of the simulated honeybee compound eye according to the sign of the rotational speed. The outputs obtained are used to estimate the angular shift $\hat{\theta}_{eye/slope}$, that feeds the eye controller and then the eye dynamics to compute the pitch in the CER frame $\theta_{eye/slope}$. The body pitch of the simulated honeybee u_θ is added to $\theta_{eye/slope}$ to compute $\theta_{eye/I}$.

8.5.5 The SuRf model for the honeybee visual odometer

The SuRf model for the honeybee visual odometer is based on the integration over time of the local translational optic flow ω_T^{meas} measured as in equation (8.5) scaled by the estimated current flight height $\hat{h}$:

$$\hat{X}_{SuRf} = \int \omega_T^{meas} \cdot \hat{h} \, dt \tag{8.12}$$

$\hat{h}$ is estimated by means of an EKF that receives as:

- input: the wing stroke amplitude of the simulated honeybee $u_{\Delta\Phi}$,
- measurement: the local optic flow divergence ω_{div}^{meas} measured as in equation (8.6).

The use of the EKF is necessary due to the non-linearity of the optic flow divergence (see equation (8.2)). See Appendix 8.10.1 for the EKF calculations.
The estimates of the distance travelled $\hat{X}_{SuRf}$ are compared to the ground truth $X_{surface}$ given by the perimeter of the surface followed.

8.6 The raw SOFIa model

For the raw SOFIa model, a compound eye consisting of one optic flow sensor facing downward at $\phi = 0°$ is simulated. The optic flow sensor has a sampling frequency of $20Hz$ and is subject to a white noise of magnitude $1e^{-6} rad/s$.
The local translational optic flow ω_T^{meas} is measured as the perceived optic flow magnitude:

$$\omega_T^{meas} = \omega(\phi) \tag{8.13}$$

The local optic flow divergence ω_{div}^{meas} is measured as the ratio of V_h and the distance of the optic flow sensor to the surface below $D_{0°}$:

$$\omega_{div}^{meas} = \frac{V_h}{D_{0°}} \tag{8.14}$$

The autopilot used to simulate the honeybees' trajectories does not include the pitch adjustment feedback loop.
The raw SOFIa model is based on the integration over time of the local translational optic flow ω_T^{meas} measured as in equation (8.13) scaled by the estimated current flight height $\hat{h}$:

$$\hat{X}_{SOFIa} = \int \omega_T^{meas} \cdot \hat{h}\, dt \tag{8.15}$$

To estimate the flight height $\hat{h}$, an EKF receives as:

- input: the wing stroke amplitude of the simulated honeybee $u_{\Delta\Phi}$,
- measurement: the local optic flow divergence ω_{div}^{meas} measured as in equation (8.14).

See Appendix 8.10.1 for the EKF calculations.
The estimates of the distance travelled $\hat{X}_{SOFIa}$ are compared to the ground truth X_{gt} given by the nominal distance flown (in this study: $70m$).

8.7 Materials and Methods

8.7.1 Honeybees' vertical dynamics

The honeybees' vertical dynamics were expressed in [180] as follows:

$$G_{Vz}(s) = \frac{V_z(s)}{u_{\Delta\Phi}(s)} = \frac{K_z}{1 + \tau_z s} \tag{8.16}$$

where $u_{\Delta\Phi}$ [deg] is the difference in the simulated honeybee wing stroke amplitude in comparison with hovering, $V_z\,[m/sec]$ is the vertical speed, $\tau_z = 0.22[sec]$ is the heave time constant and $K_z = 0.11$ is a gain. See Appendix 8.10.2 for the observability

analysis.
The honeybees' forward dynamics were expressed as follows:

$$G_{V_{air}}(s) = \frac{V_{air}(s)}{u_\theta(s)} = \frac{K_{surge}}{1+\tau_{surge}s} \tag{8.17}$$

where u_θ [deg] is the honeybee pitch during hovering, V_{air} $[m/sec]$ is the air speed, $\tau_{surge} = 0.22[sec]$ is the surge time constant and $K_{surge} = 0.10$ is a gain.

8.7.2 Wind modelling

A logarithmic law was used to model the wind profile along the altitude [240] as follows:

$$v_{wind} = k_{wind} \cdot v_0 \ln \frac{h}{h_0} \tag{8.18}$$

with the reciprocal of the Von Kármán constant $v_0 = 0.2m/s$, the current height h and the roughness height $h_0 = 0.05m$.

8.7.3 Computer simulations

The SuRf and raw SOFIa models for the honeybee visual odometer were both simulated using MATLAB/Simulink 2020 software.

8.8 Results

To test the SuRf model, honeybees' trajectories were simulated over a $70m$-long open field in the presence of wind and terrain slope irregularities. The simulation included a $5m$-tall hill: one hillside had an initial slope α of 15° changing halfway trough to 25° and the other had a constant slope of 20°. Figure 8.4 shows an example of round-trip flight. During the outward flight, the simulated honeybee tackled the hillside with the varying slope first and was subject to tail wind. During the return flight, the simulated honeybee tackled the hillside with the constant slope first and was subject to head wind. In both cases, the pitch of the simulated honeybee compound eye in the IR frame $\theta_{eye/I}$ converged quickly (within $2.5s$) to the ground truth given by the slope of the surface below. The percentage error of the estimates of the flight height $\hat{h}$ with respect to the ground truth h ranged between −47.33% and 24.59% after convergence (with an average value of −13.57%) for the outward flight and between −30.43% and 15.91% after convergence (with an average value of −3.51%) for the return flight. The final percentage error of the estimates of the distance travelled $\hat{X}_{SuRf}$ with respect to the ground truth $X_{surface}$ was −7.41% for the outward flight and 1.13% for the return flight.

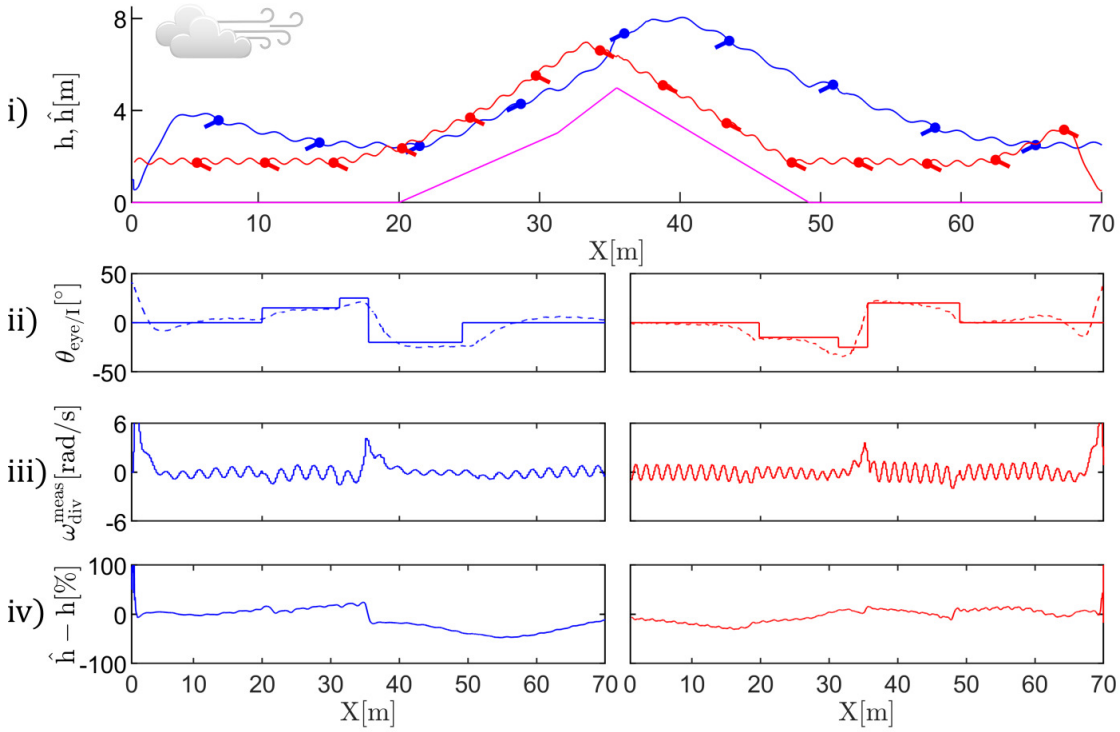

Figure 8.4: Example of round-trip flight simulated to test the Surface Reference based (SuRf) model (with $\omega_T^{set} = 2rad/s$, $u_\theta = 40°$ and a wind coefficient $k_{wind} = 1$). i) Due to the direction of the wind, the outward flight was subject to tail wind (blue) and the return flight was subject to head wind (red). ii) The pitch of the compound eye in the Inertial Reference (IR) frame $\theta_{eye/I}$ (dashed line) converged within $2.5s$ to the ground truth given by the slope of the surface below (continuous line). iii) The percentage error of the estimates of $\hat{h}$ with respect to h had an average value after convergence of -13.57% for the outward flight and of -3.51% for the return flight.

Figure 8.5 shows examples of outward flights simulated to test the SuRf and raw SOFIa models, respectively. The local optic flow divergence ω_{div}^{meas} measured with the SuRf model presented less abrupt changes in correspondence to terrain slope irregularities. In particular, the value of ω_{div}^{meas} in correspondence to the hill top was $3.79rad/s$ for the SuRf model and $5.55rad/s$ for the raw SOFIa model. The percentage error of the estimates of $\hat{h}$ with respect to h after convergence ranged between -31.05% and 16.13% (with an average of -2.78%) for the SuRf model, while it ranged between -11.01% and 45.05% (with an average value of 20.52%) for the raw SOFIa model. Since the SuRf and raw SOFIa models refer to different ground truths, the percentage errors of the estimates of the distance travelled ($\hat{X}_{SuRf}$ for SuRf, $\hat{X}_{SOFIa}$ for raw SOFIa) with respect to the ground truth ($X_{surface}$ for SuRf, X_{gt} for raw SOFIa) were computed in order to compare the odometric performance of the two visual odometers. The final percentage error of the odometry was 5.22% for the SuRf model and -14.03% for the

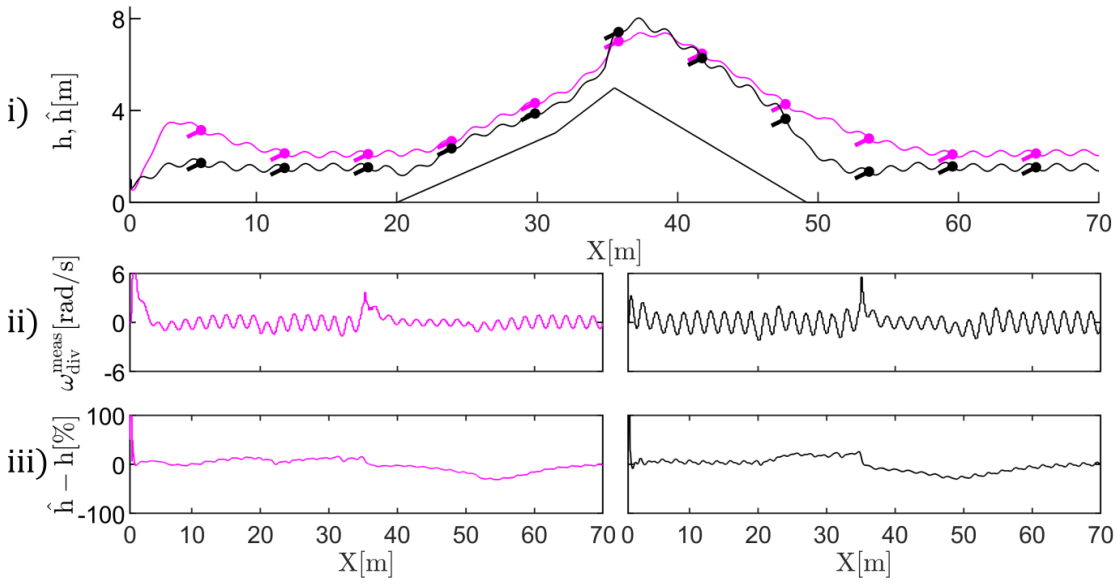

Figure 8.5: Examples of outward flights simulated to test respectively the SuRf (Surface Reference based model, in purple) and the raw SOFIa (Self-scaled Optic Flow time-based Integration model, in black) models (with $\omega_T^{set} = 2rad/s$, $u_\theta = 40°$, in absence of wind). i) Comparison of flights with the SuRf and raw SOFIa models, respectively. ii) The local optic flow divergence ω_{div}^{meas} was measured as the difference of the two optic flow magnitudes perceived downward at $\phi = \pm 20°$ for the SuRf model and as the ratio between V_h and $D_{0°}$ for raw SOFIa model. iii) The average percentage error of the estimates of $\hat{h}$ with respect to h after convergence (at $2.5s$) was -2.78% for the SuRf model and 20.52% for the raw SOFIa model.

raw SOFIa model.

To analyse the impact of the reorientation strategy, outward flights were simulated under a total number of 81 parametric conditions to test both the SuRf and the raw SOFIa models. As shown in Figure 8.6, when considering all 81 parametric conditions the final percentage error of the odometry for the SuRf model ranged between -8.76% and 10.62%, while it ranged between -29.89% and -4.14% for the raw SOFIa model.Similar results were obtained when considering wind conditions separately. In absence of wind, the final percentage error of the odometry for the SuRf model ranged between -1.2% and 6.24% (with an average value of 1.28%), while it ranged between -19.9% and -12.44% (with an average value of -15.53%) for the raw SOFIa model. Under head wind, the final percentage error of the odometry for the SuRf model ranged between -6.42% and 10.62% (with an average value of 4.97%) while it ranged between -29.89% and -8.91% (with an average value of -19.04%) for the raw SOFIa model. Under tail wind, the final percentage error of the odometry for the SuRf model ranged between -8.76% and 9.61% (with an average value of 0.36%), while it ranged between -25% and -4.14% (with an average value of -12.54%) for the raw

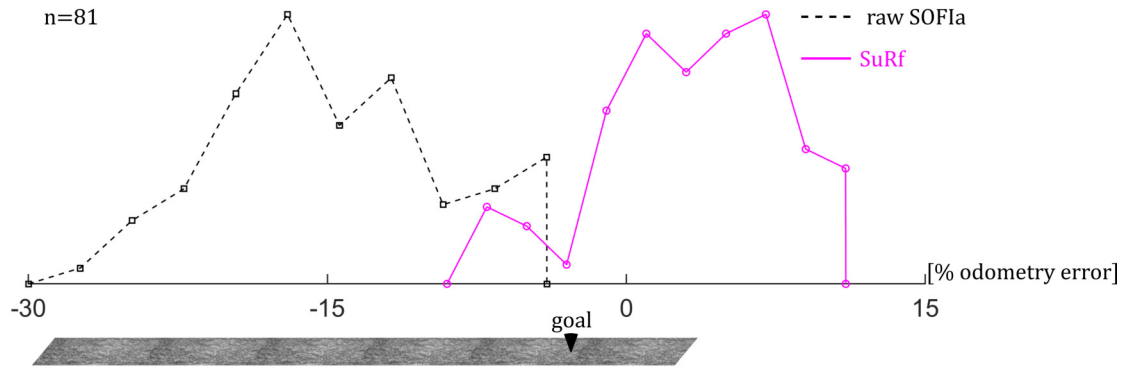

Figure 8.6: The curves show the distributions of the final percentage odometry errors for the SuRf (Surface Reference based model) and the raw SOFIa (Self-scaled Optic Flow time-based Integration model) models tested in simulation over a $70m$-long open field in the presence of wind and terrain slope irregularities, under a total number of 81 parametric conditions. The set of simulated parametric conditions were generated by varying: (i) the translational optic flow setpoint ω_T^{meas}, taking 3 different values ($1.75rad/s$, $2rad/s$ and $2.25rad/s$), (ii) the body pitch of the simulated honeybee u_θ, taking 3 different values (30°, 40° and 50°) and (iii) the wind coefficient k_{wind}, taking 9 different values (ranging between -1 and 1, with a step of 0.25). The final percentage error of the odometry for the SuRf model (in purple) ranged between -8.76% and 10.62%, with an average value of 2.51% and a Median Absolute Deviation (MAD) of 3.78%. The final percentage error of the odometry for the raw SOFIa model ranged between -29.89% and -4.14%, with an average value of -15.76% and a MAD of 4.77%.

SOFIa model.

8.9 Conclusion

In this study, we presented a model for the honeybee visual odometer, called SuRf, that relies on head pitch reorientation to perceive optic flow cues perpendicularly to a surface below. The SuRf model involves adjusting the pitch of the simulated honeybee compound eye to keep the head pitch on a level with the surface below. The SuRf model was tested in simulation over a $70m$-long open field in the presence of wind and terrain slope irregularities under a total number of 81 parametric conditions. The SuRf model was then compared to the raw SOFIa model, which was tested under the same conditions.

Our findings show that perceiving optic flow cues perpendicularly to the surface below improves the performance of the honeybee visual odometer in open field flights. The distribution of the final percentage errors of the odometry under the 81

parametric conditions tested was less spread and presented a lower average value after convergence for the SuRf model. This trend was particularly noticeable for flights in the absence of wind and under head wind. Under these conditions, the simulated honeybee tended to fly closer to the surface below and thus the measurement of the optic flow cues was more affected by the presence of ground irregularities. In general, the lack of head pitch adjustment led to an underestimation of the distance travelled in every case considered.
The accuracy of the SuRf model, combined with the fact that its output is given in meters, opens up possibilities for aerial robotic applications. The implementation of the SuRf visual odometer would be particularly beneficial for applications taking place outdoors, over irregular terrain and in the presence of big changes in ground slope. In this study, we focused on the adjustment of the honeybee pitch on the vertical plane. However, the same model applied on the lateral plane might help aerial vehicles to navigate in tunnels in the presence of abrupt turns. Future work will include simulation and experimental tests of pitch, yaw and roll adjustment onboard an aerial vehicle, with the final aim of implementing the SuRf visual odometer on a micro-drone in a 3D environment.

8.10 Appendices

8.10.1 Appendix A: Extended Kalman Filter calculations

The model of the honeybee's vertical dynamics taken from [180] was discretized and expressed as:

$$\begin{cases} X[k+1] = \Phi \cdot X[k] + \Gamma \cdot u[k] \\ y[k] = C_k \cdot X[k] + D_k \cdot u[k] \end{cases} \tag{8.19}$$

with

$$\Phi = e^{A \cdot dt} \tag{8.20}$$

$$\Gamma = (\int_0^{dt} e^{A \cdot \tau} d\tau) \cdot B = (A^T \cdot e^{A \cdot dt} - A^T) \cdot B \tag{8.21}$$

$$C_k = h(x_k) = \left[\frac{x_2[k]}{x_1[k]} \right] \tag{8.22}$$

$$D_k = 0 \tag{8.23}$$

where dt is the discretization time. To estimate the flight height h, the EKF took the following iterative steps for each k^{th} time:

Prediction step

(a) One-step ahead prediction

$$X_{k/k-1} = \Phi \cdot X_{k-1/k-1} + \Gamma \cdot u_{k-1/k-1} \tag{8.24}$$

(b) Covariance matrix of the state prediction error vector

$$P_{k/k-1} = \Phi \cdot P_{k-1/k-1} \cdot \Phi^T + Q \tag{8.25}$$

Correction step

(c) Measurement update

$$X_{k/k} = X_{k/k-1} + K_k \cdot (y_k - H_k \cdot X_{k/k-1}) \tag{8.26}$$

with K_k Kalman gain defined as:

$$K_k = P_{k/k-1} \cdot H_k^T \cdot [H_k \cdot P_{k/k-1} \cdot H_k^T + R_k]^{-1} \tag{8.27}$$

and H_k Jacobian matrix for the non linear function defined as:

$$H_k = \frac{\partial h}{\partial X}|_{X=X_{k/k-1}} = \begin{bmatrix} -\frac{\dot{h}}{h^2} & \frac{1}{h} \end{bmatrix} \tag{8.28}$$

(d) Covariance matrix of state estimation error vector

$$P_{k/k} = P_{k/k-1} + K_k \cdot [H_k \cdot P_{k/k-1} \cdot H_k^T + R_k] \cdot K_k^T \tag{8.29}$$

(e) Innovation

$$\tilde{y}_k = y_k - H_k \cdot x_{k/k} \tag{8.30}$$

8.10.2 Appendix B: Observability analysis of the honeybee vertical dynamics

Simplified honeybee vertical dynamics can be expressed as follows [177]:

$$\begin{cases} \dot{h} = v_h \\ \dot{v}_h = -\frac{v_h}{\tau_z} + \frac{K_z}{\tau_z}\Delta\Phi \\ \omega_{div} = \frac{v_h}{h} = \frac{\omega(\phi)-\omega(-\phi)}{\sin 2\phi} \end{cases} \tag{8.31}$$

To estimate the current ground height h, the Extended Kalman Filter (EKF) used i) the downward perceived optic flow divergence ω_{div} as its measurement input, ii) the model for the vertical dynamics of the simulated honeybee as expressed in equation 8.31 and iii) the control input signal (the wing stroke amplitude $\Delta\Phi$) regulating the vertical dynamics.
The continuous state space model of the honeybee vertical dynamics was therefore written as follows:

$$\begin{cases} \dot{x}(t) = f(x(t), \Delta\Phi(t)) = \begin{bmatrix} \dot{h}(t) \\ \dot{v}_h(t) \end{bmatrix} = \begin{bmatrix} 0 & 1 \\ 0 & \frac{-1}{\tau_z} \end{bmatrix} \begin{bmatrix} h \\ v_h \end{bmatrix} + \begin{bmatrix} 0 \\ \frac{K_z}{\tau_z} \end{bmatrix} \Delta\Phi \\ y(t) = g(x(t)) = \frac{v_h}{h} = \frac{\dot{h}}{h} = \omega_{div} \end{cases} \tag{8.32}$$

where $x = \begin{bmatrix} h \\ v_h \end{bmatrix}$ is the state vector. It is worth noting that the model's dynamics are linear, whereas the EKF's observation equation is nonlinear.
To check the observability of the system, the observability rank condition was analysed. First the observability matrix was calculated using the EKF observation equation with respect to the model dynamics [99]. To do so, the successive Lie derivatives of $g(.)$ were calculated, as follows:

$$L_f^0(g(x(t)) = g(x(t)) = \frac{V_h(t)}{h(t)} \tag{8.33}$$

$$L_f^1(g(x(t)) = \frac{g(x(t)}{\partial x(t)} * f(x(t), u(t)) = -\frac{V_h(t)^2}{h(t)^2} + \frac{u}{h} \tag{8.34}$$

Thus, the observability matrix was expressed as follows:

$$O = \begin{bmatrix} L_f^0(g(x(t)) \\ L_f^1(g(x(t)) \end{bmatrix} = \begin{bmatrix} \frac{V_h(t)}{h(t)} \\ \frac{-V_h(t)^2}{h(t)^2} + \frac{u}{h} \end{bmatrix} \tag{8.35}$$

A system is observable if and only if the Jacobian function of the observability matrix is full rank. Thus, an analysis of the observability matrix O as expressed in equation (8.35) was performed in order to check whether its Jacobian was full-rank. In the present case, the system is (locally) observable if and only if the input disturbance $u \neq 0$, and $h \neq 0$ and $v_h \neq 0$. The continuous variation of the control signal u due to the self-induced input disturbances ensured that the values of the states h and v_h and the control signal were rarely zeroed. Therefore, the oscillatory movements made the ground height observable via the optic flow divergence.

9 Discussion, conclusions and future work

In aerial robotic applications, visual odometry is most often performed by processing the stream of images captured by a camera with algorithms that require high computational costs. This thesis addresses the issue of performing visual odometry onboard micro- and nano-drones, on which computational and perception resources available tend to be low. The strategy presented is based on a model for the honeybee visual odometer based solely on optic flow cues.

9.1 Thesis contributions

The SOFIa model for the honeybee visual odometer In this thesis is presented a model for the honeybee visual odometer, called SOFIa (Self-scaled time-based Optic Flow Integration model), which relies solely on the translational and divergence optic flow cues. The SOFIa model involves the use of a scaling factor extracted from the ventral optic flow vector field. This scaling factor is the ground height estimated by means of an Extended Kalman Filter (EKF), which receives as measurement the optic flow divergence generated by the up-and-down self-oscillatory movements performed by the honeybee while flying forward. Due to the scaling of the translational optic flow, the SOFIa model is less sensitive to changes occurring in the environment (such as variations in the wind direction or in the flight trajectory) than the model for the honeybee visual odometer based solely on the raw integration optic flow. Tested on honeybees' trajectories in open field simulations under a total number of 630 different parametric conditions, the SOFIa model was found to be reliable even in the presence of multiple disturbances and changes in the internal parameters of the simulated honeybee (such as optic flow setpoint and ground speed). The statistical dispersion of the estimates of the distance travelled obtained with the SOFIa model was reduced 10-fold compared to the one obtained with the raw mathematical integration of translational optic flow under the same conditions. This analysis suggests that in open field honeybees need to self-oscillate to retrieve the distance of a food source from the hive, return to the hive, recruit their nestmates, etc... Thanks to the scaling of the translational optic flow by means of the ground height estimates, the output of the SOFIa visual odometer is given in $metres$ and not in $radians$.

The measurement of the optic flow cues by means of optic flow sensors In this thesis, it is mathematically and experimentally demonstrated that both the divergence and translational optic flow cues can be measured by means of two optic flow magnitudes perceived by two optic flow sensors placed at angles ϕ and $-\phi$ with respect to the normal to a surface. The measurement of the optic flow divergence cue was tested for the first time on a test bench equipped with two optic flow sensors performing a back-and-forth oscillatory motion in front of a panorama. The measured local optic flow divergence was then exploited to estimate the distance of the optic flow sensors from the panorama without the need for prior knowledge of the environment or emissive sensors. The translational and divergence optic flow cues were then measured onboard a hexarotor.

Implementation of the SOFIa visual odometer onboard a hexarotor The SOFIa visual odometer was tested for the first time onboard a hexarotor following $50m$-long circular bouncing trajectories in the Mediterranean Flight Arena. The use of oscillating trajectory information to improve the measurement of translational and divergence optic flow cues was also investigated. Two sensor fusion strategies, based respectively on a precise and rough prior knowledge of optic flow variations, were presented and experimentally tested onboard the hexarotor equipped with four optic flow sensors. The experimental results obtained show that the sensor fusion strategies allow to measure the optic flow cues more reliably thanks to additional Kalman Filters (KF). This was the case even when only a rough prior knowledge of the optic flow variations (more specifically only the general shape and timing of the oscillations during the trajectory) was taken into account. This prior knowledge can be considered acceptable, as the general shape and timing of the oscillations are imposed by the drone itself on its forward trajectory. The sensor fusion strategies reduced the error in the ground height estimates and thus the percentage error in the estimates of the distance travelled in all cases considered, improving odometric performance. Preliminary tests were also performed outdoors, where the hexarotor followed $20m$-long longitudinal bouncing trajectories over a field irregularly covered with grass in the presence of wind.

Head reorientation increases the reliability of the honeybee visual odometer A second model for the honeybee visual odometer, called SuRf (Surface Reference based model), is presented as well. The SuRf model is also based on the scaling of the translational optic flow, but in this case, the optic flow taken into account is always perceived perpendicularly to the surface below. For this purpose, an active reorientation process is added so as to always keep the visual plane parallel to the surface below. The SuRf model was tested on honeybees' trajectories in open field simulations in the presence of wind and terrain irregularities under a total number of 81 different parametric conditions. The distribution of the final percentage errors of the estimates of the distance travelled obtained with the SuRf model was less spread and had a lower average value than the one obtained with the SOFIa model tested under the

same conditions. The results obtained show that the perception of the optic flow cues perpendicularly to the surface below improves the performance of the honeybee visual odometer in open field flights.

9.2 Future perspectives for aerial robotic applications

The minimalistic SOFIa visual odometric strategy presented in this thesis can be implemented onboard flying robots, and more specifically onboard micro- and nano-drones that present Speed, Size, Weight and Power (SSWaP) constraints [99, 82], due to:

- the low weight of the optic flow sensors, which amounts to about $1-2g$ for each sensor including the circuit board,
- the low computational power required to measure the translational and divergence optic flow cues by means of optic flow sensors.

Thus, the SOFIa visual odometer allows to perform accurate visual odometry without computationally heavy algorithms to process the stream of large images captured by one or more cameras. The SOFIa visual odometer is most effective in high-contrast environments under illuminance conditions that allow to accurately measure the translational and divergence optic flow cues. Experimental results illustrated in this thesis show that it is possible to measure the optic flow cues under illuminances as low as $117lux$. The measurement of optic flow cues could be possible even for lower illuminances, depending on the optic flow sensors used.
The SOFIa visual odometer is particularly interesting for aerial robotic applications taking place in environments where GPS is only intermittently or not at all available (such as buildings or tunnels) to estimate the distance travelled in order to fly from landmark to landmark. The estimates of the distance travelled are subject to a small cumulative error, as the odometric strategy presented is a dead reckoning method based on optic flow and does not require any feedback from the environment. However, the SOFIa visual odometer is sufficiently accurate and precise to allow a drone to move close to a target without GPS, both indoors and outdoors. This minimalistic odometric strategy based on optic flow could also be used by a drone to assess whether it is returning close to its base station without the need for GPS.

9.2.1 The implementation of the SOFIa visual odometer in autonomous aerial robotic applications

Steps to implement the SOFIa visual odometer in autonomous aerial robotic applications should include:

- an accurate analysis of robustness to large drone pitch, oscillation amplitude and the presence of strong reliefs,
- the development of optic flow sensors adapted to high speed and both very high and very low illuminance conditions.

The SOFIa visual odometer could also be combined with other odometric strategies to improve its accuracy. An example of hybrid solution involving GPS could rely on the estimates of the distance travelled assessed with the SOFIa visual odometer, periodically fused with information provided by GPS to reduce cumulative error. Another possible solution could be to fuse the estimates of the distance travelled obtained with the SOFIa visual odometer to information provided by sonar or laser sensors. The use of landmarks (i.e. detected by a camera) could also be considered to reduce cumulative error for aerial robotic applications taking place in known environments. Developing a device consisting of optic flow sensors that autonomously oscillate up and down would also facilitate the implementation of the SOFIa visual odometer onboard small flying robots. Such a device would allow to measure the local translational and divergence optic flow cues without the need for the drone to perform bouncing trajectories. Another possible solution could be based on a numerical zoom and de-zoom of the visual scene below by means of a camera.

9.2.2 The advantages of the SuRf visual odometer

The implementation of the SuRf visual odometer would be particularly advantageous for applications taking place outdoors, over uneven terrain and in the presence of strong slope variations. In this thesis, only the pitch adjustment to always keep the visual plane of the simulated honeybee parallel to the surface below is considered. However, the same strategy applied also on the lateral plane could help aerial vehicles to navigate in constrained environments (such as tunnels with sharp turns). Steps to implement the SuRf visual odometer in autonomous aerial robotic applications should include both simulation and experimental tests of pitch, roll and yaw adjustment onboard a flying robot.

9.2.3 Optic flow for aerial robotic applications

Optic flow cues can be easily measured with computationally low-cost algorithms. Thus, optic flow represents a powerful tool for robotic applications, and more specifically for aerial robotic applications relying on platforms that present SSWaP constraints. Although this thesis focuses on the use of optic flow for visual odometry, applications based on translational and divergence optic flow cues could also be developed for obstacle avoidance or autonomous navigation in cluttered environments, for example.

9.3 Feedback to biology

In order to reach a food source in the immediate vicinity, honeybees are believed to rely on various mechanisms, such as those based on landmarks and smell. This makes it difficult to assess the accuracy of the honeybee visual odometer alone, as it has not yet been established when and at what point in the trajectory the honeybees conclude they have reached their target. However, honeybees are able to retrieve the distance of a food source from the hive and communicate it to their nestmates during the waggle dance with sufficient accuracy to forage.
Neurophysiological evidence shows the presence of neurons in the honeybee brain that are sensitive to translational and divergence optic flow cues [230]. The SOFIa visual odometer is therefore based on biologically plausible cues. The scaling factor estimator based on optic flow is a non-linear filter that relies on i) a non-linear model, ii) a control input (or efference copy) and iii) a biologically plausible sensory output (the optic flow divergence). Thus, the SOFIa model can be said to be biologically plausible even though it is not completely anatomically constrained.
In this thesis, the SOFIa model was tested in simulation under conditions similar to those of an open field or a very large tunnel, where honeybees appear to oscillate at lower frequencies. Under these conditions, the ventral optic flow controller of the simulated honeybee is free to adjust its altitude without being constrained by the height of a tunnel. The impact of the geometric configuration of a tunnel on the flight trajectory of a honeybee seems to be more pronounced in narrow, low-roofed tunnels. So far, the SOFIa model has been tested in simulation on straight honeybees' trajectories on a vertical plane (x, z). However, the SOFIa model does not depend on the honeybees' vertical dynamics, but only on the extraction of optic flow cues from the visual scene. The translational and divergence optic flow cues can both be extracted along more complex 3D trajectories, according to the definition of optic flow [126]. Thus, the SOFIa model may be generalized to the case of holonomic flights such as those performed by honeybees [42]. Future studies should include testing the SOFIa model in simulation in a 3D environment.

9.3.1 The self-scaling of the SOFIa model assesses the ground speed

The odometric performance of the SOFIa model corresponds to the fact that visual cues, and more specifically optic flow, can reliably feed the visual odometer over distances of the order of a few hundred metres, regardless of the trajectory. Furthermore, the SOFIa model would be reliable irrespective of the base unit and coding in which the information flow is processed, including those possibly used by honeybees.
It certainly seems that the honeybee estimates the distance travelled on its trajectory [247, 219, 63]. Even if the honeybee does not gauge the distance travelled (i.e. the honeybee does not explicitly track the distance travelled on a trajectory) but instead continuously "accumulates its velocity", the problem of estimating its ground speed

at different heights would still need to be solved. The SOFIa model provides a solution to this issue thanks to the self-scaling of the optic flow.

9.3.2 Better understand how honeybees react to the optic flow divergence

A considerable number of studies have suggested that honeybees rely on the translational optic flow cue to perform several fundamental tasks, such as assessing the distance of a food source from the hive [60, 58, 61, 238], landing [226, 225, 263] and control forward flight speed in tunnels [225, 178, 10, 10], for example. Considerably less is known about the behavior of the honeybee with respect to the optic flow divergence cue. Some studies have suggested that the optic flow divergence cue could be used by bees to perform landing [217, 89, 7] and by flies to control altitude [233].
Some studies have reported self-oscillations in honeybees' flights in tunnels, both horizontally [124, 8] and vertically [178]. In a recent study, the authors have also suggested that lateral (not vertical) self-oscillations combined with information about the changes in airspeed could be used by honeybees to estimate the ground height in open field, but without describing a precise perceptual mechanism [8]. Due mostly to the experimental difficulty in performing accurate observations under outdoor conditions on such small and fast targets, little is known of free-flying honeybees' trajectories outdoors, where the flying insects are not constrained by the geometry of the chosen experimental tunnel. Lepidopterans might be an easier model for such

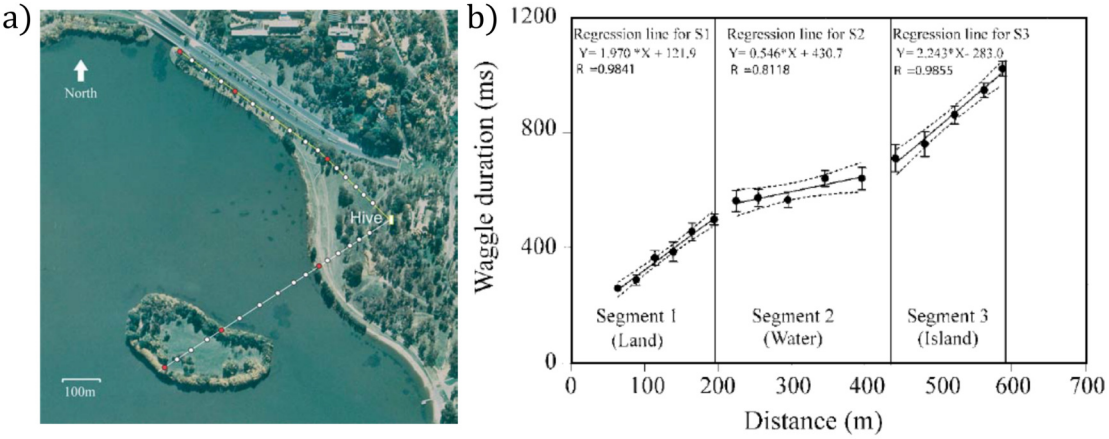

Figure 9.1: a) Aerial view of the experimental site, where honeybees were trained to fly either towards the south-west over a stretch of land and then over water to reach an island, or towards the north-west entirely over land. b) Linear approximation of the variation in waggle duration with respect to the distance of the feeder from the hive reported for foraging honeybees flying over a stretch of land (segment 1) and then over water (segment 2) and again over land (segment 3) (adapted from J. Tautz et al., 2004 [238]).

experimental observations, due to their bigger size and colorful wings. Studies on free-flying moths and butterflies seem to indicate that such flying insects perform up-and-down self-oscillations while flying in open field [257, 201, 174, 227].
Steps to better understand the role of the self-oscillations and of the optic flow divergence cue in the honeybee visual odometer could include:

- a study on honeybees flying in vertically-striped tunnels of various shapes and sizes, in order to assess (i) the impact of geometric configurations on self-oscillations and (ii) the oscillation frequencies displayed,
- a study on lepitoderans flying in open field, possibly involving several high-resolution cameras disposed over at least a few tens of meters,
- a similar open-field study on hymenopterans (such as bumblebees or ideally honeybees), possibly involving several high-resolution cameras disposed over at least a few tens of meters between the hive and a feeding station.

9.3.3 The dependence of the integration rate on the optic flow density

Previous studies have reported that foraging honeybees trained to fly in short, narrow tunnels with textured walls perform waggle dances indicating a greater distance than actually travelled [223]. Subsequent experiments have compared the slope of the relationship between the waggle duration and the distance travelled reported for waggle dances performed by honeybees flying either over land or over land and water [238] (see Figure 9.1). The slope of this relationship was flatter for honeybees whose outward trajectories included water overflight, suggesting that the integration rate of the honeybee visual odometer decreases on low contrast surfaces due to low optic flow density. The SOFIa model does not account for this dependence of the integration rate on the optic flow density.

General conclusion

This thesis suggests a new principle that might help to better understand how honeybees assess the distance travelled to a food source from the hive. This same principle can be implemented onboard micro- and nano-drones as an optic flow based dead reckoning solution. Flying insect navigation is far from being a solved mystery. The integration of neuroethology and robotics may help shed light on how the tiny brains of insects handle complex tasks on which their own survival depends.

10 Résumé en francais

Introduction

Comment l'abeille indique une source de nourriture

En 1967, K. von Frisch décrit dans son livre "The Dance Language and Orientation of Bees" la danse en huit exécutée par les abeilles butineuses une fois de retour à la ruche. Au cours de cette danse, les abeilles butineuses informent leurs congénères de la direction et la distance à parcourir pour atteindre une source de nourriture [247]. Les abeilles butineuses peuvent être observées en train de parcourir une courte ligne droite tout en agitant latéralement leur corps avant de revenir au point de départ en

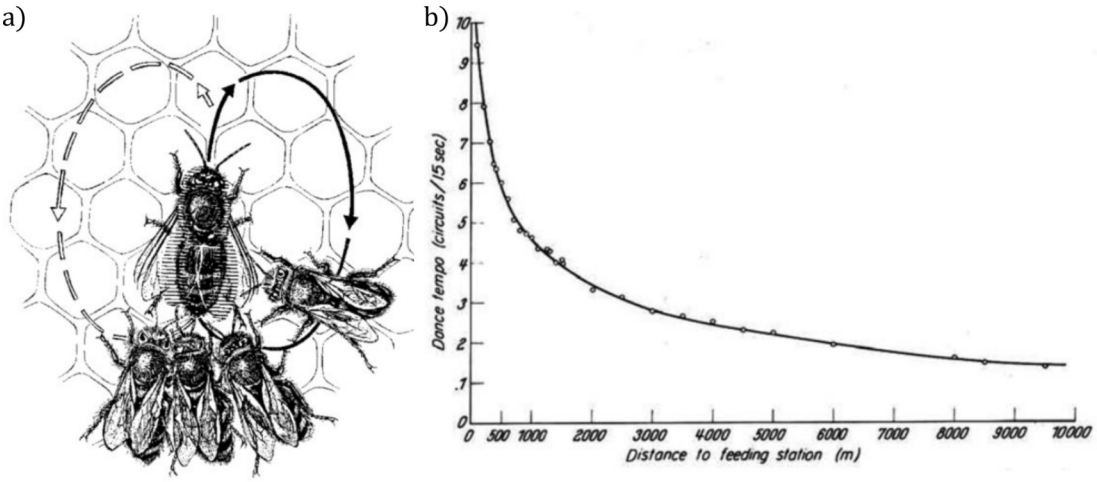

Figure 10.1: a) Au cours de la danse en huit, l'abeille butineuse effectue une course en ligne droite tout en agitant latéralement son corps. L'abeille butineuse revient ensuite à son point de départ en demi-cercle, alternativement vers la droite et vers la gauche. Ses congénères assistent à la danse en huit pour extraire les informations pertinentes sur la distance et la direction à suivre pour atteindre la source de nourriture indiquée. b) Relation entre les distances indiquées pendant les danses en huit et le tempo des danses en huit rapporté pour des expériences menées sur $10km$, sur la base de 6267 danses observées (adapté de "The Dance Language and Orientation of Bees", K. von Frisch, 1967 [247]).

demi-cercle alternativement à droite et à gauche (voir Figure 10.1.a).
Les abeilles butineuses évaluent la direction vers une source de nourriture depuis la ruche au moyen de la position du soleil [183, 139]. La capacité des abeilles à estimer la distance entre la ruche et une source de nourriture est appelée “odomètre". K. von Frisch a observé une relation monotone entre la distance à la source de nourriture et le tempo de la danse en huit [247] (voir Figure 10.1.b). Plusieurs études ont suggeré l’hypothèse selon laquelle l’odomètre des abeilles repose sur des indices visuels [60, 58, 225, 224, 223], et plus particulièrement sur le flux optique [61] (voir [40] pour une revue bibliographique). D’autres études proposent que les abeilles évaluent la distance entre la ruche et une source de nourriture en intégrant mathématiquement le flux optique brut de translation perçu dans le champ visuel ventral [60, 58, 61, 238], mais le fonctionnement de cet odomètre reste encore sujet à débat.

Le problème de l’estimation de la distance en robotique

Comme pour les abeilles, l’estimation de la distance parcourue afin de naviguer dans l’environnement pour effectuer des tâches et revenir à un point de départ est un problème récurrent dans les applications robotiques. Le terme "odométrie" fait référence à l’utilisation de capteurs pour estimer le déplacement linéaire d’un agent (tel qu’un robot, une caméra, un véhicule, etc.) à partir d’un point de départ connu, de manière incrémentale. Diverses solutions basées sur l’utilisation de différentes techniques et

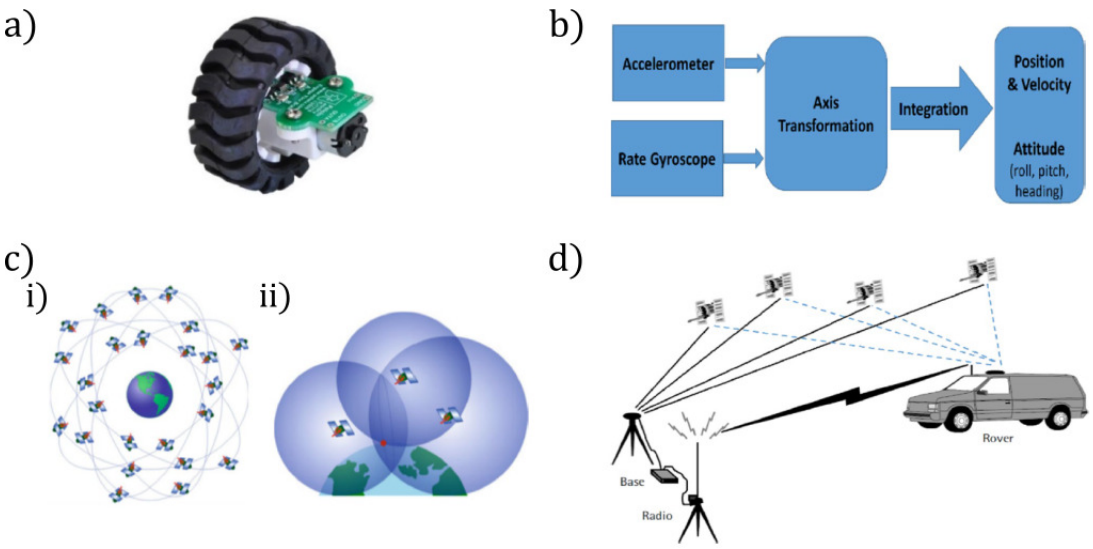

Figure 10.2: a) Exemple d’encodeur optique pour l’odométrie basée sur l’utilisation de roues (d’après Pololu Corporation, 2016). b) Exemple de système de navigation inertielle (adapté de M.O.A. Aquel et al, 2016 [4]). c) Schéma du système satellitaires (GPS) (i) et trilatération au moyen de 3 satellites (ii) (adapté de A. Noureldin et al., 2013 [173]). d) Schéma du GPS différentiel en temps réel (DGPS) (adapté de M.O.A. Aquel et al., 2016 [4]).

capteurs ont été proposées pour mettre en oeuvre des strategiés d'odométrie dans les applications robotiques [4]. Des exemples de stratégies odométriques sont basés sur l'utilisation de roues, de systèmes de navigation inertielle, de systèmes satellitaires, de capteurs ultrasoniques et *laser* (voir Figure 10.2).
Le terme "odométrie visuelle" a été proposé pour la première fois en 2004 [170] et fait référence à la capacité d'estimer la position d'un agent en utilisant le flux d'images prises par une ou plusieurs caméras qui lui sont attachées [203, 169, 161]. L'odométrie visuelle est une méthode sans contact et peut donc être appliquée aux robots aériens [164].
Les principaux inconvénients des stratégies odométriques visuelles basées sur des caméras sont la dépendance aux conditions environnementales et la puissance de calcul élevée requise pour l'analyse des images [87, 164, 172, 260]. En intérieur, les conditions environnementales peuvent être contrôlées pour réduire la lumière directe du soleil, le flou de l'image, les ombres, etc..... Cependant, cela n'est pas possible à l'extérieur. De plus, pour les applications robotiques aériennes, l'utilisation d'algorithmes à forte intensité de calcul est le plus souvent incompatible avec un faible charge utile. Cela est particulièrement difficile dans le cas des micro et nano-drones, où les contraintes de vitesse, de taille, de poids et de puissance (*SSWaP*) jouent un rôle clé. De ces contraintes découle l'importance d'utiliser des équipements minimalistes et des solutions de traitement à faible coût.

Le flux optique

Le flux optique peut être défini comme le motif dû au mouvement apparent des objets et des surfaces dans l'environnement causé par le mouvement relatif entre l'observateur et la scène visuelle [33]. Le concept de flux optique a été introduit par le psychologue américain J.J. Gibson en 1950 dans son livre "The perception of the visual word", où il était défini comme le stimulus visuel fourni aux animaux se déplaçant dans le monde [85] (voir Figure 10.3).

Les capteurs de flux optique

Les capteurs de flux optiques reposent sur des matrices de pixels monochromatiques, dont la taille varie de 18×18 à 35×35 pixels environ.???? Ainsi, les capteurs de flux optique peuvent être considérés comme de petites caméras à très basse résolution, avec un échantillonnage d'image pouvant atteindre $1000 images/s$ et plus. La mesure du flux optique repose sur la cross-corrélation des signaux visuels : les images sont capturées à fréquence fixe et comparées entre elles pour déterminer de combien les contrastes se sont déplacés angulairement dans le champs visuel.

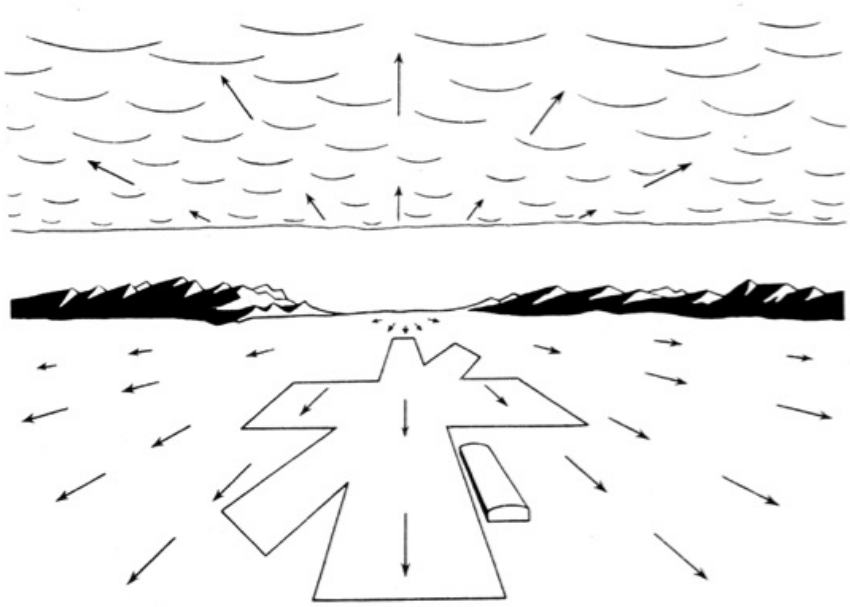

Figure 10.3: Représentation du flux optique comme un champ de vecteurs pour un observateur avançant frontalement (d'après "The perception of the visual world", J.J. Gibson, 1950 [85]).

Approches robotiques inspirées par les insectes et basées sur le flux optique

Bien que les mécanismes relatifs à sa perception chez les insectes ne soient pas encore totalement compris [251], le flux optique –indice visuel biologiquement plausible– a été largement utilisé en robotique comme une perception visuelle alternative, souvent à faible coût [209]. En s'inspirant des insectes, il est possible de développer des approches minimalistes nécessitant moins de ressources en termes de capteurs et de puissance de calcul pour des tâches impliquant la navigation [131, 101, 93] ou la vision [76, 75], par exemple. Les approches robotiques peuvent également contribuer à expliquer les capacités et les performances des insectes à naviguer dans leur environnement encombré [79, 218, 132, 115]. Des stratégies robotiques inspirées des insectes et basées sur le flux optique ont été développées pour effectuer le contrôle de la vitesse, la navigation dans un tunnel, l'évitement d'obstacles, le décollage et l'atterrissage, l'évitement du sol et le suivi du sol, etc... (voir Figure 10.4).

Les oscillations en vol

Des études menées dans des tunnels horizontaux [124] et verticaux [178] ont montré que les abeilles oscillent en volant vers l'avant (voir Figure 10.5). Les fréquences

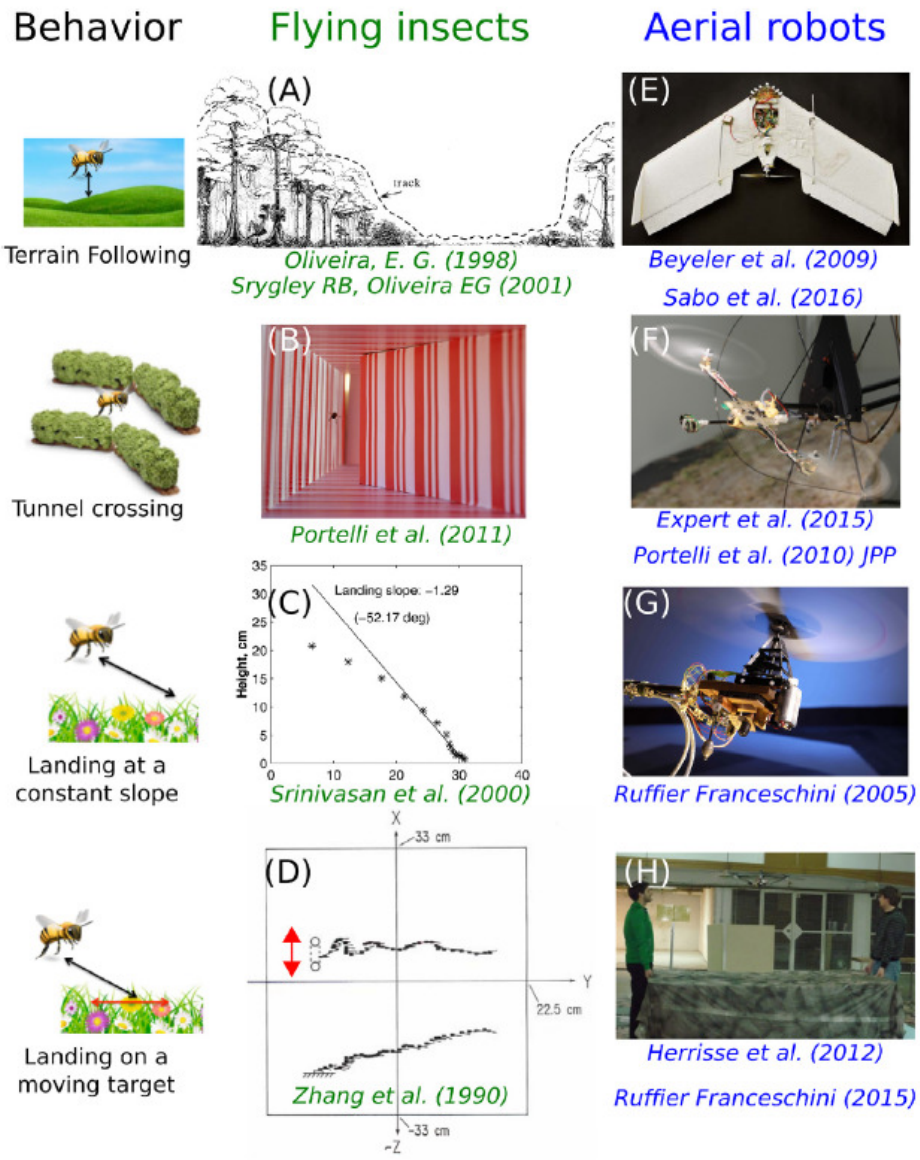

Figure 10.4: Exemples de comportements observés chez les insectes volants et leurs équivalents robotiques n'utilisant que le flux optique. (A) Comportement de suivi du terrain [174, 227] qui a inspiré (E) le développement d'un robot aérien en vol libre suivant le terrain [24, 198]. (B) Navigation dans un tunnel [178] qui a inspiré (F) le suivi du terrain et l'ajustement de la vitesse dans des tunnels complexes [64, 177]. (C) Descente et atterrissage à pente constante (sans variomètre) [226] qui ont inspiré (G) le régulateur de flux optique ventral [192]. (D) Atterrissage sur une cible mobile [263] qui a inspiré (H) un robot aérien se posant sur une cible placée sur une plateforme en mouvement [194] (d'après J. Serres et F. Ruffier, 2017 [209]).

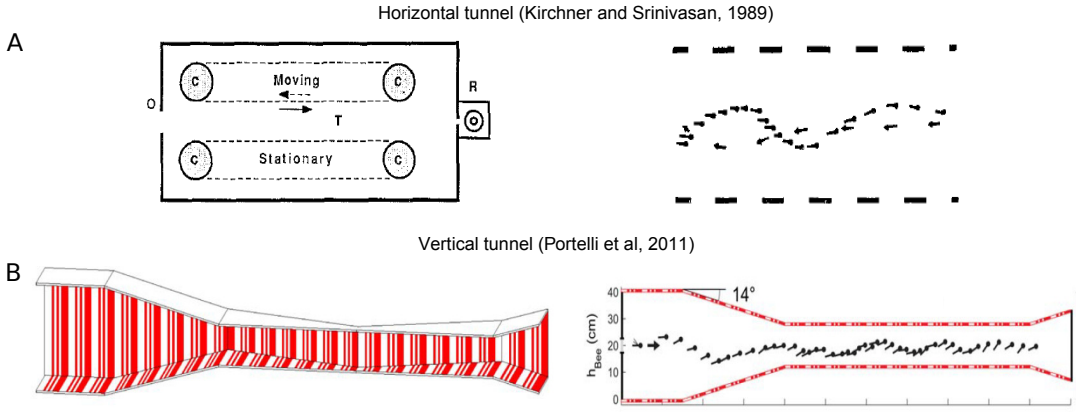

Figure 10.5: A) Vue de dessus de la trajectoire d'une abeille présentant des oscillations latérales (à droite) dans un tunnel horizontal (à gauche) (adapté de W.H. Kirchener et M.V. Srinivasan, 1989 [124]) B) Vue latérale de la trajectoire d'une abeille présentant des oscillations de haut en bas (à droite) dans un tunnel vertical (à gauche) (adapté de G. Portelli et al, 2011 [178]).

d'oscillation rapportées se situent autour de $2Hz$, tandis que l'amplitude des oscillations est d'environ $3cm$ en largeur (dans des tunnels étroits de $12cm$ de large) [124] et $10cm$ en hauteur (dans des tunnels de $40cm$ de haut) [178]. Selon une étude récente, les abeilles volant dans des tunnels étroits pourraient contrôler leur hauteur de vol au moyen d'oscillations latérales d'une fréquence moyenne de $4,7 \pm 1,6Hz$ [8]. Des oscillations similaires ont également été observées chez les lépidoptères [257, 201, 12, 174, 227].

Les indices de flux optique durant le vol de l'abeille

Le champ de vecteurs du flux optique perçu par la région ventrale de l'œil composé de l'abeille pendant les vols vers l'avant tout en oscillant en milieu ouvert est illustré à la Figure 10.6. Trois indices de flux optique peuvent être identifiés : les indices de flux optique de translation, de divergence et de rotation.
L'indice de flux optique de translation est le motif dû au mouvement de translation de l'abeille qui survole le sol [85]. Le flux optique local de translation ω_T dépend du rapport entre la vitesse sol V_x – composante horizontale de la vitesse V de l'abeille – et la hauteur sol h – hauteur de vol de l'abeille – [256] (représenté en rouge sur la Figure 10.6) :

$$\omega_T = \frac{V_x}{h} \tag{10.1}$$

Le mouvement oscillatoire de haut en bas génère une série de contractions et d'expansions dans le champ de vecteurs du flux optique ventral, qui peut être quantifié comme l'indice de divergence du flux optique. La divergence du flux optique est superposée dans le champ de vecteurs du flux optique sur la composante translationnelle du

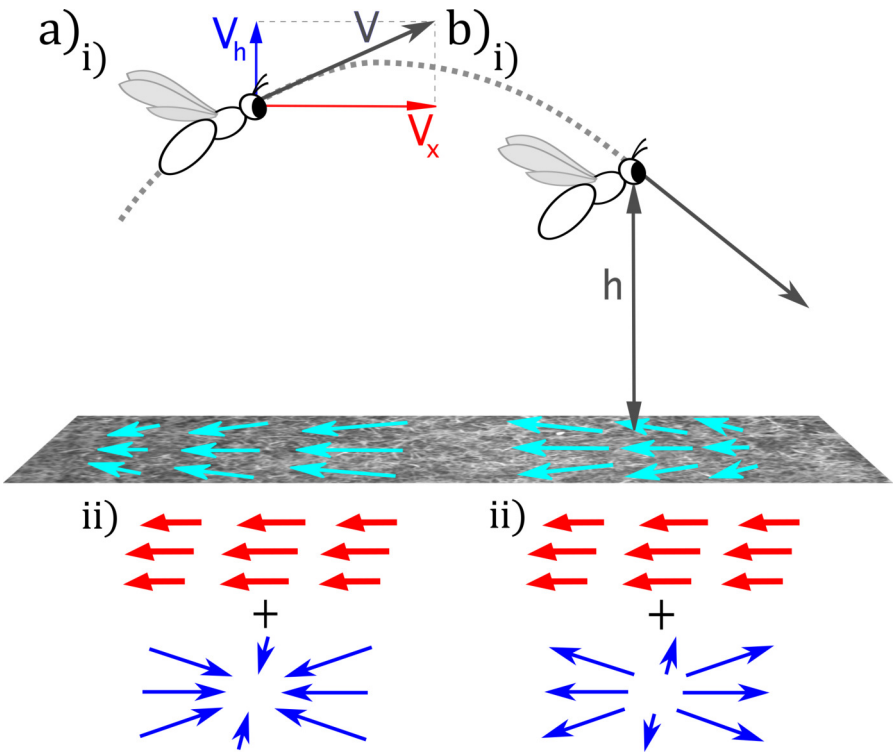

Figure 10.6: Les abeilles oscillent vers le haut (a.i) et vers le bas (b.i) tout en volant vers l'avant au-dessus du sol, générant une série de contractions (a.ii) et d'expansions (b.ii) dans le champ de vecteurs du flux optique ventral, quantifié comme l'indice de divergence du flux optique (en bleu). La divergence du flux optique est superposée dans le champ de vecteurs du flux optique sur le flux optique de translation (en rouge).

flux optique (voir Figure 10.6). La divergence locale du flux optique ω_{div} dépend du rapport entre la composante verticale V_h de la vitesse de l'abeille V et h (représentée en bleu sur la Figure 10.6) :

$$\omega_{div} = \frac{V_h}{h} \tag{10.2}$$

Les abeilles effectuent également des virages et des saccades lorsqu'elles volent vers l'avant en oscillant. Ces mouvements de rotation se rajoutent au champ de vecteurs du flux optique : cet indice se nomme le flux optique de rotation. Le flux optique de rotation dépend de la vitesse de rotation de l'abeille et se superpose dans le champ de vecteurs du flux optique aux composantes du flux optique de translation et de divergence. Le flux optique local de rotation ω_R peut être exprimé comme la dérivée dans le temps du tangage de l'abeille θ :

$$\omega_R = \frac{d(\theta)}{dt} \tag{10.3}$$

Contributions de la thèse

L'objectif de cette thèse est de développer une approche odométrique visuelle minimaliste pour de micro- et nano-robots volants inspirée des abeilles et basée sur l'utilisation de capteurs de flux optiques.

Le modèle SOFIA d'odomètre visuel des abeilles

Dans cette thèse, nous proposons un modèle d'odomètre visuel des abeilles, appelé SOFIa (Self-scaled time-based Optic Flow Integration model). L'odomètre visuel SOFIa implique l'utilisation d'un facteur d'échelle extrait du champ de vecteurs du flux optique ventral. Ce facteur d'échelle est la hauteur de vol estimée au moyen d'un Filtre de Kalman Etendu (EKF). Pour ce faire,l'EKF reçoit comme mesure la divergence du flux optique générée sur le champ de vecteurs du flux optique ventral par les mouvements oscillatoires de haut en bas. Grâce à la mise à l'échelle du flux optique

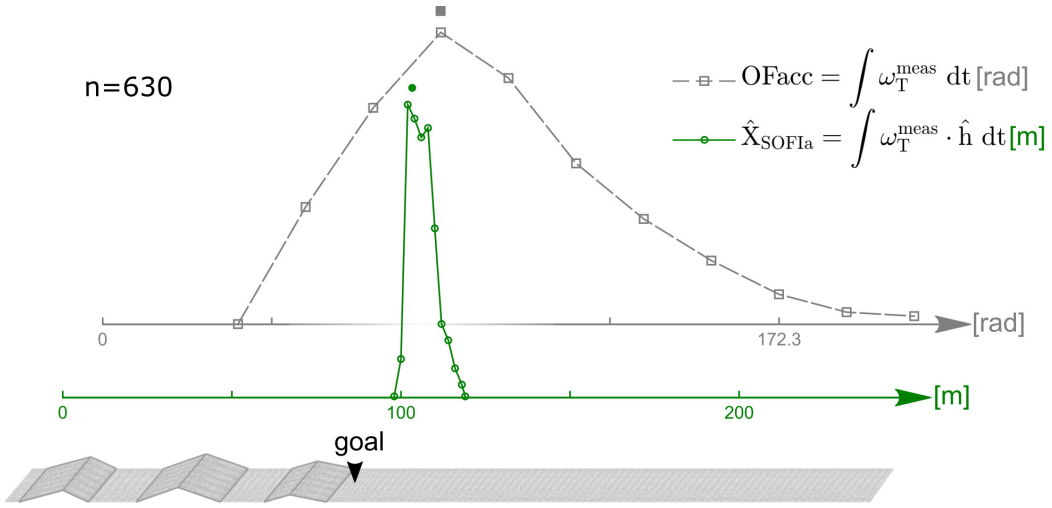

Figure 10.7: Les courbes donnent les distributions de fréquences relatives des sorties des deux modèles pour l'odomètre visuel simulé lors d'un vol de $100m$ de long au-dessus de 3 petites collines à pentes douces séparées par des zones plates, sous un nombre total de 630 conditions paramétriques. À des fins de comparaisons visuelles, la valeur médiane en $radians$ du modèle OFacc a été alignée avec la tache de $100m$ sur l'abscisse en mètre. La dispersion des sorties des deux modèles diffère significativement (test de Brown-Forsythe, df = 502, F : 383.66, p-value << 0.001). La dispersion statistique de la distribution obtenue avec le modèle SOFIa s'est avérée considérablement plus faible que celle obtenue avec le modèle OFacc : l'écart absolu médian du modèle SOFIa était de $3.09m$, tandis que celui du modèle OFacc s'élevait à $25.62rad$, soit $29.74m$.

de translation avant son intégration dans le temps, l'odomètre visuel SOFIa est moins sensible aux changements de trajectoires par exemple dû au vent que le précédent modèle d'odomètre visuel basé uniquement sur l'intégration brute du flux optique de translation. Testé sur des simulations "en milieu ouvert" de $100m$ de long dans un nombre total de 630 conditions paramétriques différentes, l'odomètre visuel SOFIa s'est avéré fiable même en présence de multiples perturbations et changements des paramètres internes de l'abeille simulée (tels que le point de consigne du flux optique et la vitesse de vol). La dispersion statistique des résultats odométriques obtenus avec le modèle SOFIa a été réduite de 10 fois par rapport à celle des résultats odométriques obtenus avec l'intégration mathématique brute du flux optique de translation dans les mêmes conditions (appelé ici OFacc pour Optic Flow accumulation model, voir Figure 10.7). Cette analyse suggère qu'en milieu ouvert, les abeilles peuvent mettre à l'échelle leur flux optique grâce à leurs oscillations verticales, ceci les aidant à retrouver l'emplacement d'une source de nourriture, à retourner à la ruche, et donc à recruter leurs congénères, etc. Grâce à la mise à l'échelle du flux optique de translation au moyen des estimations de la hauteur de vol, la sortie de l'odomètre visuel SOFIa est donnée en mètres et non en radians.

Mesure des indices du flux optique au moyen des capteurs de flux optique

Dans cette thèse, il a été démontré mathématiquement et expérimentalement que les indices de flux optique de divergence et de translation peuvent être mesurés au moyen de deux magnitudes de flux optique perçues par deux capteurs de flux optique placés à des angles ϕ et $-\phi$ par rapport à la normale à une surface. La mesure de l'indice de divergence du flux optique a été testée pour la première fois sur un banc d'essai équipé de deux capteurs de flux optique effectuant un mouvement oscillatoire de va-et-vient devant un panorama (voir Figure 10.8). La divergence locale du flux optique mesurée a été exploitée pour estimer la distance entre les capteurs de flux optique et le panorama sans avoir besoin d'une connaissance préalable de l'environnement ou des capteurs émissifs. Les tests ont été réalisés avec une large gamme de vitesses de panorama dans des conditions de luminosité faible et forte, qui n'ont pas affecté les résultats expérimentaux obtenus. Les indices de flux optique de translation et de divergence ont ensuite été mesurés en utilisant deux magnitudes de flux optique perçues par deux capteurs de flux optique sur un hexarotor.

Tests de l'odomètre visuel SOFIa sur un hexarotor

L'odomètre visuel SOFIa a été testé pour la première fois sur un hexarotor suivant des trajectoires circulaires rebondissantes de $50m$ de long dans une arène de vol, dans des conditions de forte et de faible luminosité (voir Figure 10.9). L'utilisation d'informations sur les trajectoires oscillantes pour améliorer la mesure des indices de

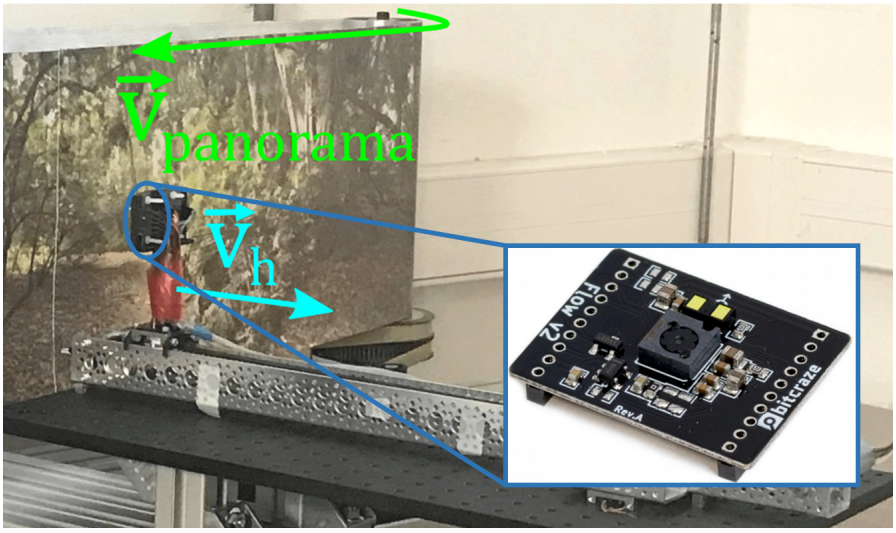

Figure 10.8: Le banc d'essai est composé de deux capteurs de flux optique placés sur un chariot à ϕ et $-\phi$ (avec $\phi = 15\,\text{deg}$) par rapport à l'axe horizontal z et placés sur une glissière devant un panorama. Un moteur à courant continu connecté à l'extrémité de la glissière opposée au panorama induit un mouvement oscillatoire de va-et-vient du chariot sur l'axe horizontal z à la vitesse V_h (en bleu). Le panorama se déplace sur l'axe x à une vitesse variable $V_{panorama}$ (en vert).

flux optique de translation et de divergence a également été étudiée. Deux stratégies de fusion de capteurs, basées respectivement sur une connaissance préalable précise et approximative des variations de flux optique, ont été présentées et testées expérimentalement sur l'hexarotor équipé de quatre capteurs de flux optique. Les résultats expérimentaux obtenus montrent que les stratégies de fusion de capteurs permettent une mesure plus fiable des indices de flux optique grâce à des Filtres de Kalman (KF) supplémentaires, même lorsque seule une connaissance préalable approximative des variations du flux optique (seulement la forme générale et le temps des oscillations au cours de la trajectoire) est prise en compte. Cette connaissance préalable peut être considérée comme acceptable, car la forme générale et le temps des oscillations sont imposés par le drone lui-même sur sa trajectoire vers l'avant. Les stratégies de fusion de capteurs ont réduit l'erreur dans l'estimation de la hauteur de vol et donc le pourcentage d'erreur dans l'estimation de la distance parcourue dans tous les cas considérés, améliorant ainsi les performances odométriques (voir Figure 10.10). Les résultats n'ont pas été affectés par les conditions de luminosité. Des tests préliminaires ont également été effectués en extérieur, où l'hexarotor a suivi des trajectoires longitudinales rebondissantes de $20m$ de long sur un terrain irrégulier en présence de vent. Les considérations faites pour les vols en intérieur se sont également avérées valables pour les quelques tests en extérieur réalisés.

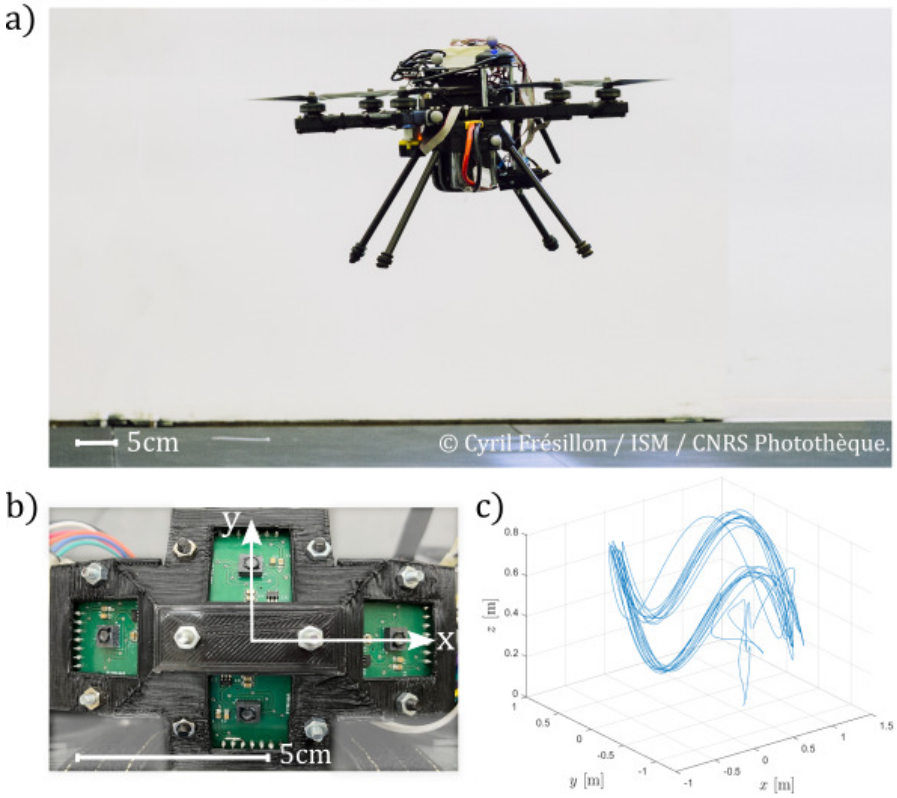

Figure 10.9: a) Hexarotor équipé de 4 capteurs de flux optique orientés vers le sol volant le long d'une trajectoire circulaire rebondissante dans une arène de vol. b) Deux capteurs de flux optique ont été placés le long de l'axe longitudinal x à des angles $\phi = \pm 30$ deg par rapport à l'axe vertical z de l'hexarotor, tandis que les deux autres capteurs de flux optique ont été placés le long de l'axe latéral y à des angles $\phi = \pm 30$ deg par rapport à l'axe z. c) Exemple d'une trajectoire sur une distance de $53m$ à une fréquence d'oscillation de $0.28Hz$.

La réorientation de la tête augmente la fiabilité de l'odomètre visuel des abeilles

Une stratégie odométrique visuelle, appelée SuRf (Surface Reference based), basée sur la mise à l'échelle du flux optique de translation toujours perçu perpendiculairement à la surface survolée a également été présentée. La stratégie SuRf consiste à réorienter constamment le tangage de l'œil composé de l'abeille simulé pour que l'équateur de son oeil composé reste parallèle à la surface survolée. Ainsi, la stratégie SuRf permet d'évaluer les longueurs des pentes et autres périmètres des formes survolées. la stratégie SuRf a été testée sur des simulations en milieu ouvert de $70m$ de long en présence de vent et d'irrégularités du terrain dans un nombre total de 81 conditions paramétriques différentes. Les performances odométriques de la stratégie SuRf ont ensuite été comparées à celles de la stratégie SOFIa brute, dans laquelle le

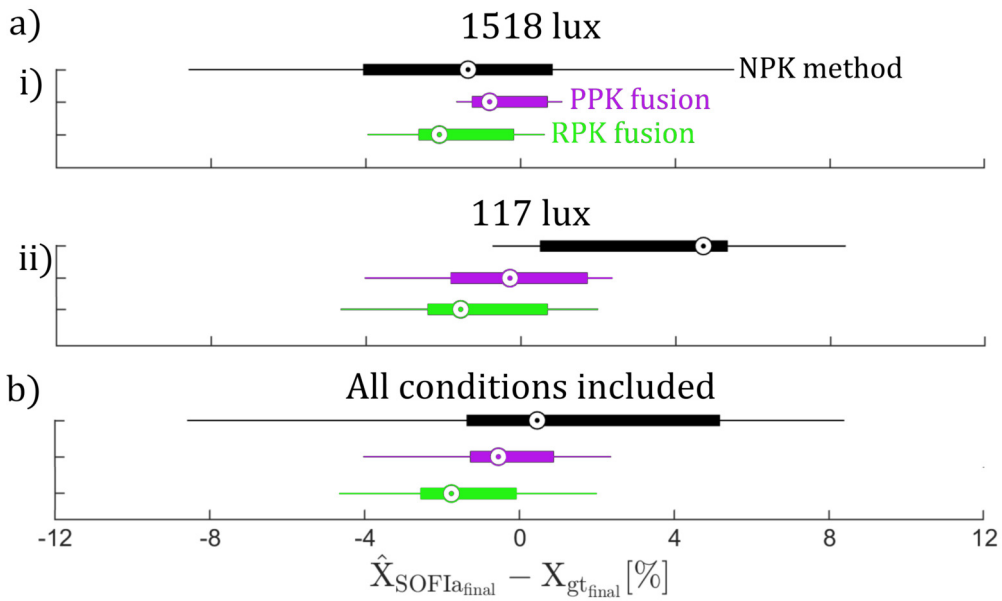

Figure 10.10: Distributions des erreurs finales en pourcentage des estimations de la distance parcourue $\hat{X}_{SOFIa}$ par rapport à la vérité terrain X_{gt} (parcourue le long de l'axe x) pour 7 ensembles de données enregistrés à $1518lux$ et 7 ensembles de données enregistrés à $117lux$. a.i) Pour une luminosité de $1518lux$, la valeur médiane est de $1,14\%$ dans le cas de la méthode sans connaissance préalable des variations du flux optique (NPK, en noir), -0.8% dans celle de la stratégie avec connaissance précise des variations du flux optique (PPK, en violet) et -1.55% dans celle de la stratégie avec connaissance approximative des variations du flux optique (RPK, en vert). a.ii) Pour une luminosité de $117lux$, la valeur médiane est de $4,73\%$ avec la méthode NPK, $0,27\%$ avec la stratégie PPK et $1,14\%$ avec la stratégie RPK. b) En combinant les 14 ensembles de données enregistrés, la valeur médiane est de 0.47% avec la méthode NPK, $-0,53\%$ avec la stratégie PPK et $-1,34\%$ avec la stratégie RPK.

réorientation du plan visuel n'est pas réalisée. La distribution des erreurs finales en pourcentage des estimations de la distance parcourue obtenues avec la stratégie SuRf était moins étendue et avait une valeur moyenne après convergence plus faible que celle obtenue avec la stratégie SOFIa brute testée dans les mêmes conditions. Les résultats obtenus montrent que la perception d'indices de flux optique perpendiculairement à la surface survolée améliore les performances de l'odomètre visuel des abeilles lorsque les abeilles doivent tout de même suivre un terrain très irrégulier. Une implémentation sur drone n'a cependant pas encore été réalisée.

Conclusion

Perspectives pour les applications robotiques aériennes

La stratégie odométrique visuelle minimaliste SOFIa présentée dans cette thèse peut être implémentée sur de robots volants, et plus particulièrement sur de micro- et nano-drones qui présentent des contraintes de vitesse, de taille, de poids et de puissance (*SSWaP*), en raison de :

- le faible poids des capteurs de flux optique, qui s'élève à environ $1-2gr$ pour chaque capteur, y compris la carte de circuit imprimé,
- la faible puissance de calcul nécessaire pour mesurer les indices de flux optique avec les capteurs de flux optique.

Ainsi, la méthode SOFIa permet de réaliser une odométrie visuelle précise sans avoir recours à des algorithmes lourds en calcul pour traiter le flux d'images capturées par une ou plusieurs caméras. La méthode SOFIa est plus efficace dans des environnements à fort contraste et dans des conditions de luminosité qui permettent de mesurer avec précision les indices de flux optique de translation et de divergence. Cependant, les résultats expérimentaux illustrés dans cette thèse montrent qu'il est possible de mesurer les indices de flux optique de translation et de divergence sous des luminosité aussi faibles que $117lux$. La mesure des indices de flux optique pourrait être possible même pour des luminosités plus faibles, en fonction des capteurs de flux optique utilisés.
L'odomètre visuel SOFIa est particulièrement intéressant pour les applications robotiques aériennes se déroulant dans des environnements où le GPS n'est disponible que par intermittence ou pas du tout (comme les bâtiments ou les tunnels) pour estimer la distance parcourue afin de voler de babise en balise. Les estimations de la distance parcourue sont sujettes à une petite erreur cumulative, car la stratégie odométrique est une méthode à l'estime basée sur l'intégration du flux optique remis à l'échelle et n'utilise aucun mécanisme de rétroaction avec l'environnement visuel. Cependant, l'odomètre visuel SOFIa est suffisamment exact et précis pour permettre à un drone de se rapprocher d'une cible sans utiliser de GPS, à l'intérieur comme à l'extérieur. Cette stratégie odométrique minimaliste basée sur le flux optique pourrait également être utilisée pour permettre à un drone d'évaluer s'il revient à proximité de sa station de base sans avoir besoin de GPS.

Retour pour la biologie

Afin d'atteindre une source de nourriture située à proximité immédiate, les abeilles butineuses s'appuieraient sur divers mécanismes, tels que ceux basés sur les points de repère et l'odorat. Il est donc difficile de caractériser la précision du seul odomètre visuel des abeilles, car il est difficile d'établir à quel moment de leur trajectoire, les abeilles concluent qu'elles ont atteint leur cible. Cependant, les abeilles sont capables

de retrouver l'emplacement d'une source de nourriture et de le communiquer à leurs congénères pendant la danse en huit avec suffisamment de précision pour pouvoir butiner.
L'odomètre visuel SOFIa est basé uniquement sur des indices visuels biologiquement plausibles et prend en compte les performances odométriques observées chez les abeilles butineuses. Ainsi, on peut dire que le modèle SOFIa est biologiquement plausible même s'il n'est pas complètement contraint sur le plan anatomique.
Dans cette thèse, le modèle SOFIa a été testé dans des conditions similaires à celles d'un milieu ouvert ou d'un très grand tunnel, où les abeilles semblent osciller à des fréquences plus basses. Dans ces conditions, le régulateur de flux optique ventral de l'abeille simulée est libre d'ajuster son altitude sans être contraint par la hauteur d'un tunnel. L'impact de la configuration géométrique d'un tunnel sur la hauteur de vol de l'abeille et donc sur les performances de l'odomètre visuel est plus prononcé dans les tunnels étroits et à toit bas.
La distribution et la précision des résultats obtenus avec le modèle SOFIa correspondent au fait que les indices visuels, plus précisément le flux optique, peuvent alimenter de manière fiable l'odomètre visuel des abeilles sur des distances de l'ordre de quelques centaines de mètres, quelle que soit leur trajectoire. De plus, le modèle SOFIa serait fiable quels que soient l'unité de base et le codage dans lesquels le flux d'information est traité, y compris ceux éventuellement utilisés par les abeilles butineuses.

Bibliography

[1] I.P. Alonso, D.F. Llorca, M. Gavilan, et al. “Accurate global localization using visual odometry and digital maps on urban environments”. In: *IEEE Transactions on Intelligent Transportation Systems* 13.4 (2012), pp. 1535–1545 (cit. on p. 37).

[2] P. Anandan. “A computational framework and an algorithm for the measurement of visual motion”. In: *International Journal of Computer Vision* 2.3 (1989), pp. 283–310 (cit. on p. 50).

[3] M.J. Anderson, J.G. Sullivan, T.K. Horiuchi, et al. “A bio-hybrid odor-guided autonomous palm-sized air vehicle”. In: *Bioinspiration & Biomimetics* 16.2 (2020), p. 026002 (cit. on p. 32).

[4] M.O.A. Aqel, M.H. Marhaban, M.I. Saripan, et al. “Review of visual odometry: types, approaches, challenges, and applications”. In: *SpringerPlus* 5.1 (2016), pp. 1–26 (cit. on pp. 30, 31, 33, 34, 172, 173).

[5] A.A. Argyros, D.P. Tsakiris, and C. Groyer. “Biomimetic centering behavior [mobile robots with panoramic sensors]”. In: *IEEE Robotics & Automation Magazine* 11.4 (2004), pp. 21–30 (cit. on p. 53).

[6] H. Azartash, N. Banai, and T.Q. Nguyen. “An integrated stereo visual odometry for robotic navigation”. In: *Robotics and Autonomous Systems* 62.4 (2014), pp. 414–421 (cit. on p. 37).

[7] E. Baird, N. Boeddeker, M.R. Ibbotson, et al. “A universal strategy for visually guided landing”. In: *Proceedings of the National Academy of Sciences* 110.46 (2013), pp. 18686–18691 (cit. on pp. 69, 169).

[8] E. Baird, N. Boeddeker, and M.V. Srinivasan. “The effect of optic flow cues on honeybee flight control in wind”. In: *Proceedings of the Royal Society B* 288.1943 (2021), p. 20203051 (cit. on pp. 61, 80, 169, 176).

[9] E. Baird, T. Kornfeldt, and M. Dacke. “Minimum viewing angle for visually guided ground speed control in bumblebees”. In: *Journal of Experimental Biology* 213.10 (2010), pp. 1625–1632 (cit. on p. 47).

[10] E. Baird, M.V. Srinivasan, S. Zhang, et al. “Visual control of flight speed in honeybees”. In: *Journal of experimental biology* 208.20 (2005), pp. 3895–3905 (cit. on pp. 46, 47, 169).

[11] S. Baker, D. Scharstein, J.P. Lewis, et al. “A database and evaluation methodology for optical flow”. In: *International journal of computer vision* 92.1 (2011), pp. 1–31 (cit. on pp. 49, 50).

[12] T.C. Baker and K.F. Haynes. “Pheromone-mediated optomotor anemotaxis and altitude control exhibited by male oriental fruit moths in the field”. In: *Physiological Entomology* 21.1 (1996), pp. 20–32 (cit. on pp. 61, 80, 176).

[13] G. Baratoff, C. Toepfer, and H. Neumann. “Combined space-variant maps for optical-flow-based navigation”. In: *Biological Cybernetics* 83.3 (2000), pp. 199–209 (cit. on p. 56).

[14] J.L. Barron, D.J. Fleet, and S.S. Beauchemin. “Performance of optical flow techniques”. In: *International journal of computer vision* 12.1 (1994), pp. 43–77 (cit. on p. 49).

[15] G.L. Barrows. “Optic flow sensors for MAV navigation”. In: *Fixed, flapping and rotary vehicles at very low Reynolds Numbers, Proceedings of the Conference, Notre Dame, IN*. 2000, pp. 464–476 (cit. on p. 56).

[16] L. Bergantin, C. Coquet, J. Dumon, et al. “Indoor and outdoor in-flight odometry based solely on optic flows with oscillatory trajectories”. In: *International Journal of Micro Air Vehicles* 15 (2023), p. 17568293221148380 (cit. on pp. 148, 149).

[17] L. Bergantin, C. Coquet, A. Negre, et al. “Minimalistic in-flight odometry based on two optic flow sensors along a bouncing trajectory”. In: *IEEE International Conference on Control, Automation and Systems (ICCAS)*. Busan, South Korea, Dec. 2022 (cit. on p. 115).

[18] L. Bergantin, C. Coquet, A. Negre, et al. “Using trajectory oscillation timing improves in-flight odometry based solely on optic flows”. In: *13^{th} International Micro Air Vehicle Conference*. Ed. by G. de Croon and C. De Wagter. Delft, the Netherlands, Sept. 2022, pp. 66–74 (cit. on pp. 149, 152).

[19] L. Bergantin, N. Harbaoui, T. Raharijaona, et al. “Oscillations make a self-scaled model for honeybees’ visual odometer reliable regardless of flight trajectory”. In: *Journal of the Royal Society Interface* 18.182 (2021), p. 20210567 (cit. on pp. 115, 120, 131, 148).

[20] L. Bergantin, T. Raharijaona, and F. Ruffier. “Estimation of the distance from a surface based on local optic flow divergence”. In: *2021 International Conference on Unmanned Aircraft Systems (ICUAS)*. IEEE. 2021, pp. 1291–1298 (cit. on pp. 115, 119, 148, 152).

[21] S. Bermúdez i Badia, U. Bernardet, and P.F.M.J. Verschure. “Non-linear neuronal responses as an emergent property of afferent networks: A case study of the locust lobula giant movement detector”. In: *PLoS computational biology* 6.3 (2010), e1000701 (cit. on p. 56).

[22] M. Bertozzi, A. Broggi, A. Fascioli, et al. “Stereo vision-based vehicle detection”. In: *Proceedings of the IEEE Intelligent Vehicles Symposium 2000 (Cat. No. 00TH8511)*. IEEE. 2000, pp. 39–44 (cit. on p. 96).

[23] A. Beyeler, J.C. Zufferey, and D. Floreano. "3D vision-based navigation for indoor microflyers". In: *Proceedings 2007 IEEE International Conference on Robotics and Automation*. IEEE. 2007, pp. 1336–1341 (cit. on p. 56).

[24] A. Beyeler, J.C. Zufferey, and D. Floreano. "Vision-based control of near-obstacle flight". In: *Autonomous robots* 27.3 (2009), pp. 201–219 (cit. on pp. 54, 56, 175).

[25] N.J. Bidwell and L.J. Goodman. "Possible functions of a population of descending neurons in the honeybee's visuo-motor pathway". In: *Apidologie* 24.3 (1993), pp. 333–354 (cit. on p. 80).

[26] M.J. Black and P. Anandan. "The robust estimation of multiple motions: Parametric and piecewise-smooth flow fields". In: *Computer vision and image understanding* 63.1 (1996), pp. 75–104 (cit. on p. 49).

[27] J. Borenstein and L. Feng. "Measurement and correction of systematic odometry errors in mobile robots". In: *IEEE Transactions on robotics and automation* 12.6 (1996), pp. 869–880 (cit. on p. 30).

[28] A. Borst and J. Haag. "Neural networks in the cockpit of the fly". In: *Journal of Comparative Physiology A* 188.6 (2002), pp. 419–437 (cit. on p. 24).

[29] H.D. Bräuninger. "Über den Einfluss meteorologischer Faktoren auf die Entfernungsweisung im Tanz der Bienen". In: *Zeitschrift für vergleichende Physiologie* 48.1 (1964), pp. 1–130 (cit. on pp. 74, 79).

[30] A. Briod, J.-C. Zufferey, and D. Floreano. "A method for ego-motion estimation in micro-hovering platforms flying in very cluttered environments". In: *Autonomous Robots* 40.5 (2016), pp. 789–803 (cit. on p. 69).

[31] E. Buchner. "Behavioural analysis of spatial vision in insects". In: *Photoreception and vision in invertebrates*. Springer, 1984, pp. 561–621 (cit. on pp. 44, 45).

[32] R. Bunschoten and B. Krose. "Robust scene reconstruction from an omnidirectional vision system". In: *IEEE Transactions on Robotics and Automation* 19.2 (2003), pp. 351–357 (cit. on p. 37).

[33] A. Burton and J. Radford. *Thinking in perspective: critical essays in the study of thought processes*. Vol. 646. Routledge, 1978 (cit. on pp. 43, 173).

[34] J. Campbell, R. Sukthankar, I. Nourbakhsh, et al. "A robust visual odometry and precipice detection system using consumer-grade monocular vision". In: *Proceedings of the 2005 IEEE International Conference on robotics and automation*. IEEE. 2005, pp. 3421–3427 (cit. on p. 35).

[35] J.S. Chahl, M.V. Srinivasan, and S.W. Zhang. "Landing strategies in honeybees and applications to uninhabited airborne vehicles". In: *The International Journal of Robotics Research* 23.2 (2004), pp. 101–110 (cit. on pp. 51, 56).

[36] H. Chao, Y. Gu, and M. Napolitano. "A survey of optical flow techniques for robotics navigation applications". In: *Journal of Intelligent & Robotic Systems* 73.1 (2014), pp. 361–372 (cit. on pp. 49, 51).

[37] D. Chen, H. Sheng, Y. Chen, et al. "Fractional-order variational optical flow model for motion estimation". In: *Philosophical Transactions of the Royal Society A: Mathematical, Physical and Engineering Sciences* 371.1990 (2013), p. 20120148 (cit. on p. 50).

[38] J. Cheng, Z. Wang, H. Zhou, et al. "DM-SLAM: A feature-based SLAM system for rigid dynamic scenes". In: *ISPRS International Journal of Geo-Information* 9.4 (2020), p. 202 (cit. on p. 38).

[39] Y.M. Chukewad and S. Fuller. "Yaw control of a hovering flapping-wing aerial vehicle with a passive wing hinge". In: *IEEE Robotics and Automation Letters* 6.2 (2021), pp. 1864–1871 (cit. on p. 32).

[40] M. Collett and T.S. Collett. "How do insects use path integration for their navigation?" In: *Biological cybernetics* 83.3 (2000), pp. 245–259 (cit. on pp. 29, 69, 79, 148, 172).

[41] T.S. Collett. "Peering-a locust behaviour pattern for obtaining motion parallax information". In: *Journal of experimental Biology* 76.1 (1978), pp. 237–241 (cit. on p. 97).

[42] T.S. Collett. "Path integration: how details of the honeybee waggle dance and the foraging strategies of desert ants might help in understanding its mechanisms". In: *Journal of Experimental Biology* 222.11 (2019), jeb205187 (cit. on p. 168).

[43] G. Cook and F. Zhang. *Mobile robots: Navigation, control and sensing, surface robots and AUVs*. John Wiley & Sons, 2020 (cit. on p. 34).

[44] D. Coombs and K. Roberts. "'Bee-bot': using peripheral optical flow to avoid obstacles". In: *Intelligent Robots and Computer Vision XI: Algorithms, Techniques, and Active Vision*. Vol. 1825. SPIE. 1992, pp. 714–721 (cit. on p. 53).

[45] P. Corke, D. Strelow, and S. Singh. "Omnidirectional visual odometry for a planetary rover". In: *2004 IEEE/RSJ International Conference on Intelligent Robots and Systems (IROS)(IEEE Cat. No. 04CH37566)*. Vol. 4. IEEE. 2004, pp. 4007–4012 (cit. on p. 37).

[46] V. Creuze. "Monocular odometry for underwater vehicles with online estimation of the scale factor". In: *IFAC 2017 World Congress*. 2017 (cit. on pp. 50, 52, 115, 148).

[47] G. CHE de Croon. "Monocular distance estimation with optical flow maneuvers and efference copies: a stability-based strategy". In: *Bioinspiration & biomimetics* 11.1 (2016), p. 016004 (cit. on pp. 56, 96, 97, 115, 148).

[48] A. Cumani. "Feature localization refinement for improved visual odometry accuracy". In: *Int J Circuits Syst Signal Process* 5.2 (2011), pp. 151–158 (cit. on p. 37).

[49] G. CHE De Croon, J.J.G. Dupeyroux, S.B. Fuller, et al. "Insect-inspired AI for autonomous robots". In: *Science Robotics* 7.67 (2022), eabl6334 (cit. on p. 29).

[50] A. Denuelle and M.V. Srinivasan. “A sparse snapshot-based navigation strategy for UAS guidance in natural environments”. In: *2016 IEEE International Conference on Robotics and Automation (ICRA)*. IEEE. 2016, pp. 3455–3462 (cit. on pp. 37, 69, 115).

[51] D. Dhingra, Y.M. Chukewad, and S.B. Fuller. “A device for rapid, automated trimming of insect-sized flying robots”. In: *IEEE Robotics and Automation Letters* 5.2 (2020), pp. 1373–1380 (cit. on p. 32).

[52] J.K. Douglass and N.J. Strausfeld. “Visual motion-detection circuits in flies: parallel direction-and non-direction-sensitive pathways between the medulla and lobula plate”. In: *Journal of Neuroscience* 16.15 (1996), pp. 4551–4562 (cit. on p. 24).

[53] I. Dryanovski, R.G. Valenti, and J. Xiao. “Fast visual odometry and mapping from RGB-D data”. In: *2013 IEEE international conference on robotics and automation*. IEEE. 2013, pp. 2305–2310 (cit. on p. 38).

[54] A.P. Duchon and W.H. Warren. “Robot navigation from a Gibsonian viewpoint”. In: *Proceedings of IEEE international conference on systems, man and cybernetics*. Vol. 3. IEEE. 1994, pp. 2272–2277 (cit. on pp. 48, 56).

[55] M. Egelhaaf, R. Kern, H.G. Krapp, et al. “Neural encoding of behaviourally relevant visual-motion information in the fly”. In: *Trends in neurosciences* 25.2 (2002), pp. 96–102 (cit. on p. 24).

[56] H. Eichner, M. Joesch, B. Schnell, et al. “Internal structure of the fly elementary motion detector”. In: *Neuron* 70.6 (2011), pp. 1155–1164 (cit. on p. 24).

[57] J. Engel, T. Schöps, and D. Cremers. “LSD-SLAM: Large-scale direct monocular SLAM”. In: *European conference on computer vision*. Springer. 2014, pp. 834–849 (cit. on p. 38).

[58] H. Esch and J. Burns. “Distance estimation by foraging honeybees”. In: *Journal of Experimental Biology* 199.1 (1996), pp. 155–162 (cit. on pp. 29, 49, 63, 69, 79, 148, 169, 172).

[59] H. Esch, F. Goller, and J.E. Burns. “Honeybee waggle dances: the “energy hypothesis” and thermoregulatory behavior of foragers”. In: *Journal of Comparative Physiology B* 163.8 (1994), pp. 621–625 (cit. on pp. 28, 68).

[60] H.E. Esch and J.E. Burns. “Honeybees use optic flow to measure the distance of a food source”. In: *Naturwissenschaften* 82.1 (1995), pp. 38–40 (cit. on pp. 27–29, 49, 69, 148, 169, 172).

[61] H.E. Esch, S. Zhang, M.V. Srinivasan, et al. “Honeybee dances communicate distances measured by optic flow”. In: *Nature* 411.6837 (2001), pp. 581–583 (cit. on pp. 29, 48, 49, 63, 69, 79, 148, 169, 172).

[62] C. Evangelista, P. Kraft, M. Dacke, et al. “The moment before touchdown: landing manoeuvres of the honeybee Apis mellifera”. In: *Journal of Experimental Biology* 213.2 (2010), pp. 262–270 (cit. on p. 82).

[63] C. Evangelista, P. Kraft, M. Dacke, et al. "Honeybee navigation: critically examining the role of the polarization compass". In: *Philosophical Transactions of the Royal Society B: Biological Sciences* 369.1636 (2014), p. 20130037 (cit. on p. 168).

[64] F. Expert and F. Ruffier. "Flying over uneven moving terrain based on optic-flow cues without any need for reference frames or accelerometers". In: *Bioinspiration and Biomimetics* 10 (2015) (cit. on pp. 54, 59, 96, 115, 148, 149, 152, 175).

[65] F. Expert, S. Viollet, and F. Ruffier. "A mouse sensor and a 2-pixel motion sensor exposed to continuous illuminance changes". In: *IEEE Sensors* (2011), pp. 974–977. ISSN: 1930-0395 (cit. on pp. 51, 97).

[66] J. Fabian and G.M. Clayton. "Error analysis for visual odometry on indoor, wheeled mobile robots with 3-d sensors". In: *IEEE/ASME Transactions on Mechatronics* 19.6 (2014), pp. 1896–1906 (cit. on p. 37).

[67] J.R. Fabian and G.M. Clayton. "Adaptive visual odometry using RGB-D cameras". In: *2014 IEEE/ASME International Conference on Advanced Intelligent Mechatronics*. IEEE. 2014, pp. 1533–1538 (cit. on p. 37).

[68] M. Faessler, F. Fontana, C. Forster, et al. "Autonomous, vision-based flight and live dense 3D mapping with a quadrotor micro aerial vehicle". In: *Journal of Field Robotics* 33.4 (2016), pp. 431–450 (cit. on pp. 38, 115).

[69] Z. Fang and Y. Zhang. "Experimental evaluation of RGB-D visual odometry methods". In: *International Journal of Advanced Robotic Systems* 12.3 (2015), p. 26 (cit. on p. 37).

[70] D. Fernandez and A. Price. "Visual odometry for an outdoor mobile robot". In: *IEEE Conference on Robotics, Automation and Mechatronics, 2004*. Vol. 2. IEEE. 2004, pp. 816–821 (cit. on p. 31).

[71] D.J. Fleet and A.D. Jepson. "Computation of component image velocity from local phase information". In: *International journal of computer vision* 5.1 (1990), pp. 77–104 (cit. on p. 50).

[72] D. Floreano, R. Pericet-Camara, S. Viollet, et al. "Miniature curved artificial compound eyes". In: *Proceedings of the National Academy of Sciences* 110.23 (2013), pp. 9267–9272 (cit. on p. 97).

[73] C. Forster, M. Pizzoli, and D. Scaramuzza. "SVO: Fast semi-direct monocular visual odometry". In: *2014 IEEE international conference on robotics and automation (ICRA)*. IEEE. 2014, pp. 15–22 (cit. on p. 37).

[74] N. Franceschini. "Sampling of the visual environment by the compound eye of the fly: fundamentals and applications". In: *Photoreceptor optics* (1975), pp. 98–125 (cit. on p. 23).

[75] N. Franceschini. “Small brains, smart machines: from fly vision to robot vision and back again”. In: *Proceedings of the IEEE* 102.5 (2014), pp. 751–781 (cit. on pp. 53, 174).

[76] N. Franceschini, J.M. Pichon, and C. Blanes. “From insect vision to robot vision”. In: *Philosophical Transactions of The Royal Society Of London. Series B: Biological Sciences* 337.1281 (1992), pp. 283–294 (cit. on pp. 53, 174).

[77] N. Franceschini, A. Riehle, and A. Le Nestour. *Directionally Selective Motion Detection By Insect Neurons*. 1989 (cit. on p. 24).

[78] N. Franceschini, F. Ruffier, and J. Serres. “A bio-inspired flying robot sheds light on insect piloting abilities”. In: *Current Biology* 17.4 (2007), pp. 329–335 (cit. on pp. 53, 56, 69, 71, 154).

[79] M.O. Franz and H.A. Mallot. “Biomimetic robot navigation”. In: *Robotics and autonomous Systems* 30.1-2 (2000), pp. 133–153 (cit. on pp. 53, 174).

[80] C. A. Freas and M. L. Spetch. “Varieties of visual navigation in insects”. In: *Animal Cognition* (2022), pp. 1–24 (cit. on p. 23).

[81] E. Frontoni. *Vision based mobile robotics: mobile robot localization using vision sensors and active probabilistic approaches*. Lulu. com, 2012 (cit. on p. 35).

[82] S. Fuller, Z. Yu, and Y.P. Talwekar. “A gyroscope-free visual-inertial flight control and wind sensing system for 10-mg robots”. In: *Science Robotics* 7.72 (2022), eabq8184 (cit. on pp. 29, 32, 38, 166).

[83] R. García-García, M.A. Sotelo, I. Parra, et al. “3D visual odometry for road vehicles”. In: *Journal of Intelligent and Robotic Systems* 51.1 (2008), pp. 113–134 (cit. on p. 37).

[84] K.K. Garvey. *https://ucanr.edu/blogs/blogcore/postdetail.cfm?postnum=26759*. 2018. URL: https://ucanr.edu/blogs/blogcore/postdetail.cfm?postnum=26759 (visited on 10/2022) (cit. on p. 24).

[85] J.J. Gibson. “The perception of the visual world.” In: (1950) (cit. on pp. 43, 44, 62, 117, 150, 173, 174, 176).

[86] R. Gonzalez, F. Rodriguez, J.L. Guzman, et al. “Combined visual odometry and visual compass for off-road mobile robots localization”. In: *Robotica* 30.6 (2012), pp. 865–878 (cit. on pp. 34–37).

[87] R. Gonzalez, F. Rodriguez, J.L. Guzman, et al. “Control of off-road mobile robots using visual odometry and slip compensation”. In: *Advanced Robotics* 27.11 (2013), pp. 893–906 (cit. on pp. 37, 38, 173).

[88] L.J. Goodman, W.A. Fletcher, R.G. Guy, et al. “Motion sensitive descending interneurons, ocellar L D neurons and neck motoneurons in the bee: a neural substrate for visual course control in Apis mellifera”. In: *Neurobiology and behavior of honeybees*. Springer, 1987, pp. 158–171 (cit. on p. 80).

[89] P. Goyal, J.L. van Leeuwen, and F.T. Muijres. "Bumblebees land rapidly by intermittently accelerating and decelerating toward the surface during visually guided landings". In: *Iscience* 25.5 (2022), p. 104265 (cit. on pp. 48, 169).

[90] W.E. Green, P.Y. Oh, and G. Barrows. "Flying insect inspired vision for autonomous aerial robot maneuvers in near-earth environments". In: *IEEE International Conference on Robotics and Automation, 2004. Proceedings. ICRA'04. 2004.* Vol. 3. IEEE. 2004, pp. 2347–2352 (cit. on p. 56).

[91] S. Griffiths, J. Saunders, A. Curtis, et al. "Maximizing miniature aerial vehicles". In: *IEEE Robotics & Automation Magazine* 13.3 (2006), pp. 34–43 (cit. on p. 51).

[92] D.V. Hamme, W. Goeman, P. Veelaert, et al. "Robust monocular visual odometry for road vehicles using uncertain perspective projection". In: *EURASIP Journal on Image and Video Processing* 2015.1 (2015), pp. 1–21 (cit. on p. 37).

[93] M. Hartbauer. "Simplified bionic solutions: a simple bio-inspired vehicle collision detection system". In: *Bioinspiration & biomimetics* 12.2 (2017), p. 026007 (cit. on pp. 53, 174).

[94] R. Hartley and A. Zisserman. *Multiple view geometry in computer vision*. Cambridge university press, 2003 (cit. on p. 37).

[95] K. Hausen. "Motion sensitive interneurons in the optomotor system of the fly". In: *Biological Cybernetics* 45.2 (1982), pp. 143–156 (cit. on p. 24).

[96] D.M. Helmick, Y. Cheng, D.S. Clouse, et al. "Path following using visual odometry for a mars rover in high-slip environments". In: *2004 IEEE Aerospace Conference Proceedings (IEEE Cat. No. 04TH8720)*. Vol. 2. IEEE. 2004, pp. 772–789 (cit. on p. 37).

[97] H. Heran. "Ein Beitrag zur Frage nach der Wahrnehmungsgrundlage der Entfernungsweisung der Bienen (Apis mellifica L.)" In: *Zeitschrift für vergleichende Physiologie* 38.1-2 (1956), pp. 168–218 (cit. on p. 79).

[98] B. Herissé, T. Hamel, R. Mahony, et al. "Landing a VTOL unmanned aerial vehicle on a moving platform using optical flow". In: *IEEE Transactions on robotics* 28.1 (2011), pp. 77–89 (cit. on pp. 54, 69, 96, 115, 148).

[99] H.W. Ho, G. CHE de Croon, and Q. Chu. "Distance and velocity estimation using optical flow from a monocular camera". In: *International Journal of Micro Air Vehicles* 9.3 (2017), pp. 198–208 (cit. on pp. 38, 45, 56, 69, 83, 96–98, 107, 115, 119, 148, 150, 162, 166).

[100] H.W. Ho, G. CHE de Croon, E. Van Kampen, et al. "Adaptive gain control strategy for constant optical flow divergence landing". In: *IEEE Transactions on Robotics* 34.2 (2018), pp. 508–516 (cit. on p. 63).

[101] A.D. Horchler, R.E. Reeve, B. Webb, et al. "Robot phonotaxis in the wild: a biologically inspired approach to outdoor sound localization". In: *Advanced robotics* 18.8 (2004), pp. 801–816 (cit. on pp. 53, 174).

[102] B.K.P. Horn and B.G. Schunck. "Determining optical flow". In: *Artificial intelligence* 17.1-3 (1981), pp. 185–203 (cit. on p. 49).

[103] J. Horn and G. Schmidt. "Continuous localization of a mobile robot based on 3D-laser-range-data, predicted sensor images, and dead-reckoning". In: *Robotics and Autonomous Systems* 14.2-3 (1995), pp. 99–118 (cit. on p. 35).

[104] G. A. Horridge. "The compound eye of insects". In: *Scientific American* 237.1 (1977), pp. 108–121 (cit. on pp. 23, 24, 148).

[105] A. Howard. "Real-time stereo visual odometry for autonomous ground vehicles". In: *2008 IEEE/RSJ international conference on intelligent robots and systems*. IEEE. 2008, pp. 3946–3952 (cit. on pp. 35, 37).

[106] A.S. Huang, A. Bachrach, P. Henry, et al. "Visual odometry and mapping for autonomous flight using an RGB-D camera". In: *Robotics research*. Springer, 2017, pp. 235–252 (cit. on p. 38).

[107] J.S. Humbert. "Bio-inspired visuomotor convergence in navigation and flight control systems". PhD thesis. California Institute of Technology, 2005 (cit. on pp. 23, 25, 148).

[108] J.S. Humbert, A. Hyslop, and M. Chinn. "Experimental validation of wide-field integration methods for autonomous navigation". In: *2007 IEEE/RSJ International Conference on Intelligent Robots and Systems*. IEEE. 2007, pp. 2144–2149 (cit. on p. 53).

[109] A.M. Hyslop and J.S. Humbert. "Autonomous navigation in three-dimensional urban environments using wide-field integration of optic flow". In: *Journal of guidance, control, and dynamics* 33.1 (2010), pp. 147–159 (cit. on p. 53).

[110] M.R. Ibbotson. "Wide-field motion-sensitive neurons tuned to horizontal movement in the honeybee, Apis mellifera". In: *Journal of Comparative Physiology A* 168.1 (1991), pp. 91–102 (cit. on p. 80).

[111] M.R. Ibbotson. "Evidence for velocity–tuned motion-sensitive descending neurons in the honeybee". In: *Proceedings of the Royal Society of London. Series B: Biological Sciences* 268.1482 (2001), pp. 2195–2201 (cit. on pp. 24, 80).

[112] M.R. Ibbotson and L.J. Goodman. "Response characteristics of four wide-field motion-sensitive descending interneurones in Apis Melufera". In: *Journal of Experimental Biology* 148.1 (1990), pp. 255–279 (cit. on p. 80).

[113] M.R. Ibbotson, Y.-S. Hung, H. Meffin, et al. "Neural basis of forward flight control and landing in honeybees". In: *Scientific reports* 7.1 (2017), pp. 1–15 (cit. on p. 80).

[114] F. Iida. "Biologically inspired visual odometer for navigation of a flying robot". In: *Robotics and autonomous systems* 44.3-4 (2003), pp. 201–208 (cit. on pp. 69, 96, 115, 148).

[115] A.J. Ijspeert. "Biorobotics: Using robots to emulate and investigate agile locomotion". In: *science* 346.6206 (2014), pp. 196–203 (cit. on pp. 53, 174).

[116] CentEye Inc. *https://www.centeye.com/vision-chips/vision-chip-technologies/*. 2022. URL: https://www.centeye.com/vision-chips/vision-chip-technologies/ (visited on 10/2022) (cit. on pp. 52, 53).

[117] PixArt Imaging Inc. *https://www.codico.com/en/mpattachment/file/download/id/560/*. 2022. URL: https://www.codico.com/en/mpattachment/file/download/id/560/ (visited on 10/2022) (cit. on pp. 51, 52).

[118] Y. Jiang, Y. Xu, and Y. Liu. "Performance evaluation of feature detection and matching in stereo visual odometry". In: *Neurocomputing* 120 (2013), pp. 380–390 (cit. on p. 37).

[119] F. Kendoul, I. Fantoni, and K. Nonami. "Optic flow-based vision system for autonomous 3D localization and control of small aerial vehicles". In: *Robotics and autonomous systems* 57.6-7 (2009), pp. 591–602 (cit. on pp. 37, 50, 69, 96, 115, 148).

[120] J.S. Kennedy. "The Migration of the Desert Locust (Schistocerca gregaria Forsk.). I. The Behaviour of Swarms. II. A Theory of Long-Range Migrations". In: *Philosophical Transactions of the Royal Society of London. Series B, Biological Sciences* 235.625 (1951), pp. 163–290 (cit. on p. 74).

[121] C. Kerl, J. Sturm, and D. Cremers. "Robust odometry estimation for RGB-D cameras". In: *2013 IEEE international conference on robotics and automation*. IEEE. 2013, pp. 3748–3754 (cit. on p. 37).

[122] R. Kern, N. Boeddeker, L. Dittmar, et al. "Blowfly flight characteristics are shaped by environmental features and controlled by optic flow information". In: *Journal of Experimental Biology* 215.14 (2012), pp. 2501–2514 (cit. on pp. 56, 57).

[123] J. Kim and G. Brambley. "Dual optic-flow integrated navigation for small-scale flying robots". In: *Proc. of Australasian Conference on Robotics and Automation, Brisbane, Australia*. Citeseer. 2007 (cit. on p. 51).

[124] W.H. Kirchner and M.V. Srinivasan. "Freely flying honeybees use image motion to estimate object distance". In: *Naturwissenschaften* 76.6 (1989), pp. 281–282 (cit. on pp. 47, 61, 69, 80, 86, 97, 107, 115, 148, 169, 174, 176).

[125] B.M. Kitt, J. Rehder, A.D. Chambers, et al. "Monocular visual odometry using a planar road model to solve scale ambiguity". In: (2011) (cit. on p. 36).

[126] J.J. Koenderink and A.J. van Doorn. "Facts on optic flow". In: *Biological cybernetics* 56.4 (1987), pp. 247–254 (cit. on pp. 44, 168).

[127] K. Kral. "Side-to-side head movements to obtain motion depth cues:: A short review of research on the praying mantis". In: *Behavioural Processes* 43.1 (1998), pp. 71–77 (cit. on p. 97).

[128] H.G. Krapp. "Optic Flow Processing". In: *Jaeger, D., Jung, R. (eds) Encyclopedia of Computational Neuroscience*. Springer, 2014 (cit. on p. 45).

[129] H.G. Krapp, B. Hengstenberg, and R. Hengstenberg. "Dendritic structure and receptive-field organization of optic flow processing interneurons in the fly". In: *Journal of neurophysiology* 79.4 (1998), pp. 1902–1917 (cit. on pp. 24, 45).

[130] B. Kreczmer. "Objects localization and differentiation using ultrasonic sensors". In: *Robot Localization and Map Building*. IntechOpen, 2010 (cit. on p. 35).

[131] D. Lambrinos, R. Möller, T. Labhart, et al. "A mobile robot employing insect strategies for navigation". In: *Robotics and Autonomous systems* 30.1-2 (2000), pp. 39–64 (cit. on pp. 53, 174).

[132] T. Landgraf, M. Oertel, D. Rhiel, et al. "A biomimetic honeybee robot for the analysis of the honeybee dance communication system". In: *2010 IEEE/RSJ International Conference on Intelligent Robots and Systems*. IEEE. 2010, pp. 3097–3102 (cit. on pp. 53, 174).

[133] B. Lee, K. Daniilidis, and D.D. Lee. "Online self-supervised monocular visual odometry for ground vehicles". In: *2015 IEEE International Conference on Robotics and Automation (ICRA)*. IEEE. 2015, pp. 5232–5238 (cit. on p. 37).

[134] D.N. Lee. "A theory of visual control of braking based on information about time-to-collision". In: *Perception* 5.4 (1976), pp. 437–459 (cit. on p. 48).

[135] S.H. Lee and G. CHE de Croon. "Stability-based scale estimation for monocular SLAM". In: *IEEE Robotics and Automation Letters* 3.2 (2018), pp. 780–787 (cit. on pp. 38, 115).

[136] S.Y. Lee and J.B. Song. "Mobile robot localization using optical flow sensors". In: *International Journal of Control, Automation, and Systems* 2.4 (2004), pp. 485–493 (cit. on p. 52).

[137] C. Lei and Y.H. Yang. "Optical flow estimation on coarse-to-fine region-trees using discrete optimization". In: *2009 IEEE 12th International Conference on Computer Vision*. IEEE. 2009, pp. 1562–1569 (cit. on p. 50).

[138] N. Linander, M. Dacke, and E. Baird. "Bumblebees measure optic flow for position and speed control flexibly within the frontal visual field". In: *The Journal of Experimental Biology* 218.7 (2015), pp. 1051–1059 (cit. on p. 47).

[139] Martin Lindauer. "Sonnenorientierung der Bienen unter der Äquatorsonne und zur Nachtzeit". In: *Naturwissenschaften* 44.1 (1957), pp. 1–6 (cit. on pp. 26, 172).

[140] J.P. Lindemann, H. Weiss, R. Möller, et al. "Saccadic flight strategy facilitates collision avoidance: closed-loop performance of a cyberfly". In: *Biological cybernetics* 98.3 (2008), pp. 213–227 (cit. on p. 56).

[141] K. Lingemann, A. Nüchter, J. Hertzberg, et al. "High-speed laser localization for mobile robots". In: *Robotics and autonomous systems* 51.4 (2005), pp. 275–296 (cit. on p. 35).

[142] S. Lovegrove, A.J. Davison, and J. Ibanez-Guzmán. "Accurate visual odometry from a rear parking camera". In: *2011 IEEE Intelligent Vehicles Symposium (IV)*. IEEE. 2011, pp. 788–793 (cit. on p. 37).

[143] D.G. Lowe. "Distinctive image features from scale-invariant keypoints". In: *International journal of computer vision* 60.2 (2004), pp. 91–110 (cit. on p. 50).

[144] Y. Lu, Z. Xue, Gui-Song Xia, et al. "A survey on vision-based UAV navigation". In: *Geo-spatial information science* 21.1 (2018), pp. 21–32 (cit. on pp. 36–38).

[145] B.D. Lucas, T. Kanade, et al. *An iterative image registration technique with an application to stereo vision*. Vol. 81. Vancouver, 1981 (cit. on p. 49).

[146] K.Y. Ma, P. Chirarattananon, S.B. Fuller, et al. "Controlled flight of a biologically inspired, insect-scale robot". In: *Science* 340.6132 (2013), pp. 603–607 (cit. on pp. 29, 32).

[147] S. Mafrica, A. Servel, and F. Ruffier. "Minimalistic optic flow sensors applied to indoor and outdoor visual guidance and odometry on a car-like robot." In: *Bioinspiration & biomimetics* 11.6 (2016), p. 066007 (cit. on p. 97).

[148] O. Maklouf and A. Adwaib. "Performance evaluation of GPS\INS main integration approach". In: *International Journal of Aerospace and Mechanical Engineering* 8.2 (2014), pp. 476–484 (cit. on p. 34).

[149] G.R. Martin. "Visual fields and their functions in birds". In: *Journal of Ornithology* 148.2 (2007), pp. 547–562 (cit. on p. 81).

[150] G.R. Martin. "What is binocular vision for? A birds' eye view". In: *Journal of Vision* 9.11 (2009), pp. 14–14 (cit. on p. 81).

[151] G. Martinez. "Monocular visual odometry from frame to frame intensity differences for planetary exploration mobile robots". In: *2013 IEEE Workshop on Robot Vision (WORV)*. IEEE. 2013, pp. 54–59 (cit. on p. 37).

[152] L. Matthies and S. Shafer. "Error modeling in stereo navigation". In: *IEEE Journal on Robotics and Automation* 3.3 (1987), pp. 239–248 (cit. on p. 37).

[153] C. McCarthy, N. Barnes, and R. Mahony. "A robust docking strategy for a mobile robot using flow field divergence". In: *IEEE Transactions on Robotics* 24.4 (2008), pp. 832–842 (cit. on p. 63).

[154] C. McManus, P. Furgale, and T.D. Barfoot. "Towards lighting-invariant visual navigation: An appearance-based approach using scanning laser-rangefinders". In: *Robotics and Autonomous Systems* 61.8 (2013), pp. 836–852 (cit. on p. 37).

[155] L. Meier, D. Honegger, and M. Pollefeys. "PX4: A node-based multithreaded open source robotics framework for deeply embedded platforms". In: *2015 IEEE International Conference on Robotics and Automation (ICRA)*. 2015, pp. 6235–6240 (cit. on p. 117).

[156] R. Milijas, L. Markovic, A. Ivanovic, et al. “A comparison of lidar-based slam systems for control of unmanned aerial vehicles”. In: *2021 International Conference on Unmanned Aircraft Systems (ICUAS)*. IEEE. 2021, pp. 1148–1154 (cit. on pp. 38, 115).

[157] R.J.D. Moore, S. Thurrowgood, D. Bland, et al. “A stereo vision system for uav guidance”. In: *2009 IEEE/RSJ International Conference on Intelligent Robots and Systems*. IEEE. 2009, pp. 3386–3391 (cit. on p. 96).

[158] H.P. Moravec. *Obstacle avoidance and navigation in the real world by a seeing robot rover*. Stanford University, 1980 (cit. on p. 37).

[159] V. More, H. Kumar, S. Kaingade, et al. “Visual odometry using optic flow for Unmanned Aerial Vehicles”. In: *2015 International Conference on Cognitive Computing and Information Processing(CCIP)*. 2015, pp. 1–6 (cit. on p. 114).

[160] T. Mouats, N. Aouf, A.D. Sappa, et al. “Multispectral stereo odometry”. In: *IEEE Transactions on Intelligent Transportation Systems* 16.3 (2014), pp. 1210–1224 (cit. on p. 37).

[161] R. Munguia and A. Grau. “Monocular SLAM for visual odometry”. In: *2007 IEEE International Symposium on Intelligent Signal Processing*. IEEE. 2007, pp. 1–6 (cit. on pp. 35, 173).

[162] R. Mur-Artal, J.M. Martinez Montiel, and J.D. Tardos. “ORB-SLAM: a versatile and accurate monocular SLAM system”. In: *IEEE transactions on robotics* 31.5 (2015), pp. 1147–1163 (cit. on p. 38).

[163] L. Muratet, S. Doncieux, Y. Briere, et al. “A contribution to vision-based autonomous helicopter flight in urban environments”. In: *Robotics and Autonomous Systems* 50.4 (2005), pp. 195–209 (cit. on p. 56).

[164] K. Nagatani, A. Ikeda, G. Ishigami, et al. “Development of a visual odometry system for a wheeled robot on loose soil using a telecentric camera”. In: *Advanced Robotics* 24.8-9 (2010), pp. 1149–1167 (cit. on pp. 35, 37, 38, 173).

[165] K. Nakayama and J.M. Loomis. “Optical velocity patterns, velocity-sensitive neurons, and space perception: a hypothesis”. In: *Perception* 3.1 (1974), pp. 63–80 (cit. on p. 45).

[166] S. Nedevschi, R. Danescu, D. Frentiu, et al. “High accuracy stereo vision system for far distance obstacle detection”. In: *IEEE Intelligent Vehicles Symposium, 2004*. IEEE. 2004, pp. 292–297 (cit. on p. 96).

[167] V. Neese. “Entfernungsmessung der Sammelbiene: ein energetisches und zugleich sensorisches Problem”. In: *The flying honeybee: aspects of energetics / Die fliegende Honigbiene: Aspekte der Energetik, Werner Nachtigall (ed.)* Stuttgart: Gustav Fischer, 1988 (cit. on pp. 28, 68).

[168] R. Nelson and J. Aloimonos. “Using flow field divergence for obstacle avoidance in visual navigation”. In: *Science Applications International Corp, Proceedings: Image Understanding Workshop,* vol. 2. 1988 (cit. on pp. 48, 56).

[169] K. Ni and F. Dellaert. "Stereo Tracking and Three-Point/One-Point Algorithms - A Robust Approach in Visual Odometry". In: *2006 International Conference on Image Processing*. 2006, pp. 2777–2780. DOI: 10.1109/ICIP.2006.313123 (cit. on pp. 35, 173).

[170] D. Nister, O. Naroditsky, and J. Bergen. "Visual odometry". In: *Proceedings of the 2004 IEEE Computer Society Conference on Computer Vision and Pattern Recognition, 2004. CVPR 2004.* Vol. 1. 2004, pp. I–I. DOI: 10.1109/CVPR.2004.1315094 (cit. on pp. 35, 173).

[171] D. Nistér, O. Naroditsky, and J. Bergen. "Visual odometry for ground vehicle applications". In: *Journal of Field Robotics* 23.1 (2006), pp. 3–20 (cit. on p. 35).

[172] N. Nourani-Vatani, J. Roberts, and M.V. Srinivasan. "Practical visual odometry for car-like vehicles". In: *2009 IEEE International Conference on Robotics and Automation*. IEEE. 2009, pp. 3551–3557 (cit. on pp. 31, 35, 36, 38, 173).

[173] A. Noureldin, T.B. Karamat, and J. Georgy. "Fundamentals of inertial navigation, satellite-based positioning and their integration". In: (2013) (cit. on pp. 34, 36, 172).

[174] E.G. de Oliveira. *Migratory and foraging movements in diurnal neotropical Lepidoptera: experimental studies on orientation and learning*. The University of Texas at Austin, 1998 (cit. on pp. 54, 61, 62, 148, 170, 175, 176).

[175] D. Palossi, A. Marongiu, and L. Benini. "Ultra low-power visual odometry for nano-scale unmanned aerial vehicles". In: *Design, Automation Test in Europe Conference Exhibition (DATE), 2017*. 2017, pp. 1647–1650 (cit. on p. 131).

[176] T. Poggio and N. Ancona. *Optical Flow from 1D Correlation: Application to a Simple Time-to-Crash Detector*. Tech. rep. MASSACHUSETTS INST OF TECH CAMBRIDGE ARTIFICIAL INTELLIGENCE LAB, 1993 (cit. on pp. 48, 56).

[177] G. Portelli, F. Ruffier, and N. Franceschini. "Honeybees change their height to restore their optic flow". In: *Journal of Comparative Physiology A* 196.4 (2010), pp. 307–313 (cit. on pp. 54, 57, 58, 69, 78, 115, 149, 162, 175).

[178] G. Portelli, F. Ruffier, F.L. Roubieu, et al. "Honeybees' speed depends on dorsal as well as lateral, ventral and frontal optic flows". In: *PloS one* 6.5 (2011), e19486 (cit. on pp. 46, 54, 61, 69, 78, 80, 86, 97, 107, 115, 148, 169, 174–176).

[179] G. Portelli, J. Serres, and F. Ruffier. "Altitude control in honeybees: joint vision-based learning and guidance". In: *Scientific Reports* 7.9231 (2017) (cit. on pp. 78, 79, 115, 149).

[180] G. Portelli, J. Serres, F. Ruffier, et al. "Modelling honeybee visual guidance in a 3-D environment". In: *Journal of Physiology - Paris* 104.1-2 (2010), pp. 27–39 (cit. on pp. 69, 71, 82, 154, 155, 161).

[181] A. El-Rabbany. *Introduction to GPS: the global positioning system*. Artech house, 2002 (cit. on p. 34).

[182] M.B. Reiser and M.H. Dickinson. "A test bed for insect-inspired robotic control". In: *Philosophical Transactions of the Royal Society of London. Series A: Mathematical, Physical and Engineering Sciences* 361.1811 (2003), pp. 2267–2285 (cit. on p. 56).

[183] M. Renner. "Über ein weiteres Versetzungsexperiment zur Analyse des Zeitsinnes und der Sonnenorientierung der Honigbiene". In: *Zeitschrift für vergleichende Physiologie* 42.5 (1959), pp. 449–483 (cit. on pp. 26, 172).

[184] M. Rezaei and F. Saghafi. "Optical flow-based obstacle avoidance of a fixed-wing MAV". In: *Aircraft Engineering and Aerospace Technology* (2011) (cit. on p. 56).

[185] J.R. Riley, U. Greggers, A.D. Smith, et al. "The flight paths of honeybees recruited by the waggle dance". In: *Nature* 435.7039 (2005), pp. 205–207 (cit. on pp. 79, 85, 90).

[186] F.C. Rind, R.D. Santer, J.M. Blanchard, et al. "Locust's looming detectors for robot sensors". In: *Sensors and sensing in biology and engineering*. Springer, 2003, pp. 237–250 (cit. on p. 56).

[187] W. Rone and P. Ben-Tzvi. "Mapping, localization and motion planning in mobile multi-robotic systems". In: *Robotica* 31.1 (2013), pp. 1–23 (cit. on pp. 31, 35).

[188] S. Roth and M.J. Black. "On the spatial statistics of optical flow". In: *International Journal of Computer Vision* 74.1 (2007), pp. 33–50 (cit. on p. 49).

[189] F.L. Roubieu, F. Expert, G. Sabiron, et al. "Two-Directional 1-g Visual Motion Sensor Inspired by the Fly' s Eye". In: *IEEE Sensors* 13.3 (2013), pp. 1025–1035 (cit. on p. 97).

[190] F.L. Roubieu, J. Serres, F. Colonnier, et al. "A biomimetic vision-based hovercraft accounts for bees' complex behaviour in various corridors". In: *Bioinspiration & biomimetics* 9.3 (2014), p. 036003 (cit. on pp. 56, 58).

[191] F.L. Roubieu, J. Serres, N. Franceschini, et al. "A fully-autonomous hovercraft inspired by bees: Wall following and speed control in straight and tapered corridors". In: *2012 IEEE International Conference on Robotics and Biomimetics, ROBIO 2012* Robio (2012), pp. 1311–1318 (cit. on p. 56).

[192] F. Ruffier and N. Franceschini. "Optic flow regulation: The key to aircraft automatic guidance". In: *Robotics and Autonomous Systems* 50.4 (2005), pp. 177–194 (cit. on pp. 53–56, 69, 96, 115, 148, 175).

[193] F. Ruffier and N. Franceschini. "Aerial robot piloted in steep relief by optic flow sensors". In: *2008 IEEE/RSJ International Conference on Intelligent Robots and Systems*. IEEE. 2008, pp. 1266–1273 (cit. on pp. 52, 53).

[194] F. Ruffier and N. Franceschini. "Optic flow regulation in unsteady environments: A tethered MAV achieves terrain following and targeted landing over a moving platform". In: *Journal of Intelligent & Robotic Systems* 79.2 (2015), pp. 275–293 (cit. on pp. 54, 56, 175).

[195] F. Ruffier, J. Serres, G. Masson, et al. "A bee in the corridor: regulating the optic flow on one side". In: *31st Göttingen Neurobiology Conference-7th Meeting of the German Neuroscience Society*. T14-7B. 2007 (cit. on p. 48).

[196] F. Ruffier, S. Viollet, S. Amic, et al. "Bio-inspired optical flow circuits for the visual guidance of micro air vehicles". In: *Proceedings of the 2003 International Symposium on Circuits and Systems, 2003. ISCAS '03.* 3 (2003), pp. 846–849 (cit. on pp. 53, 56).

[197] G. Sabiron, P. Chavent, T. Raharijaona, et al. "Low-speed optic-flow sensor onboard an unmanned helicopter flying outside over fields". In: *Proceedings - IEEE International Conference on Robotics and Automation* (2013), pp. 1742–1749 (cit. on p. 97).

[198] C.M. Sabo, A. Cope, K. Gurney, et al. "Bio-inspired visual navigation for a quadcopter using optic flow". In: *AIAA Infotech@ Aerospace*. 2016, p. 0404 (cit. on pp. 54, 56, 175).

[199] A. Sanchez, A. de Castro, S. Elvira, et al. "Autonomous indoor ultrasonic positioning system based on a low-cost conditioning circuit". In: *Measurement* 45.3 (2012), pp. 276–283 (cit. on p. 35).

[200] J. Santos-Victor, G. Sandini, F. Curotto, et al. "Divergent stereo in autonomous navigation: From bees to robots". In: *International Journal of Computer Vision* 14.2 (1995), pp. 159–177 (cit. on pp. 53, 55).

[201] R. Savita and M.M. Trigunayat. "First checklist of observations on the moth diversity (Lepidoptera: Heterocera) in and around Jaipur city, Rajasthan, India". In: *International Journal of Entomology Research* 6.2 (2021), pp. 39–45 (cit. on pp. 61, 80, 148, 170, 176).

[202] A. Saxena, J. Schulte, A.Y. Ng, et al. "Depth Estimation Using Monocular and Stereo Cues." In: *IJCAI*. Vol. 7. 2007, pp. 2197–2203 (cit. on p. 96).

[203] D. Scaramuzza and F. Fraundorfer. "Visual Odometry [Tutorial]". In: *IEEE Robotics & Automation Magazine* 18.4 (2011), pp. 80–92. DOI: 10.1109/MRA.2011.943233 (cit. on pp. 35, 37, 173).

[204] D. Scaramuzza, F. Fraundorfer, and M. Pollefeys. "Closing the loop in appearance-guided omnidirectional visual odometry by using vocabulary trees". In: *Robotics and Autonomous Systems* 58.6 (2010), pp. 820–827 (cit. on p. 37).

[205] D. Scaramuzza and R. Siegwart. "Appearance-guided monocular omnidirectional visual odometry for outdoor ground vehicles". In: *IEEE transactions on robotics* 24.5 (2008), pp. 1015–1026 (cit. on p. 37).

[206] T.D. Seeley and W.F. Towne. "Tactics of dance choice in honey bees: do foragers compare dances?" In: *Behavioral Ecology and Sociobiology* 30.1 (1992), pp. 59–69 (cit. on p. 79).

[207] J. Serres, D. Dray, F. Ruffier, et al. "A vision-based autopilot for a miniature air vehicle: joint speed control and lateral obstacle avoidance". In: *Autonomous robots* 25.1 (2008), pp. 103–122 (cit. on pp. 47, 55).

[208] J. Serres, T.J. Evans, S. Åkesson, et al. "Optic flow cues help explain altitude control over sea in freely flying gulls". In: *Journal of the Royal Society Interface* 16.159 (2019), p. 20190486 (cit. on p. 81).

[209] J. Serres and F. Ruffier. "Optic flow-based collision-free strategies: From insects to robots". In: *Arthropod structure & development* 46.5 (2017), pp. 703–717 (cit. on pp. 46, 48, 53, 54, 96, 115, 148, 174, 175).

[210] J. Serres, F. Ruffier, and N. Franceschini. "Two optic flow regulators for speed control and obstacle avoidance". In: *The First IEEE/RAS-EMBS International Conference on Biomedical Robotics and Biomechatronics, 2006. BioRob 2006.* IEEE. 2006, pp. 750–757 (cit. on pp. 47, 55).

[211] J.R. Serres, G.P. Masson, F. Ruffier, et al. "A bee in the corridor: centering and wall-following". In: *Naturwissenschaften* 95.12 (2008), pp. 1181–1187 (cit. on pp. 46–48, 115).

[212] J.R. Serres and F. Ruffier. "Biomimetic autopilot based on minimalistic motion vision for navigating along corridors comprising U-shaped and S-shaped turns". In: *Journal of Bionic Engineering* 12.1 (2015), pp. 47–60 (cit. on p. 57).

[213] A. Shurin and I. Klein. "QDR: A Quadrotor Dead Reckoning Framework". In: *IEEE Access* 8 (2020), pp. 204433–204440 (cit. on pp. 32, 33, 115).

[214] R. Siddiqui and S. Khatibi. "Visual tracking using particle swarm optimization". In: *arXiv preprint arXiv:1401.4648* (2014) (cit. on p. 37).

[215] D. Soccol, S. Thurrowgood, and M.V. Srinivasan. "A vision system for optic-flow-based guidance of UAVs". In: *Proceedings of the Australasian Conference on Robotics and Automation*. 2007 (cit. on p. 49).

[216] A. Souici, M. Courdesses, A. Ouldali, et al. "Full-observability analysis and implementation of the general SLAM model". In: *International journal of systems science* 44.3 (2013), pp. 568–581 (cit. on p. 38).

[217] M. V. Srinivasan, S. Zhang, and J. S. Chahl. "Landing strategies in honeybees, and possible applications to autonomous airborne vehicles". In: *The Biological Bulletin* 200.2 (2001), pp. 216–221 (cit. on p. 169).

[218] M.V. Srinivasan. "Honeybees as a model for the study of visually guided flight, navigation, and biologically inspired robotics". In: *Physiological reviews* 91.2 (2011), pp. 413–460 (cit. on pp. 53, 174).

[219] M.V. Srinivasan. “Going with the flow: a brief history of the study of the honeybee’s navigational ‘odometer’”. In: *Journal of Comparative Physiology A* 200 (2014), pp. 563–573 (cit. on p. 168).

[220] M.V. Srinivasan. “Where paths meet and cross: navigation by path integration in the desert ant and the honeybee”. In: *Journal of Comparative Physiology A* 201 (2015), pp. 533–546 (cit. on p. 39).

[221] M.V. Srinivasan, J.S. Chahl, K. Weber, et al. “Robot navigation inspired by principles of insect vision”. In: *Robotics and Autonomous Systems* 26.2-3 (1999), pp. 203–216 (cit. on pp. 29, 53).

[222] M.V. Srinivasan, M. Lehrer, W.H. Kirchner, et al. “Range perception through apparent image speed in freely flying honeybees”. In: *Visual neuroscience* 6.05 (1991), pp. 519–535 (cit. on pp. 47, 48).

[223] M.V. Srinivasan, S. Zhang, M. Altwein, et al. “Honeybee Navigation: Nature and Calibration of the" Odometer"”. In: *Science* 287.5454 (2000), pp. 851–853 (cit. on pp. 27, 29, 31, 48, 69, 79, 148, 170, 172).

[224] M.V. Srinivasan, S. Zhang, and N. Bidwell. “Visually mediated odometry in honeybees”. In: *Journal of Experimental Biology* 200.19 (1997), pp. 2513–2522 (cit. on pp. 29, 30, 63, 69, 79, 90, 148, 172).

[225] M.V. Srinivasan, S. Zhang, M. Lehrer, et al. “Honeybee navigation en route to the goal: visual flight control and odometry”. In: *Journal of Experimental Biology* 199.1 (1996), pp. 237–244 (cit. on pp. 29, 46–48, 63, 69, 79, 148, 169, 172).

[226] M.V. Srinivasan, S.-W. Zhang, J.S. Chahl, et al. “How honeybees make grazing landings on flat surfaces”. In: *Biological cybernetics* 83.3 (2000), pp. 171–183 (cit. on pp. 47, 48, 54, 69, 79, 169, 175).

[227] R.B. Srygley and E.G. Oliveira. “Orientation mechanisms and migration strategies within the flight boundary layer.” In: *Insect movement: mechanisms and consequences. Proceedings of the Royal Entomological Society’s 20th Symposium, London, UK, September 1999*. CABI Wallingford UK. 2001, pp. 183–206 (cit. on pp. 54, 61, 170, 175, 176).

[228] J. Stankiewicz and B. Webb. “Looking down: a model for visual route following in flying insects”. In: *Bioinspiration & Biomimetics* 16.5 (2021), p. 055007 (cit. on p. 29).

[229] F. Steinbrücker, J. Sturm, and D. Cremers. “Real-time visual odometry from dense RGB-D images”. In: *2011 IEEE international conference on computer vision workshops (ICCV Workshops)*. IEEE. 2011, pp. 719–722 (cit. on p. 37).

[230] T. Stone, B. Webb, A. Adden, et al. “An Anatomically Constrained Model for Path Integration in the Bee Brain”. In: *Current Biology* 27.20 (2017), 3069–3085.e11 (cit. on pp. 29, 69, 168).

[231] N.J. Strausfeld. *Arthropod brains: evolution, functional elegance, and historical significance*. Belknap Press, 2012 (cit. on p. 24).

[232] N.J. Strausfeld and U.K. Bassemir. "Lobula plate and ocellar interneurons converge onto a cluster of descending neurons leading to neck and leg motor neuropil in Calliphora erythrocephala". In: *Cell and tissue research* 240.3 (1985), pp. 617–640 (cit. on p. 24).

[233] A.D. Straw, S. Lee, and M.H. Dickinson. "Visual control of altitude in flying Drosophila". In: *Current Biology* 20.17 (2010), pp. 1550–1556 (cit. on p. 169).

[234] R. Strydom, S. Thurrowgood, and M.V. Srinivasan. "Visual odometry: autonomous uav navigation using optic flow and stereo". In: *Proceedings of Australasian conference on robotics and automation*. 2014 (cit. on pp. 37, 69, 114, 115).

[235] J. Sun, N.N. Zheng, and H.Y. Shum. "Stereo matching using belief propagation". In: *IEEE Transactions on pattern analysis and machine intelligence* 25.7 (2003), pp. 787–800 (cit. on p. 50).

[236] T. Takahashi. "2D localization of outdoor mobile robots using 3D laser range data". In: *Robotics Institute Carnegie Mellon University Pittsburgh, Pennsylvania* 15213 (2007) (cit. on p. 35).

[237] J.P. Tardif, Y. Pavlidis, and K. Daniilidis. "Monocular visual odometry in urban environments using an omnidirectional camera". In: *2008 IEEE/RSJ International Conference on Intelligent Robots and Systems*. IEEE. 2008, pp. 2531–2538 (cit. on p. 38).

[238] J. Tautz, S. Zhang, J. Spaethe, et al. "Honeybee odometry: performance in varying natural terrain". In: *PLoS Biol* 2.7 (2004), e211 (cit. on pp. 48, 49, 63, 69, 148, 169, 170, 172).

[239] G.K. Taylor and H.G. Krapp. "Sensory systems and flight stability: what do insects measure and why?" In: *Advances in insect physiology* 34 (2007), pp. 231–316 (cit. on p. 24).

[240] H. Tennekes. "The Logarithmic Wind Profile". In: *Journal of the Atmospheric Sciences* 30.2 (1973), pp. 234–238 (cit. on pp. 84, 156).

[241] A. Toth. *https://slideplayer.com/slide/5903985/*. 2007. URL: https://slideplayer.com/slide/5903985/ (visited on 10/2022) (cit. on p. 27).

[242] O. Tretiak. "Velocity estimation from image sequence with second order differential operatios". In: *Proc. Int. Conf. Pattern Recognition*. 1984, pp. 16–19 (cit. on p. 49).

[243] D. Valiente García, Lo. Fernández Rojo, A. Gil Aparicio, et al. "Visual odometry through appearance-and feature-based method with omnidirectional images". In: *Journal of Robotics* 2012 (2012) (cit. on p. 36).

[244] F. Van Breugel, K. Morgansen, and M.H. Dickinson. "Monocular distance estimation from optic flow during active landing maneuvers". In: *Bioinspiration & biomimetics* 9.2 (2014), p. 025002 (cit. on pp. 69, 96, 115, 148).

[245] E. Vanhoutte, S. Mafrica, F. Ruffier, et al. "Time-of-travel methods for measuring optical flow on board a micro flying robot". In: *Sensors* 17.3 (2017), p. 571 (cit. on p. 97).

[246] A.R. Vidal, H. Rebecq, T. Horstschaefer, et al. "Ultimate SLAM? Combining events, images, and IMU for robust visual SLAM in HDR and high-speed scenarios". In: *IEEE Robotics and Automation Letters* 3.2 (2018), pp. 994–1001 (cit. on pp. 37, 114, 115).

[247] K. Von Frisch. *The dance language and orientation of bees*. Havard University Press, Cambridge, Massachusetts USA, London, England, UK., 1967 (cit. on pp. 25–28, 68, 79, 148, 168, 171, 172).

[248] M.R. Walter, R.M. Eustice, and J.J. Leonard. "Exactly sparse extended information filters for feature-based SLAM". In: *The International Journal of Robotics Research* 26.4 (2007), pp. 335–359 (cit. on p. 38).

[249] D. Wang, H. Liang, H. Zhu, et al. "A bionic camera-based polarization navigation sensor". In: *Sensors* 14.7 (2014), pp. 13006–13023 (cit. on pp. 31, 34).

[250] B. Webb. "Neural mechanisms for prediction: do insects have forward models?" In: *Trends in Neurosciences* 27.5 (2004), pp. 278–282 (cit. on p. 81).

[251] B. Webb and A. Wystrach. "Neural mechanisms of insect navigation". In: *Current Opinion in Insect Science* 15 (2016), pp. 27–39 (cit. on pp. 53, 174).

[252] K. Weber, S. Venkatesh, and M.V. Srinivasan. "Insect inspired behaviours for the autonomous control of mobile robots". In: *Proceedings of 13th International Conference on Pattern Recognition*. Vol. 1. IEEE. 1996, pp. 156–160 (cit. on pp. 29, 56).

[253] A. Wedel, D. Cremers, T. Pock, et al. "Structure-and motion-adaptive regularization for high accuracy optic flow". In: *2009 IEEE 12th International Conference on Computer Vision*. IEEE. 2009, pp. 1663–1668 (cit. on p. 50).

[254] A.M. Wenner. "The flight speed of honeybees: a quantitative approach". In: *Journal of Apicultural Research* 2.1 (1963), pp. 25–32 (cit. on p. 74).

[255] T. Whelan, H. Johannsson, M. Kaess, et al. "Robust real-time visual odometry for dense RGB-D mapping". In: *2013 IEEE International Conference on Robotics and Automation*. IEEE. 2013, pp. 5724–5731 (cit. on p. 38).

[256] T.C.D. Whiteside and G.D. Samuel. "Blur zone". In: *Nature* 225.5227 (1970), pp. 94–95 (cit. on pp. 45, 62, 176).

[257] S. Woodhall. *Field guide to butterflies of South Africa*. Bloomsbury Publishing, Struik Nature, Cape town, South Africa., 2020 (cit. on pp. 61, 80, 148, 170, 176).

[258] O.J. Woodman. *An introduction to inertial navigation*. Tech. rep. University of Cambridge, Computer Laboratory, 2007 (cit. on p. 31).

[259] F. Xiao, P. Zheng, J. di Tria, et al. "Optic flow-based reactive collision prevention for mavs using the fictitious obstacle hypothesis". In: *IEEE Robotics and Automation Letters* 6.2 (2021), pp. 3144–3151 (cit. on p. 56).

[260] Y. Yu, C. Pradalier, and G. Zong. "Appearance-based monocular visual odometry for ground vehicles". In: *2011 IEEE/ASME International Conference on Advanced Intelligent Mechatronics (AIM)*. IEEE. 2011, pp. 862–867 (cit. on pp. 37, 38, 173).

[261] J. Zeil. "Visual navigation: properties, acquisition and use of views". In: *Journal of Comparative Physiology A* (2022), pp. 1–16 (cit. on p. 23).

[262] J. Zhang, S. Singh, and G. Kantor. "Robust monocular visual odometry for a ground vehicle in undulating terrain". In: *Field and service robotics*. Springer. 2014, pp. 311–326 (cit. on p. 36).

[263] S.W. Zhang, W. Xiang, L. Zili, et al. "Visual tracking of moving targets by freely flying honeybees". In: *Visual neuroscience* 4.4 (1990), pp. 379–386 (cit. on pp. 48, 54, 169, 175).

[264] H. Zimmer, A. Bruhn, J. Weickert, et al. "Complementary optic flow". In: *International Workshop on Energy Minimization Methods in Computer Vision and Pattern Recognition*. Springer. 2009, pp. 207–220 (cit. on p. 50).

[265] J.C. Zufferey and D. Floreano. "Toward 30-gram autonomous indoor aircraft: Vision-based obstacle avoidance and altitude control". In: *Proceedings of the 2005 IEEE International Conference on Robotics and Automation*. IEEE. 2005, pp. 2594–2599 (cit. on p. 56).

[266] J.C. Zufferey and D. Floreano. "Fly-inspired visual steering of an ultralight indoor aircraft". In: *IEEE Transactions on Robotics* 22.1 (2006), pp. 137–146 (cit. on p. 52).